Decoding Signs of Life

Gas-phase FT-IR Analysis of Microbial Biosignature in Simulated Exoplanetary Environments

AE5822: Master Thesis

Shristi Santosh

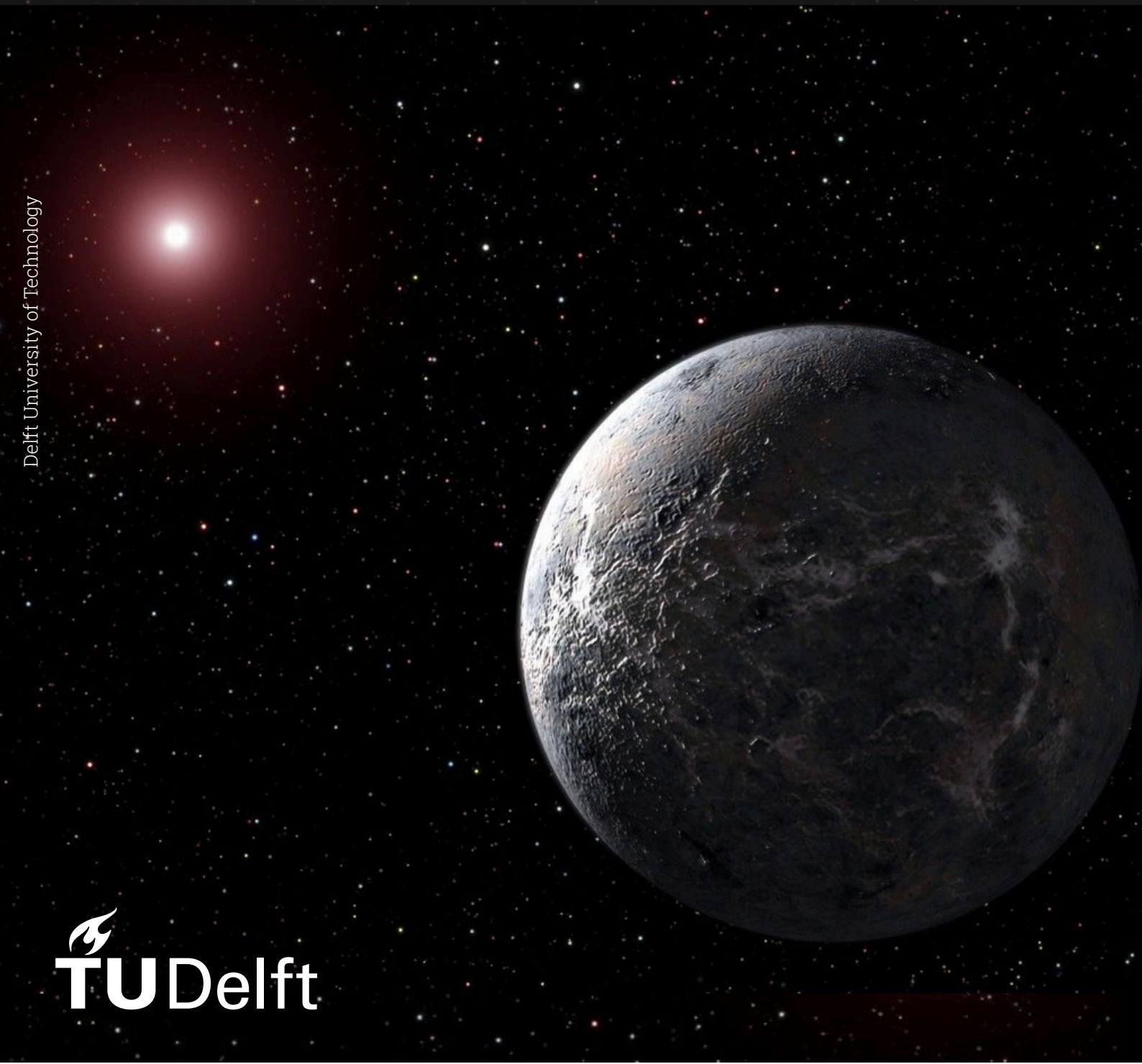

Delft University of Technology

TU Delft

Decoding Signs of Life

Gas-phase FT-IR Analysis of Microbial Biosignature in Simulated Exoplanetary Environments

by

Shristi Santosh

6196195

Thesis Committee:

Chair:	Dr. Rudolf Saathof
Supervisor:	Dr. Niels Ligterink
	Wouter van Straalen
External Examiner:	Prof. Kunal Masania
Project Duration:	November 2025 - July, 2026
Faculty:	Faculty of Aerospace Engineering, Delft

Cover:	Illustration of icy world orbiting a distant star, NASA
Style:	TU Delft Report Style, with modifications.

TU Delft

Preface and Acknowledgement

This thesis has been an incredibly transformative experience. Never in my wildest dreams did I imagine working with microorganisms as part of a Master's degree in Aerospace Engineering at TU DELFT in the Netherlands. My fascination with planetary science and looking for life elsewhere is what led me to pursue this crazy, yet deeply rewarding, direction for my thesis.

I am profoundly grateful to Dr. Niels Ligterink for being such a supportive supervisor, both within the scope of this thesis and regarding career advice and beyond. His advice to "be pragmatic" when approaching experimental work is a lesson I will value far outside of academics. His enthusiasm for the subject, deep involvement, and guidance made this a truly enriching learning experience, where even the most unconventional ideas were met with encouragement.

The support of Wouter van Straalen was equally crucial during the entire course of this thesis. He provided constant encouragement at every step of this journey, and the regular constructive feedback from both of my supervisors helped me push my limits and overcome the unique challenges encountered during this work. I always walked out of each thesis update meeting with a sense of calmness, clarity, a clear step forward, and a genuine curiosity to learn more.

During the initial stages of this research, critical insights into extremophiles and microbial cultivation were provided by Dr. Marta Cortesão and her team at the University of Porto. I am also grateful to Dr. Robbert Kleerebezem, Associate Professor in Environmental Biotechnology at TU Delft, for his ideas regarding the experimental setup and for patiently answering my queries. I extend my thanks to Dr. Santiago Garcia Espallargas from the Department of Aerospace Engineering at TU Delft for his valuable inputs on microalgal characteristics and metabolism, and to Dr. Marrick Braam from the University of Bern for his insights into the atmospheres of planets and icy moons. Sharing their knowledge on prebiotic chemistry was foundational in helping me understand these concepts and effectively shape the direction of this thesis.

I am extremely grateful to Christiaan Snaathorst for teaching me how to keep these microorganisms happy, alive and healthy. I also want to thank Ramon ter Horst and Mascha Slingerland, who patiently put up with my endless questions, helped me whenever I was stuck, and ensured I could set up my experiments safely. Additionally, I would like to extend my thanks to Mojtaba Raouf Hajar Zarrin, and Fabrizio Giordano for providing key insights into the inner workings and operation of the FTIR spectrometer.

I am incredibly thankful to my *Amma*, *Appa* and Sanskriti for their relentless support and unconditional love. Without their sacrifices and their commitment to providing me with the best possible education, pursuing this degree at one of the world's leading universities would not have been possible.

Finally, I am grateful to Shresth who has been my cheerleader throughout. I thank my friends who stayed by my side during the most challenging times, constantly reassuring me and pushing me to keep moving forward. Thank you all for the extended lunch breaks, the lively discussions in the laboratory, the collaborative brainstorming sessions, and the continuous positive energy.

I am grateful to everyone who supported me directly or indirectly throughout this journey and helped me grow into a more confident individual and even a better researcher. It has truly been a wild ride.

Shristi Santosh
Delft, July 2026

Summary

The search for extraterrestrial life relies fundamentally on the remote detection of atmospheric biosignatures. As observational technologies such as the James Webb Space Telescope (JWST) advance the chemical characterisation of exoplanetary atmospheres, interpreting these distant signals requires rigorous terrestrial analogues. This thesis systematically evaluates the empirical detection limits of primary metabolic gases and trace biogenic volatile organic compounds (VOCs) released by microorganisms when subjected to severe, exoplanet-analogue environmental stresses.

The research established a modular, closed-loop gas-phase Fourier-transform infra-red (FT-IR) spectroscopy system to monitor the metabolic emissions of two distinct microbial models: the heterotrophic yeast *Saccharomyces cerevisiae* and the photosynthetic marine diatom *Cylindrotheca fusiformis*. These organisms were subjected to standard Earth conditions, an anoxic (nitrogen-dominated) atmosphere, and an oxidative environment induced by hydrogen peroxide (H_2O_2). Discrete interval sampling was employed to capture time-resolved headspace profiles, while morphological changes were tracked via optical microscopy.

Under Earth-like conditions, the spectral profiles for both organisms were dominated by stable carbon dioxide (CO_2) and water vapour (H_2O) absorption bands. However, the introduction of environmental stressors revealed highly dynamic, metabolism-dependent gaseous responses. Under nitrogen-induced anoxia, *S. cerevisiae* exhibited a reduction in CO_2 evolution punctuated by transient metabolic bursts, reflecting a shift to endogenous fermentation. In contrast, the phototrophic *C. fusiformis* maintained a stable CO_2 baseline, indicating a complex physiological adaptation where reductions in active carbon fixation balanced the decline in respiratory outgassing. Under severe oxidative stress, both species exhibited a multi-phase decline in CO_2 evolution, including a hyper-respiratory “last stand” by the yeast ultimately leading to metabolic arrest and physical cellular degradation (plasmolysis).

Crucially, despite macroscopic evidence of severe cellular stress and degradation, secondary trace VOC biomarkers (such as acetic acid or acetaldehyde) remained undetected within the target spectral windows. This absence is attributed to the inherent physical limitations of the short path-length (10 cm) gas cell, severe spectral masking by background water vapour, and the transient, non-linear nature of biological outgassing. As organisms trigger internal regulatory mechanisms to mitigate stress, they frequently shift into low-emission survival modes or recycle their own volatile waste, effectively dropping biogenic emissions below standard detection thresholds.

These laboratory findings carry direct implications for astrobiological surveys. They demonstrate that biological gaseous outputs are highly transient and that relying on discrete, snapshot observations of a single atmospheric component risks yielding false negatives. Consequently, the absence of trace non-equilibrium gases in an exoplanetary atmosphere cannot be used to definitively rule out the presence of life. Future biosignature detection strategies must integrate continuous, multi-wavelength observations capable of tracking dynamic temporal and stress-induced atmospheric fluxes, shifting the analytical focus from static chemical profiles to holistic planetary metabolisms.

Contents

List of Figures

List of Tables

Nomenclature

Abbreviations

Abbreviation	Definition
ARPLS	Asymmetric Reweighted Penalized Least Squares
ATP	Adenosine Triphosphate
ATR	Attenuated Total Reflectance
CFU	Colony Forming Units
CHZ	Continuous Habitable Zone
CIA	Collision-Induced Absorption
CLS-NNLS	Classical Least Squares with a Non-Negative Constraint
CMB	Cosmic Microwave Background
CVA	Canonical Variate Analysis
ELT	Extremely Large Telescope
EM	Electromagnetic
EPS	Extracellular Polymeric Substances
ESA	European Space Agency
EUV	Extreme Ultraviolet
FFT	Fast Fourier Transform
FT-IR	Fourier-Transform Infrared
FWHM	Full Width at Half Maximum
GC-MS	Gas Chromatography-Mass Spectrometry
HAPI	HITRAN Application Programming Interface
HITRAN	High-resolution Transmission molecular absorption database
HPLC-FD	High Performance Liquid Chromatography with Fluorescence Detection
HZ	Habitable Zone
ILS	Instrumental Line Shape
IR	Infrared
IRS	Infrared Spectroscopy
JWST	James Webb Space Telescope
LED	Light Emitting Diode
LN-MCT	Liquid Nitrogen-cooled Mercury Cadmium Telluride
LOD	Limit of Detection
LOOH	Lipid Hydroperoxide
MCMC	Markov Chain Monte Carlo
MDA	Malondialdehyde
MDC	Minimum Detectable Concentration
MFC	Mass Flow Controller
MIP	Minimum Inhibitory Pressure
mVOC	Microbial Volatile Organic Compound
NADPH	Nicotinamide Adenine Dinucleotide Phosphate
NASA	National Aeronautics and Space Administration
NHEJ	Non-Homologous End Joining
NIST	National Institute of Standards and Technology
OVOC	Oxygenated Volatile Organic Compound
PCA	Principal Component Analysis
PCD	Programmed Cell Death
PNNL	Pacific Northwest National Laboratory

Abbreviation	Definition
ppb	parts-per-billion
ppm	parts-per-million
PVA	Polyvinyl Alcohol
QED	Quantum Electrodynamics
QqQ-MS	Triple Quadrupole Mass Spectrometry
RMS	Root-Mean-Square
ROS	Reactive Oxygen Species
SASP	Small Acid Soluble Spore Proteins
SETI	Search for Extraterrestrial Intelligence
SIMCA	Soft Independent Modeling of Class Analogy
S-MIF	Sulfur Isotope Mass-Independent Fractionation
SNR	Signal-to-Noise Ratio
SP	Spore Photoproduct
SPL	Spore Photoproduct Lyase
TGO	Trace Gas Orbiter
UV	Ultraviolet
VOC	Volatile Organic Compound
VOSC	Volatile Sulfur Compound
YPD	Yeast Peptone Dextrose

Symbols

Symbol	Definition	Unit
Latin Symbols		
A	Absorbance	[AU]
B	Magnetic flux density (Magnetic field)	[T]
c	Sample concentration	[mol/L]
E	Energy	[J]
$\mathbf{E}$	Electric field vector	[V/m]
E_{el}	Electronic energy	[J]
E_{rot}	Rotational energy	[J]
E_{vib}	Vibrational energy	[J]
f_{ILS}	Instrumental attenuation factor	[-]
$F(J)$	Rotational term symbol	[cm^{-1}] or [Hz]
I	Moment of inertia	[kg·m^2]
I	Radiant power / Intensity	[W/m^2]
J	Current density	[A/m^2]
J	Rotational quantum number	[-]
k	Force constant	[N/m]
l or L_{path}	Optical path length	[m] or [cm]
m	Mass	[kg]
M	Molecular mass	[g/mol]
n	Molecular number density	[molecules/cm^3]
N	Number of atoms / total instances	[-]
N_{col}	Column density	[molecules/cm^2]
P	Pressure	[Pa] or [mbar]
q_i	Magnitude of charge	[C]
r	Displacement from equilibrium	[m]
R	Internuclear distance	[m]
R_e	Equilibrium bond length	[m]
S	Spectral line strength	[cm/molecule]
t	Time	[s]

Symbol	Definition	Unit
T	Temperature	[K]
v	Vibrational quantum number	[-]
V	Potential Energy	[J]
V	Volume	[m^3]
w_i	Statistical weight	[-]
Greek Symbols		
γ_L	Lorentzian half-width	[cm^{-1}]
Δ	Difference / change operator	[-]
ϵ	Molar extinction coefficient	[L/(mol·cm)]
θ	Angle / Similarity phase	[rad]
λ	Wavelength	[m] or [μm]
μ	Reduced mass	[kg]
$\vec{\mu}$	Dipole moment vector	[C·m]
ν	Frequency	[s^{-1}] or [Hz]
$\tilde{\nu}$	Wavenumber	[cm^{-1}]
ρ	Electric charge density	[C/m^3]
σ	Absorption cross-section	[cm^2/molecule]
σ_D	Doppler half-width (Gaussian std. dev.)	[cm^{-1}]
ω	Angular frequency	[rad/s]
ω_{osc}	Angular oscillation frequency	[rad/s]
∇	Divergence operator	[-]
$\nabla\times$	Curl operator	[-]

Physical Constants

Symbol	Constant Name	Value	Unit
c	Speed of light in vacuum	$299,792,458$	[m/s]
h	Planck's constant	$6.62607015 \times 10^{-34}$	[J·s]
$\hbar$	Reduced Planck's constant	$1.05457181 \times 10^{-34}$	[J·s]
k_B or k	Boltzmann constant	1.380649×10^{-23}	[J/K]
R	Universal gas constant	8.314462618	[J/(mol·K)]
ϵ_0	Permittivity of free space	$\approx 8.854 \times 10^{-12}$	[F/m]
μ_0	Permeability of free space	$\approx 1.256 \times 10^{-6}$	[N/A^2]

1

Introduction

The document opens with the preface and acknowledgments, followed by a brief summary of the entire work. The main body is structured into three parts. Part 1 comprises the literature review, which is divided into separate chapters that establish the theoretical foundation for the research. These chapters cover overarching concepts, including the fundamentals of astrobiology and biosignatures, the survival of extremophiles in diverse planetary environments, microbial stress responses, the physical basics of light-matter interaction, and analogue experiments. This extensive literature survey led to the definition of the research questions and the methodologies required to answer them.

Once this guiding framework is established, Part 2 presents the core research in the format of a standalone scientific paper. This section encompasses an abstract, materials and methods, results, discussion, and future work. The methodology section systematically details the practical execution of the research. This includes the selection of specific experimental parameters, such as the model microorganisms, the nature of the applied environmental stressors, and the precise instrumental configurations of the FT-IR spectrometer. Furthermore, it outlines the engineering and assembly of the gas-tight, closed-system bioreactor apparatus designed for non-invasive headspace tracking.

Following the experimental outline, the results section presents the empirical findings and their corresponding inferences. Here, the spectral plots obtained from the FT-IR headspace analysis are correlated directly with microscopic evaluations of the microorganisms' changing cellular morphology and metabolic states. Next, the discussion places these localized laboratory findings into a broader astrobiological context, evaluating the implications for detecting life on distant worlds. This section critically examines the technical and temporal limitations identified during testing and provides an actionable blueprint for future engineering and computational upgrades to overcome these constraints. The paper also includes supporting appendices (Appendix A, Appendix B), which contain a detailed explanation of the development of the infra-red spectrum simulator and the complete data analysis pipeline used to analyze the spectra.

In Part 3, supplementary results are presented, wherein the liquid-phase FT-IR results are analyzed and discussed. Finally, the document ends with the overall conclusion of the entire thesis. The references for Parts 1 and 3 are provided at the end of the document, while the references for the scientific paper are contained within Part 2 itself.

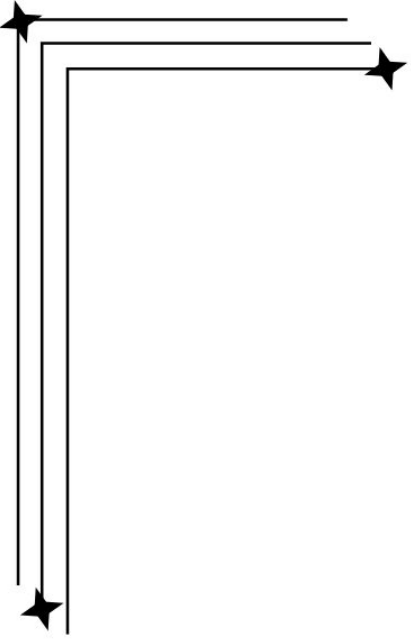

Part 1: Literature Review

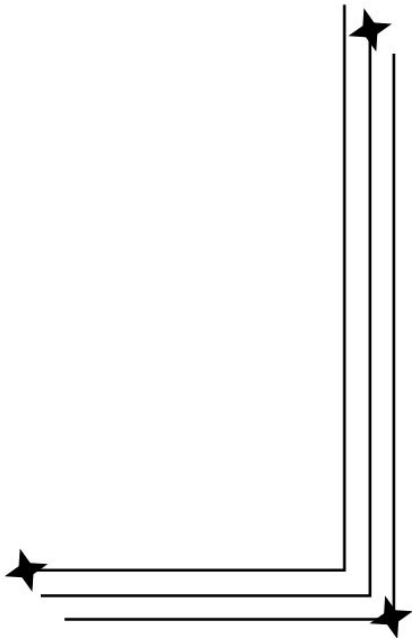

2

Introduction to Literature Review

The central objective of this thesis is to evaluate the detection limits of trace volatile organic compounds (VOCs) released by microorganisms when subjected to extreme environmental stress, particularly under conditions mimicking potential habitats within the Solar System and beyond. To achieve this, the investigation was conducted systematically, beginning with a comprehensive, multi-layered literature review in which each governing principle and core concept is explored in a dedicated chapter.

The foundational framework is established in chapter 3, which introduces the field of astrobiology and examines the planetary environments necessary for habitability. This chapter explores the concept of the habitable zone and the atmospheric conditions of planetary bodies within our Solar System including early Earth, Mars, and Venus as well as icy moons like Titan and some exoplanetary systems.

Expanding from these planetary scales to the biological level, chapter 4 focuses on the search for life. It defines biosignatures and classifies extremophiles based on their survival characteristics. This chapter closely analyses the biological mechanisms that allow life to adapt to Earth's most hostile environments, before identifying the primary challenges of detecting such signatures elsewhere. It further evaluates the observational limitations that hinder our ability to validate potential life-detection claims across astronomical distances.

Combining the biological insights of the earlier chapters with an understanding of the limits of survival, chapter 5 highlights methods for inducing environmental stress within a laboratory setting, taking into account experimental feasibility, and describes the possible volatiles generated in response to this stress. It largely discusses stress resulting from the absence of oxygen in the atmosphere and the oxidative stress.

Then the next step is to accurately interpret these atmospheric signals, the underlying physics of data collection must be understood. chapter 6 reviews the fundamentals of photon-matter interactions, focusing on the principles of electromagnetic radiation and molecular spectroscopy. Particular emphasis is placed on infra-red (IR) spectroscopy and the mechanical and mathematical principles behind Fourier-Transform infra-red (FT-IR) systems. This chapter concludes with an analysis of the IR spectra of common volatile compounds, providing the necessary basis for the analytical methods employed in the experimental phase of this work.

Next, chapter 7 brings together the concepts required for setting up the experiments for this thesis and reviews the analogue methods and experiments that served as the direct inspiration for this work. By evaluating past experimental setups, testing conditions, and analytical conclusions, this chapter establishes the baseline context that shaped the experimental design of this study.

Ultimately, this comprehensive literature review serves as the essential synthesis of current knowledge required to bridge the gap between terrestrial microbial physiology and the remote characterisation of exoplanetary atmospheres. Based on the findings presented herein, the primary research question and four sub-questions are formulated and justified in chapter 8, which outlines the targeted approach used to address them.

3

Astrobiology and the Planetary Context

The literature review first examines the fundamental principles of astrobiology, framing them within the broader context of the search for extraterrestrial life. It is essential to determine where life could potentially exist before identifying specific signs of life . Therefore, the chapter begins by exploring the habitable zone, which defines the key astronomical and planetary requirements needed to support biological activity. Diverse extraterrestrial environments are examined as potential analogues, spanning from the inner planets of our Solar System (Venus, early Earth, and Mars) and the icy moon Titan to distant exoplanetary systems.

3.1. Astrobiology

Astrobiology seeks to understand how life began on Earth and to look for signs of life elsewhere in the universe (De Mol 2023). Historically, this field has been referred to as exobiology, astrobiology, bioastronomy, and cosmobiology (Brack 2012). Astrobiology has evolved significantly since the start of the new millennium. New theories, advanced technologies, and major discoveries have created an exciting range of opportunities for interdisciplinary research (Cottin et al. 2017). It also helps elucidate the key environmental parameters that enabled life to emerge on Earth (Cottin et al. 2017). To achieve this goal, it is important to determine the physical and chemical boundaries within which life can exist on Earth and to understand the biophysical traits that define those boundaries (Trent 2000). Insights into the origin and boundaries of life on Earth are now guiding how we search for life elsewhere in the Solar System and beyond (Cottin et al. 2017). The search for life beyond Earth requires an interdisciplinary approach, integrating chemistry, biology, geology, physics, and astronomy (Malaterre et al. 2023). The Copernican and Darwinian principles suggest that Earth is not unique and should not be regarded as the only planet capable of supporting environments where life can evolve through natural selection (Nascimento-Dias and Martinez-Frias 2023). Astrobiology further plays a crucial role in advancing our knowledge of planetary habitability (Méndez et al. 2021). The goal of astrobiology is to determine the distribution and diversity of life in the universe (H. B. Smith and Mathis 2023). It should be noted that astrobiology is distinct from the Search for Extraterrestrial Intelligence (SETI) (Helmreich 2006). To expand our understanding of life and its place in the universe, scientists utilise biosignatures to search for signs of past or present life (De Mol 2023).

3.2. Habitable Zone

The first step in the search for evidence of life is characterising the star–planet system (Edward W Schwieterman and Leung 2024). Figure 3.1 shows the Hertzsprung–Russell diagram, which plots a star's luminosity (intrinsic brightness) against its surface temperature, or alternatively its absolute magnitude against its colour or spectral type. This diagram helps scientists classify stars. Based on their spectral characteristics, stars are grouped into the O, B, A, F, G, K, and M types. Table 3.1

summarises the temperature ranges, masses relative to the Sun, and representative examples for each stellar spectral type. According to NASA, a star is considered a main-sequence star when it actively converts hydrogen into helium in its core, and about 90% of all stars in the universe belong to this group. These stars vary significantly in brightness, colour, and size, ranging from roughly one-tenth to nearly 200 times the mass of the Sun, and can exist for millions to billions of years.

Table 3.1: Spectral Types of Stars and Their Characteristics (Hinkel et al. 2024)

Spectral Type	Colour	Temperature Range	Mass ($M_\odot$)	Prevalence Among Main Sequence Stars	Examples
O	Blue-violet	$> 31{,}500$ K	> 18	0.00003%	Stars of Orion's Belt, Zeta Ophiuchi
B	Blue-white	$10{,}000$–$31{,}500$ K	2.7–18	0.13%	Rigel
A	White	$7{,}500$–$10{,}000$ K	1.7–2.7	0.6%	Sirius, Altair
F	Yellow-white	$6{,}000$–$7{,}500$ K	1.1–1.7	3%	Polaris, Procyon A
G	Yellow	$5{,}300$–$6{,}000$ K	0.9–1.1	7.6%	Sun
K	Orange	$3{,}900$–$5{,}300$ K	0.6–0.9	12.1%	Arcturus, Epsilon Indi
M	Red-orange	$2{,}300$–$3{,}700$ K	0.08–0.6	76.5%	Proxima Centauri, Betelgeuse

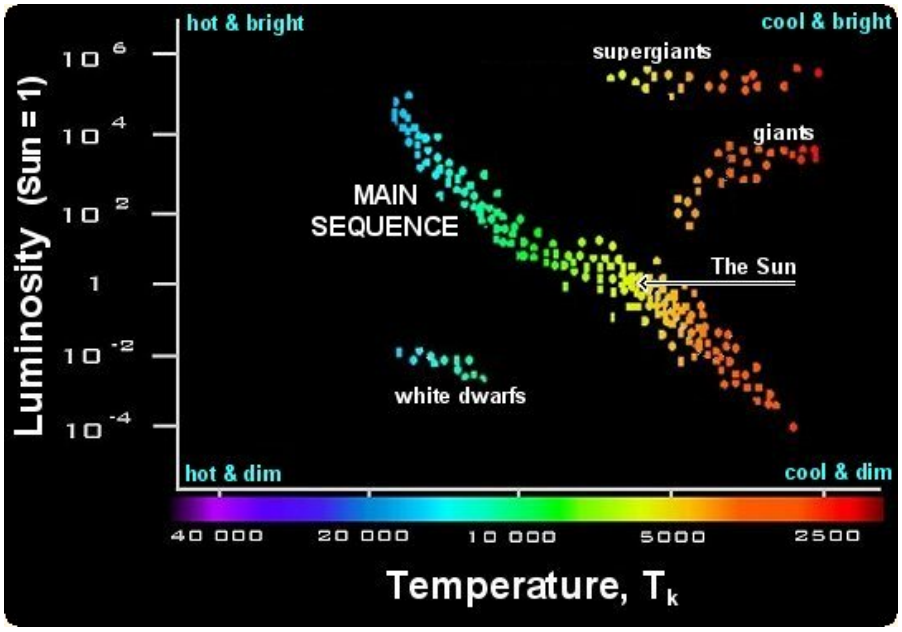

Figure 3.1: Hertzsprung Russell Diagram (credit: Western Washington University)

The habitable zone (HZ) is the region around a star where temperatures allow liquid water to exist on a planet's surface. Often referred to as the "Goldilocks zone", it identifies the area where conditions are neither too hot nor too cold, but potentially suitable for life. Although the definition of the HZ is highly debated, it still serves as a guiding framework for selecting promising planets or bodies for detailed observation. While simply being located within the HZ does not guarantee that a planet hosts life, it remains one of the most effective tools for identifying worlds with the potential for habitability (Ramirez 2018). The classical HZ concept considers environments suitable for both simple and more complex life forms, where "complex life" includes organisms such as higher plants, animals, and potentially intelligent beings (Ramirez 2018).

The width of the continuously habitable zone (CHZ) around a star depends on how long a planet must remain habitable and whether a frozen world could thaw as its host star progressively brightens. CHZs

around K- and M-type stars are generally wider than that of the Sun because these stars evolve more slowly. However, planets orbiting late K and M stars may still be unsuitable for life, as they often become tidally locked, with one side permanently facing the star. In contrast, F-type stars have much narrower CHZs due to their rapid evolution. Altogether, these findings suggest that mid-to-early K stars, along with G-type stars, represent the most promising stellar systems in the search for extraterrestrial life (James F Kasting et al. 1993). Pedbost et al. 2020 humorously define the "Really Habitable Zone" as "the region around a star where acceptable gin and tonics are likely to be abundant"[1]. Although planets outside the HZ could still support life, detecting biosignatures on such worlds via remote observation would be highly challenging (James F Kasting et al. 1993). The traditional definition of the habitable zone as a strict annulus with fixed radial boundaries is challenged by observations within our own Solar System. Notably, Jupiter's moon Europa and Saturn's moon Enceladus reside well outside this conventional region yet maintain subsurface liquid water, sustained by internal tidal heating rather than solar irradiation. Observing exoplanets is inherently difficult because they are significantly smaller and fainter than the stars they orbit. While current technology can effectively study Jupiter-sized giants, characterising habitable Earth-like worlds remains a major obstacle. However, recent breakthroughs in astrophotonics provide a crucial solution, offering the precision needed to analyse these smaller targets and search for potential signs of life (Guyon 2017). Recent theoretical models examining the super-Earth LHS 1140b by Wunderlich et al. 2021 reveal significant hurdles in the search for atmospheric biosignatures. Even under ideal, cloud-free conditions, detecting potential biomarkers such as ammonia, phosphine, chloromethane, and nitrous oxide would necessitate 10 to 50 transit observations, translating to 40–200 hours of JWST time. However, logistical constraints regarding the system's visibility mean that accumulating this data could take nearly a decade. These challenges are further compounded by atmospheric realities: the likely presence of signal dampening clouds or hazes, common on small exoplanets, would drastically increase the required observation time. Moreover, the spectral signatures of these gases frequently overlap with dominant background signals from methane or carbon dioxide, making definitive identification difficult.

3.3. Planetary Environment

The composition of a planet's atmosphere plays a major role in shaping its climate, influencing both its potential to support life and the rates of key geochemical processes (Casey and White 2018). This section discusses the evolution of atmospheric compositions, the gases detected, and the potential gases that can be linked to the presence of life.

Within the Solar System

Although Venus, Earth, and Mars formed at different distances from the Sun, they evolved under the same early solar activity and therefore must be described consistently within a unified model of the Sun's past. To better understand how their early atmospheres formed and changed, it is essential to improve our knowledge of the young Sun, particularly its extreme ultraviolet (EUV) radiation output during the first billion years. Each of the terrestrial planets still carries distinct signatures that reflect the early history of the Solar System. Yet, to this day, the exact evolutionary path of the Sun in terms of high-energy radiation remains unknown (Lammer et al. 2018).

The terrestrial planets in the Solar System are Mercury, Venus, Earth, and Mars. In Table 3.2, the present-day atmospheric components are compared between these planets. Their atmospheres have been shaped by the volatile materials they originally acquired and by billions of years of subsequent evolution. Unlike the gas giants, which retain much of the primordial gas they captured from the solar nebula, terrestrial planets rapidly lost their initial hydrogen-rich atmospheres. They later developed secondary atmospheres through processes such as outgassing, volcanic activity, and impacts from comets and asteroids. As a result, the atmospheric composition of any terrestrial planet depends strongly on the volatile material delivered during its formation. These early atmospheres were then further modified by photochemical reactions, interactions with the planet's surface and interior, and atmospheric escape processes (Seager and V. Meadows 2010).

Mercury, however, possesses an extremely thin, almost non-existent atmosphere known as an exosphere, which offers no real stability or protection. Because it lacks a substantial atmosphere capable

[1] This is from an April Fool's Day paper

of sustaining or preserving any form of life, Mercury is not considered a promising target in the search for life and is therefore excluded from further discussion.

Table 3.2: Comparison of major atmospheric species on Venus (V. I. Oyama et al. 1980), Earth (NOAA Earth System Research Laboratory), and Mars (Webster et al. 2013)

Species	Venus	Earth	Mars
CO_2	96.5%	0.0407%[a]	95.97%
N_2	3.5%	78.084%	1.89%
O_2	$\ll$	20.946%	0.146%
Ar	70 ppm	0.9340%	1.93%
SO_2	150 ppm	–	–

[a] An estimated 60–80 bar worth of CO_2 is stored in Earth's crust as carbonate minerals (David C Catling and Kevin J Zahnle 2020).

3.3.1. Early Earth

The Archean eon precedes the Proterozoic eon, which spans from 2.5 billion years ago to about 541 million years ago. The Archean itself is divided into four eras that frame the timeline for this discussion: the Eoarchean (4.0–3.6 Ga), Paleoarchean (3.6–3.2 Ga), Mesoarchean (3.2–2.8 Ga), and Neoarchean (2.8–2.5 Ga) (David C Catling and Kevin J Zahnle 2020). The most notable feature of the Archean eon was the almost complete absence of O_2, in contrast to modern Earth's atmosphere, which is composed of roughly 21% O_2, 78% N_2, 0.9% Ar, and 0.1% trace gases by dry volume. The surface O_2 levels were less than one-millionth of today's values, while N_2 concentrations were comparable to modern levels or perhaps somewhat lower. In contrast, CO_2 and CH_4 concentrations were much higher, approximately 10–2,500 times and 100–10,000 times present-day levels, respectively (David C Catling and Kevin J Zahnle 2020). Approximately 2.45 billion years ago, atmospheric O_2 experienced a rapid increase, a transition now known as the Great Oxidation Event (Sessions et al. 2009). Biologically significant molecules can form readily in an atmosphere that is strongly reducing, such as one rich in methane and ammonia (Millerl 1953; Chyba and Sagan 1997). (Harrison et al. 2017) suggest that life on Earth originated during the Hadean period. The Hadean eon is an informal subdivision of Precambrian time that spans from roughly 4.6 billion to 4.0 billion years ago (David C Catling and Kevin J Zahnle 2020).

Table 3.3 shows the Archean environmental constraints, including limits on atmospheric gases at the surface (unless noted otherwise) as well as certain marine species. Gas concentrations are reported in the units used in the original studies, either as partial pressures in bar or atm (1 bar = 0.9869 atm), or as mixing ratios such as ppmv. S-MIF refers to sulfur isotope mass-independent fractionation. Figure 3.2 shows that during the period when the essential ingredients for life were accumulating in the oceans—whether delivered by meteorite impacts or produced in the atmosphere through energetic particle interactions, photochemistry, and lightning—the atmosphere possessed a characteristic composition. Around 3.7–4.0 billion years ago, methanogenic organisms emerged and began releasing the greenhouse gas CH_4 into the atmosphere. The chemistry of this methane-rich early atmosphere led to the enhanced formation of organic haze. In this process, some of the lighter xenon isotopes became trapped within the haze, while others escaped into space without being selectively filtered by isotope mass (Lammer et al. 2018). Titan is one such body enveloped by a dense organic haze, which is essentially a layer of complex aerosol particles clumped into fractal agglomerates. This haze originates from abiotic chemical reactions, where sunlight and energetic electrons irradiate atmospheric methane and nitrogen to synthesise solid organic matter (Trainer et al. 2006).

Table 3.3: Archean atmospheric gas constraints (David C Catling and Kevin J Zahnle 2020)

Parameter or species	Published constraint	Age (years before present)	Basis of constraint
O_2	$< 10^{-6}\times$ present O_2 $< 3.2 \times 10^{-5}$ atm	> 2.4 Ga 2.415 Ga	Modeled S_8 flux needed to create and carry S-MIF (K. Zahnle et al. 2006) Detrital uraninite (J. E. Johnson et al. 2014) (river length required if Koegas subgroup accurate)
O_3 column	$< 10^{19}$ molecules m^{-2}	> 2.4 Ga	Modelled ground-level $O_2 < 0.2$ ppmv (J. F. Kasting et al. 1985; K. Zahnle et al. 2006)
Surface barometric pressure	0.52–1.1 bar 0.23 $\pm$ 0.23 bar (2σ)	2.7 Ga 2.74 Ga	Maximum fossil raindrop imprint size (Som et al. 2012) Fossil vesicles at basaltic flow tops(Som et al. 2016)
N_2	< 1.1 bar (2σ)	3.5-3.0 Ga	$N_2/^{36}Ar$ in fluid inclusions (Marty et al. 2013)
	< 1 bar (2σ)	3.3 Ga	Derived from Fig.4A and Table 2 of (Avice et al. 2018)
HCN	Up to $\sim$100 ppmv	> 2.4 Ga	Photochemistry if CH_4 was $\sim 10^3$ ppmv (Tian et al. 2011; Kevin J Zahnle 2819)
N_2O	Few ppbv	> 2.4 Ga	Lightning production of NO and HNO in reducing atmosphere; dissolution; evapouration (David C Catling and Kevin J Zahnle 2020)
CO_2	0.0004–0.02 bar (0 $^\circ$ C); 0.0025 bar (25° C); 0.26 bar (100° C)	3.2 Ga	Siderite weathering rinds on river gravel (Hessler et al. 2004)
	0.03–0.15 bar	2.77 Ga	Mt. Roe paleosol (Australia) (Kanzaki and Murakami 2015)
	0.02–0.75 bar	2.75 Ga	Bird paleosol (South Africa)(Kanzaki and Murakami 2015)
	0.003–0.015 bar	2.69 Ga	Alpine Lake paleosol (United States) (Driese et al. 2011)
	0.05–0.15 bar	2.46 Ga	Pronto/NAN paleosol (Canada) (Kanzaki and Murakami 2015)
	< 0.8 bar	3.8–2.4 Ga	Enough UV to make S-MIF(Farquhar et al. 2001)
CH_4	> 20 ppmv	> 2.4 Ga	Lower limit for S-MIF (K. Zahnle et al. 2006)
	> 5000 ppmv	$\sim$3.5 Ga	Enough methane to allow hydrogen escape and Xe isotope fractionation (Kevin J. Zahnle et al. 2019)
CO	Less than few ppmv < 300 ppmv	After origin of CO consumers	Thermodynamic limit if methanogens used free energy of CO; atmospheric-ocean interface constraints (Krissansen-Totton et al. 2018b) CH_4 production limited by H_2 availability and atmospheric escape (Kharecha et al. 2005)
H_2	10 s–100 ppmv	After origin of methanogens	H_2 used by methanogens + atmospheric-ocean transfer constraints (Kral et al. n.d.; James F Kasting et al. 2001; Kharecha et al. 2005)
	< 0.01 bar	3.0–2.7 Ga	Survival of detrital magnetite in rivers "Fe^{2+} reducing" microbes assumed absent(Kadoya and David C. Catling 2019)

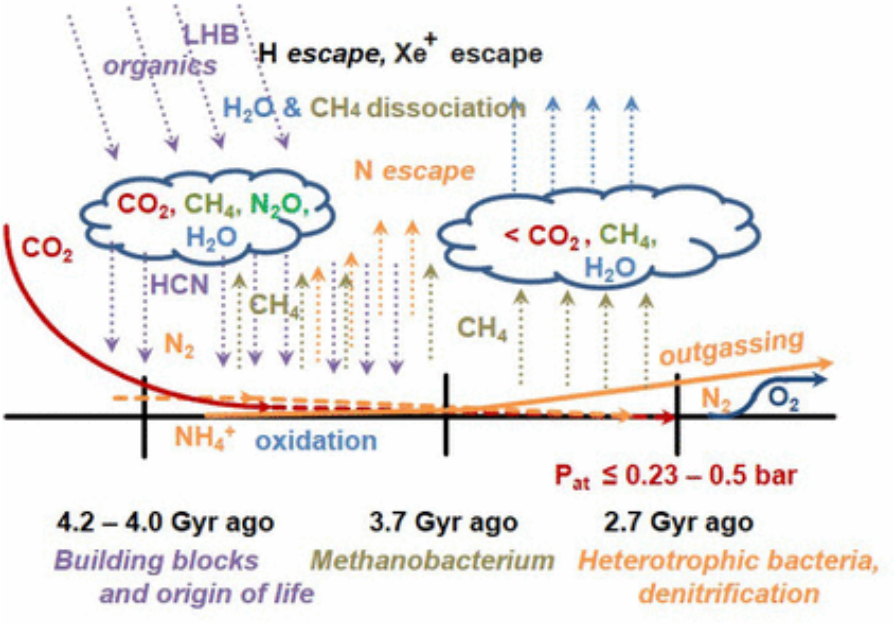

Figure 3.2: Atmospheric constituents of earth when life was evolving on Earth (Lammer et al. 2018)

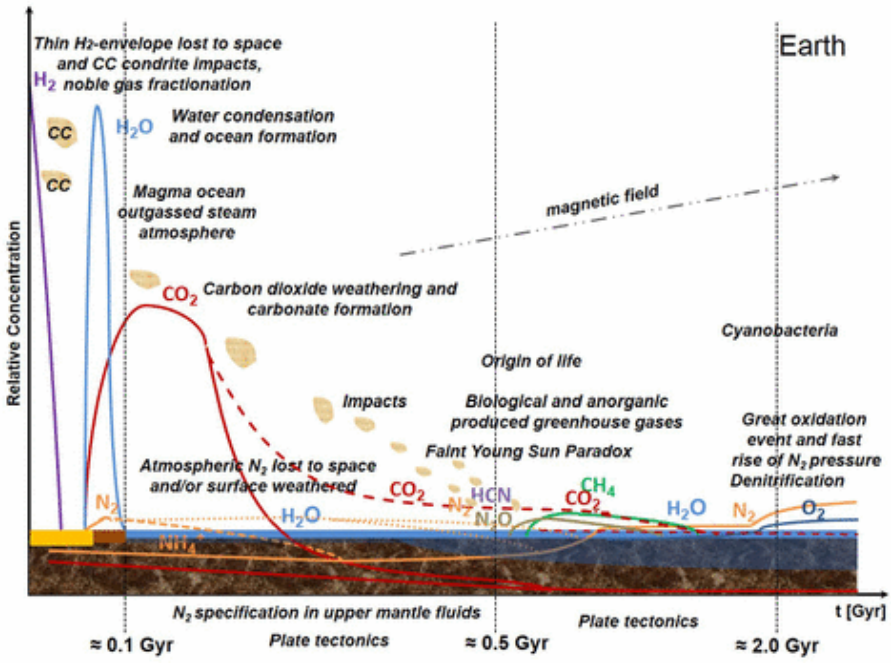

Figure 3.3: Illustration of Earth's atmosphere evolution since its origin (Lammer et al. 2018)

The evolution of Earth's atmosphere, as illustrated in Figure 3.3, began with the delivery of volatile compounds early in the planet's formation, primarily through impacts from carbonaceous chondrites originating in the outer Solar System. While a substantial portion of this delivered water was sequestered in the mantle, the planet initially lost its thin, nebula-derived H_2 envelope. Following the formation of the Moon, Earth's deep global magma ocean cooled and solidified, releasing a massive steam atmosphere which subsequently condensed to form the first oceans on the surface.

The emergence of liquid water was a pivotal development, facilitating the removal of atmospheric CO_2 through weathering and its storage as carbonates. Favourable mantle temperatures and internal water likely enabled the onset of primitive plate tectonics; however, residual atmospheric CO_2 persisted,

functioning as both a greenhouse gas and an infra-red coolant in the upper atmosphere throughout the Archean eon.

As Earth's crust and upper mantle became oxidised (approximately 3.5–4.0 Ga), volcanic activity resumed the efficient release of N_2. Following the origin of life, greenhouse gases such as CO_2, CH_4, and N_2O maintained surface temperatures conducive to preventing freezing, subject to local pressure and albedo conditions. Over time, biological denitrification further increased atmospheric N_2 levels, and as oxidation progressed, O_2 eventually accumulated. This sequence of geochemical and biological processes established present-day nitrogen levels and set the trajectory for Earth's modern atmospheric composition. Understanding this complex evolutionary history provides a critical baseline for identifying life beyond our Solar System. Consequently, a key objective of NASA's Origins Program is to identify habitable planets orbiting other stars and assess which of them may support life, using Earth's atmospheric history as a comparative model (Pilcher 2003). Research on Earth's earliest biosphere, together with observations of modern microbial communities that resemble those ancient systems, indicates that organosulphur compounds, especially methanethiol (CH_3SH, the sulphur analogue of methanol) may have been produced biologically on the early Earth (Pilcher 2003). Most discussions of signs of life have centred on identifying spectral features of gases found in today's Earth atmosphere, especially ozone, which forms through the photolysis of molecular oxygen produced by life (Pilcher 2003).

3.3.2. Mars

Mars Express, launched in 2003 as ESA's first planetary mission, reported detecting small amounts of methane in the Martian atmosphere. Then, in March 2016, the ExoMars Trace Gas Orbiter (TGO) was sent to Mars . Although the initial methane detection was heavily debated, a new methane spike was observed in 2019 by both the Curiosity rover and Mars Express. In contrast, the ExoMars Trace Gas Orbiter, which is specifically designed to search for gases like methane, has not detected any. As a result, the presence of methane remains uncertain, though more credible than before. This uncertainty is significant because the source of the methane is unknown: it may be produced through geological processes, such as gas seeping from the subsurface, but on Earth methane is also generated by certain microorganisms. Therefore, the detection could hint at, though certainly does not confirm, possible biological activity on Mars.

Both missions continue to deliver high-quality measurements of the Martian atmosphere, including the abundances of major species such as CO_2, CO, H_2O, and O_3, which play key roles in the planet's atmospheric cycles. They also provide valuable data on several important trace gases, including O_2 (with mixing ratios of 3.1–5.8×10^{-3} above 90 km), the newly detected HCl (up to 4 ppbv below 30 km), and the elusive CH_4, for which only strict upper limits of around 20 pptv have been observed (Vandaele et al. 2024). Today, Mars' atmosphere contains roughly five times more deuterium (D) than Earth's (Vandaele et al. 2024).

Figure 3.4 depicts the evolution of the Martian atmosphere. The figure can be explained as follows: depending on how much CO_2 was released and on the early Sun's EUV radiation levels, Mars may have supported large, long-lasting lakes or possibly even a surface ocean during its first 100–300 million years. If Mars's crust and upper mantle were sufficiently oxidised, volcanic activity could have released nitrogen during the first billion years, but this nitrogen likely escaped rapidly to space. After about 4.0 billion years ago, CO_2 levels at the surface began to decline due to thermal escape, and from roughly 3.5–4.0 billion years ago onward, non-thermal escape processes and surface weathering further reduced atmospheric CO_2. For Mars, the planet's gravity was too weak to retain a nebular H_2 atmosphere during its formation, preventing such an envelope from accumulating in the first place (Lammer et al. 2018).

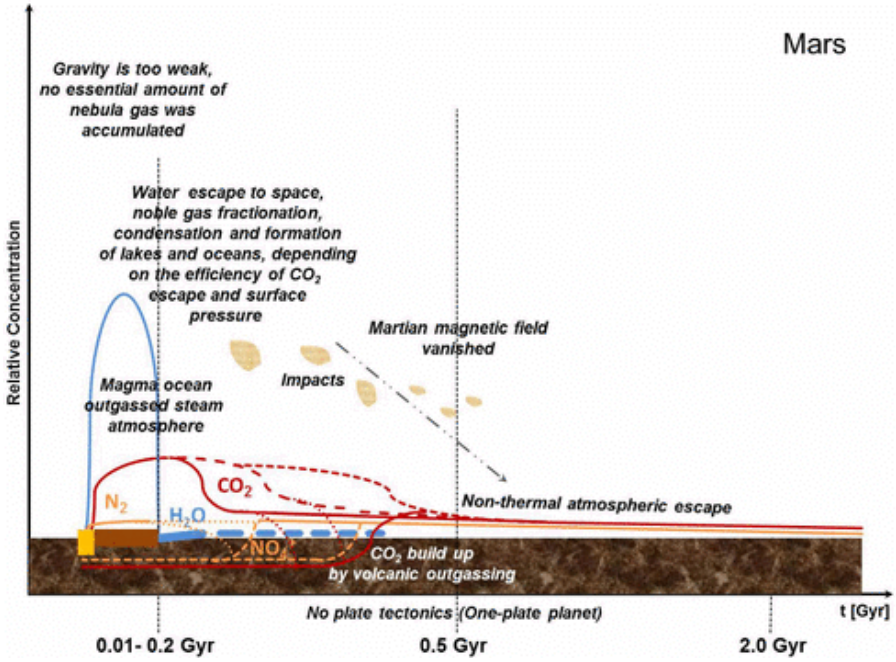

Figure 3.4: An illustration showing how Mars's atmosphere has changed over time since the planet formed (Lammer et al. 2018)

Table 3.4 presents possible gases that can indicate life, identified in terrestrial Mars analogues through various astrobiological investigations. The table includes both atmospheric and non-atmospheric biosignatures.

Table 3.4: Relevant biosignatures from representative terrestrial Mars analogues (Lin et al. 2022)

Mars Period	Geological Time	Biosignature
Early–Middle Noachian	4.1–3.8 Ga	Amino acids; carbon isotopes; 2-methylhopanoids; organosulphur gas
Late Noachian–Early Hesperian	3.8–3.4 Ga	Amino acids; biogenic microtextures; Nanohaloarchaea; nucleic acids; pigments; cellular structures; high carbon and phosphorus; organic molecules; silica deposits; cyanobacterial scytonemin; saccharides
Late Hesperian–Early Amazonian	3.4–(2.1–1.4) Ga	Amino acids; biolipids; chirality; chlorophylls; clay-rich subsurface; microbial colonies; nitrate isotopes; organic carbon isotopes; organomineralized structures; secondary metabolites; polyextremotolerant bacteria
Middle–Late Amazonian	(2.1–1.4) Ga – Present	Endolithic microbial content; nitrate isotopes; (per)chlorate concentrations; microstructures; organic carbon and nitrogen and their isotopes; quadruple sulphur isotope

3.3.3. Venus

In Figure 3.5, the evolution of Venus's atmosphere is illustrated and can be explained as follows: after Venus lost its initial hydrogen-rich atmosphere, its global magma ocean cooled and released large amounts of H_2O and CO_2, forming a dense steam atmosphere. Depending on surface temperature, cloud cover, and volcanic outgassing, this steam may have briefly condensed into an ocean or remained entirely in vapour form. If an early ocean existed, it was later removed by a runaway greenhouse effect, with hydrogen escaping to space and the remaining oxygen reacting with or being absorbed by the surface. If no ocean ever formed, hydrogen still escaped efficiently, and the leftover oxygen oxidised the crust and upper mantle. Without liquid water, CO_2 could not be removed by weathering and therefore accumulated in the atmosphere, while small amounts of N_2 were intermittently released by volcanism. These processes ultimately produced the hot, dry, CO_2-rich atmosphere observed on Venus today. Table 3.5 shows a list of discovered elements in Venus and year of discovery.

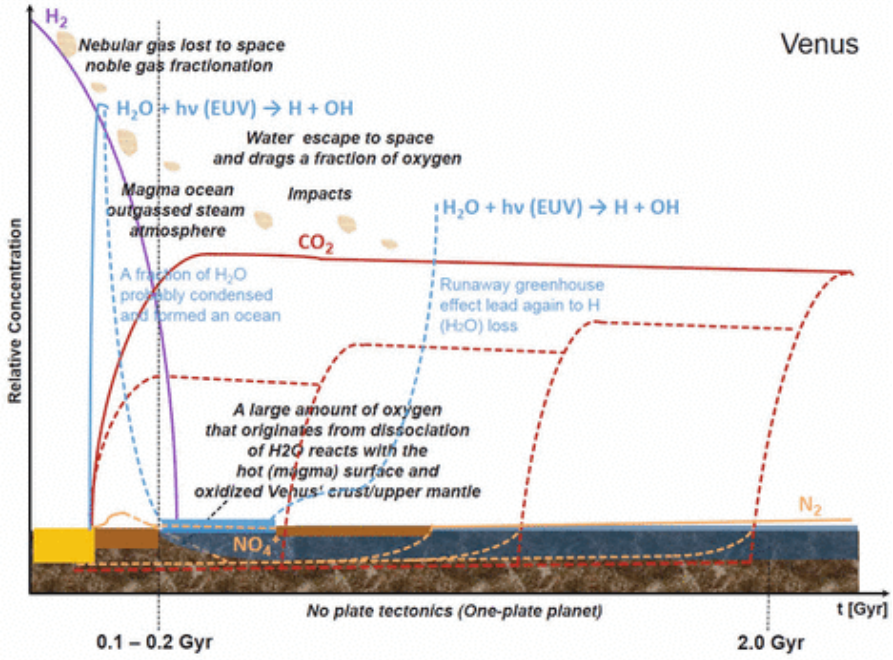

Figure 3.5: An illustration of how Venus's atmosphere may have evolved over time, assuming the planet never underwent plate tectonics or any comparable form of crustal recycling (Lammer et al. 2018)

Table 3.5: Elements and compounds detected in the atmosphere of Venus (Kotsyurbenko 2023)

Elements and compounds	Authors and year of discovery
H_2O	(F. S. Johnson 1968)
CO	(V. I. Oyama et al. 1980)
CO_2	(V. I. Oyama et al. 1980)
COS	(Mukhin et al. 1982)
N_2	(V. I. Oyama et al. 1980)
O_2	(V. I. Oyama et al. 1980)
P	(Andreichikov et al. 1997)
$P_2O_5 + H_3PO_4$	(Krasnopolsky 2006)
PH_3	(Greaves et al. 2021; Mogul et al. 2021)
S_8	(Andreichikov et al. 1997)
H_2SO_4	(Porshnev et al. 1987)
SO_2	(Barker 1979)
Cl	(Surkov et al. 1982)
Fe	(Andreichikov et al. 1997)
$FeCl_3$	(Zasova et al. 1981)

The most plausible environment for Earth-like life on Venus is thought to be its dense cloud layer, where hypothetical microbial communities might survive within aerosol droplets composed of highly concentrated sulphuric acid solutions (Kotsyurbenko 2023). The potential abundance of PH_3 cannot currently be explained by any known chemical processes, necessitating the invocation of a previously unknown mechanism, which could include biological activity (Bains et al. 2021a).

High levels of molecular oxygen have been detected in Venus's cloud layer (Von Zahn' and Moroz 1985). At present, no known abiotic mechanisms can generate O_2 locally in such quantities, although it may be produced as part of a proposed ammonia (NH_3) formation pathway (Bains et al. 2021b), potentially involving biological processes. In addition, Venus's clouds exhibit strong UV absorption between 320 and 500 nm due to an unidentified absorber, which might be iron chloride ($FeCl_3$) dissolved in sulphuric acid droplets (Krasnopolsky 2006). However, various biomolecules, including nucleic acids,

iron-containing proteins, and photosynthetic pigments, also absorb light within this range and could either explain or contribute to the observed UV absorption (Limaye et al. 2018).

Ligterink et al. 2022 propose the ORIGIN Space instrument for the Venus Life Finder mission to explore and potentially clarify several unresolved issues regarding Venus's atmosphere and the possibility of life within its cloud layers. Currently, Venus has no liquid water on its surface because of its extremely high temperatures. However, small amounts of water do exist in the atmosphere as water vapour, at concentrations of roughly 40–200 ppm (Donahue and Hodges 1992). Meanwhile, the planet's cloud layer is thought to be composed largely of sulphuric acid. This sulphuric acid likely forms through photochemical reactions involving water vapour, CO_2, and SO_2, with sulphur dioxide entering the atmosphere primarily through volcanic activity (Kotsyurbenko 2023).

3.3.4. Icy Moons

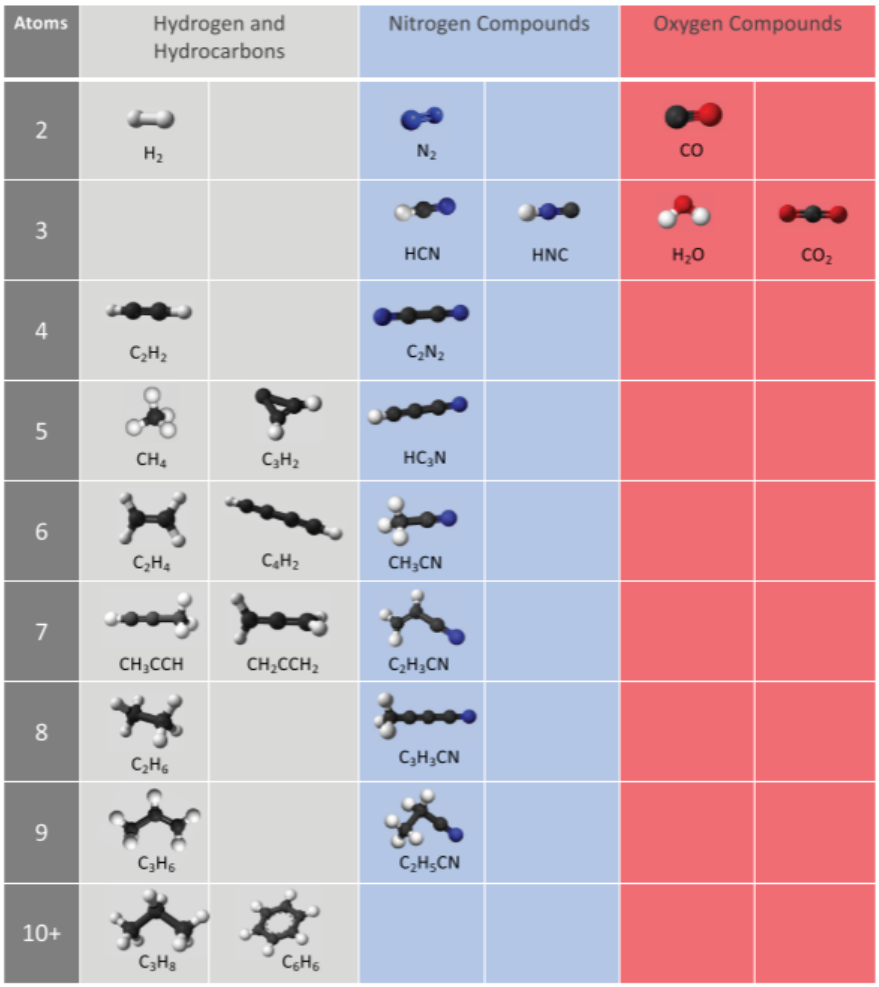

Figure 3.6: Molecules identified on Titan (Nixon 2024)

Titan, Saturn's largest moon, is the only moon in the Solar System with a thick atmosphere. It is also the only world besides Earth known to have stable surface liquids. Titan features clouds, rainfall, rivers, lakes, and seas, though they are composed of liquid hydrocarbons such as methane and ethane rather than water. According to NASA and ESA, Titan's atmosphere is primarily composed of nitrogen (95%), methane (5%) and small amounts of other carbon-rich compounds. Titan is an extremely inhospitable environment for life. Its surface is far too cold for liquid water essential for all known organisms to exist with temperatures around –180° C. Instruments aboard NASA and ESA's Cassini–Huygens mission measured the nitrogen-14 and nitrogen-15 isotopes present in Titan's atmosphere. The origin of

methane on this icy moon is still unknown. Researchers suspect that methane may be released into Titan's atmosphere through cryovolcanism, volcanoes that erupt cold water rather than molten rock, but it remains uncertain whether this process or another mechanism is responsible.

Figure 3.6 lists the molecules identified in Titan's neutral atmosphere, grouped by their size and chemical composition, showing that hydrocarbons are the most common and complex species present, followed by nitriles. So far, no complex oxygen-containing molecules or oxygen-bearing organics have been detected on Titan.

3.4. Presence of H_2O_2 in the Solar System

While the primary focus of exoplanetary research is generally placed on atmospheric composition, an active interest in surface composition has evolved as a more pragmatic approach for this thesis. Investigating surface components allows for a better understanding of alternative environmental stressors and conditions that can be simulated in the laboratory to characterise released biosignatures. Beyond terrestrial planets, icy ocean worlds such as Enceladus, Europa, Ganymede, and Callisto represent prime targets for future astrobiological missions searching for signatures of life. Within these environments, hydrogen peroxide (H_2O_2) has been directly detected at the poles of Ganymede (Trumbo et al. 2023), while on Europa, it is hypothesised to exist as isolated trimers of $\mathrm{H_2O_2 \cdot 2H_2O}$ dispersed within the surface water ice. Structurally, the crust of Europa consists primarily of water ice alongside potent oxidants such as H_2O_2, molecular oxygen (O_2), and a dark material composed of currently unidentified hydrated salts (Pasek 2020). Hydrogen peroxide carries profound astrobiological significance across various planetary bodies. On Earth, trace amounts of surface oxidants, including free O_2 and H_2O_2, could have been supplied to primitive organisms prior to the origin of oxygenic photosynthesis (Haqq-Misra et al. 2011). Several researchers have suggested that the regular presence of H_2O_2 may have played a critical evolutionary role in transitioning non-oxygenic photosynthetic organisms into oxygenic ones, ultimately driving the generation of Earth's oxygen-rich atmosphere (Newman et al. 2007).

Beyond the icy moons, H_2O_2 serves as a key component in understanding the atmospheric evolution of Mars. Initial observations from the Viking landers and the associated Gas Exchange Experiment suggested the presence of a powerful surface oxidiser, with H_2O_2 proposed as a likely candidate (Vance I. Oyama and Berdahl 1977). The definitive detection of gaseous hydrogen peroxide in the Martian atmosphere was achieved in 2003 through two independent ground-based measurements (Encrenaz et al. 2011). Photochemical models indicate that a wet, oxidised atmosphere can maintain sufficient quantities of H_2O_2 gas in its upper layers due to rapid photochemical production paired with slow condensation conditions. These mechanisms demonstrate how a warm, wet environment could have been sustained on an oxidised early Mars, suggesting a direct link between its ancient atmospheric redox state and a viable aqueous surface environment (Ito et al. 2020). This gas-phase behaviour contrasts sharply with modern Earth, where H_2O_2 remains a minor atmospheric species restricted to a maximum level of approximately 3.5 ppb. This low concentration is primarily driven by the rapid dissolution of gaseous H_2O_2 into atmospheric water droplets at lower altitudes, followed by its efficient removal from the system via precipitation. Investigating how these diverse planetary environments govern the presence of H_2O_2 provides context for simulating similar oxidative stress conditions in the laboratory.

3.4.1. Exoplanetary Systems

An exoplanet is a planet located outside our Solar System. Most exoplanets orbit other stars, although some, known as rogue planets, drift through space without being gravitationally bound to any star. To date, more than 6,000 exoplanets have been confirmed, out of the billions thought to exist in the galaxy (source: NASA). Basak et al. 2021 classify exoplanets as follows: Mesoplanets (or M-planets) are worlds with average surface temperatures between 0° C and 50° C, conditions suitable for complex terrestrial life, making them broadly comparable to Earth. Psychroplanets, by contrast, have mean surface temperatures between −50° C and 0° C, which are colder than ideal for sustaining Earth-like life. Planets falling outside these two categories lack the necessary thermal conditions for surface liquid water, and while subsurface habitability remains theoretically possible in colder regimes, these bodies are considered non-habitable for the purposes of this study.

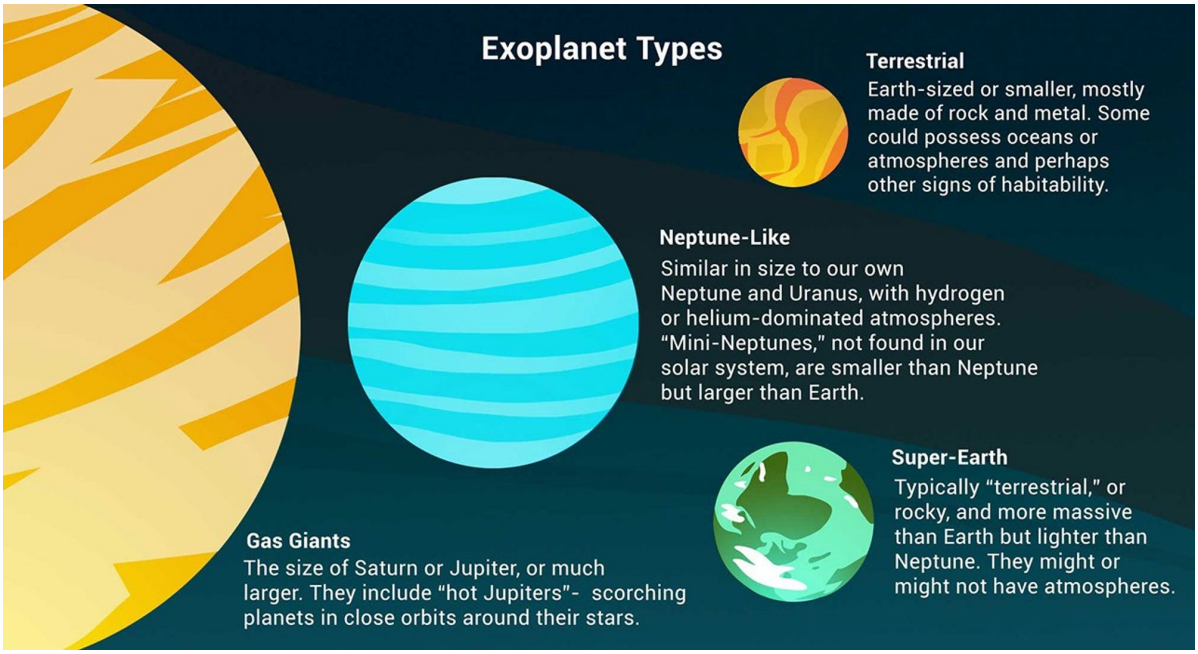

Figure 3.7: Types of exoplanets (credit: NASA)

As shown in Figure 3.7, exoplanets exhibit an enormous range of types, some differing significantly from the planets in our Solar System. Unlike the planets in our own Solar System, exoplanets cannot be easily reached or explored directly (Ramirez 2018). Figure 3.8 shows the traditional CO_2–H_2O habitable zone plotted against stellar effective temperature (2600–7200 K) and effective stellar flux. The "recent Venus" and "early Mars" boundaries (solid blue lines) mark the empirical, more optimistic limits of the classical HZ. In contrast, the Leconte et al. 2013 and "Maximum Greenhouse" boundaries define the more conservative, or pessimistic, estimates of the HZ.

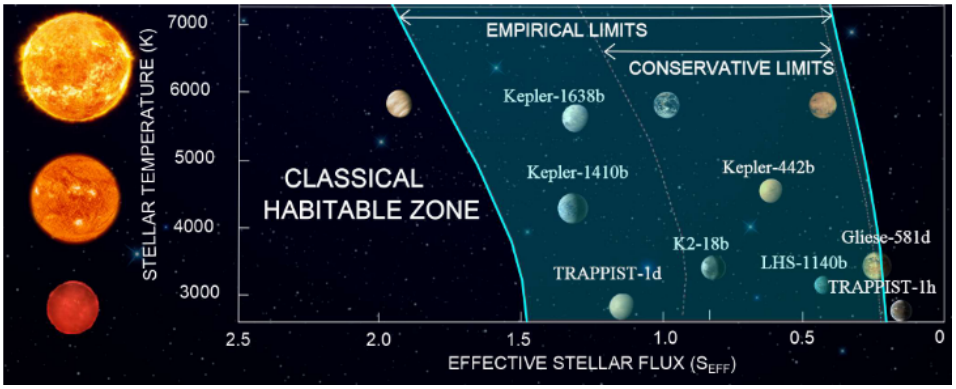

Figure 3.8: Some solar system planets and confirmed exoplanets (Ramirez 2018)

The spectrum of the host star plays both a direct and indirect role in shaping a planet's atmospheric chemistry (Edward W. Schwieterman et al. 2018). Going from a G-type star to an M-type star alters the UV environment, which can cause certain biogenic gases such as N_2O, O_3, and DMS, to increase in concentration (Antígona Segura et al. 2005; Rugheimer et al. 2015).

Table 3.6: Exoplanetary Systems with Rocky Planets

Exoplanetary System	Type of Star	Distance from Earth (ly)	Rocky/Terrestrial Planets
Proxima Centauri	M-Type	4.2	Proxima Centauri b,d
Lalande 21185	M-Type	8	GJ411b
Lacaille 9352	M-Type	11	GJ887 b,c
Tau Ceti	G-Type	11.9	Tau Ceti e, f, g, h
82 Eridani	G-Type	20	HD 20794 b,d,e
HD 219134	K-Type	21	HD 219134 b,c,d,f
Gliese 12	M-Type	40	Gliese 12 b
TRAPPIST-1	M-Type	40	TRAPPIST-1 b,c,d,e,f,g,h
Nu Lupi	G-Type	48	HD 136352 b
Rho Coronae Borealis	G-Type	57	Rho Coronae Borealis e
K2-18	M-Type	124	K2-18b
Kepler 186	M-Type	579	Kepler 186 b,c,d,e,f
Kepler 22	G-Type	635	Kepler 22b

The list of exoplanetary systems in Table 3.6 is taken from the Target Star Catalogue, and several of them have been widely discussed in the literature for their potential habitability, making them valuable analogues for further study. The stars mentioned here are considered ideal targets for missions such as the Habitable Worlds Observatory (HWO) because their habitable zones lie far enough from the star to give the telescope an unobstructed view of potential planets. HWO will be the first telescope built with the specific goal of finding life on other planets. Moreover, any Earth-sized planet in those zones would be sufficiently bright for scientists to study its atmospheric composition through spectroscopy.

3.4.2. TRAPPIST-1

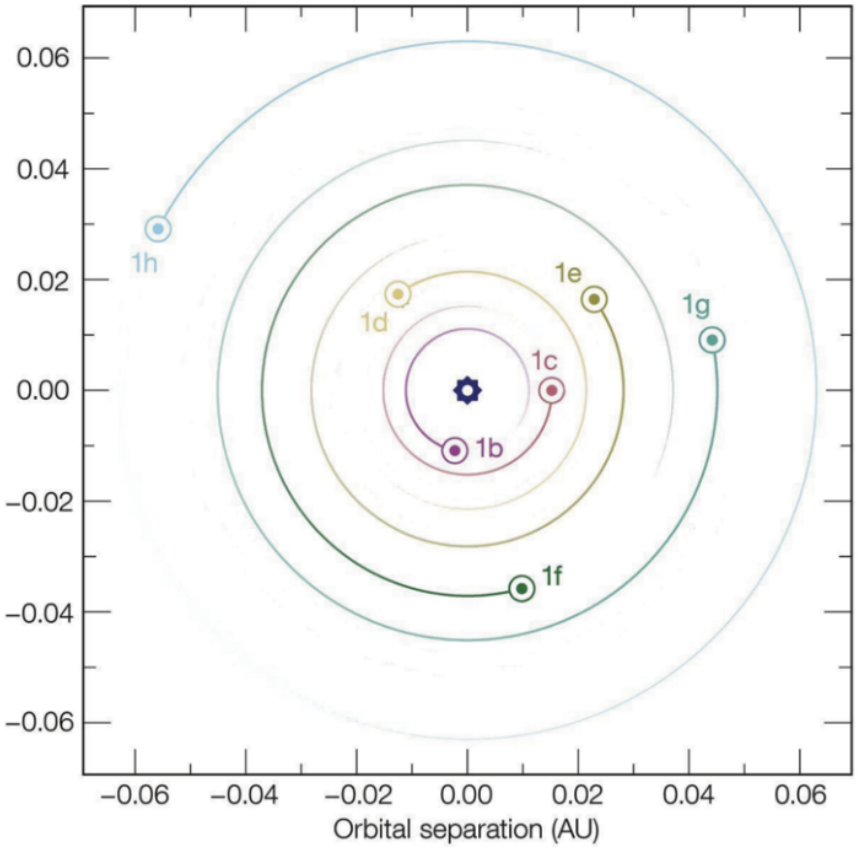

Figure 3.9: TRAPPIST-1 System when looked from above (Rodrigo Luger et al. 2017)

Out of all the planets listed in Table 3.6, the TRAPPIST-1 system is particularly compelling to study because several of its planets lie within or near the habitable zone. The system's compact orbital configuration allows for precise determinations of planetary masses, radii, and compositions, making it an exceptional laboratory for comparative habitability studies. Since M-dwarfs are the most common stars in the Milky Way, TRAPPIST-1 also serves as a crucial benchmark for evaluating whether life could exist on planets orbiting such stars. For these reasons, TRAPPIST-1 remains one of the most promising systems for advancing the search for biosignatures beyond our Solar System.

TRAPPIST-1 is an exceptional nearby planetary system, located about 39 light-years away, consisting of a 0.09 $M_\odot$ star that hosts seven Earth-sized, Earth-mass planets receiving moderate levels of stellar radiation (S. Huang and Ormel 2022; Turbet et al. 2020). It remains the most accessible and promising system of potentially habitable worlds discovered so far (Turbet et al. 2020). Figure 3.9 is the illustration of TRAPPIST-1 planets (b,c,d,e,f,g) when viewed from the top. Even with numerous observations from a range of telescopes such as Spitzer, Hubble, K2, and the Very Large Telescope, the available transit transmission spectra are still insufficient to determine the atmospheric molecular composition (if an atmosphere exists) of the TRAPPIST-1 planets (Turbet et al. 2020). Wolf 2017 used the National centre for Atmospheric Research's Community Atmosphere Model version 4 and explored the potential climates and habitability of the TRAPPIST-1 planets. The simulations assumed ocean-covered worlds with atmospheres made of N_2, CO_2, and H_2O, along with observed orbital and geophysical characteristics. The model suggests that the three innermost planets b, c, and d currently lie inside the inner edge of the traditional liquid-water habitable zone. Planet e offers the strongest potential for being an ocean-covered world that is currently habitable. Planets e and f can sustain at least some regions with surface liquid water when atmospheric CO_2 levels range from 0 to 2 bar, depending on how much background N_2 is present (Hu et al. 2020). Hu et al. 2020 suggest that O_2, O_3, and CO along with CO_2 should be treated as key target molecules when searching for atmospheric signatures on temperate, rocky planets orbiting TRAPPIST-1 and other M-dwarf stars.

The James Webb Space Telescope (JWST) offers the first real chance to detect atmospheric gases on terrestrial planets orbiting M-dwarf stars and to look for possible signs of life (V. S. Meadows et al. 2023). V. S. Meadows et al. 2023 suggest that detecting O_2 and O_3 in modern-Earth-like TRAPPIST-1 e environments is challenging, and similarly, TRAPPIST-1 d fails to produce the stronger atmospheric signals expected from its smaller size and larger scale height. Moreover, biosignature gases such as O_2, O_3, and CH_4 remain undetectable in fewer than 100 transits because a high-altitude cloud layer forms in its warm, humid atmosphere, masking these features. They also evaluated whether CH_3Cl could serve as an indicator of oxygenic photosynthesis from vegetation and found that JWST would require a flux at least 100 times higher than Earth's present output or about 20 times greater than that produced by tropical vegetation to detect it in fewer than 100 transits. Furthermore, they conclude that the CH_4/CO_2 ratio is the most readily detectable biosignature across all TRAPPIST-1 e habitable environment and metabolism scenarios examined, including one resembling pre-industrial Earth, which features both oxygen producing photosynthesis and a methanogenic biosphere.

To interpret potential atmospheric biosignatures on exoplanets, it is crucial to determine whether the combined spectral signatures of multiple gases can be reproduced by abiotic processes or require biological activity (Eager-Nash et al. 2024). Eager-Nash et al. 2024, using predicted transmission spectra of CH_4, CO, O_2/O_3, and CO_2 across a range of tectonic reductant flux scenarios, found that biologically produced CH_4 would only be detectable under conditions of high reductant input. Additionally, CO is expected to appear prominently in the transmission spectra of planets orbiting M-dwarfs, which may complicate or weaken the confidence in biosignature interpretations associated with such biospheres.f

4

Biosignatures and Extremophiles

Having established the planetary conditions necessary for habitability, the discussion shifts to the types of organisms that might inhabit these harsh environments, providing a classification of extremophiles based on their survival characteristics. To detect these organisms remotely, the focus narrows to biosignatures: any substance, element, or phenomenon providing scientific evidence of past or present life. While these indicators range from physical fossils to surface reflectance features, this work concentrates primarily on gaseous metabolic by-products. Different potential atmospheric biosignatures are catalogued according to their production sources and associated spectral ranges. Understanding these ranges is critical, as they reveal the precise infra-red "windows" where unique molecular fingerprints can be isolated from abiotic background noise. Finally, the chapter concludes by evaluating the key observational and analytical challenges involved in detecting and validating these biosignatures across astronomical distances.

4.1. Biosignatures

Several definitions exist for the term "biosignature". For instance, it can be defined as "an object, substance, and/or pattern created by a biological source. The value of a biosignature is determined not only by the probability of life producing it, but also by the improbability of non-biological processes making it" (Malaterre et al. 2023; Cavalazzi and Westall 2019). Alternatively, it is defined as "any phenomenon for which biological processes are a known possible explanation and whose potential abiotic causes have been reasonably explored and ruled out" (Gillen et al. 2023). In exoplanet research, a biosignature refers to any remotely detectable sign that living processes are affecting a planet's atmosphere or surface. It may consist of a specific gas (or combination of gases), a surface characteristic (or set of characteristics), or variations over time in atmospheric or surface properties that can be attributed to biological activity (Edward W Schwieterman and Leung 2024). Agnostic biosignatures facilitate the detection of life without assuming it shares Earth-like biochemistry. This approach looks for unusual complexity in a planet's environment or in preserved molecules that nature is highly unlikely to produce on its own (National Academies of Sciences and Medicine and Division on Engineering and Physical Sciences and Space Studies Board and Committee on Astrobiology Science Strategy for the Search for Life in the Universe 2019).

A compelling biosignature possesses three major attributes: detectability, survivability, and specificity. Detectability refers to how strongly a molecule absorbs, scatters, or emits light. For a biosignature to be observable, it must leave a measurable imprint on the light that is reflected, emitted, or passed through a planetary atmosphere. Survivability describes how well a biosignature molecule or substance withstands rapid destruction from planetary or stellar processes, such as UV radiation. To be useful, a biosignature must build up to detectable levels, which depends on factors like chemical reaction rates and dissociation cross-sections in the atmosphere. Finally, specificity determines whether the biosignature can be definitively differentiated as originating from a biotic rather than an abiotic source (Edward W Schwieterman and Leung 2024).

Biosignatures are broadly classified into three main categories: gaseous (or atmospheric), surface, and temporal. Gaseous biosignatures involve the presence of specific gases, such as O_2 and O_3. Surface biosignatures are distinctive signals created when light interacts with living material on a planet's surface, such as the photosynthetic "red edge"—a sharp increase in plant reflectance in the near-infra-red region of the spectrum. Temporal biosignatures encompass variations over time in features such as atmospheric or surface properties, including seasonal changes in biological activity (Malaterre et al. 2023; Edward W Schwieterman and Leung 2024). Table 4.1 outlines the various categories utilised in the search for extraterrestrial life.

Table 4.1: Categories of Biosignatures (De Mol 2023)

Category	Explanation
Isotopic patterns	Isotopic patterns requiring biological processes
Organic matter	Organics formed by biological processes
Minerals	Composition and/or morphology indicating biological activity
Chemical signatures	Chemical features requiring biological activity
Microscopic structures	Biologically formed microtextures, microfossils, and films
Macroscopic structures	Indications of microbial ecosystems, biofilms, or fossils
Atmospheric gases	Gases formed by metabolic and/or aqueous processes
Surface reflectance	Large-scale reflectance features due to biological pigments
Temporal variability	Variations in atmospheric gases, reflectivity, or macroscopic structures indicating life
Technosignatures	Indication of a technologically advanced civilisation

The primary focus of this thesis is to study gaseous biosignatures. Seager and her team (S. Seager et al. 2016) catalogued roughly 14,000 molecules that could serve as possible biosignatures. Of these, about 2,500 are formed from the six key biogenic elements (C, N, O, P, S, H), around 900 are inorganic molecules, and nearly 11,000 are halogenated compounds. The exceptionally large number of halogenated compounds results from the numerous possible ways halogens can attach to carbon-based structures. Table 4.2 and Table 4.3 present the potential atmospheric biosignature gases found in Earth's atmosphere and in alternate atmospheres, respectively, alongside their main spectral features. The gases listed in Table 4.3 do not represent an exhaustive list; in the context of exoplanets, life can produce a vast array of small molecules, many of which have yet to be thoroughly examined within the growing exoplanet biosignature literature.

Table 4.2: Abundant and/or Prominent Earth Atmospheric Biosignature Molecules (Edward W Schwieterman and Leung 2024)

Biosignature	Production Environment	Concentration on Earth	False Positives and Secondary Outcomes	Main Spectral Features (μm)	Citation
Oxygen (O_2)	Photic terrestrial and marine environments; produced by cyanobacteria, algae, and plants	20.95%	• Low incondensable inventories (Wordsworth and Pierrehumbert 2014) • Ocean loss (R. Luger and Barnes 2015; Tian 2015) • CO_2 photolysis (Domagal-Goldman et al. 2014; Gao et al. 2015; Harman et al. 2015) • High CO_2/H_2O or very low initial H_2O (Krissansen□Totton et al. 2021) • Atmospheric exchange / exogenous delivery (Felton et al. 2022)	O_2: 0.63, 0.69, 0.76, 1.27; CIA/O_4: 0.445, 0.475, 0.53, 0.57, 0.63, 1.06, 1.27, 6.4	(V. S. Meadows 2017; V. S. Meadows et al. 2018)

Continued on next page

Table 4.2 – continued from previous page

Biosignature	Production Environment	Concentration on Earth	False Positives and Secondary Outcomes	Main Spectral Features (μm)	Citation
Ozone (O_3)	Photochemical product of O_2, H_2O, SO_2, CO_2	0.07 ppm	• Abiotic O_2 or CO_2 can produce O_3 features (Domagal-Goldman et al. 2014; Gao et al. 2015; Harman et al. 2015)	0.25; 0.4–0.7; 2.6; 4.7; 9.65; 14.6	(V. S. Meadows et al. 2018; Kozakis et al. 2022)
Methane (CH_4)	Wetlands, rice paddies, livestock emissions, biomass burning and decomposition	1.90 ppm	• Serpentinisation (Edward W Schwieterman and Leung 2024) • Fischer–Tropsch reactions (Edward W Schwieterman and Leung 2024) • High-temperature mantle reactions (Edward W Schwieterman and Leung 2024) • High-temperature gas giant reactions (Edward W Schwieterman and Leung 2024)	1.65; 2.4; 3.3; 7.7	(Etiope and Sherwood Lollar 2013; Thompson et al. 2022)
Nitrous Oxide (N_2O)	Marine settings; some soils	0.33 ppm	• Production by StEPs (Edward W Schwieterman and Leung 2024) • Chemodenitrification (Edward W Schwieterman and Leung 2024) • Trace production by lightning and NO_x reactions (Edward W Schwieterman and Leung 2024)	1.5; 1.6; 1.7; 1.8; 2.3; 2.6; 2.9; 3.7; 4.0; 4.5; 7.8; 8.5; 17	(Edward W. Schwieterman et al. 2022)

Table 4.3: Alternative Atmospheric Biosignatures (Edward W Schwieterman and Leung 2024)

Biosignature	Production Environment	Concentration on Earth	False Positives and Secondary Outcomes	Main Spectral Features (μm)	Citation
Organic sulphur gases e.g. DMS ($(CH_3)_2S$), DMDS ($(CH_3)_2S_2$)	Marine/lacustrine settings	$\sim$100 ppt	Secondary ethane signature may be produced abiotically if sulphur gases do not reach detectable levels	2.3, 3.4, $\sim$7 (DMS, DMDS), $\sim$9 (DMDS), $\sim$10 (DMS, CH_3SH), 14 (DMS, CH_3SH), 18 (DMDS)	(Pitcher 2003); (Domagal-Goldman et al. 2011)
Methyl Chloride (CH_3Cl), Methyl Bromide (CH_3Br)	Marine algae, terrestrial and marine algae; salt marshes and wetlands	$\sim$500 ppt (CH_3Cl), $\sim$9 ppt (CH_3Br)	High-temperature perchlorate pyrolysis; exogenous delivery; limited hydrothermal/high-T processes	3.3, 7.0, 9.9, 13.7 (Cl); 3.5, 6.9, 10.2, 16.4 (Br)	(Antígona Segura et al. 2005), (Leung et al. 2022)
Organic Haze	Photochemical product of CH_4, CH_3X species	Not present at high altitude on modern Earth due to oxidising conditions	Abiotic methane can lead to haze production	NIR spectral slope, $\sim$6	(Arney et al. 2018)
Phosphine (PH_3)	Strictly anoxic environments including paddy fields, lakes/rivers, wetlands/marshes	Ppq–ppb levels, spatially and temporally variable	Phosphite & phosphate degradation, lightning, volcanism, exogenous delivery	2.9, 3.4, 4.4, 5.0, 8.9, 9.5	(Sousa-Silva et al. 2020)
Isoprene (C_5H_8)	Deciduous trees and land plants	$\sim$1–5 ppb, localised and time varying	No known (energetically unfavourable)	3.4, 5.6, 6.3, 9.4, 10.2, 11.4	(Zhan et al. 2021)
Methanol (CH_3OH)	Plants via demethylation of pectin	10 ppb (surface)	Abiotic photochemistry, comets, primitive material	2.9, 3.3, 4.6, 7.5, 9.7	(J. Huang et al. 2022b)
Formaldehyde (CH_2O)	About 80% of biological compounds contain carbonyls	$\sim$0.4 ppb (CDC)	Detectable signature is CO, which can be produced abiotically	1.18, 1.57, 2.35, 4.6	(Zhuchang Zhan et al. 2022)
Ammonia (NH_3)	Anaerobic nitrogen-fixing organisms; ammonification and nitrate reduction	Spatially and temporally variable	Volcanism, photochemistry, high-temperature synthesis, equilibrium thermochemistry	1.2, 1.3, 1.5, 2.0, 2.3, 3.0, 3.9, 6.1, 10.5	(S. Seager et al. 2013), (J. Huang et al. 2022a)

Based on the findings of J. Huang 2022, ammonia (NH_3) stands out as a promising biosignature for terrestrial planets, largely because these worlds lack significant abiotic mechanisms to generate it. For NH_3 to accumulate in an atmosphere, biological activity must serve as a net producer, generating a sufficient volume to completely saturate any existing surface sinks. Conversely, methanol (CH_3OH) is a weak candidate for a biosignature gas; the production flux necessary to cross the threshold of instrument detection is prohibitively massive. While CH_3OH could theoretically accumulate in atmospheres dominated by CO_2 or N_2, the low atmospheric scale height and faint signals characteristic of these specific planets make them impractical targets for near-term observation. Lastly, despite possessing several traits that initially suggest usefulness as a bioindicator, hydrogen chloride (HCl) is ultimately unsuitable. In an H_2-dominated atmosphere orbiting an M5V dwarf star, HCl cannot accumulate to levels detectable by current instrumentation.

Table 4.4 presents halomethanes (excluding those containing fluorine), which are methane derivatives where one or more hydrogen atoms are replaced by halogen atoms. In the structures shown, the central carbon atom is implied. Of the 34 possible non-fluorinated halomethanes, 12 are not known to be produced by biological processes, while the remaining 22 are produced by life, although the evolutionary or biochemical reasons why only these particular compounds are biologically generated remains unclear (S. Seager et al. 2016).

Table 4.4: Halogenated Compounds Made and Not Made by Life (S. Seager et al. 2016)

Not Made by Life	**Made by Life**
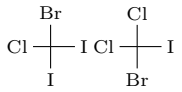	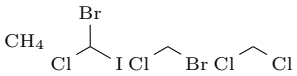
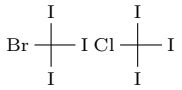	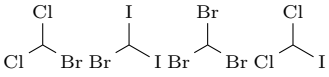
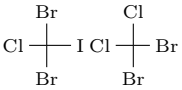	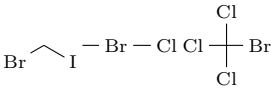
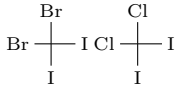	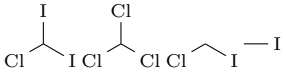
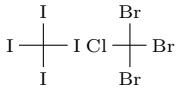	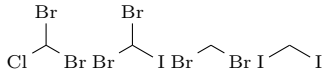
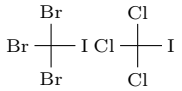	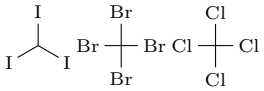

Furthermore, atmospheric gases may exist in a state of thermodynamic disequilibrium; no single biosignature is likely sufficient on its own to definitively confirm the presence of life (Edward W Schwieterman and Leung 2024). Table 4.5 presents several gas combinations that, when found in disequilibrium, act as robust potential biosignatures.

Table 4.5: Disequilibrium Biosignature Combinations (Edward W Schwieterman and Leung 2024)

Pairing	Indication of	Observational Strategy (μm) (e.g.)	Citations
O_2/O_3 + CH_4 (oxic atmospheres)	"redox disequilibrium", since oxidation to CO_2 and H_2O does not occur, sources of O_2 and CH_4 must be present	Combined detections of O_2: 0.76, O_3: 9.65, CH_4: 1.65, 3.3, 7.7	(J. Lovelock 1965), (Hitchcock and J. E. Lovelock 1967), (Carl Sagan et al. 1993)
CO_2 + CH_4 (anoxic/Archaean-like atmospheres)	non-volcanic source of CH_4 if observed without significant CO	Combined detections of CH_4: 1.65, 3.3, 7.7; CO_2: 1.6, 2.0, 4.3, 15	(Krissansen-Totton et al. 2018a), (Krissansen-Totton et al. 2018b)
N_2 + O_2 + H_2O	largest thermodynamic disequilibrium on the modern Earth	Combined detections of oceans (via glint or polarimetry), N_2 (via N_2–N_2 CIA centred at 4.3 μm or scattering), O_2: 0.76	(Krissansen-Totton et al. 2016)
N_2O + O_2/O_3 and/or CH_4	redox disequilibrium, since oxidation states differ between N_2O, O_2, and CH_4	Combined IR detection of N_2O: 7.8, 8.5, O_3: 9.65, and CH_4: 7.7	(Kaltenegger 2017), (Edward W. Schwieterman et al. 2022)

4.2. Extremophiles

Extremophiles play a key role in identifying biosignatures that can aid in the detection of potentially habitable environments beyond Earth (Ali et al. 2023). Outer space presents exceptionally harsh and uninhabitable conditions, characterised by intense radiation, extreme temperatures, altered gravity, and severe limitations in both salinity and nutrients (Thombre et al. 2020). On Earth, extremophiles are defined as organisms that thrive in extreme cold, severe desiccation, high mineral content, or intense radiation (Bhartia et al. 2012). The resilience demonstrated by terrestrial extremophiles suggests that similar microorganisms might withstand severe extraterrestrial conditions, establishing them as valuable model systems for studying biological viability in space environments (Olsson-Francis and Cockell 2010). A primary challenge in the search for life is that planetary bodies with tenuous atmospheres have surfaces exposed to intense radiation, complicating biological survival (Bhartia et al. 2012).

Table 4.6: Classification of Extremophiles (Thombre et al. 2020; Ali et al. 2023)

Classification of Extremophiles	Characteristics	Example
Acidophiles	Optimally grow at very low pH values (pH ≤ 2.0)	*Picrophilus torridus* (pH 0.07) (Rampelotto 2013); *Acidithiobacillus thiooxidans* (D. B. Johnson and Quatrini 2020); *Cyanidium caldarium* (pH 0) (Duarte et al. 2012)
Alkaliphiles	Optimally grow at pH ≥ 9.0	*Bacillus firmus* (Duarte et al. 2012)
Anaerobic	No O_2	*Methanococcus jannaschii* (methanogenic Archaea) (Duarte et al. 2012)
Barophiles / Piezophiles	Capable of surviving pressures ≥ 0.1 MPa	*Shewanella oneidensis* (Duarte et al. 2012)
Xerophiles	Able to survive extreme drying and dehydration (desiccation)	*Trichosporonoides nigrescens* (yeast) (Duarte et al. 2012)
Halophiles	Optimally grow at salt concentrations above 15% NaCl	*Halorubrum*, *Halobacterium* spp. (Kaur et al. 2024), *Dunaliella salina* (Ali et al. 2023)
Metallophiles	Able to survive in high concentrations of heavy metals	*Cupriavidus metallidurans* (Rozycki and Nies 2009)
Oligotrophs (Oligophiles)	Survive in environments with very low nutrient concentrations	*Nitrosopumilus* (ammonia-oxidising archaea) (Duarte et al. 2012)
Osmophiles	Tolerant to high osmotic pressures	*Zygosaccharomyces rouxii* (Dakal et al. 2014)
Psychrophiles	Survive and grow at very low temperatures (below 15° C)	*Psychrobacter* sp. (Duarte et al. 2012), *Penicillium* (Ali et al. 2023)

Continued on next page

Table 4.6 – continued from previous page

Classification of Extremophiles	Characteristics	Example
Radiophiles	Resistant to high doses of ionising radiation (UVR above 110 nm)	*Deinococcus radiodurans*; *Geodermatophilus dictyosporus*; *Cryptococcus neoformans*; *Cladosporium sphaerospermum* (Bhartia et al. 2012); *Cladosporium sphaerospermum*, *Cremonium murorum* (Cosciotti et al. 2019; Blachowicz et al. 2019)
Thermophiles	Grow optimally above 55° C	*Methanopyrus kandleri* strain 116 (Rampelotto 2013); *Pyrolobus fumarii* (113° C); *Synechococcus lividus* (Duarte et al. 2012)
Poly-extremophiles	Can withstand multiple extreme conditions	*Knufia chersonesos* (Tesei et al. 2021); *Bacillus pumilus* (Schultz et al. 2023); *Chroococcidiopsidales* (Billi et al. 2021; Napoli et al. 2022)

To understand how biology overcomes such extreme challenges, these resilient organisms are broadly categorised into two types: extremophilic organisms, which strictly require extreme conditions to grow, and extremotolerant organisms, which can survive such harsh environments but grow optimally under standard conditions (Rampelotto 2013). Taxonomically, extremophiles occur across all three domains of life—Archaea, Bacteria (Prokarya), and Eukarya—though the majority are found within the Archaea (Thombre et al. 2020). Building upon this, Thombre et al. 2020 classified extremophiles based on their specific survival characteristics, as outlined in Table 4.6.

Table 4.7: Microbial Viability in Different Atmospheric Compositions (Sara Seager et al. 2025)

N_2-dominated atmospheres	N_2 is a dominant gas in Earth's atmosphere throughout its geological history. N_2-dominated atmospheres are not only compatible with life's continuous persistence but also allow for its origin. N_2 is a chemically inert gas.
CO_2-dominated atmospheres	The inhibitory effect of high CO_2 concentrations is not universal. Cyanobacteria can grow in $> 95\%$ CO_2 atmospheres, under Earth-like pressures or under simulated Martian low-pressure conditions. More complex organisms (e.g., lichens) can also adapt to simulated Martian conditions. Microbial growth under supercritical CO_2 has been observed.
CO-dominated atmospheres	Many microbial species are completely unaffected by 100% CO atmospheres. For example, *T. thermohydrosulfuricus* and *T. kivui* can live in 100% CO and use it as their sole energy and carbon source.
H_2-dominated atmospheres	H_2 is not toxic. Many species can survive and grow in 100% H_2. Examples include *E. coli*, *S. cerevisiae*, and many others.
O_2-dominated atmospheres	Many species can survive and reproduce in 100% O_2 atmospheres at 1 atm, such as *E. coli*, *S. faecalis*, *B. subtilis*, and *S. cerevisiae*.
Any other atmospheres?	Life can often adapt to atmospheres with artificial gas compositions. Atmospheric composition is generally not a limiting factor for life's persistence.

These survival characteristics are highly relevant to astrobiological exploration. As discussed in chapter 3, many planetary bodies exhibit a wide range of physical and chemical conditions, some of which closely resemble extreme terrestrial habitats. Linking these biological limits to extraterrestrial settings, Table 4.7 illustrates the survival potential of microorganisms across these diverse gas mixtures. To

map the deep biological origins of these resilient traits across the aforementioned domains, Figure 4.1 depicts the evolutionary divergence of species, based on SSU rDNA studies conducted by Pace (1997). Within this framework, the lengths of the line segments represent the amount of evolutionary change, while the asterisks specifically highlight organisms classified as thermophiles or hyperthermophiles. Finally, while true extremophiles (such as the previously detailed radiophiles or piezophiles) represent the absolute boundaries of life, cultivating them requires highly specialised bioreactors and presents significant safety issues. Therefore, a pragmatic approach was adopted when selecting the model microorganisms for the experimental phase of this thesis.

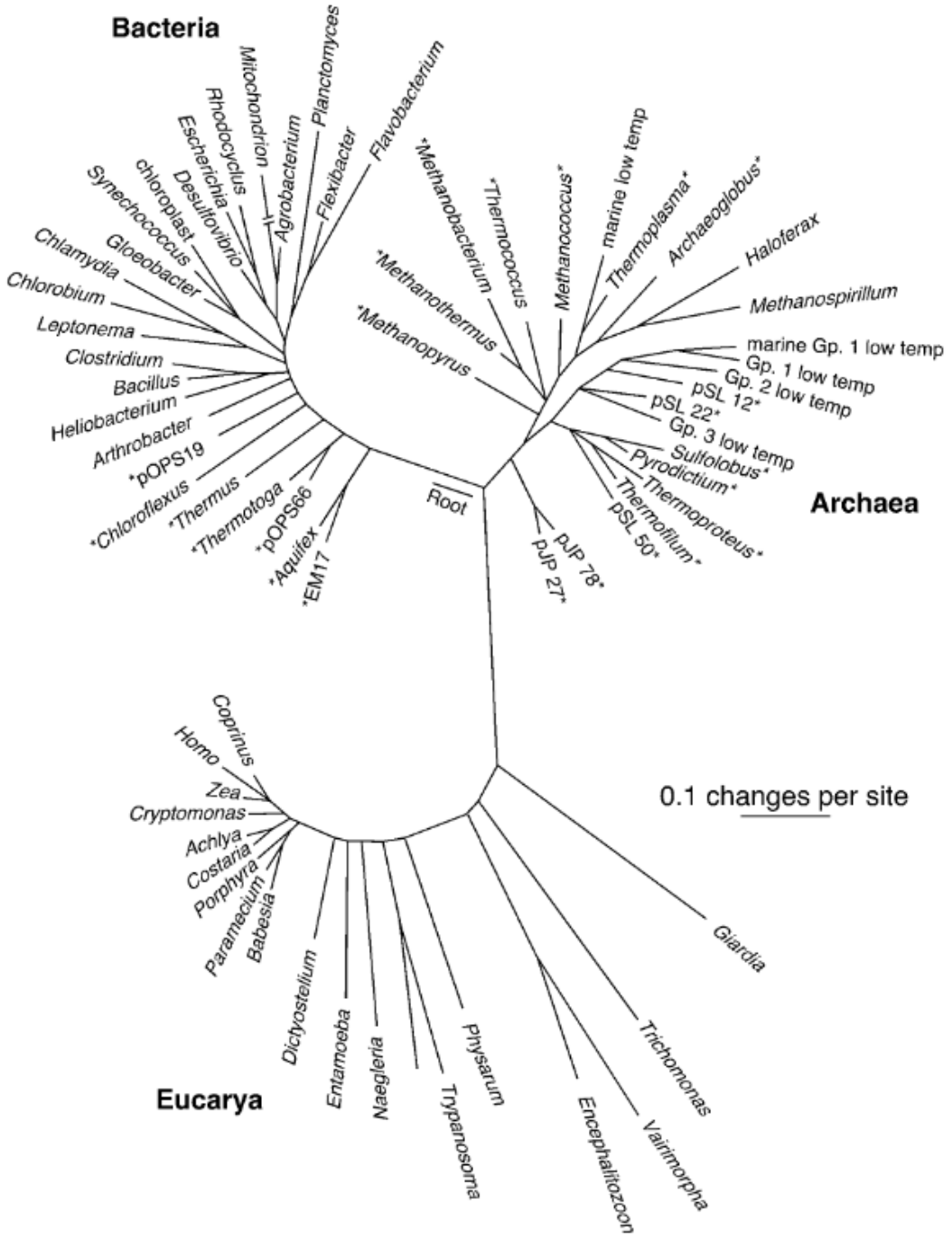

Figure 4.1: Universal Tree of Life (Forterre 2015; Pitcher 2003)

4.3. Challenges of Detecting Biosignatures

Detecting biosignatures and subsequently confirming them as definitive evidence of life is an exceptionally challenging endeavour. Signals received from astronomical distances are often weak, inherently ambiguous, or characterised by very low signal-to-noise ratios. Furthermore, our limited understanding of the complex surface and atmospheric processes occurring on distant worlds makes it difficult to evaluate the reliability of any potential life-detection claim. To date, the Viking landers on Mars represent the only mission that has attempted the in situ validation of life (Thombre et al. 2020), and no comparable direct verification has been achieved since. This section discusses the major limitations currently impeding the reliable detection of gaseous or atmospheric biosignatures.

4.3.1. False Positives and False Negatives

A primary concern is how to detect life on exoplanets using features shared by both living and non-living systems, given that biosignatures can originate from both biotic and abiotic mechanisms (H. B. Smith and Mathis 2023). Consequently, it cannot be assumed that principles derived from terrestrial life will uniformly apply to other planetary bodies (Barge et al. 2022). False positives occur when abiotic geological or atmospheric processes mimic biological activity, creating a deceptive biosignature. Conversely, false negatives happen when genuine biosignatures are too subtle, dispersed, or degraded to be detected. Therefore, the threshold for identifying a biosignature must be rigorously adjusted based on the specific context of the planet under investigation. Figure 4.2 illustrates the framework of a ”dead” planet capable of mimicking biological activity. Several compounding factors severely limit the effectiveness of life-detection missions, including the potential alteration or degradation of organic molecules on planetary surfaces, the inability to perform extensive wet-chemical processing of remote samples, and the restricted analytical capabilities of spacecraft instruments, which often cannot reliably differentiate between high–molecular weight isomers (Barge et al. 2022).

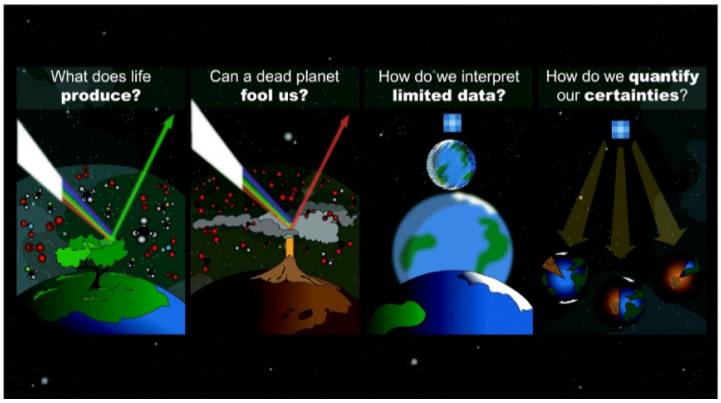

Figure 4.2: In this framework, a “dead” planet refers to a world without any biology, yet with geological processes that can imitate biological activity (Courtesy NASA/Aron Gronstal) (Impey 2022)

4.3.2. Faint Signals

The biosignature gases discussed in section 4.1 generally occur in exceptionally low atmospheric abundances. Potential biosignature gases like O_3 are highly sensitive to input stellar spectra. Beyond standard UV radiation, energetic particles released during stellar flares can significantly reduce atmospheric O_3 levels, depending on the strength and frequency of the flare events (Edward W Schwieterman and Leung 2024). In the context of biosignature gases on Earth, it has been noted that nearly all atmospheric gases present at parts-per-trillion levels (excluding noble gases and synthetic fluorocarbons) are produced by biological activity, even if some also possess notable abiotic sources (S. Seager et al. 2016). However, given the vast astronomical distances involved in these observations, remotely utilising VOCs as biosignatures remains currently impractical, as their overall bulk concentration within an entire planetary atmosphere would be far too low for effective instrumental detection (Batty et al. 2024).

4.3.3. Instrument Limitations

Any VOCs released into a planetary atmosphere would rapidly dissipate or, on certain bodies, be heavily degraded by ultraviolet and ionising radiation. This continuous exposure leads to their swift destruction or alteration into variant forms that cannot be readily identified by current remote sensing technologies or lander instrumentation (Batty et al. 2024). Instruments deployed on space missions face strict operational limits regarding sensitivity, observable wavelength ranges, and spatial resolution. As a result, they may be unable to detect trace amounts of biosignatures or effectively distinguish ambiguous signals from deep background noise. Literature has heavily examined false-positive scenarios in which potential signs of life on an exoplanet could be fundamentally misinterpreted. For instance, Rein et al. 2014 demonstrate that when two distinct chemical species appear together in a spectrum, they may not actually originate from the same planetary object. A telescope could simultaneously detect light from both a planet and its moon, each harbouring different gases. But because the celestial system cannot be spatially resolved at such great distances, their independent spectra blend together. This optical blending creates the false illusion that a single planetary body contains both chemicals in thermodynamic disequilibrium (a feature often considered a strong potential biosignature), when in reality, the gases belong to two entirely separate, abiotically stable bodies (Rein et al. 2014). Detecting and accurately distinguishing signals from distant planetary bodies remains extremely challenging. The inherent faintness of these signals, combined with overwhelming light interference from the host star and the fundamental diffraction limits of telescope resolution, makes separating the atmospheric contribution of one body from another a formidable task.

4.3.4. No Means of Validation

A primary challenge in detecting life beyond the Solar System is the inability to directly verify the surface processes responsible for the observed atmospheric features (H. B. Smith and Mathis 2023). Without in situ sampling or surface rovers to provide ground truth, astronomers must rely entirely on remote spectral data, making absolute validation virtually impossible with current technology. However, analytical models such as Bayesian inference help evaluate claims of life detection by mathematically estimating the likelihood of a biological explanation based on available data (H. B. Smith and Mathis 2023). The Bayesian equation used to weigh these probabilities is given by:

$$P(L \mid D) = \frac{P(D \mid L)\, P(L)}{P(D \mid L)\, P(L) + P(D \mid A)\, \big(1 - P(L)\big)}$$

where $P(L \mid D)$ represents the probability of the biological model given the data, $P(L)$ is the prior probability of the biological model, $P(D \mid L)$ is the probability of observing the data given the biological model, and $P(D \mid A)$ is the probability of observing the data given an abiotic model (H. B. Smith and Mathis 2023).

5

Microbial Stress Response and VOC Production

Following the examination of extreme planetary conditions and the diverse extremophiles that inhabit extreme conditions on Earth, this chapter explores the various mechanisms by which environmental stress can be induced in an organism and the resulting metabolic by-products. This section determines which gases or compounds discussed in chapter 4 can be confidently linked to a biological by-product or a stress response. Environmental stress refers to any change in external conditions that triggers a biological response. In biological terms, stress is broadly categorised into abiotic and biotic forms. Abiotic stress stems from non-living physical or chemical fluctuations in the environment, while biotic stress arises from interactions with other living entities, such as predation and interspecies competition. Additionally, organisms coordinate their internal defences and behavioural responses to these biological threats through mechanisms like immune activation and quorum sensing (Thammavongs et al. 2008). The focus of this chapter is primarily on abiotic stresses that are likely to be encountered in extraterrestrial environments.

5.1. Types of Stresses

Abiotic stressors include osmotic, oxidative, thermal, pH variations, starvation (Ding et al. 2009; Li et al. 2020), irradiance, sound frequency and intensity (Adadi et al. 2021), and exposure to toxins and other environmental disruptions (Tiquia-Arashiro et al. 2023). Such stressful conditions directly alter population dynamics. Table 5.1 outlines the different types of stress induced by abiotic factors, providing examples of the specific microorganisms they affect. Notably, stress due to radiation, extreme temperatures, magnetic fields, and oxidative conditions can be directly correlated with environments found on other planets and celestial bodies.

In the context of designing experiments for this thesis, the primary focus lies in understanding the characteristics of organisms within modified environments that serve as analogues for exoplanetary atmospheres. These include CO_2-rich atmospheres similar to Venus, or H_2- and N_2-dominated environments, as detailed in chapter 3. For instance, experiments by Seager and her team (Seager et al. 2020) demonstrated that both a simple cellular architecture like *E. coli* (a prokaryote) and a complex single-celled microorganism like yeast (a eukaryote) can thrive in a pure H_2 gas environment while producing a variety of by-product gases. At normal pressures, inert gases such as nitrogen and argon appear to be harmless. However, their low solubility in aqueous systems at atmospheric pressure makes it difficult to evaluate the true effects of exposure on microbial growth in unpressurised vessels. To properly assess these impacts, the effects of various high-pressure gases (up to 30 MPa) including nitrogen, argon, krypton, nitrous oxide, oxygen, and air were examined on yeast growth by Arao and his team (Arao et al. 2005). Based on the minimum inhibitory pressure (MIP) values derived from their findings, the gases were ranked from most toxic to least toxic in the following order: O_2 > N_2O > air > Kr > N_2 > Ar.

This section further emphasises oxidative stress as an analogue for water-worlds where there is a high probability of finding a substantial presence of hydrogen peroxide (H_2O_2), drawing upon the planetary parameters discussed in chapter 3.

Specifically, oxidative stress occurs when a cell's antioxidant and survival mechanisms fail to manage reactive oxygen species (ROS) or repair the damage they inflict (Morano et al. 2012). This form of stress, which can also be triggered by factors like acidity, heavy metals, ultraviolet radiation, and nutrient deficiencies, has been shown to stimulate the production of protective antioxidants across numerous species of photosynthetic green micro-algae and blue-green algae (Gauthier et al. 2020).

Table 5.1: Non-exhaustive list of abiotic stresses (Thammavongs et al. 2008)

Stress	**Synonym, similar or close to**	**Example of concerned micro-organisms**	**Taxonomic position**	**Ref.**
Physical				
Temperature	Thermal			
Heat				
Sublethal	Mild	*Sulfolobus islandicus*	Hyperthermophilic Archaea Crenarchaeota	(López-García and Forterre 1999)
Lethal		*Bacillus cereus*	Bacteria Gram+	(Periago et al. 2002)
Cold	Hypothermic Cooling			
Above 0° C	Chilling	*Arthrobacter globiformis*	Psychrotrophic Bacteria Gram+	(Oise Berger et al. 1997)
Under 0° (Freezing)		*Geotrichum candidum*	Fungi Yeast	(Panoff et al. 2000)
Drying				
Freeze drying	lyophilisation	*Lactobacillus reuteri*	Bacteria Gram+	(Palmfeldt and Hahn-Hagerdal 2000)
Spray drying	atomisation	*Beijerinckia* sp.	Bacteria Gram–	(Boza et al. 2004)
Pressure	Barotolerance Pressurisation	*Saccharomyces cerevisiae*	Fungi Yeast	(Dong et al. 2007)
Gravity	Gravitational			
Microgravity		*Streptomyces clavuligerus*	Bacteria Gram+ Actinomycete Streptomycete	(Fang et al. 1997)
Hypergravity		*Synechocystis* sp.	Cyanobacterium	(Erdmann et al. 1997)
Radiation	Irradiation			
Gamma		*Lactobacillus sake*	Bacteria Gram+	(Bower and Daeschel 1999)
Ultraviolet		*Saccharomyces cerevisiae*	Fungi Yeast	(Kale and Jazwinski 1996)
Visible light		*Escherichia coli*	Bacteria Gram–	(Rozen and Belkin 2001)
Ultrasonic	Acoustic	*Pseudomonas aeruginosa*	Bacteria Gram–	(Qian et al. 1999)
Electrical stress		*Pseudomonas oleovorans*	Bacteria Gram–	(Anglade et al. 2006)
Magnetic field		*Escherichia coli*	Bacteria Gram–	(Nakasono et al. 2000)
Mechanical stress				
Vibration	Vibrational	*Escherichia coli*	Bacteria Gram–	(S N et al. 2001)

Continued on next page

Table 5.1 – continued from previous page

Stress	Synonym, similar or close to	Example of concerned micro-organisms	Taxonomic position	Ref.
Shear	Shearing	*Lactobacillus delbrueckii subsp. bulgaricus*	Bacteria Gram+	(Arnaud et al. 1993)
Chemical				
Starvation	Deprivation Nutritional stress Nutrient limitation			
Carbon				
glucose starvation		*Lactococcus lactis*	Bacteria Gram+	(Kim et al. 2001)
Energy stress		*Macrophomina phaseolina*	Fungi Mould Phytopathogen	(Jana et al. 2000)
Phosphate		*Synechococcus* sp.	Cyanobacterium	(Scanlan et al. 1997)
Iron		*Helicobacter pylori*	Bacteria Gram–	(Merrell et al. 2003)
Overexposure				
Heavy metal		*Chlamydomonas reinhardtii*	Microalgae Chlorophyta	(Hanikenne et al. 2001)
Bile salt		*Enterococcus faecalis*	Bacteria Gram+	(Rincé et al. 2003)
Ethanol		*Oenococcus oeni*	Bacteria Gram+	(Tourdot-Marechal et al. 2000)
Organic solvent		*Pseudomonas putida*	Bacteria Gram–	(Ana Segura et al. 2004)
Sanitiser		*Yersinia enterocolitica*	Bacteria Gram–	(Favier et al. 2000)
Food Preservatives		*Gluconobacter oxydans*	Bacteria Gram+	(Eyles and Warth 1989)
Nitrosating agents	Nitrosative	*GiardiaCore intestinalis*	Protozoa Flagellate	(Lloyd et al. 2003)
Oxidative	Oxidation Superoxide Oxygen Peroxide Peroxidative Hydroperoxide	*Streptococcus thermophilus*	Bacteria Gram+	(Thibessard et al. 2004)
O_2		*Bifidobacterium* sp.	Bacteria Gram+	(Nebra et al. 2002)
Reductive		*Saccharomyces cerevisiae*	Fungi Yeast	(Trotter and Grant 2002)
Acid	Low pH			
Strong acid		*Rhodococcus equi*	Bacteria Gram+ Actinomycete Nocardioform	(Benoit et al. 2001)
Weak acid		*Zygosaccharomyces bailii*	Fungi Yeast	(Piper et al. 2001)
Alkaline		*Enterococcus faecalis*	Bacteria Gram+	(Flahaut et al. 1997)
Low water activity				
Desiccation	Dehydration Drought tolerance water stress	*Pseudomonas fluorescens*	Bacteria Gram–	(Schnider-Keel et al. 2001)
Hyperosmolarity	Salinity NaCl	*Lactobacillus plantarum*	Bacteria Gram+	(Poirier et al. 1998)
High water activity	Hypo-osmotic dilution stress	*Dunaliella tertiolecta*	Microalgae Chlorophyta	(Goyal 1989)

5.2. Reaction to Stress

This section examines how an organism might respond to environmental stress, focusing specifically on the profiles of volatile organic compounds (VOCs) that are associated with stress responses and are not typically produced under favourable conditions. Eukaryotic cells, such as yeast, have developed diverse strategies to combat the harmful effects of various stress conditions (Ding et al. 2009). For instance, during programmed cell death (PCD), the dynamic release of VOCs from these cells alters markedly; total VOC emissions rise significantly, peaking at approximately two hours. Among the seven primary types of detected VOCs-alkanes, alkenes, terpenoids, alcohols, aldehydes, ketones, and esters, three oxygenated compounds (aldehydes, ketones, and esters) demonstrate the most significant increase (Zuo et al. 2015). In one experiment, Pham's research group (Pham et al. 2008) cultivated the brewing yeast *Saccharomyces cerevisiae* BRAS291 in a defined medium under continuous sparging with hydrogen, helium, and oxygen, alongside a control without gas exposure, to evaluate three distinct external redox potentials. They observed profound differences regarding viable cell numbers, cell size, and specific metabolite production. Under these altered conditions, ethanol yields diminished, whereas the yields of glycerol, succinate, acetoin, acetate, and acetaldehyde were significantly enhanced.

Parallel responses are observed in marine environments, which are highly dynamic and subject organisms to rapid changes in temperature, light, pH, and nutrient availability. Diatoms respond to shifts in these environmental conditions by altering their physiological state, resulting in distinct changes to community composition and productivity (Li et al. 2020). When examining the broader spectrum of VOCs released by the microalgae-water phase in environments like Taihu Lake in China, Yu and his team (Y. j. Yu et al. 2019) detected alkanes, alkenes, oxygenated VOCs (OVOCs), and volatile sulphide chemicals (VOSCs). Similarly, a study by Colomb et al. demonstrated that investigated microalgae across three different algal classes possess the potential to produce isoprene, halogenated compounds, chlorobenzene, and dichlorobenzene to varying extents, although no simple, cell-associated typical VOC emission scheme could be universally established (Colomb et al. 2008). Nevertheless, targeted stressors do induce distinct volatile signatures; when *Chlamydomonas reinhardtii Dang.* cells are stressed by NaCl and Na_2CO_3, they release abundant VOCs, including a complex mixture of alkanes, alkenes, terpenoids, alcohols, aldehydes, ketones, and esters.

At a biochemical level, many of these volatile secondary products stem from lipid peroxidation. Lipid peroxidation refers to the oxidative breakdown of any highly unsaturated molecule containing multiple carbon-carbon double bonds. This process affects a wide range of substances, including unsaturated fatty acids, phospholipids, glycolipids, cholesterol, and various polyunsaturated hydrocarbons (Fu et al. 2015). The reaction of oxygen with unsaturated lipids produces a wide variety of oxidation products, primarily lipid hydroperoxides (LOOH). Among the many different aldehydes formed as secondary products during lipid peroxidation are malondialdehyde (MDA), propanal, hexanal, and 4-hydroxynonenal (4-HNE) (Ayala et al. 2014).

Experimentally, hydrogen peroxide (H_2O_2) can be utilised to induce oxidative stress and initiate these metabolic changes in microalgae (Barone et al. 2021). The effects of H_2O_2 exposure are visible via FT-IR analyses, which show overall reductions in proteins, carbohydrates, and lipids, alongside distinct variations triggered within the organisms' fatty acid signatures. While CO_2 acts as a baseline by-product of various standard metabolic processes in living systems, and methane (CH_4) serves as a common metabolite for methanogenic bacteria (Apolonski and Maiti 2021), the specific generation of complex VOCs under stress highlights localised survival networks.

The potential mechanisms driving these changes in VOC release involve the modulation of metabolic substrates and oxidative stress levels through stress-responsive signalling networks. The VOCs released by yeast cells are generated through various metabolic activities; components produced via primary metabolic pathways are typically considered waste from the detoxification process, whereas those generated by secondary metabolism function as defence or communication mechanisms. According to literature, ethyl acetate acts as a distinct VOC marker released by yeast cells in response to H_2O_2 stimulation (Liu and Yao 2025). Furthermore, a study conducted by Chen and his team (Chen et al. 2022) quantitatively analysed 117 VOC species and established that the levels of ethyl acetate and ethyl propanoate (ethyl n-propionate) altered in response to all three toxicants utilised (H_2O_2, CO_2, and O_3). Because the total VOC baseline released from yeast is relatively minor, continuous sampling is required to gather enough VOCs for quantitative analysis.

While H_2O_2 exposure most severely affects yeast cell proliferation, ethyl acetate and ethyl propanoate likely represent common metabolites generated by *S. cerevisiae* to cope with external toxic stress, even though *S. cerevisiae* can also actively biodegrade VOCs like ethanol, ethyl acetate, 1-propanol, and 2-propanol under normal conditions.

The yeast cell death triggered by low H_2O_2 concentrations is not caused by passive cell damage but involves the active, apoptotic cooperation of the cell (Madeo et al. 1999). A massive corruption of cellular structures and metabolism prevents this internal cooperation during the death process; high concentrations of H_2O_2 result in rapid cell death associated with a total disintegration of intracellular structures, lacking the typical phenotypic markers of apoptosis. Additionally, stationary cells of *S. cerevisiae* exhibit much less sensitivity to oxidative stress than exponentially growing cells (Madeo et al. 1999). For many of these stress conditions, however, it remains unclear whether reactive oxygen species (ROS) production is the fundamental factor that triggers the apoptotic response, or if ROS generation is merely a downstream by-product of the cell death pathway itself (Morano et al. 2012).

5.3. Limits of Volatile Production and Detection Challenges

The identification of bacterial volatile organic compounds (VOCs) predominantly relies on the time-intensive analysis of bacterial culture headspace. A more efficient approach is to identify bacterial VOCs directly from host biofluids, thereby facilitating rapid diagnoses (Zenner et al. 2025). For instance, the limit of detection (LOD) of current spectrometers is 10 parts per billion (ppb) for VOCs such as methane, acetone, and carbon monoxide, estimated using a one-litre sample of gaseous bio-fluid (Apolonski and Maiti 2021). To complement these systems, VOC species can also be qualitatively identified using the National Institute of Standards and Technology (NIST) library, where the ion response signal of the mass spectrum is used for semi-quantification (Chen et al. 2022).

While advanced spectroscopic methods offer powerful detection capabilities, extracting meaningful biological data from these instruments remains challenging. A primary hurdle stems from sample preparation sensitivity, where variations in sample thickness and uniformity can easily distort spectral quality and affect overall reproducibility. Furthermore, the limited spatial resolution of standard instrumentation restricts the detailed observation of microscopic cell wall variations, while overlapping absorption peaks can complicate the identification of specific functional groups, potentially leading to misinterpretations. This characterisation process is further hindered by a heavy dependence on reference spectra, particularly when dealing with scarce data for unique compounds. Finally, the instrument's sensitivity to environmental factors, such as ambient temperature and humidity, can introduce substantial variability into the final results (Tiquia-Arashiro et al. 2023).

Addressing these limitations is crucial for ensuring accurate and meaningful interpretations of Fourier-transform infra-red (FT-IR) spectroscopic data in cellular analysis. To minimise variability, sample preparation protocols must be strictly standardised, including the precise control of sample thickness, uniformity, and purity. Building comprehensive reference databases dedicated to microbial cell wall components can likewise facilitate more accurate spectral comparisons and identification. During data acquisition, implementing rigorous environmental controls, such as tightly regulating temperature and humidity, can help mitigate external variations. Furthermore, combining FT-IR with complementary high-resolution structural analysis techniques, such as electron microscopy and atomic force microscopy, can provide a deeper, more comprehensive understanding of the complex interactions within microbial cell walls. The fundamental working principles, underlying physics, and advanced data analysis techniques required to resolve these spectroscopic challenges are detailed in the subsequent chapter.

6

Detection Physics: Molecular Spectroscopy

After examining the various planetary environments and their potential biosignature gases, the next question that arises is how these gases can be detected remotely. Molecular spectroscopy provides a means to address this by studying how molecules interact with electromagnetic radiation [1]. In this chapter, the fundamental concepts of electromagnetic radiation are discussed, with particular emphasis on the infra-red region. This is followed by an explanation of the different ways radiation can interact with molecules and how these interactions can be utilized for molecular detection. Then the operating principles of the FT-IR spectrometer and the limitations associated with data analysis are discussed.

6.1. Electromagnetic Radiation

Electromagnetic radiation propagates through space at a constant speed in the form of waves or particles, with visible light and radio waves serving as common examples (Hamblin 2022). These waves consist of oscillating electric and magnetic fields that vary synchronously in both time and space. As illustrated in Figure 6.1, the electric field, the magnetic field, and the direction of propagation are all mutually perpendicular, demonstrating their transverse nature. EM radiation is described by several fundamental properties: energy, intensity, frequency, and wavelength. Wavelength is the physical distance between successive peaks or troughs of a wave and is typically expressed in metres, centimetres (10^{-2}) m, or nanometres (10^{-9} m). Frequency refers to the number of complete wave cycles that pass a fixed point per unit time and is measured in cycles per second, or hertz (Hz) (Sinha et al. 2023). Radiation intensity describes the amount of energy emitted per unit area[6].

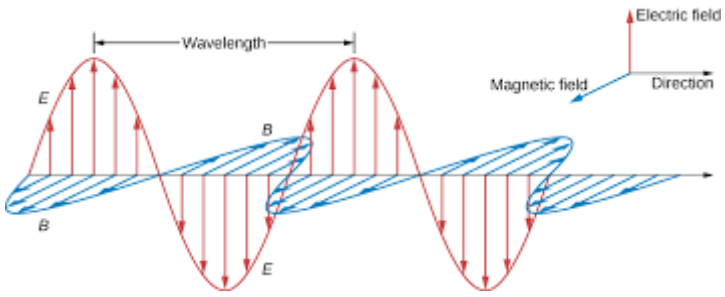

Figure 6.1: Generation of electromagnetic waves through oscillating electric and magnetic fields. The electric field, magnetic field, and direction of propagation are mutually perpendicular (credit: Stackexchange)

Figure 6.2 illustrates the full range of frequencies and wavelengths across the electromagnetic spectrum, with particular emphasis on the infra-red region. This portion of the spectrum is especially im-

[1] https://LibreTexts.org

portant for this thesis because it forms the basis for identifying and analysing chemical molecules in subsequent sections.

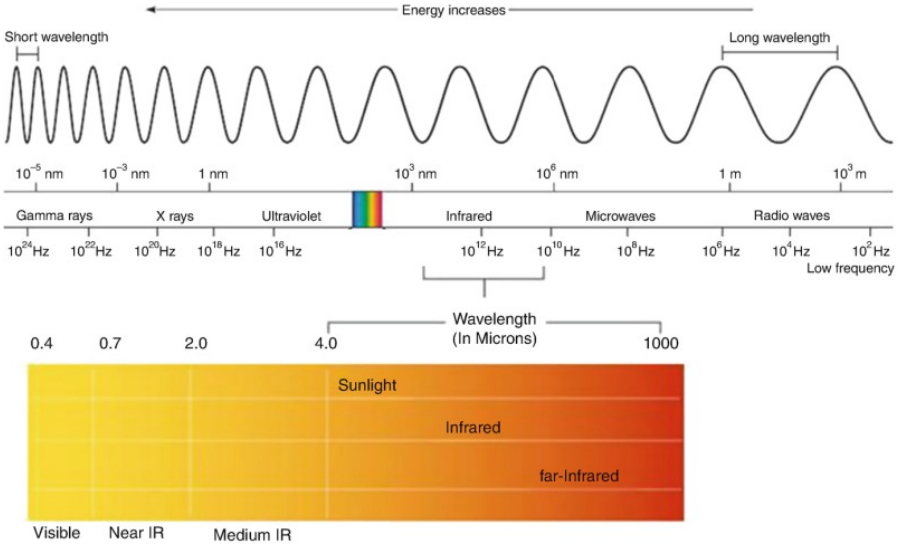

Figure 6.2: The electromagnetic spectrum includes infra-red (IR) radiation, which is divided into three regions: IR-A (0.7–1.4 μm), IR-B (1.4–3 μm), and IR-C (3–1000 μm)(Hamblin 2022)

Electromagnetic radiation can be produced in two main ways (Bhattacharjee 2023).

- Continuous-spectrum sources, such as the Sun, which emit radiation spanning a wide and uninterrupted range of frequencies. Table 6.1 shows the sources of different types of radiation and the temperatures associated with them.
- Discrete-frequency sources, which emit or absorb radiation only at specific characteristic frequencies, such as a radio transmitter or receiver tuned to a single channel.

Table 6.1: Types of radiation, associated temperatures, and typical sources (credit: ESA)

Type of radiation	Temperature	Typical sources
Gamma-rays	$> 10^8$ K	Matter falling into black holes
X-rays	10^6–10^8 K	Gas in clusters of galaxies Supernova remnants Stellar coronae
Ultraviolet	10^4–10^6 K	Supernova remnants Very hot stars
Visible	10^3–10^4 K	Stars Hot planets
infra-red	10–10^3 K	Very cool stars Planets Cool clouds of dust
Radio	< 10 K	Cool clouds of gas The Cosmic Microwave Background (CMB) Electrons moving in magnetic fields

In 1905, Albert Einstein challenged the classical wave theory of light by introducing the concept of light quanta, laying the groundwork for the later formulation of wave-particle duality. According to this theory, electromagnetic radiation displays a dual nature: it behaves like a wave, spreading out and interfering across space, while also acting as a stream of particles photons that carry discrete packets of energy. This wave–particle duality means that electromagnetic radiation possesses wavelike properties such as wavelength and frequency, yet simultaneously exhibits particle-like behaviour through quantized energy units. This understanding forms a crucial foundation for interpreting spectroscopic interactions between light and matter.

The wave–particle behaviour of electromagnetic radiation naturally introduces the need to understand how energy is exchanged between radiation and matter. This is described by Planck's Quantum Theory, which explains how matter emits and absorbs radiation. The key ideas are:

- Energy is released or absorbed in fixed, discrete packets rather than in a continuous flow. These packets are called quanta.
- A quantum represents a discrete unit of energy. When referring to light, this elementary packet is known as a photon.
- Planck's quantisation of energy is described by the his famous equation:

$$E = h\nu$$

  where the proportionality constant h = $6.62607015 \times 10^{-34}$,J·s is the Planck's constant and ν is the frequency in s^{-1}.

For electromagnetic waves,

$$c = h\nu$$

, where c is the speed of light in vacuum. The relationship of wavelength with energy can be given using

$$E = \frac{hc}{\lambda}$$

.

An electromagnetic wave travelling in an open, unbounded medium can have any frequency. However, when EM waves are confined for example, inside a cavity, or between reflective boundaries, only certain discrete frequencies can exist, forming standing electromagnetic waves. This restriction arises because the waves must satisfy boundary conditions imposed by the enclosure. In quantum mechanics, a similar principle applies to photons or charged particles confined by a potential, only specific standing wave patterns are allowed, leading to quantized frequencies and therefore quantized energy levels.

The relationship between wave propagation, confinement, and energy quantisation arises from the fundamental behaviour of electric and magnetic fields. These fields and the way they evolve in space and time are governed by Maxwell's equations, which form the mathematical foundation for understanding electromagnetic radiation in any setting. Maxwell's equations in differential form is given as:

$$\nabla \cdot \mathbf{E} = \frac{\rho}{\varepsilon_0} \tag{6.1}$$

$$\nabla \cdot \mathbf{B} = 0 \tag{6.2}$$

$$\nabla \times \mathbf{E} = -\frac{\partial \mathbf{B}}{\partial t} \tag{6.3}$$

$$\nabla \times \mathbf{B} = \mu_0 \left(\mathbf{J} + \varepsilon_0 \frac{\partial \mathbf{E}}{\partial t} \right) \tag{6.4}$$

where: $\mathbf{E}$ is electric field (vector), $\mathbf{B}$ is magnetic field (magnetic flux density),ρ is electric charge density, $\mathbf{J}$ is current density, ε_0 is permittivity of free space, μ_0 is permeability of free space, $\nabla\cdot$ is divergence operator, $\nabla\times$ is curl operator, and $\frac{\partial}{\partial t}$ is partial derivative with respect to time.

Maxwell's equations serve as the basis of classical electromagnetism, bringing together electric and magnetic fields within a single framework. Developed by James Clerk Maxwell in the 19th century, these four equations explain how electric charges generate electric fields, how electric currents give rise to magnetic fields, and how time-varying magnetic fields induce electric fields. Equation 6.1 stems from Gauss's law which states that the electric flux through a closed surface depends on the charge contained within it. Gauss's law for magnetism establishes that magnetic monopoles do not exist, meaning the total magnetic flux through any closed surface is zero given as Equation 6.2. Faraday's law describes how a changing magnetic field produces an electromotive force in a conductor shown in Equation 6.3. The Ampère–Maxwell law extends Ampère's original formulation by including the

displacement current, showing that a changing electric field also generates a magnetic field given by Equation 6.4. Taken together, these equations predict the existence of electromagnetic waves and reveal that light itself is an electromagnetic wave.

Maxwell's equations have also transformed our understanding of the universe in two major ways. First, by revealing the full electromagnetic spectrum, they enabled astronomers to observe the cosmos far beyond what the human eye can detect. Instruments tuned to different wavelengths uncover phenomena otherwise hidden, such as the debris of supernova explosions or the shrouded surface of Venus.

Second, Maxwell's formulation introduced a new way of expressing physical laws. His theory captured all known electromagnetic effects without relying on any mechanical medium, treating the field itself as a fundamental entity. This shift, together with Maxwell's discovery that the speed of light is a universal constant, laid essential groundwork for Einstein, ultimately helping him develop the ten field equations that form the basis of general relativity (credit: Institute of Physics).

6.2. Interaction Mechanisms

The way light interacts with matter is fundamental across numerous scientific disciplines, enabling key technologies such as spectroscopy, sensing, quantum information processing, and lasers. In most of these applications, light is described as electromagnetic plane waves that travel at the speed of light in a vacuum (Rivera and Kaminer 2020).Photons behave differently while interacting with matter compared to charged particles because they carry no electric charge. The likelihood that a photon will interact with matter depends on its energy and on the atomic number and density of the material, which determine the electron density of the absorber.

An electron in an atom, or the chemical bonds within a molecule, can absorb energy from incoming light (photons) or heat-induced vibrations (phonons) only when the energy matches the difference between two specific allowed states, whether those are electronic, vibrational, or rotational levels. A photon with the appropriate wavelength can elevate an electron from a lower to a higher energy state. However, the electron cannot remain in the excited state for long,it eventually returns to a lower energy level, releasing a photon in the process. This emitted photon has an energy

$$E_2 - E_1 = h\nu$$

which is equal to the difference between the two levels (Bhattacharjee 2023).

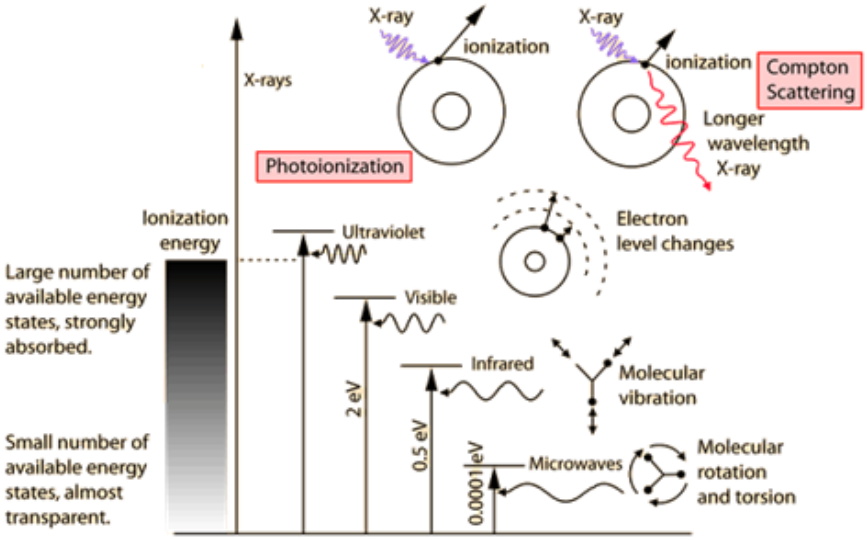

Figure 6.3: Interaction of radiation with matter (credits:HyperPhysics)

Figure 6.3 illustrates how different regions of the electromagnetic spectrum interact with matter by inducing distinct atomic or molecular processes. High-energy X-rays cause ionization, removing electrons

from atoms, and may undergo Compton scattering. Ultraviolet and visible radiation excite electrons to higher electronic energy levels. infra-red radiation excites molecular vibrations, while microwaves stimulate molecular rotation and torsion. The shaded bar indicates that absorption strength depends on the availability of accessible energy states. High-energy regions have many possible transitions and are strongly absorbed, whereas low-energy regions have fewer transitions and appear nearly transparent. Together, the diagram links radiation energy to the type of molecular interaction it produces.

Since molecular vibrations occur in the infra-red region, this part of the spectrum is discussed in the further sections. Examining the absorption spectrum in the infra-red provides detailed, bond specific information about molecular concentrations and has become an essential and widely used technique in chemical analysis (Steele 2006). Absorbance analysis measures how much light is absorbed by the molecules in a sample, with the degree of absorption depending on the wavelength of the incident light. When light is absorbed, its energy and momentum are transferred to a charged particle, causing the individual photons to cease to exist. This absorbed energy may increase the particle's kinetic or potential energy, resulting in effects such as heating or atomic transitions. All electromagnetic processes, including absorption, are fundamentally governed by Maxwell's equations Equation 6.4, as expressed in their quantum form known as quantum electrodynamics (QED).

6.3. Molecular Spectroscopy Fundamentals

Molecules possess several types of quantized energy levels, each separated by characteristic energy gaps. Among the various possible energy transitions, the primary modes discussed in this context are electronic, vibrational, and rotational. Other transitions include fine splitting, magnetic quadrupole, etc., which are out of the scope of this thesis. Generally, rotational energy levels have the smallest energy spacings, and transitions between them occur within the same vibrational state. Vibrational energy levels exhibit intermediate energy gaps, larger than rotational gaps but much smaller than electronic ones. In contrast, electronic energy levels are separated by very large energy differences, requiring significantly more energy for transitions to occur.

6.3.1. Electronic

A molecular electronic transition occurs when a molecule absorbs a photon, promoting an electron from a lower-energy molecular orbital to a higher-energy one. These transitions typically take place in the ultraviolet (UV) or visible regions of the electromagnetic spectrum, producing distinctive spectral bands that provide insight into a molecule's electronic structure [6].

To fully understand these transitions, one must first grasp the concept of hybridization. According to localized valence bond theory, standard atomic orbitals (s, p, d, and f) that are similar in energy but not entirely equivalent can combine mathematically to form hybrid atomic orbitals. These newly hybridized orbitals are equivalent in energy and are properly oriented to maximize bonding efficiency. Generally, the head-on overlap of these orbitals forms sigma (σ) bonds between two atoms, whereas the lateral overlap of un-hybridized p orbitals creates pi (π) bonds.

The Figure 6.4 shows the formation of these orbitals. The specific electrons responsible for electronic transitions are classified into three primary categories:

- **Sigma (σ) electrons:** Found in saturated molecules, such as alkanes. Because these compounds contain exclusively single bonds, they are generally highly stable and less reactive.
- **Pi (π) electrons:** Present in unsaturated molecules, such as alkenes and alkynes. The presence of at least one double or triple bond makes these compounds significantly more reactive and susceptible to addition reactions.
- **Non-bonding (n) electrons:** Located on heteroatoms. In organic chemistry, a heteroatom is any atom other than carbon or hydrogen (e.g., nitrogen, oxygen, phosphorus, sulphur, halogens, or metals like lithium and magnesium) that is incorporated into the molecular framework.

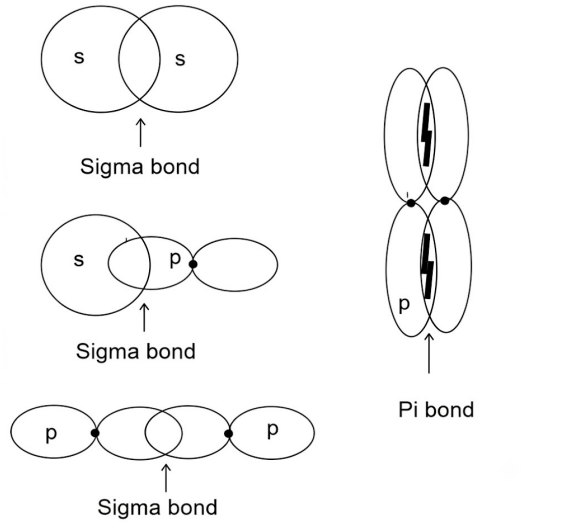

(a) The sigma bond formation via the head-on overlap of s-s, s-p, and end-to-end p-p orbitals. The pi bond formation through the lateral, side-on overlap of two parallel p-orbitals.

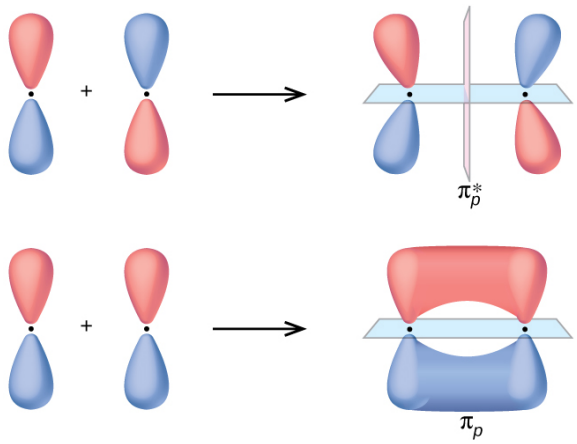

(b) The lateral overlap of two p atomic orbitals produces a pair of π molecular orbitals. An in-phase combination yields a bonding orbital, which features electron density concentrated in lobes above and below a central node located along the internuclear axis. Conversely, an out-of-phase combination creates an anti-bonding orbital characterised by two distinct nodes: one lying directly on the internuclear axis, and another intersecting it perpendicularly.

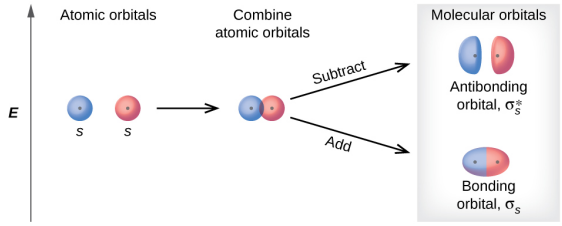

(c) The interaction of two s atomic orbitals generates both bonding sigma (σ) and anti-bonding sigma-star (σ^*) molecular orbitals.The plus ($+$) symbols are used to denote the positions of the atomic nuclei

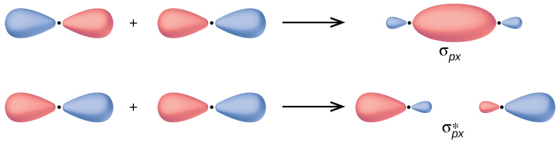

(d) The linear combination of the wave functions for two p atomic orbitals along the internuclear axis yields a pair of molecular orbitals, denoted as σ_p and σ_p^*.

Figure 6.4: Schematic representations of atomic orbital interactions, detailing the geometric overlap that forms σ and π bonds, as well as the generation of bonding and anti-bonding molecular orbitals from constituent s and p atomic orbitals.[2]

When these electrons absorb UV radiation, they are excited into higher-energy states as shown in Figure 6.5. The fundamental electronic transitions include:

- $\sigma \rightarrow \sigma^*$ **transition:** An electron in a bonding σ orbital is promoted to an anti-bonding σ^* orbital. This process requires the highest energy input and is typically observed in completely saturated molecules, such as methane, which contain only single bonds like C – H.
- $n \rightarrow \sigma^*$ **transition:** A non-bonding (n) electron is excited into an anti-bonding σ^* orbital. This transition requires relatively low energy and is exhibited by molecules containing heteroatoms.
- $\pi \rightarrow \pi^*$ **transition:** An electron moves from a bonding π orbital to an anti-bonding π^* orbital. The energy required for this transition is intermediate between that of $n \rightarrow \sigma^*$ and $n \rightarrow \pi^*$. It is a characteristic feature of compounds with π-electron systems, including aromatics, alkenes, alkynes, nitriles, and carbonyls.
- $n \rightarrow \pi^*$ **transition:** A non-bonding electron is promoted to an anti-bonding π^* orbital. This is generally the lowest-energy transition and is common in unsaturated molecules containing heteroatoms.

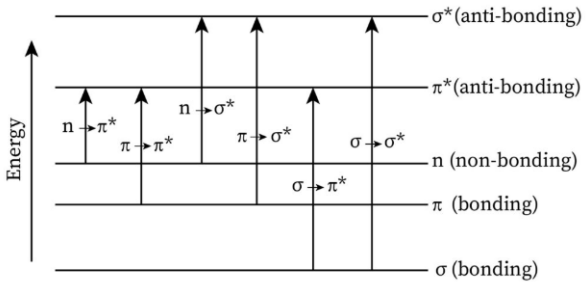

Figure 6.5: Types of electronic transition (credit: Bartleby)

The net contribution of these electrons to a molecule's overall stability is quantified by its bond order, which is determined by how electrons fill the bonding and anti-bonding molecular orbitals. Bond order serves as a direct indicator of a covalent bond's strength and length: as the order increases between two specific atoms, the bond becomes stronger and shorter. Consequently, a triple bond is both shorter and stronger than a double bond, requiring far more energy to break, just as a double bond is stronger than a single bond. It is worth noting, however, that bonds of the identical order between entirely different atoms can exhibit a wide range of inherent bond energies.

Finally, the electronic transitions moving between these energy levels can occur via two pathways: radiative and nonradiative. Radiative transitions explicitly involve the absorption or emission of a photon, whereas nonradiative transitions occur without any photon involvement, dissipating the excess energy internally through molecular vibrations.

6.3.2. Vibrational

When a molecule absorbs sufficient energy to shift between vibrational energy levels without altering its electronic state, a vibrational transition occurs. These transitions correspond to changes in the internal vibrational motions of the constituent atoms. Such transitions generally manifest in the infra-red region of the electromagnetic spectrum, and the resulting spectral features are consequently referred to as infra-red spectra. Much like electronic transitions, vibrational transitions can be radiative (involving the absorption or emission of an infra-red photon) or non-radiative (where vibrational energy is dissipated internally or through collisions as heat). For pure vibrational transitions, the fundamental requirement is that the molecule must experience a change in its dipole moment during the vibrational motion. Under the harmonic oscillator approximation, the vibrational selection rule dictates that transitions must occur between adjacent energy levels:

$$\Delta v = \pm 1$$

Molecular vibration is characterised by the periodic displacement of atoms relative to one another, maintaining a stationary overall centre of mass. The frequency of this vibration can be determined using the following expression:

$$\nu = \frac{1}{2\pi c}\sqrt{\frac{k}{\mu}},$$

where k represents the force constant and μ denotes the reduced mass. For a vibrational mode to be excited, the molecule must absorb an energy quantum, ΔE, that exactly matches its vibrational frequency, defined as:

$$\Delta E = h\nu,$$

where h is Planck's constant. Non-linear tri-atomic and more complex polyatomic molecules undergo various stretching and bending vibrational modes (Sinha et al. 2023). Figure 6.6 illustrates several of these stretching configurations.

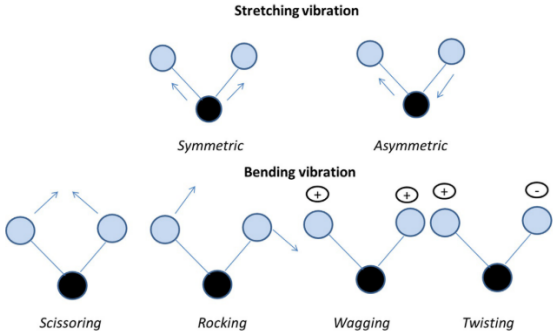

Figure 6.6: Stretching modes include symmetric and asymmetric motions, while bending modes consist of scissoring, rocking, wagging, and twisting movements (Sinha et al. 2023)

Diatomic molecular vibrations consist of the cyclic extension and compression of the covalent bond. For minimal internuclear displacements, this behavior is well-approximated by a simple harmonic oscillator. However, a physically realistic representation requires an anharmonic oscillator model. This model acknowledges that nuclear repulsion increases steeply at short distances, and that excessive stretching ultimately leads to bond dissociation. As a result, vibrational energy levels become increasingly closely spaced at higher energies. In an anharmonic system, the restoring force is no longer strictly proportional to the displacement. Real-world anharmonicity typically involves two forms of nonlinearity: elastic anharmonicity and damping anharmonicity. In practice, anharmonic systems are treated by starting with a harmonic approximation and calculating the anharmonic deviation using perturbation theory.

For a molecule modelled as a simple harmonic oscillator, the angular frequency is expressed as:

$$\omega_{\text{osc}} = \frac{1}{2\pi}\sqrt{\frac{k}{\mu}},$$

where k is the force constant and μ is the reduced mass, defined by the formula:

$$\mu = \frac{m_x m_y}{m_x + m_y},$$

with m_x and m_y representing the masses of the respective atoms x and y.

The force constant, k, is highly dependent on the nature of the chemical bond, which is inherently linked to molecular structure and atomic hybridization. A standard single bond generally consists of one sigma (σ) bond. In contrast, double and triple bonds incorporate additional pi (π) bonds. This increased electron sharing draws the atoms closer together, resulting in multiple bonds being significantly shorter, stronger, and stiffer (yielding a higher k) than single bonds. The formation of these multiple bonds is explained by hybrid orbitals, where standard atomic orbitals mix to optimize molecular bonding geometry. A single bond generally corresponds to sp^3 hybridization. A double bond requires sp^2 hybridization, leaving an unhybridized p-orbital available to form a π bond. A triple bond necessitates sp hybridization to accommodate two π bonds. Because an sp-hybridized bond has the highest s-orbital character, it holds the atoms the tightest. Consequently, bond strength, hybridization, and the resulting force constant are intrinsically unified, following the order $\mathrm{sp} > \mathrm{sp}^2 > \mathrm{sp}^3$. Therefore, stronger bonds with higher sp character vibrate at higher frequencies. Conversely, bonds connecting heavier atoms exhibit lower vibrational frequencies than those connecting lighter atoms, due to the inverse relationship with reduced mass. Additionally, phenomena such as resonance can alter both bond lengths and strengths, thereby impacting the associated force constant (Vvedensky 2016).

Converted to wavenumbers, the vibrational frequency is formulated as:

$$\tilde{\nu} = \frac{1}{2\pi c}\sqrt{\frac{k}{\mu}} \ \text{cm}^{-1},$$

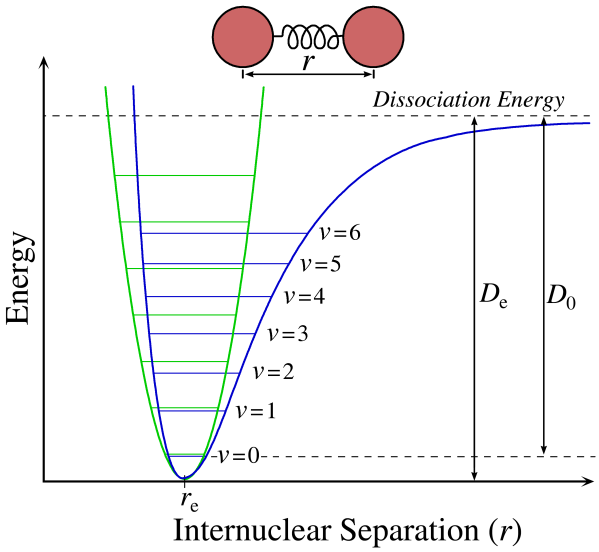

Figure 6.7: A potential energy diagram for a diatomic molecule comparing the realistic anharmonic oscillator (blue curve) with the idealized harmonic oscillator approximation (green parabola). The potential energy, $V(R)$, is plotted as a function of the internuclear distance, R. Bond compression is represented towards the left, while bond extension is shown towards the right. (CC BY-SA 3.0; Mark Somoza, March 26, 2006)

where k remains the force constant and μ the reduced mass. The corresponding quantized energy states for a simple harmonic oscillator are defined by:

$$E_v = \left(v + \tfrac{1}{2}\right)\hbar\omega_{\text{osc}}, \qquad v = 0, 1, 2, \ldots$$

where ω_{osc} represents the angular vibrational frequency and v denotes the vibrational quantum number (Vvedensky 2016).

A molecule's total number of vibrational modes is dictated by its degrees of freedom. For standard non-linear molecules, this equates to $3N - 6$ vibrational modes, with N representing the total number of constituent atoms. Linear molecules, however, possess slightly fewer degrees of freedom, amounting to $3N - 5$ (Wenzel n.d.).

As illustrated in Figure 6.7, the idealized harmonic oscillator potential (green parabola) provides only a local approximation of the more realistic anharmonic potential well (blue curve). The anharmonic curve successfully models bond dissociation at significant internuclear distances (R), a critical physical behavior completely absent in the harmonic approximation. This divergence highlights just one fundamental distinction between harmonic and actual anharmonic oscillators.

The true potential energy function can be expanded using a Taylor series:

$$V(R) = V(R_e) + \frac{1}{2!}\left(\frac{d^2V}{dR^2}\right)_{R=R_e}(R-R_e)^2 + \frac{1}{3!}\left(\frac{d^3V}{dR^3}\right)_{R=R_e}(R-R_e)^3 + \frac{1}{4!}\left(\frac{d^4V}{dR^4}\right)_{R=R_e}(R-R_e)^4 + \ldots \tag{6.5}$$

The first derivative term vanishes because it is evaluated at the equilibrium distance (R_e), which corresponds to the absolute minimum of the potential well. The harmonic oscillator approximation truncates the series after the quadratic term:

$$V_{HO}(R) \approx V(R_e) + \frac{1}{2!}\left(\frac{d^2V}{dR^2}\right)_{R=R_e}(R - R_e)^2$$

By neglecting the constant absolute energy term ($V(R_e)$), establishing a spring constant k, and defining r as the displacement from equilibrium ($r = R - R_e$), the standard harmonic oscillator potential is derived:

$$V_{HO}(R) = \frac{1}{2}kr^2$$

Conversely, retaining the expansion from Equation 6.5 up to the cubic term results in the following expression:

$$V(x) = \frac{1}{2}kr^2 + \frac{1}{6}\gamma r^3 \tag{6.6}$$

where

- $V(x_0) = 0$, and $r = R - R_0$.
- k is the harmonic force constant, and
- γ is the first (i.e., cubic) *anharmonic* term

6.3.3. Rotational

Before discussing the complex interplay of coupled transitions, it is helpful to first examine rotational transitions also independently.

For pure rotational transitions, a molecule's rotations are commonly treated as those of a rigid rotor (ignoring centrifugal distortion). The rotational energy is quantized in discrete levels given by:

$$E_r = \frac{h^2}{8\pi^2 I} J(J+1)$$

where I is the moment of inertia, defined as

$$I = \mu r^2$$

with μ being the reduced mass and r the equilibrium bond length.

Experimentally, frequencies or wave numbers are often measured instead of energies. Dividing E_r by h or by hc gives the more commonly used term symbols $F(J)$, expressed using the rotational quantum number J and the rotational constant B.

In frequency units:

$$F(J) = \frac{E_r}{h} = \frac{h}{8\pi^2 I} J(J+1) = BJ(J+1)$$

In wave number units:

$$F(J) = \frac{E_r}{hc} = \frac{h}{8\pi^2 cI} J(J+1) = BJ(J+1)$$

To observe a pure rotational spectrum, a molecule must possess a permanent dipole moment. The fundamental rotational selection rule is:

$$\Delta J = \pm 1$$

since a photon carries one quantum of angular momentum, and conservation of angular momentum must be satisfied.

At room temperature, states with $J \neq 0$ can be populated because they constitute the fine structure of vibrational states and have smaller energy spacings than successive vibrational levels. The population of energy levels in a macroscopic sample is governed by the Boltzmann distribution, which relies on the available thermal energy, calculated as kT (where k is the Boltzmann constant and T is temperature). If the temperature were drastically lowered (e.g., close to absolute zero), the thermal energy would drop below the rotational energy gaps, and all molecules would collapse into the lowest possible rotational state ($J = 0$). Conversely, at extremely high temperatures (e.g., inside a star or a combustion engine), kT becomes large enough to populate higher vibrational states ($v > 0$) as well.

6.3.4. Ro-Vibrational

Having established these independent modes, the combined effect is examined. In hetero-nuclear diatomic molecules in the gas phase, each normal vibrational mode exhibits additional, closely spaced spectral lines (typically separated by 1–10 cm^{-1}) that arise from rotational transitions occurring alongside the vibrational transition. An excitation to a higher vibrational state changes the molecule's average bond length, inherently altering its moment of inertia. This structural shift directly modifies the rotational

energy states, making these coupled rotational transitions a physically expected outcome. Since the energy differences associated with vibrational transitions are much larger (spectral bands around 1000 cm^{-1}), the rotational transitions appear as a fine structure superimposed on the main vibrational bands [6]. Thus, there are rotational energy levels associated with every vibrational level.

During a ro-vibrational transition, both vibrational and rotational states change simultaneously. A transition with $\Delta J = 0$ (i.e., $J'' = 0$ to $J' = 0$), where $v_0 = 0$ and $\Delta v = +1$, is forbidden due to the conservation of angular momentum, and therefore pure vibrational transitions without accompanying rotational changes are generally not observed in these gas-phase spectra.

Instead, the combined selection rules produce two distinct branches in the spectrum:

- R-branch ($\Delta J = +1$)
- P-branch ($\Delta J = -1$)

Each spectral line in a branch is labelled $R(J)$ or $P(J)$, where J represents the quantum number of the lower rotational state as shown in Figure 6.8. A schematic shows the rotational energy levels J superimposed on vibrational energy levels v. The possible transitions that give rise to the P- and R-branches are highlighted in purple and red, respectively, while the theoretical Q-branch transition is shown in blue.

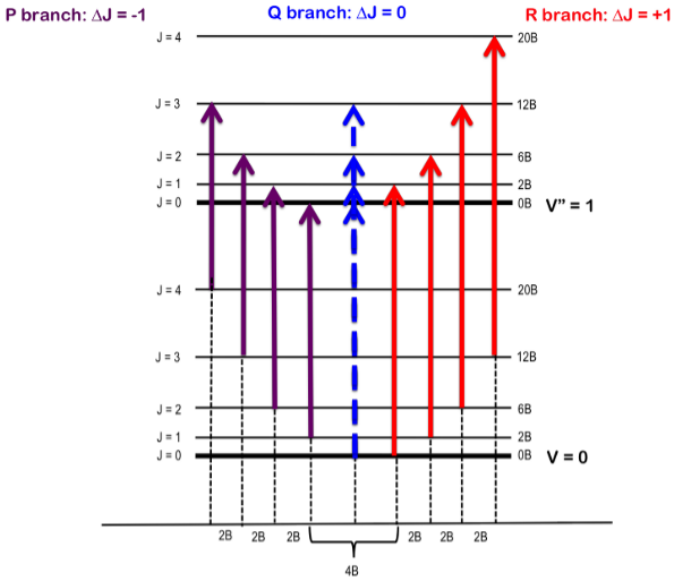

Figure 6.8: Rotational Energy Levels

Ro-vibrational spectral lines first increase in energy with increasing J, reach a maximum, and then decline toward zero as J continues to rise. In heavier molecules, the rotational constant B is smaller because the moment of inertia is larger, causing the exponential population factor to decrease less sharply. As a result, the population distribution shifts toward higher J values. Increasing temperature produces a similar effect, pushing the population to larger J levels.

As the energy increases, the R-branch lines move closer together, becoming more evenly spaced. Conversely, as the energy decreases, the P-branch lines spread farther apart. These trends arise from two key effects: rotational–vibrational coupling and centrifugal distortion.

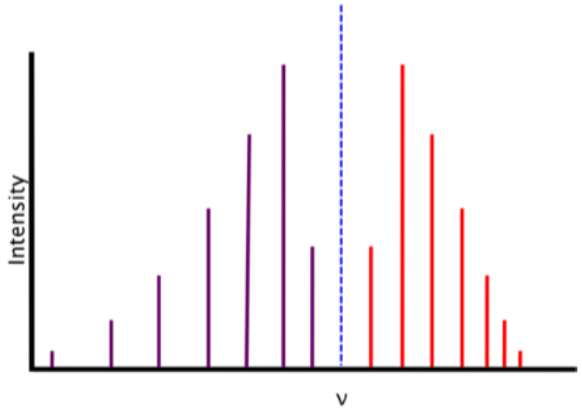

Figure 6.9: A real rovibration spectrum

The total change in energy is given by:

$$\Delta E = \Delta E_{\text{el}} + \Delta E_{\text{vib}} + \Delta E_{\text{rot}}$$

Figure 6.10 shows how a molecule's energy is organized across different scales. Within each electronic state, both ground and excited, there are several vibrational levels, and each vibrational level is further divided into many closely spaced rotational levels. These structured, quantized layers explain why molecules exhibit distinct rotational, vibrational, and electronic spectral features. The diagram highlights how energy increases progressively from rotational to vibrational and finally to electronic transitions.

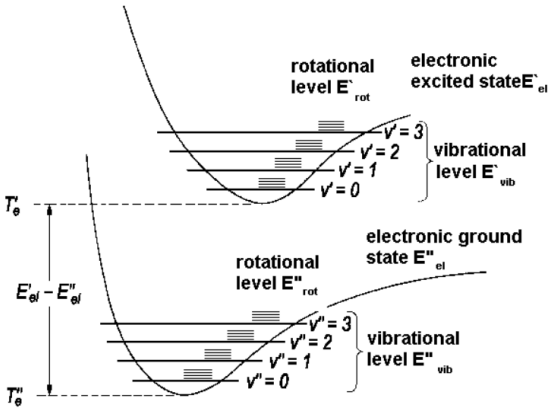

Figure 6.10: Energy-level diagram of a molecule showing the electronic ground and excited states, each containing vibrational levels (v' and v") with superimposed rotational sublevels (E_{rot}) (source: TU Braunschweig)

6.4. Infrared Spectroscopy

Spectroscopy is the study of how matter absorbs and emits light or other forms of electromagnetic radiation. It works by separating incoming radiation into its component wavelengths, much like a prism producing a rainbow and analysing the resulting spectrum. The term "spectroscopy" covers a wide range of techniques that use electromagnetic radiation to reveal the structure and properties of materials. All spectroscopic methods follow the same basic idea: a beam of radiation is directed at a sample, and the way the sample interacts with that radiation is measured.

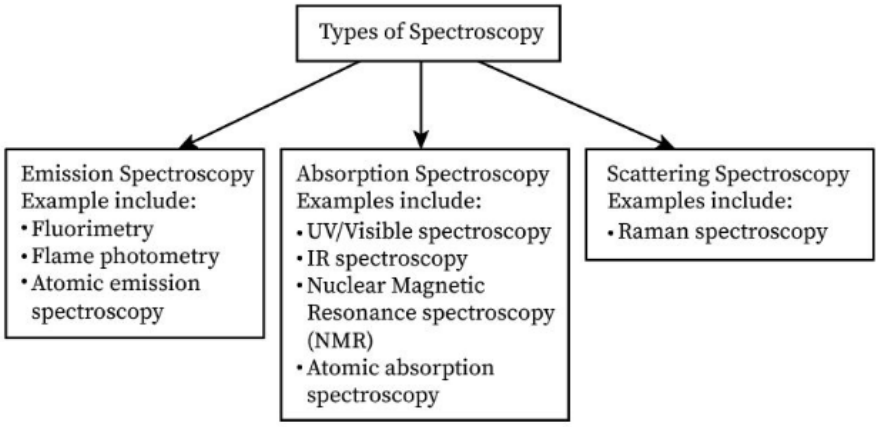

Figure 6.11: Types of Spectroscopy

Absorption spectroscopy is a technique that measures how a sample absorbs electromagnetic radiation when the two interact. The resulting data are recorded as a function of wavelength or frequency, producing what is known as an absorption spectrum. Figure 6.12 illustrates the different regions of EM spectrum and the type of spectroscopy associated with it. Since the focus of this thesis is to study molecular behaviour in the infrared region of the electromagnetic spectrum, it is discussed in detail in the following subsection. The infrared region is emphasized because it contains characteristic vibrational and rotational transitions that allow for the identification and analysis of molecular species.

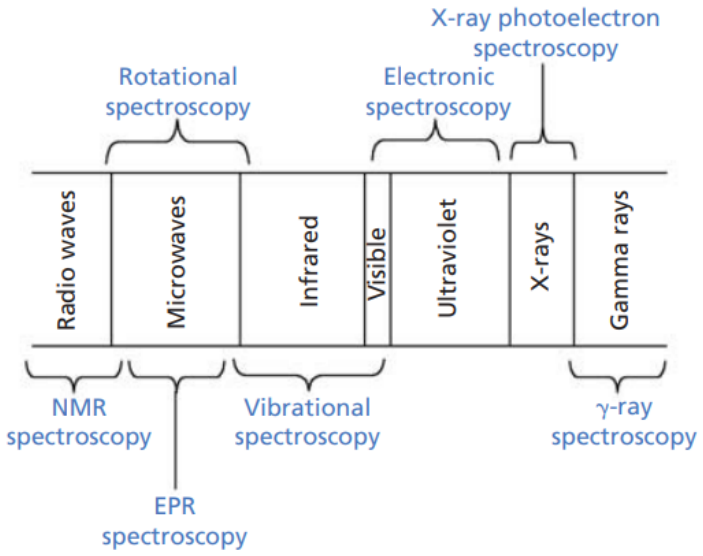

Figure 6.12: The different parts of the electromagnetic spectrum and the kinds of spectroscopy associated with each (D. Ball 2006)

A common approach to searching for life on these planets is to look for spectral clues that indicate strong chemical imbalances in the atmosphere (Rein et al. 2014). The various telescopes like James Webb, Spitzer, SOFIA, Hubble observe in infrared. To understand which molecules produce an IR spectrum (i.e., are IR active), this discussion will first introduce the key concepts that govern IR activity, followed by an analysis of the spectral features of some important molecules.

6.4.1. Absorption Bands

IR spectra typically display absorption data by plotting the wave number (cm^{-1}) on the x-axis against either absorption intensity or percent transmittance on the y-axis. Transmittance (T) is defined as the

ratio of radiant power transmitted through the sample (I) to the incident radiant power (I_0). Conversely, absorbance (A) is calculated as:

$$A = \log(1/T) = -\log(I/I_0) = \epsilon c l$$

According to the Beer-Lambert Law, the intensity of molecular absorption depends on three factors: the molar extinction coefficient (ϵ), which reflects the molecule's intrinsic transition dipole moment; the concentration of the sample (c); and the sample's path length (l). While transmittance spectra range from 0% to 100%, offering distinct contrast between the intensities of strong and weak bands, absorbance values range theoretically from zero to infinity. Finally, the width of the spectral lines is determined by the molecule's interactions with its surrounding environment[6].

6.4.2. IR Active Molecules

Infrared radiation has the appropriate energy to induce vibrational excitations in molecules. The definition of wave number is the reciprocal of the wavelength. A higher wave number indicates a shorter wavelength, signifying that the associated radiation possesses a greater frequency and energy[3]. Infrared (IR) spectroscopy measures vibrational excitation, a process that involves changes in the distances between atoms within a molecule[4]. The IR spectrum is divided into three primary regions: near, mid, and far. While these domains can be categorized by their physical wavelength: near (0.75–5 μm), mid (5–30 μm), and far (30–1000 μm), researchers generally prefer to utilize wavenumbers (cm^{-1}) for practical applications. Under this metric, the regions are defined as near ($4,000$–$12,800$ cm^{-1}), mid (200–$4,000$ cm^{-1}), and far (10–200 cm^{-1}), with the mid-IR being the most widely used for analytical studies. The relationship between the two units is given by:

$$\text{Wavenumber}(\text{cm}^{-1}) = \frac{10{,}000}{\text{Wavelength } (\mu\text{m})}$$

Wavenumbers are favoured because they provide workable figures that maintain a direct, linear relationship with the vibrational energy being analysed. Accordingly, an inverse correlation dictates the spectrum: as the wavenumber and its associated energy scale upward, the physical wavelength becomes shorter (Breeding and Ahline 2024). Double and triple chemical bonds generally exhibit strong absorption features in the mid-infrared region. However, molecular nitrogen (N_2) and molecular oxygen (O_2), which contain triple and double bonds respectively, do not absorb infrared radiation due to their molecular symmetry and lack of a dipole moment.

Difference in Energy Level

The second necessary condition for IR absorption to take place is that the energy of the light entering on a molecule must equal a vibrational energy level difference within the molecule as discussed in section 6.2.

Dipole Moment

The dipole moment quantifies the charge asymmetry around a molecule's rotation axis; this is the charge distribution that interacts with incoming photons. Simply put, a larger dipole moment allows more photons to interact with the molecule, which dictates the amount of energy absorbed during a specific molecular transition (Paynter 2008). It is given by:

$$\vec{\mu} = \sum_i q_i \, \vec{r}_i$$

where $\vec{\mu}$ is the dipole moment vector, q_i is the magnitude of the i^{th} charge and $\vec{r_i}$ is the vector representation the i^{th} charge's position[4].

[3] https://open.maricopa.edu/fundamentalsoforganicchemistry/

[4] LibreTexts Chemistry Library, https://chem.libretexts.org

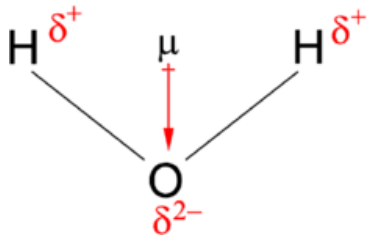

Figure 6.13: Dipole moment of water. The convention in chemistry is that the arrow representing the dipole moment goes from positive to negative[4].

A molecule must undergo a change in dipole moment during vibration to be IR active, which generally requires the presence of polar bonds. Mono-atomic elements like He, Ne, Ar are completely IR inactive as they have no bonds to vibrate or rotate, and they have no dipole moment that can change. Thus, molecules composed of different elements such as HCl, NO_2, H_2O, and CO_2 show IR absorption. In contrast, homo-nuclear molecules and elemental solids, including O_2, N_2, graphite, and silicon, are IR inactive. These molecules, which are typically IR inactive, can become temporarily active due to Collision-Induced Absorption (CIA) (Van Kranendonk and Bird 1951). The activation of the vibrational band is attributed to molecular distortions induced during binary collisions. The resulting induced dipole moment is significant only for the brief duration of the collision. The Fourier transform of the autocorrelation function of this induced dipole moment, $\mu_i(t)$, yields a broad spectral density profile. This profile is centered at zero frequency and is commonly referred to as a purely translational spectrum. In contrast, ordinary infrared absorption arises from individual polar molecules, and its line intensity increases linearly with density. CIA, however, is most notable in non-polar, infrared-inactive gases. CIA results in induced spectral lines being observed at ro-vibrational frequencies that are dipole-forbidden in single (non-interacting) molecules. Nevertheless, dipole transitions may be induced within the interacting molecular pair itself (Borysow 1994). Kowalski 2014 found that in highly compressed helium, a dipole moment is induced due to simultaneous collisions involving three or more helium atoms. Further, it is important to note that CO_2 does not have a permanent dipole moment but is still IR active and this is explained in the further section.

6.4.3. FT-IR Spectrometer

Fourier-transform infrared (FT-IR) spectroscopy is a robust analytical technique used to measure the absorption or emission of infrared radiation by a sample. By leveraging the mathematical process of the Fourier transform, these spectrometers overcome the mechanical limitations of older, dispersive instruments, allowing for the simultaneous collection of high-resolution spectral data across a wide range of wavenumbers (Griffiths and Haseth 2007). This capability provides the enhanced photon throughput and rapid signal averaging necessary for the highly sensitive detection of trace volatile organic compounds. The working principle, the spectral features and spectra of some molecules, and the challenges in volatile identification are discussed.

Working Principle

In conventional spectroscopy, a monochromator is used to scan through individual wavelengths or frequencies while measuring absorbance or emission, producing a spectrum in the frequency domain. In contrast, Fourier transform techniques collect data in the time domain and then mathematically convert it into a frequency-domain spectrum[4]. An FT-IR instrument directs infrared radiation, typically spanning 10,000 to 100 cm^{-1}, through a sample. Some of this radiation is absorbed while the rest is transmitted. The absorbed energy causes rotational and/or vibrational transitions within the sample's molecules. The detector then records the resulting signal as a spectrum, commonly displayed from 4000 to 400 cm^{-1}, which serves as a molecular fingerprint. Since each molecule or functional group produces a distinct spectral pattern, FT-IR is highly effective for chemical identification[5].

[5] https://rtilab.com/techniques/FT-IR-analysis/

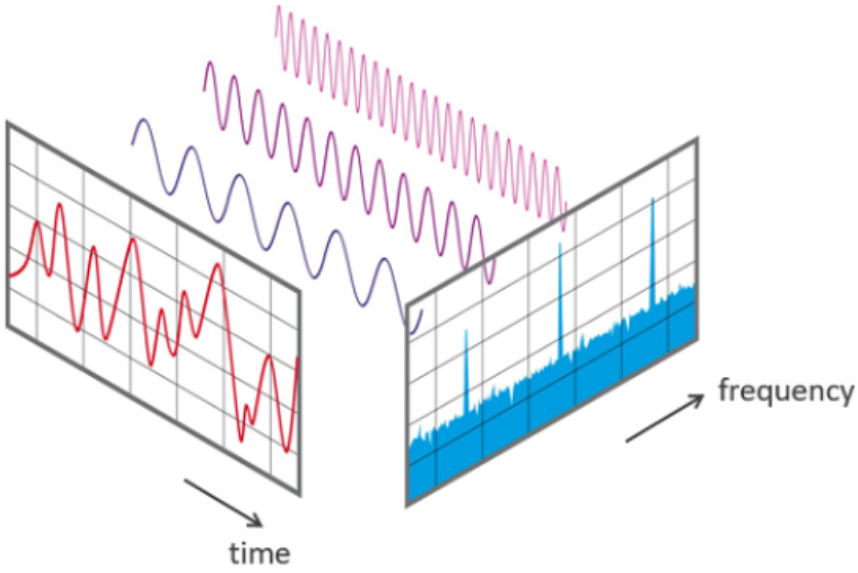

Figure 6.14: Representation of a signal in both the time and frequency domains (Zueck 2018)

Figure 6.14 shows how a wave is represented in the time and frequency domains. The Fourier transform of a time-domain signal $x(t)$ is mathematically expressed as:

$$X(\omega) = \int_{-\infty}^{\infty} x(t) e^{-j\omega t}\, dt$$

$$\omega = 2\pi f$$

where $x(t)$ is the original signal as a function of time; $X(\omega)$ the same signal represented in terms of its frequency components; ω is the angular frequency (in radians per second) and $j = \sqrt{-1}$ is the imaginary unit [6]. To record an FT-IR spectrum, the infrared radiation from the source must first be transformed into a time-domain signal. This is typically accomplished using a Michelson interferometer, which is the standard device for generating interferogram in FT-IR instruments. It is interesting that while the human visual system is highly optimized for spatial pattern recognition, allowing for the easy identification of localized absorbance peaks in the frequency domain (Goldstein and Hale 2015), it is biologically incapable of performing the complex inverse calculus required to deconstruct an interferogram. FT-IR spectroscopy only became a practical analytical tool with the advent of digital computers capable of executing the Fast Fourier Transform (FFT) algorithm to un-mix the time-domain signal (Griffiths and Haseth 2007).

[6] https://www.academyofemc.com/

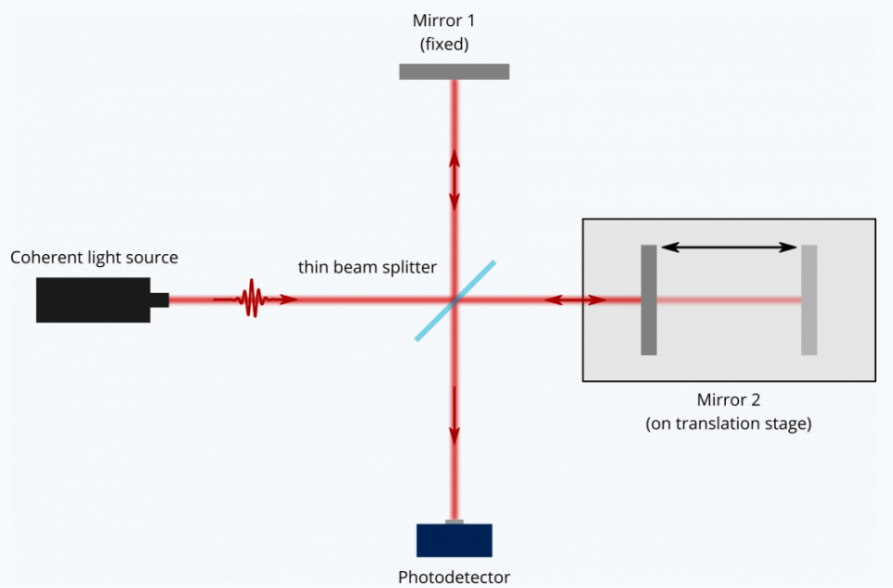

Figure 6.15: Schematic of Michelson Interferometer (credit:Wiredsense)

An interferometer is an instrument that relies on coherent light to produce interference by splitting a beam into two paths and then recombining them. The Michelson interferometer, shown in Figure 6.15, is widely used and has a straightforward design. It requires only a few optical components and is easy to align. It operates with a coherent light source, typically a monochromatic laser, either continuous wave or pulsed. When the incoming beam reaches a thin beam splitter, it is divided into two lower intensity beams that travel to separate mirrors and are then reflected back to the splitter, where they recombine. If the returning beams have no phase difference, they interfere constructively, producing a strong signal at the photodetector. If they differ by half a wavelength, they interfere destructively, resulting in minimal or zero intensity. The phase difference depends on the difference in optical path lengths, and even small changes in the mirror position generate significant intensity variations at the detector. The sensitivity of these interference patterns to optical delay depends on the wavelength used in the spectrometer.

One major benefit of FT-IR spectroscopy is the ability to rapidly record multiple spectra and average them. While a traditional scanning spectrophotometer equipped with a monochromator may require several minutes to sweep through all wavelengths, an FT-IR acquires the necessary data within just a few seconds because the mirror movement is fast and efficient. FT-IR instruments also lack slits, giving them much higher optical throughput. Nearly all the photons from the source contribute to the measurement, unlike in monochromator based systems where significant power is lost. The combination of rapid signal averaging and increased photon throughput provides FT-IR with a substantial sensitivity advantage, enabling the detection of much lower analyte concentrations. Additionally, FT-IR spectrometers offer superior spectral resolution compared to conventional scanning instruments, particularly when the mirror motion is stable and reproducible. Resolution refers to the ability to distinguish closely spaced peaks within a spectrum[6].

Another widely used technique for measuring infrared absorbance is ATR (Attenuated Total Reflectance). In ATR, the infrared beam enters a crystal at an angle that produces multiple internal reflections before exiting the opposite side, as shown in Figure 6.16. The sample is pressed against the top surface of the crystal so that interaction occurs at the points where the internally reflected beam contacts the crystal sample interface. In general, increasing the number of internal reflections enhances energy transfer and improves spectral quality, although single bounce ATR systems are preferred when analysing very small sample areas[5].

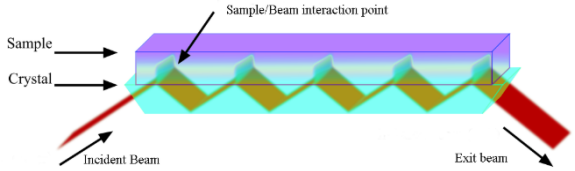

Figure 6.16: Interaction of the infrared beam with the sample using a multi-bounce ATR (Attenuated Total Reflectance) setup [5]

Absorption Peak (Wavenumber, Intensity)

The shapes of spectral bands are fundamentally governed by the interactions between vibrating molecules and their surrounding environment. Understanding this relationship improves spectral interpretation and clarifies unexpected results in qualitative and quantitative analyses (Bradley 2015). The Figure 6.17 illustrates how the line shape can transition from a Gaussian profile (typical of solids) to a Lorentzian profile (typical of gases) depending on the relative rates of relaxation and de-phasing processes. In liquids, where both processes occur on similar timescales, the line shape exhibits a combination of Gaussian and Lorentzian characteristics, known as a Voigt profile.

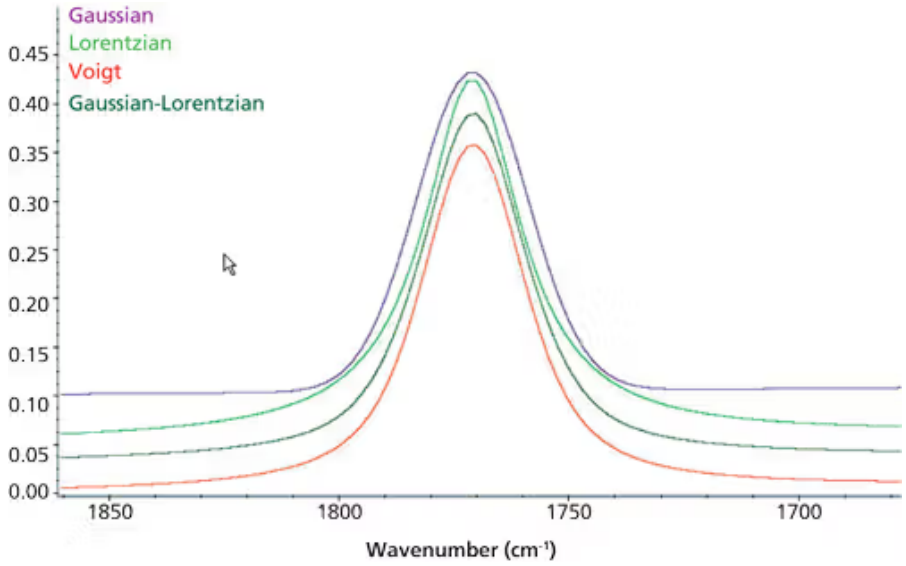

Figure 6.17: Line shape Transition (Bradley 2015)

In gas spectroscopy, the required spectral resolution depends critically on the Full Width at Half Maximum (FWHM) of the absorption feature. FWHM is a measure of peak width that is calculated as the width at the half height of a peak (B. C. Smith 2024). For gases exhibiting a broad FWHM, concentration information remains well-preserved even at lower spectral resolutions, primarily because decreasing the resolution increases the Signal-to-Noise Ratio (SNR). However, this reduction cannot be limitless, as excessively low resolution can mask the absorption features entirely, compromising the accuracy of the quantitative analysis. Conversely, for gases exhibiting a narrow FWHM, reducing the spectral resolution significantly distorts the absorption features, leading to a loss of accurate concentration information. Given that the FWHM contains vital spectral information useful for synthesising background spectra, high-resolution spectra are generally beneficial for accurately quantifying gases characterised by a narrow FWHM (Qin et al. 2023).

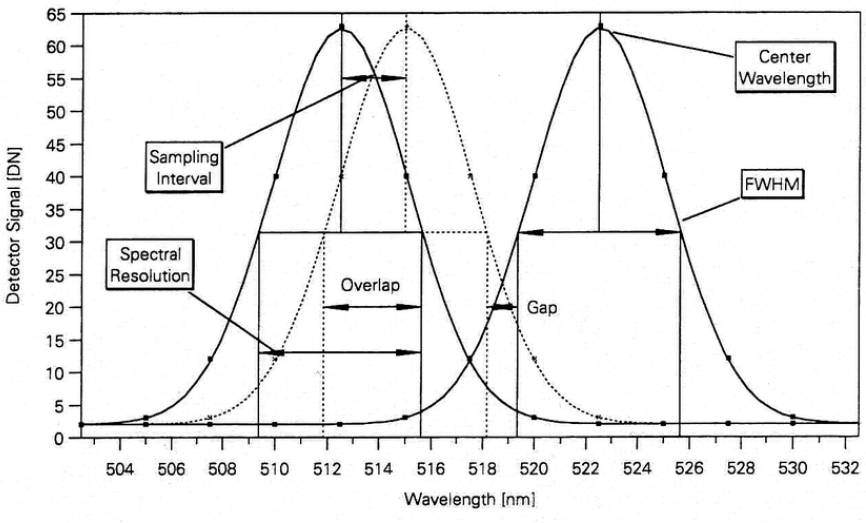

Figure 6.18: Spectral resolution, spectral sampling interval, FWHM and centre wavelength of a Gaussian response function.(Ellert et al. 1998)

Generally, the width of a peak in an infrared spectrum is directly related to the strength of the intermolecular interactions within the sample. Functional groups involved in strong intermolecular forces, such as the O – H group participating in hydrogen bonding, will typically exhibit broad peaks . Conversely, functional groups with weak intermolecular interactions, such as the vibrational peaks originating from the benzene ring in benzonitrile, will usually display narrow peaks. It is this variation in the strength of intermolecular interactions that ultimately dictates the differing peak widths observed for various functional groups (B. C. Smith 2024).

The intensity of an IR absorption signal is proportional to the square of the dipole moment change associated with a vibrational mode. IR absorption bands are typically classified as strong (s), medium (m), or weak (w) depending on their relative intensities in the spectrum. Strongly polar bonds, such as C=O, produce intense bands, while moderately polar or asymmetric bonds yield medium bands. Weakly polar or symmetric bonds often generate weak or even undetectable absorptions.

Peak Shape

Spectral lines serve as powerful diagnostic tools for determining the physical and chemical conditions present in astronomical objects. These features manifest as narrow emission or absorption lines ($\Delta\nu \ll \nu$) within the spectra of gaseous and ionized sources. Fundamentally, both spectral-line emission and absorption are quantum mechanical phenomena (Condon and Ransom 2018). Although the Schrödinger equation calculates absorption at a precise wave number, real-world absorption is always distributed across the wave number spectrum. The measured absorption cross-section (σ) at any specific wave number ($\tilde{\nu}$) is determined by the multiplication of two factors: the central line strength (S) and a normalised line shape function (L) (Paynter 2008).

$$\sigma(\nu) = S(\nu_l) f(\nu - \nu_l)$$

.

High-resolution spectrometers experimentally demonstrate that spectral lines possess a measurable, finite width rather than being infinitely narrow. This effect, dependent on various factors, is called “spectral broadening” and is essential for analysing the mechanisms behind light emission [7].

The measurable width of spectral lines arises from three primary physical phenomena:

1. **Natural Broadening:** Caused by the quantum mechanical uncertainty (ΔE) associated with energy levels that have finite lifetimes. It is a direct consequence of the Heisenberg Uncertainty Principle, a fundamental concept in quantum mechanics governing particle-wave behaviour. In

[7] [Physics Open Lab, 2017]

its energy-time formulation, the principle establishes that the uncertainties in energy (ΔE) and time (Δt) have a minimum product: $\Delta E \Delta t \approx h/2\pi$. Since the excited atomic states have finite lifetimes (typically on the order of microseconds to nanoseconds), the uncertainty in time (Δt) is non-zero. Following Heisenberg's relation, this implies the energy uncertainty (ΔE) must also be non-zero. Consequently, the frequency of the emitted photon carries an intrinsic uncertainty defined as $\Delta\nu \approx \Delta E/h \approx 1/2\pi\Delta t$. This natural line width is extremely narrow (approximately 10^{-5} nm) and is typically considered negligible in standard measurements.

2. **Thermal (Doppler) Broadening:** Thermal broadening results from the Doppler shift in observed frequency caused by the random motion of radiating atoms relative to an observer. Since this random atomic motion is directly driven by temperature, the effect is known as "thermal" broadening. According to Maxwell-Boltzmann statistics, gas atoms exhibit a Gaussian velocity distribution given by $\Delta\nu_D = \frac{\nu_0}{c}\sqrt{\frac{2kT}{m}}$, where $\Delta\nu_D$ is the Doppler line width. It represents the broadening of the spectral line frequency. ν_0 is the central frequency (or rest frequency) of the emitted spectral line. c is speed of light in a vacuum. k is the Boltzmann constant ($\approx 1.38 \times 10^{-23}$ J/K), which relates temperature to energy. T is the absolute temperature of the gas in Kelvin. Higher temperatures lead to faster atomic motion and greater broadening. m is the mass of the emitting atom or molecule. Lighter atoms move faster at a given temperature, resulting in greater broadening with mean energy on the order of kT. Consequently, the spectral line profile is also Gaussian. The width of this broadening increases with higher temperatures and is more pronounced for lighter atoms. For example, the Hydrogen Hα line at 6000 K has a width of 0.036 nm, a value generally too small for detection by standard instruments.
3. **Collisional Broadening:** This arises when interactions between excited atoms shorten the lifetime of the excited state, thereby increasing the transition's energy uncertainty (ΔE). This effect becomes the dominant broadening mechanism in high-density, high-pressure plasma environments. Unlike the Gaussian profile seen in thermal broadening, collisional broadening produces a Lorentzian spectral line shape, defined by a sharper central peak and more extended "wings". Under conditions of both high pressure and temperature, resonant self-absorption may also take place, where emitted light is re-absorbed by cooler layers of gas surrounding the source.
4. **External Fields Broadening:** External forces like magnetic or electric fields can dramatically reshape spectral lines through the Zeeman and Stark effects. The Zeeman effect happens when a magnetic field splits a single spectral line into multiple distinct components, interacting with the atom's own magnetic properties. The Stark effect occurs when an external electric field shifts the energy levels of an atom, causing its spectral lines to split. While both phenomena involve splitting discrete lines, in practice, this often looks like a broader, smeared-out line on a spectrum.

Spectral Regions: Functional Group region, fingerprint region

The graph of typical FT-IR spectrum is shown in Figure 6.19. In an infrared spectrum, the horizontal axis (x-axis) displays the range of infrared energy (usually in wave number or wavelength). The vertical axis (y-axis) indicates the amount of infrared light either absorbed or transmitted by the analysed sample. The resulting peaks, known as absorbance bands, identify the specific energies where the sample's atomic vibrations resonate upon exposure to the infrared region of the electromagnetic spectrum (Mathias 2018). Spectral analysis begins by identifying both the number and the specific location of the peaks within the spectrum (Reilly et al. 1992). Usually, it is interpreted from high-frequency end to identify the functional groups. The absorbance bands in an infrared spectrum are generally divided into two regions:

- **Group Frequencies:** Group Frequencies are typically found above 1500 cm^{-1}. These bands are characteristic of small groups of atoms or specific functional groups (e.g., $-CH_2$, OH, or C=O). Because they are often unique to a functional group, they are highly reliable for identifying these specific structures within a molecule.
- **Molecular Fingerprint Frequencies:** The Molecular Fingerprint Frequencies are usually observed below 1500 cm^{-1}. This region reflects the complex vibrations of the molecule as a whole, providing a distinct identity for the entire structure. Although some functional groups also absorb here, this region is less useful for identifying specific groups because the patterns are very complex. However, the absence of a band in this region is often more significant for structural analysis

than the presence of one. To identify unknown materials, and to ensure quick and accurate identification, reference libraries like HITRAN (Gordon et al. 2026) is used.

HITRAN, an acronym for the HIgh-resolution TRANsmission molecular absorption database, is a comprehensive, high-precision compilation of spectroscopic parameters for molecules in the gas phase. This dataset is essential for computer codes designed to predict and simulate the transmission and emission of light within gaseous media, with a specific emphasis on terrestrial and planetary atmospheres. The database is composed of five major components:

- Line-by-line Parameters: Spectroscopic data required for high-resolution radiative transfer modelling.
- Cross-sections: Experimental infrared absorption data for molecules that cannot yet be represented in line-by-line formats.
- Collision-Induced Absorption (CIA): Data describing absorption caused by molecular collisions.
- Aerosol Data: Indices of refraction for suspended particles.
- General Tables: Global reference data, such as partition sums, applicable to the entire dataset.

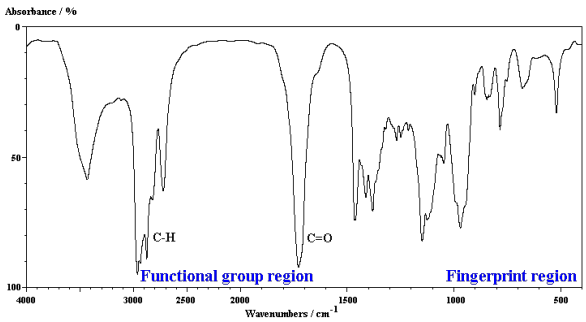

Figure 6.19: Sample FT-IR Spectrum (credits: Dr.Ian Hunt, University of Calgary)

Baseline and Artifacts: Baseline Tilt/Drift, Atmospheric Interference

The baseline method is a widely used approach for performing quantitative analysis from IR spectra. While determining the band peak's absorbance or percent transmittance is straightforward, the method derives its name from the procedure used to determine the background absorbance or transmittance. The goal is to estimate where the spectrum would lie if the component being measured were absent. Although an isolated band allows for an easy background line tangent to the spectral background, a more complex scenario arises when a band occurs on the sloping side of a major component or solvent peak. In such cases, while sketching a rounded "zero sample" background is possible, it is subjective.

The preferred technique is to draw a tangent line connecting the band wings or more distant points as shown in Figure 6.20. Achieving a consistent baseline construction is essential, as this should yield a reproducible measured absorbance that varies linearly with concentration, requiring calibration with standards. A key advantage of this method is its ability to reduce or eliminate corrections for background absorption from the solvent or major component. Care must be taken to choose tangent points that are not overly sensitive to concentration variations of other components present (Colthup 2001).

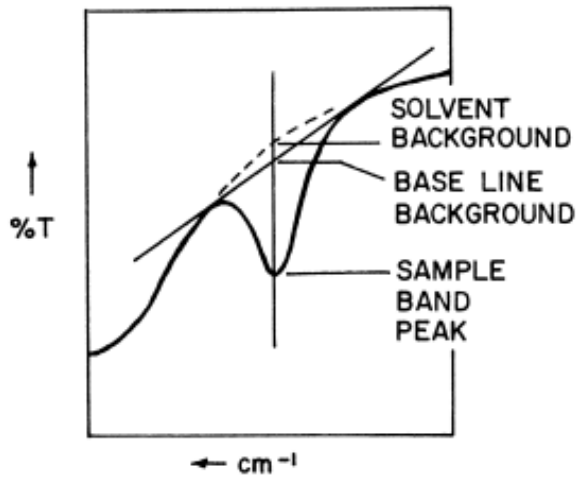

Figure 6.20: Part of an infrared spectrum showing the base line construction for the base line method used in quantitative analysis (Colthup 2001)

Quantitative Analysis

Quantitative analysis is the fundamental methodological process of determining the absolute or relative quantities of specific components that make up a system. While qualitative analysis focuses on identifying the specific substances present in a mixture, quantitative analysis seeks to measure exactly how much of a target analyte is there. In the context of spectroscopic techniques, this is fundamentally achieved by correlating a specific, measurable physical property such as the absorption or emission of electromagnetic radiation to the concentration of the molecules of interest using established mathematical relationships (Stuart 2004).

1. Integrated Band Intensity

For quantitative analysis in IR spectroscopy, peak height (absorbance) is frequently used, although this measurement is sensitive to instrumental resolution; reducing the resolution broadens narrow peaks and consequently reduces their height. Conversely, the integrated intensity (or total band area) is much less sensitive to changes in instrumental resolution and holds greater theoretical significance . This integrated intensity measures the total radiation energy absorbed by a specific vibrational mode and is proportional to the square of the change in the dipole moment with respect to the normal coordinate. Quantitatively, the integrated intensity is expressed as the integrated absorptivity over the entire band, which is calculated by dividing the band area (absorbance integrated over the band, corrected for background) by the path length (l) and concentration (c), as derived from Beer's Law (absorptivity $=$ A$/$(lc)). When concentration is measured in moles per cubic centimetre and cell length in centimetres, the standard unit for integrated absorptivity is centimetres per mole (Colthup 2001).

2. Column Density

To determine the physical characteristics of the interstellar medium, scientists frequently measure the column density, which is defined as the total number of molecules of a particular substance per unit area along the observer's line of sight (Mangum and Shirley 2014).The column density can be expressed as the number of molecules in energy level u integrated over the path length ds.

$$N_u \equiv \int n_u ds$$

.

3. Signal to Noise Ratio

Due to the increased prevalence of relatively low-cost FT-IR spectrometers in chemistry departments, students now have the opportunity to explore various aspects of real spectral data acquisition and analysis concerning signals, noise, and the signal-to-noise ratio. This exploration is made possible by

the instrument's inherent capabilities to adjust spectral resolution, perform ensemble averaging, and process spectral data (Blitz and Klarup 2002). Blitz et al. (2002) demonstrates that S/N is highest in spectral regions with the greatest single beam signal intensity, increases with the square root of the number of averaged scans (S/N $\propto \sqrt{n}$), and generally increases with decreased spectral resolution. It also conveys that while a high S/N is desirable, it is often achieved at the cost of increased measurement time or the loss of critical spectral information due to reduced resolution or smoothing. In scenarios where detector noise is the primary limiting factor rather than shot noise associated with discrete electronic transitions FT-IR spectrophotometers demonstrate a superior signal-to-noise ratio (S/N) compared to dispersive instruments. This phenomenon, known as Fellgett's advantage (or the multiplex advantage), arises from two key factors. First, because FT-IR utilizes multiplexing to measure all wavelengths simultaneously rather than sequentially, the S/N improves proportionally to the square root of the number of sampling points. Second, unlike monochromator measurements where noise concentrates at the peaks of emission lines, multiplexed measurements distribute noise uniformly across the spectrum. Consequently, FT-IR achieves significantly higher S/N at critical emission peaks (Stefanov 2015).

6.4.4. FT-IR Spectrum of some molecules

Infrared spectra contain crucial information regarding a molecule's peak position, height, and width, all of which must be correctly understood and integrated to successfully distinguish the spectra of different functional groups from one another. Specifically, peak positions (wave numbers) are determined by the intrinsic properties of the vibrating functional group, namely its force constant (bond strength) and reduced mass . The peak height (intensity) is governed by Beer's Law, which dictates its dependence on the concentration of the absorbing substance, the path length of the light, and the absorptivity of the functional group. This absorptivity, in turn, is dependent upon the square of the rate of change of the dipole moment with respect to bond length, $(\frac{d\mu}{dx})^2$, for that particular vibration. Lastly, peak widths (FWHM) are primarily determined by the strength of intermolecular interactions within the sample, such as hydrogen bonding or solvent effects.

1. Water

Water vapour possesses a permanent dipole moment and thus exhibits both a rotational and ro-vibrational structure (Paynter 2008).The Figure 6.21 illustrates four distinct types of coupling mechanisms involving the water molecule's bending motion. a. shows the coupling of the bending vibrations between two separate water molecules (intermolecular bend-bend).b. is Coupling between the bending vibration and the restricted rotation (libration) within the same water molecule (intramolecular bend-libration).c. Coupling between the bending vibration of one water molecule and the libration of another (intermolecular bend-libration).d. Mixing of the bending and librational motions caused by non-uniform (asymmetric) hydrogen-bond strengths.Oxygen atoms are red spheres; Hydrogen atoms are white spheres. Arrows indicate the H – O – H angle bisector. Hydrogen bonds are shown as broken blue lines, where thick lines denote strong bonds and thin lines denote weak bond.

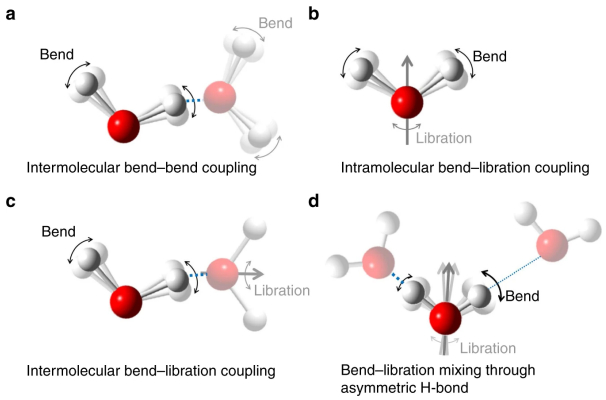

Figure 6.21: (a)intermolecular bend-bend , (b)intramolecular bend-libration,(c)intermolecular bend-libration , and (d) bend-libration mixing driven by variations in hydrogen-bond strength (C. C. Yu et al. 2020)

2. O -- H in Carboxylic acids and Alcohols

The shape of a spectral peak serves as a valuable diagnostic tool for identifying specific chemical bonds. For instance, O – H stretching modes typically shows up as broad, rounded bands rather than sharp peaks, a phenomenon caused by hydrogen bonding between hydroxyl groups. The O – H stretching band in alcohols and carboxylic acids is commonly attributed to rotational coupling and intermolecular interactions (Sinha et al. 2023). This happens because the protons are shared to varying degrees with neighbouring oxygen atoms, the individual O – H bonds vibrate at a range of slightly different frequencies. These overlapping vibrations merge to form a distinctively broad peak, making the O – H group easily recognizable in an IR spectrum [4].

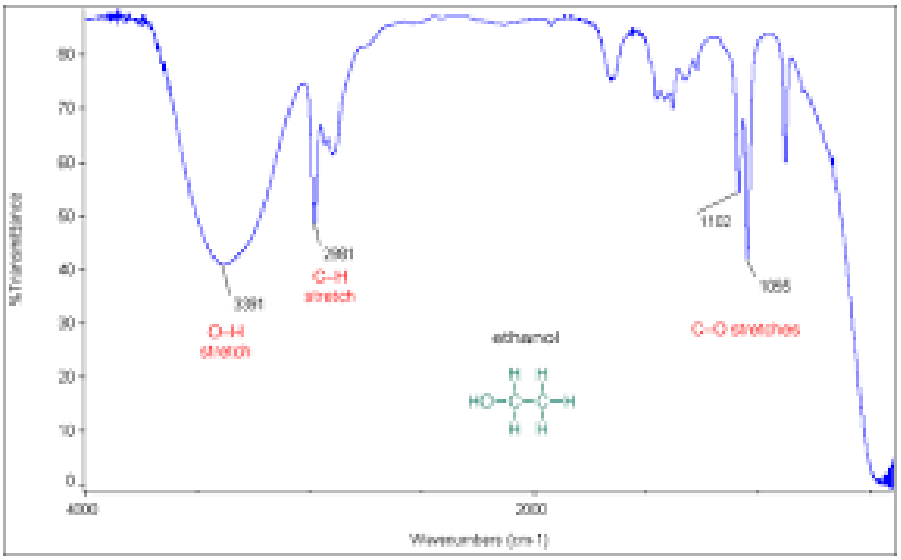

Figure 6.22: IR Spectrum of Ethanol

Carboxylic acids are characterized by a strong, wide O – H stretch band in their mid-infrared spectrum, appearing as a very broad absorption in the $3300 - 2500$ cm^{-1} region, typically centered around 3000 cm^{-1} . This broadness is primarily due to the fact that carboxylic acids commonly exist as hydrogen-bonded dimers. Figure 6.23 shows both the free carboxyl group, which is uncommon, and the dimeric structure, which is the usual way carboxylic acids exist. Since this wide O – H band overlaps with the sharp C – H stretching bands of alkyl and aromatic groups, the region between 3300 and 2500cm^{-1} often presents a somewhat “messy” absorption pattern, with the broad O – H feature superimposed upon the narrower C – H features [8]. In Figure 6.24, it is seen that a broad absorption peak resulting from the O – H stretch is observed, which is superimposed on the sharper bands corresponding to the C – H stretch . Key specific absorption frequencies identified in the spectrum include the C = O stretch at 1721 cm^{-1}, the C – O stretch at 1296 cm^{-1}, and the O – H bending vibrations at 1419 cm^{-1} and 948cm^{-1}.

Free carboxyl (uncommon), 1760 cm^{-1}

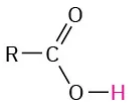

Associated carboxyl (usual case), 1710 cm^{-1}

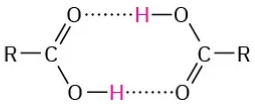

Figure 6.23: Free Carboxyl and Associated Carboxyl

[8] https://orgchemboulder.com/

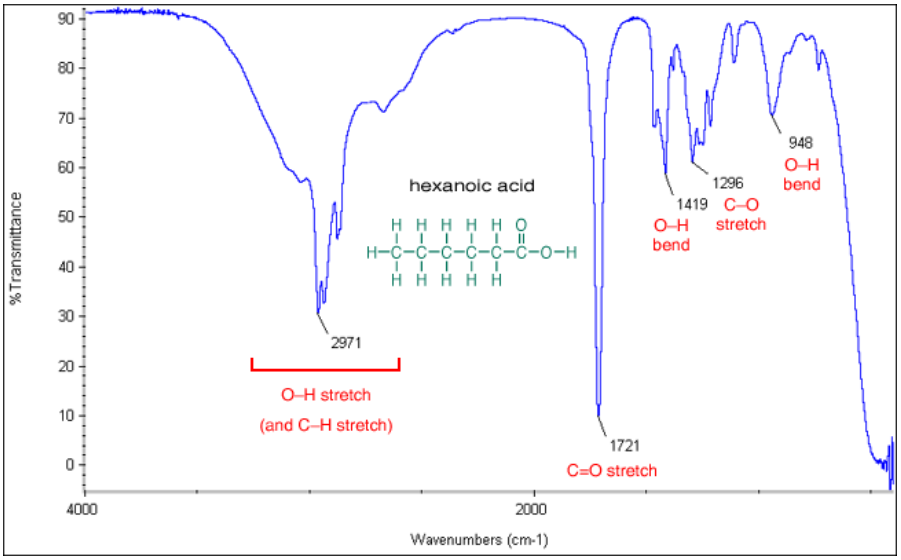

Figure 6.24: IR Spectra of Hexanoic Acid [8]

3. Carbon-dioxide

The CO_2 molecule, being linear and triatomic, is predicted to have four fundamental vibrational modes according to the $(3N-5)$ rule. The different modes of vibration is shown in Figure 6.25.These modes comprise two stretching vibrations (symmetric and asymmetric) and two bending vibrations. The symmetric stretch mode is IR inactive because the simultaneous, symmetric movement of the two oxygen atoms ensures that the opposing bond dipole moments continuously cancel out, resulting in no net change in the overall dipole moment. Conversely, the asymmetric stretch mode is IR active; the unequal displacement of the oxygen atoms generates a transient net dipole moment, leading to an absorption band observed at approximately 2350cm^{-1} . The molecule's two bending modes are identical in energy (degenerate) and are also IR active, as the bending motion creates a net dipole moment perpendicular to the molecular axis, with an absorption observed around 666 cm^{-1}. Thus, despite having four total modes, the symmetric stretch is silent, and the two bending modes overlap, resulting in only two primary absorption bands being visible in the IR spectrum as seen in Figure 6.26.

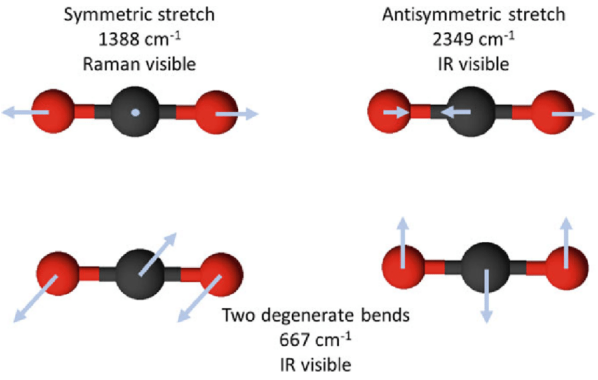

Figure 6.25: Vibrational modes of CO_2(Civiš et al. 2019)

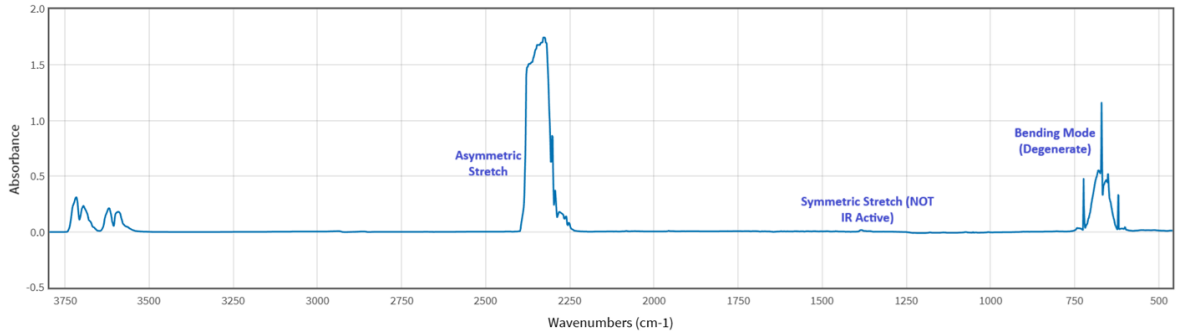

Figure 6.26: FT-IR Spectrum of CO_2

4. Air

Figure 6.27 shows a comparison of two mid-infrared spectra obtained using a 24-meter path length cell containing air: one with undried air (shown in red) and one with dried air (shown in blue). The purpose is to identify and differentiate the absorption features of water vapour (H_2o) from other trace gases. The image specifically highlights the spectral positions where the main absorption bands for several key atmospheric gases like carbon dioxide (CO_2), methane (CH_4), carbon monoxide (CO), and nitrous oxide (N_2O) are expected to occur.

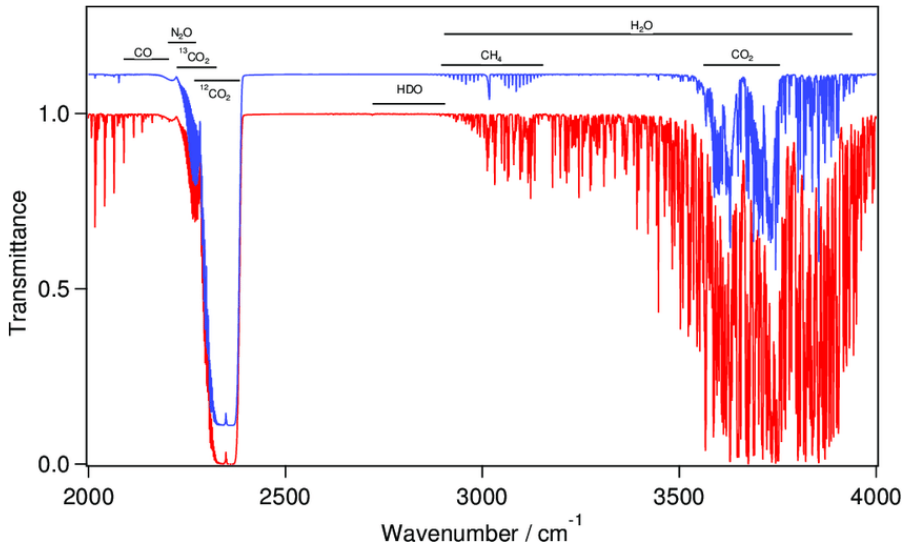

Figure 6.27: Mid-IR Spectrum of Air(Griffith et al. 2012)

To summarise, Table 6.2 shows the wave numbers corresponding to different types of common bonds.

Table 6.2: Characteristic IR Absorption Regions (Sinha et al. 2023)

Wave number (cm^{-1})	**Vibrational Mode**
2700–3700	Hydrogen stretching
1950–2700	Triple bond stretching
1550–1950	Double bond stretching
700–1500	Fingerprint region
	Types of Bond
2260-2220	C≡N
2260-2100	C≡C
1680-1600	C=C
1650-1550	C=N
~1600 and ~1500-1430	C_6H_6
1780-1650	C=O
1250-1050	C–O
1230-1020	C–N
3650-3200	O–H (alcohol)
3300-2500	O–H (Carboxylic acid)
3500-3300	N–H
3300-2700	C–H

6.4.5. Volatile Identification

FT-IR spectroscopy is increasingly used beyond structural characterisation to evaluate microbial stress and viability, offering practical insight into how microorganisms respond to environmental stressors. Interpreting Fourier-transform infrared (FT-IR) data is inherently complex and demands specialised expertise, presenting a significant hurdle in microbial research. However, while the technique provides exceptional qualitative insights into microbial composition and functional groups, true quantitative analysis remains a persistent challenge. Physical factors like sample thickness, path length, and light scattering can severely skew the accuracy of quantitative measurements, making precise concentration determinations difficult.

Interpreting FT-IR spectra requires multidisciplinary expertise spanning microbiology and spectroscopy. The sheer complexity of intact microbial samples, which naturally contain a dense multitude of overlapping functional groups and diverse biomolecules, can make deciphering raw spectral information daunting. Because these biological systems generate massive datasets containing intricate spectral variations, conventional visual inspection is insufficient. Successfully analysing these large datasets requires the integration of advanced multivariate analysis techniques and chemometric clustering algorithms, such as Principal Component Analysis (PCA), Canonical Variate Analysis (CVA), and Soft Independent Modelling of Class Analogy (SIMCA), to extract meaningful biological insights.

These spectral overlaps act as masking effects that can be resolved either through the physical removal of highly absorbing molecules or digitally by subtracting reference spectra from the raw data. For instance, the water vapour spectrum, which produces the most severe masking effect in breath analysis, can be physically suppressed using condensation techniques. By employing this approach, studies have successfully identified several molecular fingerprints, including acetone, isoprene, and methane. However, because many of these molecular signatures still overlap, digital subtraction of known species must be applied to decouple the remaining signals, allowing several previously unknown features to be confidently identified as VOCs (Apolonski and Maiti 2021).

Nevertheless, the complete digital removal of the water spectrum remains impractical for highly sensitive spectral analyses. This difficulty stems from the fact that water is an inherently complex substance, well-documented for its anomalous properties at both the microscopic and macroscopic levels (P. Ball 2008). In the gas phase, water clusters form by creating hydrogen bonds among varying numbers of water molecules. This hydrogen bond network, with its constant fluctuations and shifting dynamics, directly determines the properties of the water vapour. The continuous making and breaking of these bonds, combined with the structural changes within the clusters, creates highly complex, shifting signatures in the infrared absorption spectra. Because these spectral features are so volatile and dynamic,

simple digital subtraction is practically impossible during high-sensitivity spectral analysis (Apolonski and Maiti 2021).

The digital subtraction process begins with evaluating potential molecules based on features in the breath or head-space spectrum to ensure biological plausibility. Next, reference spectra for these candidates are obtained from experimental standards or databases like PNNL, NIST, or HITRAN. A least-squares fitting algorithm then aligns these reference spectra with the experimental data. Once aligned, the best-fitted molecular spectrum is digitally subtracted from the measurement, stripping away dominant features to reveal previously obscured signatures. For instance, removing the dominant methane spectrum via this method uncovers the signatures of ammonia and isoprene. Subtraction of the newly revealed isoprene spectrum can then expose even deeply buried fingerprints, such as methyl butyrate. By repeating this subtraction workflow sequentially, progressively subtler molecular features can be isolated, a process analogous to uncovering smaller and smaller dolls by opening a Matryoshka. The concept behind this method is illustrated in Figure 6.28.

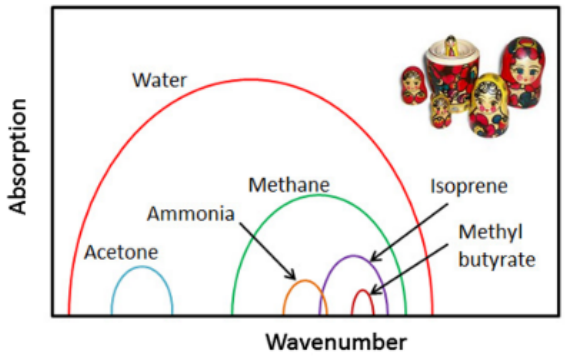

Figure 6.28: Matryoshka Method (Apolonski and Maiti 2021)

7

Overview: Analogue Experiments

Validating the methodologies used to identify VOCs as biosignatures is crucial; this requires establishing baseline data and rigorously testing analytical instrumentation within both terrestrial environments (Batty et al. 2024) and laboratories. Having established the fundamentals of planetary atmospheres, biosignatures, characteristics of microorganisms, and particle-light interactions, this chapter focuses on bringing all of this together to develop the experimental methodology. It reviews how various researchers have configured their laboratory experiments to investigate these phenomena practically. Furthermore, it explores how these experimental configurations can be modified to suit the specific requirements of this study. The primary focus here is on the physical experimental setup rather than simulation studies.

The following tables from Table 7.1 to Table 7.5 provide a summary of relevant analogue experiments from the literature, detailing the methodologies, environmental simulations, and outcomes observed by various researchers. While this list is not exhaustive, it highlights studies that serve as the primary foundation for the experimental framework developed in this thesis.

Table 7.1: Laboratory studies on the viability of *E.Coli* and *yeast* in H_2 dominated environment

Category	Description
Research	Laboratory studies on the viability of life in H_2-dominated exoplanet atmospheres (Seager et al. 2020)
Experimental Parameters	• **Micro-organism:** prokaryote *Escherichia coli* (strain K-12) and the eukaryote yeast *Saccharomyces cerevisiae* (strain S288C) • **Atmosphere:** Target: 100% H_2; Controls: Air (standard baseline), 100% Helium (inert gas control), and a mixture of 20% CO_2 / 80% N_2 • **Temperature:** All cultures were maintained at 28° C. • **Volume:** Experiments utilised 30 mL of culture media with 126 mL of space for gas exchange.
Methodology	E. coli and yeast were cultured in custom bottles flushed with target gases (H_2, He, N_2/CO_2) and incubated at 28° C under strict anoxic monitoring. Growth was tracked via optical density and cell counting while sensors ensured oxygen remained at trace levels comparable to Archaean Earth.
Experimental Set-up	Figure 7.1 outlines the three-stage process for culturing E. coli and yeast: . Starter Preparation: An initial starter culture is generated to serve as the source for the main experiment. a. Vessel Setup: Experimental bottles containing anoxic media are prepared and flushed prior to introducing the target organisms. b. Incubation and Monitoring: Cultures are grown in a shaking incubator, with growth tracked via optical density (OD600) for E. coli or direct cell counting (haemocytometer) for yeast.

Continued on next page

Table 7.1 – continued from previous page

Category	Description
Result	• Viability: Both E. coli (prokaryote) and yeast (eukaryote) successfully survived and reproduced in a 100% H_2 atmosphere, proving that hydrogen is not toxic to these organisms. • Growth Dynamics: E. coli achieved robust growth similar to anaerobic controls, whereas yeast growth was slower and limited by the lack of oxygen required for sterol synthesis rather than the hydrogen itself. • Biosignature Gases: The study catalogued a diversity of gases produced by E. coli (approx. 45 gases) and yeast (approx. 75 gases) during growth, including ammonia, nitrous oxide, and methanethiol. • The results suggest that life is not strictly limited to oxidising atmospheres and that H_2-rich environments could host life that produces detectable biosignature gases.

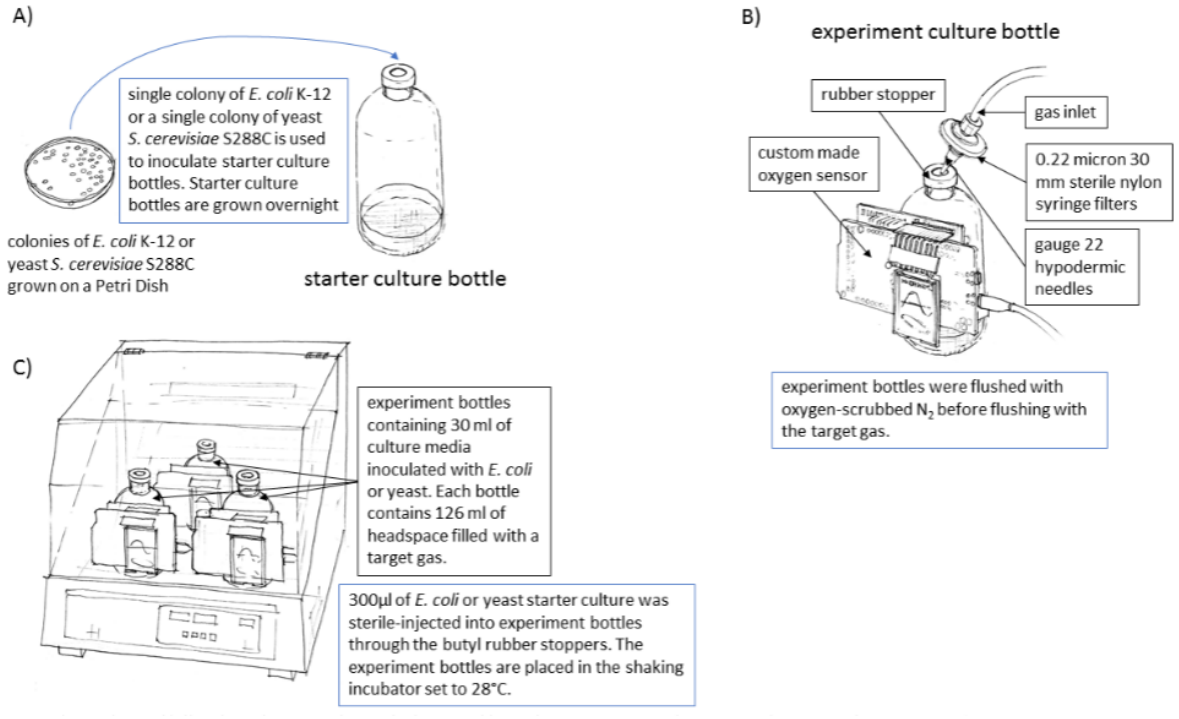

Figure 7.1: Experimental set-up for studying E.coli and yeast in H_2 environment

Table 7.2: Summary of experimental conditions and growth analysis for Escherichia coli subjected to five specific gaseous environments.

Category	Description
Research	The Role of Atmospheric Composition in Defining the Habitable Zone Limits and Supporting E. coli Growth (Kuzucan et al. 2025)
Experimental Parameters	• **Micro-organism:** *Escherichia coli* K-12 (strain CL83) • **Simulated Atmospheres (Lab):** Five specific compositions were tested: Standard Air (Control): Earth's current atmosphere. Pure CO_2: 100% Carbon Dioxide. Pure H_2: 100% Hydrogen. N_2 rich (Anaerobic): 90% Nitrogen + 10% CO_2. CH_4 rich: 80% Methane + 15% Nitrogen + 5% CO_2. • **Simulated Atmospheres (Climate Model):** H_2 dominated and CO_2 dominated atmospheres were simulated at surface pressures of 1 bar, 2.5 bar, and 5 bar. • **Temperature:** Laboratory experiments were conducted at 22° C.

Continued on next page

Table 7.2 – continued from previous page

Category	Description
Methodology	The study combined 3D Climate Modelling (to define where liquid water can exist) with Biological Laboratory Experiments (to test if life can actually survive there). • **Climate Modelling:** Used the Generic-Planetary Climate Model (G-PCM) (a 3D Global Climate Model) to calculate the "inner edge" of the Habitable Zone (HZ) for planets with H_2 and CO_2 atmospheres. This involved calculating the onset of the "runaway greenhouse effect" at different orbital distances. • **Biological Survival Assay:** . E. coli was inoculated into nutrient broth and exposed to the five different gas compositions. a. Growth was monitored over a long-term period of 30 days to observe adaptation, lag phases, and stationary phases. b. Oxygen levels were monitored to ensure anaerobic conditions were maintained in the non-air bottles.
Experimental Set-up	• Laboratory Vessels: 15 borosilicate bottles (250 ml) containing 40 ml of Lysogeny Broth (LB) were used (3 biological replicates per atmosphere) as shown in Figure 7.2. • Gas Control: Bottles were flushed with nitrogen to remove oxygen before being filled with the target gases via needles through sterile filters. • Monitoring Equipment: CASY Cell Counter: Used to count bacterial cell density. • PreSens O_2 Sensor Dots: Non-invasive sensors glued to the inside of bottles to verify anoxia. • Shaker: Bottles were agitated at 100 rpm to ensure nutrient distribution.
Result-Biological Findings	E. coli successfully adapted and grew in 100% H_2, N_2 rich, and CH_4 rich atmospheres. Although initial growth was slower than in air (aerobic), they reached similar cell densities by the stationary phase. Growth in 100% CO_2 was significantly inhibited and consistently lower than all other conditions. This suggests pure CO_2 atmospheres are challenging for non-specialised life forms.

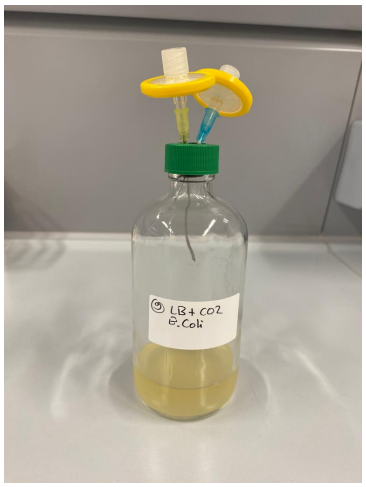

Figure 7.2: A photograph of the bottle used for the pure CO_2 atmosphere experiment. Each bottle is equipped with two needles fitted with 0.2 μm sterile filters, allowing the head-space to be flushed with nitrogen and then filled with the desired test atmosphere.

Table 7.3: Summary of the Bacillus subtilis spore resistance study under simulated Martian surface conditions.

Category	Description
Research	*Bacillus subtilis* Spore Resistance to Simulated Mars Surface Conditions (Cortesão et al. 2019)
Experimental Parameters	• **Micro-organism:** *Bacillus subtilis* spores, including wild-type strains (PS832, PY79, 168) and isogenic mutants defective in specific protection or DNA repair mechanisms. • **Simulated Mars Atmosphere:** A gas mixture of 95.54% CO_2, 2.7% N_2, 1.6% Ar, 0.13% O_2, and 0.03% H_2O. • **Physical Conditions:** Pressure maintained at 0.69 kPa ($\sim$6.9 mbar), temperature at -10° C, and relative humidity at 8%. • **Radiation Exposure:** M(+)UV: 8 hours of simulated Martian UV irradiation (Total UV fluence: 742.5 kJ m^{-2}) followed by 16 hours of darkness. M(–)UV: 24 hours of exposure to the Mars gas/pressure/temperature environment but shielded from all UV radiation.
Methodology	• Sample Preparation: Spores were purified ($>$99% purity) and air-dried onto aluminium coupons to form multi-layers ($\sim$25 layers thick), simulating spacecraft surface contamination. • Exposure: Coupons were placed in the simulation chamber for 24 hours; one set was exposed to the full UV cycle, while the other was covered with aluminium foil to block UV. • Analysis: Spores were recovered using a polyvinyl alcohol (PVA) peeling method ($>$95% recovery). Survival was quantified by Colony Forming Units (CFU), and mutagenesis was assessed by identifying asporogenous (Spo-) mutant colonies.
Experimental Set-up	• Chamber: A cylindrical stainless steel Mars Simulation Chamber (MSC) (50 cm $\times$ 70 cm) capable of regulating gas composition, pressure, and temperature. • Substrates: Aluminium coupons (10 mm $\times$ 20 mm). • Irradiation Source: A solar simulator provided a UV flux (UVC, UVB, UVA) calibrated to match the theoretical flux on the Martian surface.
Result	Wild-type spores survived under both tested conditions, but survival was substantially higher in UV-shielded samples (M(–)UV) than in UV-exposed ones (M(+)UV). In the M(+)UV environment, spore survival strongly depended on core dehydration, the presence of α/β-type small acid soluble spore proteins (SASPs) that protect DNA, and the repair of Spore Photoproduct (SP) lesions by the enzyme SP lyase (SPL). In contrast, in the M(–)UV condition, where only the simulated Martian atmosphere acted as stress, the primary determinant of survival was the integrity of the spore coat; spores lacking coats were almost 200-fold more vulnerable. Here, the dominant form of lethal injury was DNA double-strand breaks, which required repair via the Non-Homologous End Joining (NHEJ) pathway. Additionally, UV exposure greatly increased mutation rates (e.g., sporulation defects) in the surviving spores, especially in strains lacking key structural defences (such as SASPs or coats) or DNA repair mechanisms (like Mismatch Repair).

Table 7.4: Summary of Urey-Miller Experiment

Category	Description
Research	Conducting Miller-Urey Experiments (Parker et al. 2014)
Experimental Parameters	• **Atmosphere:** A reducing atmosphere consisting of CH_4 (200 mm Hg), NH_3 (200 mm Hg), and H_2 (100 mm Hg-optionally) introduced into a flask containing liquid water. The final system is typically under vacuum or reduced pressure to avoid over-pressurising. • **Energy Source:** High-voltage electric discharge (simulating lightning) provided by a Tesla coil (BD-50E) generating approximately 30,000 V. • **Duration:** The discharge is applied for 2 weeks on a 1-hour on/off cycle to prevent overheating the coil.

Continued on next page

Table 7.4 – continued from previous page

Category	Description
Methodology	• All glassware and tools are pyrolysed at 500° C for 3 hours to remove organic contaminants. • The reaction flask containing water is thoroughly evacuated (via vacuum pump) to remove all oxygen. • Gases are introduced sequentially using a vacuum manifold. Pressures are calculated carefully, accounting for the vapour pressure of water and the solubility of ammonia. • **Analysis:** Liquid samples are collected and analysed using HPLC-FD (High Performance Liquid Chromatography with fluorescence detection) and QqQ-MS (Triple Quadrupole Mass Spectrometry) to identify amino acids.
Experimental Set-up	• Reaction Vessel: A simplified 3-litre borosilicate glass flask (modified from the original 5-L dual-flask design) equipped with a condenser to reflux water as shown in Figure 7.3. • Electrodes: Two tungsten electrodes are sealed into the flask, with tips separated by $\sim$1 cm to create the spark gap. • A glass line with valves, gauges (mercury manometer), and a cold trap used to precisely measure and introduce gases.
Results	The experiment successfully produces a complex mixture of organic compounds, including glycine, alanine, α-ABA, and valine. HPLC chromatograms clearly show distinct peaks for these amino acids, confirming that simple gases can be converted into biomolecules under abiotic conditions. In classic iterations referenced, the water turns turbid and reddish, with yellow-brown organic material accumulating on the electrodes after sparking. Unlike Miller's original 1953 setup, this simplified protocol notes that heating the flask with a mantle is not strictly necessary to synthesise amino acids, though it helps circulation.

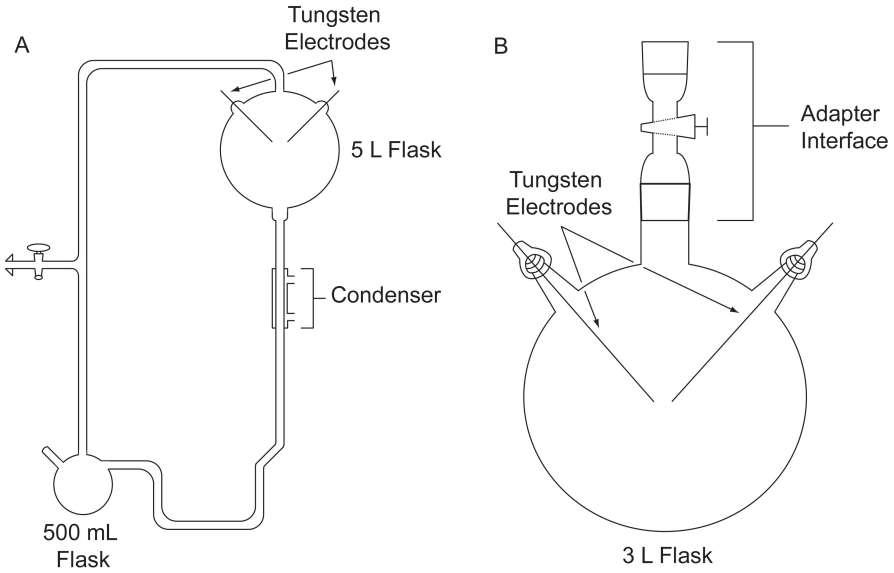

Figure 7.3: A) Classical apparatus used in Urey-Miller Experiment B) Modified apparatus for experiments by Parker,E.T et al.(2014)

Table 7.5: Summary of experimental Simulation of Titan's atmosphere

Category	Description
Research	Experimental simulation of Titan's atmosphere: Detection of ammonia and ethylene oxide (Bernard et al. 2003)
Experimental Parameters	• **Initial Gas Mixture:** N_2 (98.00%), CH_4 (1.99%), CO (0.01% or 100 ppm). • **Pressure:** $\sim$1 mbar. • **Temperature:** Room temperature ($\sim$350–450 K due to discharge). • **Energetic Input:** Cold plasma (glow discharge) established by high voltage between iron electrodes. • **Duration:** 50 hours.
Methodology	To study the influence of CO on Titan's chemistry, a cold plasma was established in a gas mixture mimicking Titan's atmosphere. Produced gaseous products were collected in a cryogenic trap and subsequently analysed by infra-red Spectroscopy (IRS) and Gas Chromatography-Mass Spectrometry (GC-MS). The goal was to detect minor species and understand the complex atmospheric chemistry.
Experimental Set-up	The reactor was a 25 cm U-tube with an internal diameter of 1.8 cm. Iron electrodes were inserted at both ends. The long path length IR cell (Multi-reflection Sirocco, 10.6 m) was used for IRS at 4 cm^{-1} resolution. The O_2 contamination, shown in Figure 7.4.
Result	• Ethylene oxide C_2H_4O was surprisingly identified as the main O-containing gaseous product. The theoretically predicted O-compounds (formaldehyde and methanol) were not detected. • Ammonia was also detected in the gaseous products, even without CO in the initial mixture. Many expected major products previously found on Titan were detected, including hydrocarbons ($C_2H_2, C_2H_4, C_2H_6, C_3H_8, C_4H_2, C_6H_6$) and nitriles ($HCN, HC_3N, CH_3CN, C_3N_2$). • Methane was totally consumed in the reactor.

Figure 7.4: Experimental Simulation developed at LISA

Further, (H. B. Smith and Mathis 2023) propose a methodology for studying life that begins by examining life on Earth, followed by searching for reachable life within the solar system, synthesizing life in a laboratory setting, and finally observing intelligent life through the detection of technosignatures.

Separately, the analysis of Volatile Organic Compounds (VOCs) offers a fast, non-invasive, and cost-effective method for identifying potential biosignatures. Given advances in analytical technology, this VOC analysis could be incorporated into future space missions (Batty et al. 2024).

Yun et al. 1998 experimental configuration for the in situ FT-IR analysis is illustrated in Figure 7.5, the setup utilized a custom-built quartz gas cell fitted with infra-red-transparent Potassium Bromide (KBr) windows, through which a collimated beam from a MIDAC spectrometer was directed. Detection was achieved using a liquid nitrogen-cooled Hg–Cd–Te (MCT) detector. Spectra were acquired across a wave number range of 400 to $4000\ cm^{-1}$ at a resolution of $8\ cm^{-1}$. To ensure an optimal signal-to-noise ratio, each spectrum consisted of 30 averaged scans, resulting in a total measurement time of approximately 5 seconds.

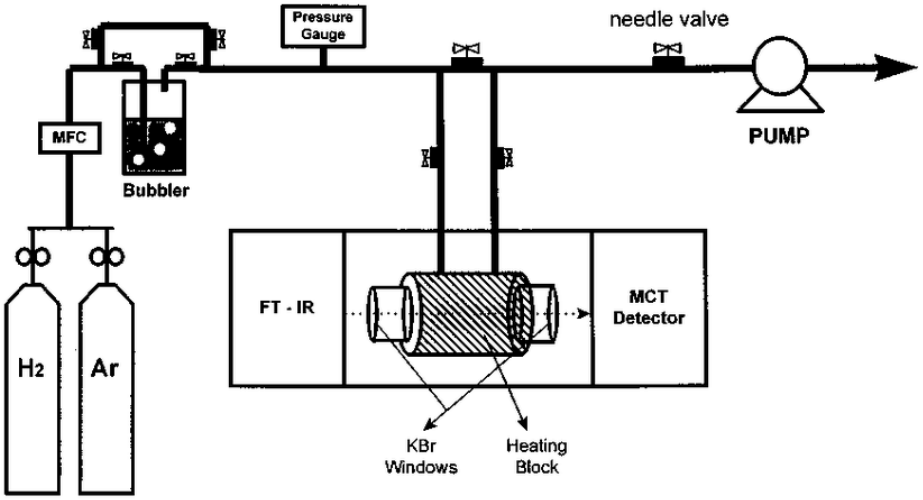

Figure 7.5: The gas cell setup used for in situ FT-IR analysis (Yun et al. 1998)

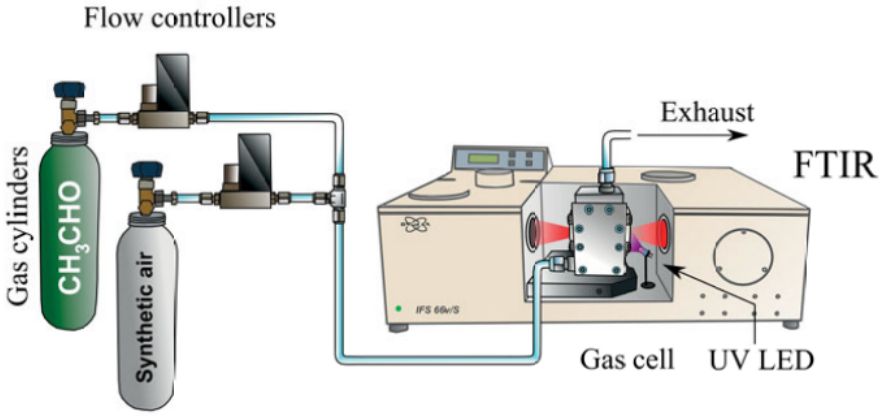

Figure 7.6: Schematic representation of the apparatus used to monitor CH_3CHO adsorption and photo-catalysis via in situ FT-IR spectroscopy (Stefanov 2015)

Figure 7.6 illustrates an experimental setup for conducting in situ FT-IR spectroscopy,to study the photo-catalytic degradation of acetaldehyde CH_3CHO. On the left, two gas sources: acetaldehyde and synthetic air are supplied via gas cylinders. Their flow rates are precisely regulated by Flow controllers (Mass Flow Controllers) before the gases are mixed. This mixture is directed into a specialized Gas cell housed inside the sample compartment of an FT-IR spectrometer. Inside the cell, the gas is simultaneously analysed by the infra-red beam (red) and exposed to a UV LED to trigger photo-catalytic reactions. Finally, the reacted gas exits through an Exhaust line. Samples were first thermally treated

at 200 ° C for 15 minutes while being purged with synthetic air. Following this, a gas mixture comprising synthetic air (20% O_2, 80% N_2 and 90 ppm acetaldehyde was introduced at a flow rate of $100\,ml\,min^{-1}$. All gases used were of high purity ($> 99.99\%$). FT-IR monitoring was conducted in the $1000-4000\,cm^{-1}$ range, collecting spectra every 60 seconds by averaging 138 scans per measurement. The resulting data were processed using baseline correction and Savitzky-Golay smoothing with nine-point window (Stefanov 2015).

As noted in the previous chapter, water vapour heavily masks the spectral signatures of other trace gases. To address this, Zenner et al. (2021) constructed a custom water suppression system for their infrared spectroscopy setup (Figure 7.7). The condenser consisted of a sealed metal chamber containing a 12-metre coiled copper tube, which transported the gas sample from the collector to the measurement cell. Using a refrigerated circulator, the chamber was pre-cooled to -60 °C. The bacterial gas sample was then driven through the chilled tubing at a controlled flow rate of 3 mL/s. This thermal trapping physically removed the water vapour, yielding a reduction factor of over 2500 before the dried sample reached the multipass cell. After each measurement, the copper line was purged by heating the chamber to 45 °C while applying a vacuum.

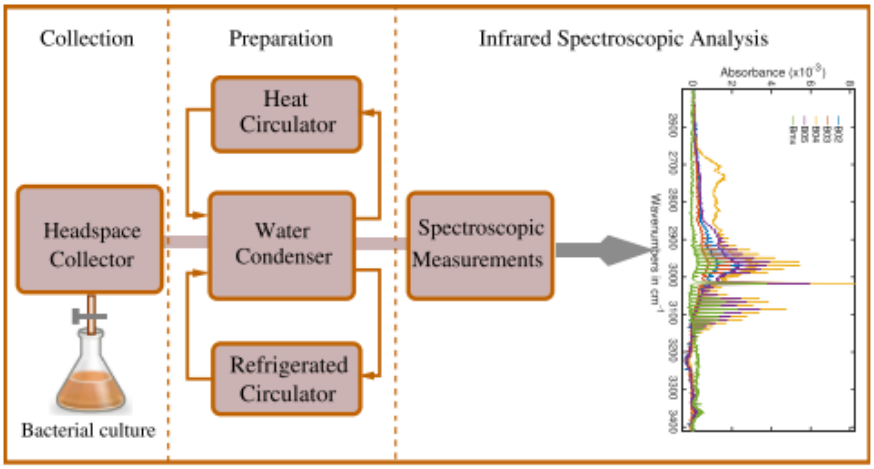

Figure 7.7: Experimental workflow for the infra-red spectroscopic analysis of gaseous biofluids. The setup comprises three main stages: head-space collection from bacterial cultures, sample preparation involving water vapour suppression, and final FT-IR spectrometer analysis using a multipass gas cell (Zenner et al. 2025)

Drawing on the practical lessons from these earlier analogue setups was essential for shaping the methodology of this thesis. Seeing how other researchers managed gas distribution, environmental controls, and spectral noise provided a blueprint for building a custom apparatus. Ultimately, these previous designs provided guidance on how the closed-loop bioreactor can be integrated with the gas cell and the FT-IR spectrometer, ensuring the system could capture trace biological emissions under simulated exoplanetary environment.

8

Thesis Proposal

8.1. Project Relevance

The relevance of this project is to bridge the gap between theoretical astrobiology and experimental verification. By investigating the limits of extremophiles, organisms capable of thriving in hostile environments, this study informs the selection of biosignature targets beyond the standard “Earth-like” indicators. Since no single gas can be considered definitive proof of life due to potential geologic mimics, this project emphasizes the detection of complex, multi-gas “fingerprints” that are in thermodynamically disequilibrium and significantly harder to produce abiotically. Crucially, the validity of these detections relies on precise reference spectra; this thesis contributes to that need by generating high-fidelity laboratory data using FT-IR spectroscopy, which is a non-destructive method for identifying gases and offers distinct advantages over mass spectrometry for remote sensing applications by directly mimicking the light-matter interactions observed by telescopes. By correlating these experimental spectra with atmospheric models, this work not only determines the specific resolving power required for future missions to distinguish biological signals from noise but also directly enhances the astrobiological research capabilities at TU Delft by establishing a rigorous “lab-to-sky” methodology.

8.2. Research Questions

In this section, the questions to be answered in this research is addressed. Starting with one main question (MQ):

Main Question (MQ)

Can FT-IR detect and differentiate specific biosignature gases when primitive earth organism is subjected to exoplanetary atmosphere?

To answer this main question, several sub-questions (SQs) have been formulated. These structured questions serve as a step-by-step guide leading to the resolution of the main question. Firstly, it is necessary to understand the gases and molecules that can be detected in the FT-IR spectrum. So it is important to see how it can be done.

Sub-Question (SQ1)

How can bioreactor be integrated with the FT-IR Spectroscopy for measuring the gas spectrum?

This experimental phase involves the integration of bioreactors, an FT-IR spectrometer, and gas cells. The systematic approach devised to address this sub-question is outlined below:

- **Preparation of microbial growth media and bioreactor configuration:** This step involves learning the protocols for sterile media preparation and optimizing bioreactor parameters (such

as pH, temperature, and agitation) to ensure viable microbial proliferation.

- **Exposure to simulated atmospheric conditions:** The selected gas composition will be circulated through the bioreactor to facilitate the interaction between the microorganisms and the environment, allowing for the study of metabolic adaptations under simulated planetary conditions.
- Collection and spectroscopic analysis of effluent gases: The metabolic by-products produced by the culture will be transferred into a specialized gas cell and analysed using FT-IR spectroscopy to identify and quantify specific molecular absorption features.
- **Implementation of discrete temporal sampling:** Initial measurements will be conducted at fixed time intervals to establish the kinetics of gas production and to determine the minimum time required for biosignatures to accumulate to detectable levels.
- (Optional) **Continuous real-time monitoring:** If feasible, the system will be upgraded to allow for real-time monitoring of gas concentrations and periodic assessment of microbial viability to dynamically correlate biological activity with observed spectral changes.

The Figure 8.1 shows the schematic of experimental set-up for performing the above experiments.

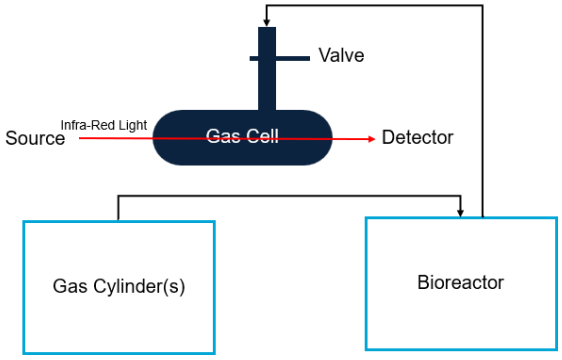

Figure 8.1: Schematic of Experimental Set-up

Once the bioreactor setup is complete, the subsequent objective is the detection of gases generated during these experiments. So the next sub-question is:

Sub-Question (SQ2)

What are the potential gaseous biosignatures produced by E.Coli and/or yeast and can it be detected with FT-IR Spectroscopy?

To address this sub-question, the following approach will be taken.

- **Identify and evaluate potential biosignature gases:** Review the literature to select relevant biosignature candidates, examine their detection history on various planetary bodies, and verify their spectral activity within the infra-red (IR) range.
- **characterise the planetary environment:** Analyse the atmospheric conditions (temperature, pressure) and theoretical gas composition of the target planetary body to understand the context in which these signals would appear.
- **Analyse the theoretical IR spectra:** Examine the specific infra-red absorption bands of the selected gases to identify unique spectral fingerprints and potential overlaps with dominant background gases.
- **Conduct a risk analysis:** Utilize Python libraries (such as CoolProp) to simulate real gas behaviour for handling these gases in a laboratory setting.
- **Acquire experimental reference spectra:** Measure the actual absorption spectra of the selected gases using Fourier Transform infra-red (FT-IR) Spectroscopy in the laboratory to validate theoretical models and obtain precise cross-section data.

Having identified which gases are detectable via spectroscopy and what specific by-products are produced by primitive organisms under Earth conditions, the focus then shifts to how these vary in different environments.

Sub-Question (SQ3)

Can E.Coli and/or yeast produce the same gases they produce on Earth when subjected to a different gaseous environment?

This question is approached in the following way:

- **Analyse extremophile environments:** Investigate the extreme environmental conditions on Earth (such as high pressure, high acidity, or anaerobic zones) where primitive organisms thrive to establish a biological analogue for the target exoplanet.
- **Identify relevant biosignatures:** Review the metabolic by-products of these extremophiles to determine which specific gases (e.g., NH_3, PH_3, CH_3Cl) serve as potential biosignatures and distinguish them from abiotic geological emissions.
- **Assess detectability in the infra-red:** Verify whether the selected gases possess distinct spectral features within the infra-red (IR) range that are detectable under standard room conditions, ensuring their suitability for spectroscopic observation.
- **Establish an experimental baseline:** Replicate and adapt the experimental methodologies outlined by S. Seager et al. 2013 to create a validated reference baseline for analysing potential biosignatures in laboratory simulations.

The final sub-question addresses the quantification of these gases, the confidence with which they can be attributed to biological origins, and the implications of these findings for future space telescopes and missions.

Sub-Question (SQ4)

How can trace biogenic signals be definitively distinguished from abiotic background noise and accurately quantified within complex spectral data?

The methodological approach to address this sub-question is outlined below:

- **Spectral fingerprinting and identification:** Cross-referencing the obtained experimental spectra with high-resolution spectroscopic databases (such as HITRAN or PNNL) to definitively identify molecular species and distinguish unique biogenic features from overlapping background absorptions.
- **Quantification of gas abundance:** Deriving gas concentrations by calculating the integrated band area and column density of the isolated spectral peaks, applying the Beer-Lambert law to translate absorbance into quantitative abundance.
- **Signal-to-Noise Ratio (SNR) enhancement:** Assessing the spectral quality by calculating the SNR and iteratively addition of scans to suppress random noise and reveal faint biogenic features. Further, correlating the population density of microorganisms with the volume of gas produced.
- **Determination of detection limits:** Establishing the statistical Limit of Detection (LOD) and Limit of Quantification (LOQ) to mathematically verify that the observed biogenic signals are significant and distinguishable from the instrument's baseline noise floor.

8.3. Revised Changes

Later, for the experiments, *E. coli* was replaced with *Cylindrotheca fusiformis*, a photosynthetic marine diatom, due to safety considerations and the specific expertise available for its culture. This substitution provides a robust comparison between a heterotrophic eukaryote and a chlorophyll-based organism.

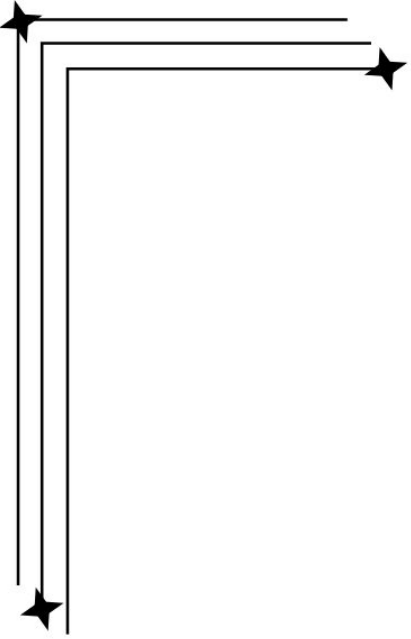

Part 2: Research Paper

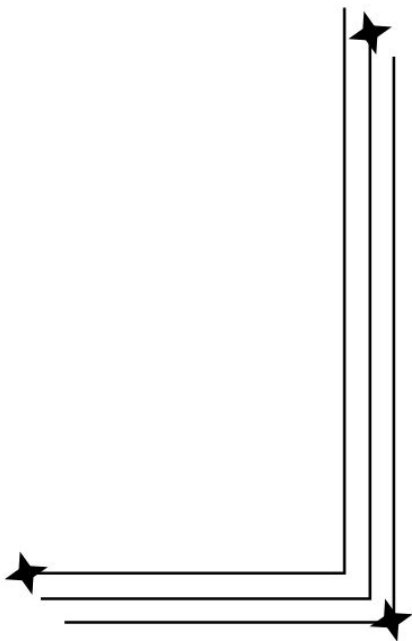

Gas-phase FT-IR Analysis of Microbial Biosignature in Simulated Exoplanetary Environments

S Shristi[1,*], Niels Ligterink[1], and Wouter van Straalen[1]

[1] *Faculty of Aerospace Engineering, Delft University of Technology, Delft, The Netherlands*
Corresponding author email: ssantosh@tudelft.nl

Abstract — The search for extraterrestrial life relies fundamentally on the identification of robust biosignatures, a pursuit facilitated by studying the metabolic emissions of terrestrial organisms under extreme environmental conditions. To this end, this study evaluates the empirical detection limits of primary metabolic gases (such as CO_2 and H_2O) alongside trace biogenic volatile organic compounds (VOCs) released by microorganisms subjected to severe environmental stresses, specifically a nitrogen-rich atmosphere and an oxidative environment. Using a gas-phase modular, closed-system Fourier-transform infra-red (FT-IR) spectroscopy system, discrete VOCs are monitored to observe the metabolic shifts of *Saccharomyces cerevisiae* (commonly known as Brewer's yeast) and *Cylindrotheca fusiformis* (a marine diatom). Prioritization was given to well-resolved spectral features, with distinct fluctuations in CO_2 and water vapour H_2O serving as real-time indicators of cellular degradation. Yeast cells exhibited stress responses in both environments, whereas *C. fusiformis* appeared unaffected by the nitrogen-rich atmosphere but was severely degraded by oxidative stress. Although visual morphological changes were present, this paper primarily focuses on the systemic vulnerabilities of discrete sampling frameworks when mapping transient gas-generation bursts. By serving as a controlled terrestrial analogue, these experiments provide critical data to understand how biological trace gases might behave and degrade in extreme extraterrestrial environments. This study discusses these observational limitations within the broader framework of remote planetary sensing. Ultimately, characterizing dynamic gas fluctuations serves a dual purpose: refining theoretical models of exoplanetary atmospheres and aiding the search for preserved, relic biogenic signals within the solar system.

Astrobiology XX, XXX–XXX.

Keywords: Biosignatures — FT-IR Spectroscopy — Simulated Environment — Volatile Organic Compounds — Astrobiology — Extremophiles.

Introduction

Finding life beyond Earth is an intricate interplay between chemistry, biology, geology, physics, and astronomy (Malaterre et al. 2023). The evolution of exoplanetary science can be categorized into three distinct eras. The first era focused primarily on the astrophysical characterization of planetary orbits and sizes using ground-based surveys and space missions such as CoRoT, Kepler, K2, Gaia, CHEOPS, TESS, and, in the near future, PLATO and WFIRST. The second era is currently shifting the focus toward the chemical characterization of atmospheric compositions across a diverse catalog of exoplanets, the majority of which are uninhabitable gaseous worlds. This phase relies on assets like the Hubble, Spitzer, and James Webb Space Telescope (JWST), alongside ground-based Extremely Large Telescopes (ELTs). Finally, the third era will focus on the astrobiological characterization of potential biosignatures and habitable environments on exoplanets. This milestone may be initiated by JWST, which is potentially capable of finding biogenic gases in the atmospheres of habitable exoplanets around low-mass stars and further realized by upcoming specialized missions (Kiang et al. 2018; Krissansen-Totton et al. 2018).The ultimate goal is to prepare for a future of remote sensing where signs of life can be conclusively attributed to atmospheric gases (Catling et al. 2018). A common approach to searching for life on these planets is to look for

spectral clues that indicate strong chemical imbalances in the atmosphere (Rein et al. 2014).

To expand our understanding of life and our place in the universe, scientists rely on these biosignatures. (Gillen et al. 2023) define a biosignature as "any phenomenon for which biological processes are a known possible explanation and whose potential abiotic causes have been reasonably explored and ruled out". For a biosignature to be observable, it must leave a measurable imprint on the light that is reflected, emitted, or transmitted through a planet's atmosphere. Furthermore, for a biosignature to be useful, it must build up to detectable levels, a process dependent on factors like atmospheric chemical reaction rates and dissociation cross-sections. Finally, it must possess high specificity, meaning the biosignature can be definitively differentiated from abiotic background sources (Schwieterman and Leung 2024).

To model potential extraterrestrial biosignatures on Earth, researchers often study extremophiles: organisms that thrive in extreme cold, dryness, high mineral content, or intense radiation (Bhartia et al. 2012). The discovery of these extremophiles suggests that microorganisms might withstand severe extraterrestrial conditions, making them valuable model systems for studying how biological life fares in space environments (Olsson-Francis and Cockell 2010). Notably, the abiotic stress factors found on other planets and celestial bodies such as radiation, extreme temperatures, magnetic fields, and oxidative conditions directly correlate with environments known to trigger distinct physiological responses in terrestrial microbes.

A primary physiological response to such environmental stress is the emission of microbial volatile organic compounds (mVOCs) (Parrilli et al. 2021; Abis et al. 2020). Microbes can emit a wide variety of compounds, including alcohols, ketones, nitrogen- and sulfur-based molecules, esters, hydrocarbons, carbonyl compounds, and halogenated species (Kai 2020; Thorn and Greenman 2012). For example, eukaryotic cells like yeast have developed diverse strategies to combat harmful conditions(Ding et al. 2009). During programmed cell death (PCD), the VOC emission profile of these cells changes markedly. Total emissions rise and peak at approximately two hours, with oxygenated compounds showing increases (Zuo et al. 2015). Similarly, oxidative stress, which occurs when a cell's survival mechanisms fail to manage reactive oxygen species (ROS) has been shown to stimulate the production of protective antioxidants across numerous species of photosynthetic micro-algae (Morano et al. 2012; Gauthier et al. 2020).

Consequently, VOC analysis offers a non-invasive, rapid, and cost-effective approach for detecting potential biosignatures. Laboratory simulations have begun to explore this potential; experiments by Seager and her team (Seager et al. 2020) demonstrated that both simple prokaryotes like *E. coli* and complex eukaryotes like yeast can thrive in a pure H_2 gas environment while producing a variety of by-product gases. However, at normal pressures, inert gases such as nitrogen and argon appear harmless and exhibit low aqueous solubility, making it difficult to evaluate the effects of atmospheric exposure on microbial growth using unpressurised liquid vessels.To correctly interpret the influx of remote atmospheric observations from these diverse exoplanets, such laboratory analogue experiments are becoming increasingly vital. Sophisticated theoretical models of exoplanet atmospheres heavily rely on ground-truth laboratory data to provide critical inputs and constraints, particularly because extraterrestrial environments drastically differ from modern Earth. Furthermore, experimental simulations are essential to understand how potential biosignature gases might accumulate both biotically and abiotically under varied atmospheric and irradiation conditions (Thompson 2026).

This data is crucial not only for identifying false positive scenarios, but also for assessing how life might survive, grow, and modify non-Earth-like environments in spectroscopically observable ways. While theoretical models of exoplanetary biosignatures are expanding (S. Seager et al. 2016), the real-time, dynamic metabolic responses of living microorganisms under non-Earth conditions remain poorly constrained. This is largely due to the analytical difficulty of continuously isolating trace biogenic signals from complex abiotic background noise. To reliably track these metabolic variations, Fourier-transform infra-red (FT-IR) spectroscopy is an exceptionally suited analytical tool. By operating within the mid-infra-red spectral fingerprint region, FT-IR allows for the continuous, real-time, and non-destructive quantification of complex gas mixtures without disturbing the delicate biological environment.

This study details the integration of a closed-loop bioreactor with discrete interval FT-IR spectroscopy to evaluate the detection and differentiation of biogenic gases under simulated exoplanetary conditions. This work also characterises the metabolic head-space profiles and physiological adaptability of *Saccharomyces cerevisiae* and the chlorophyll-based diatom *Cylindrotheca fusiformis*

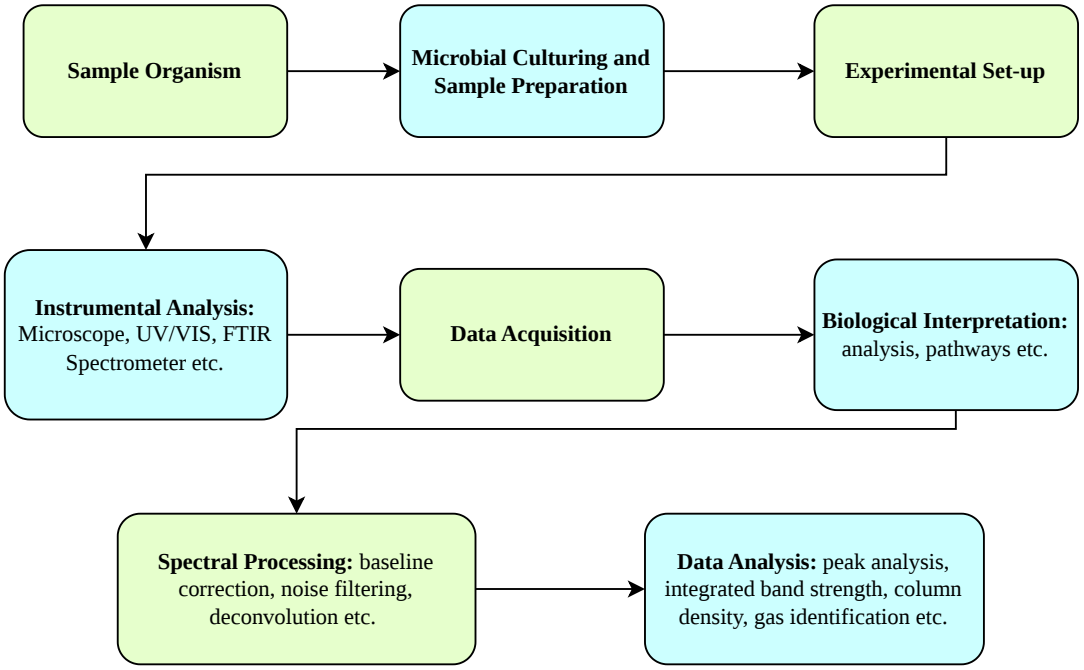

Figure 1: Schematic overview of the multi-phase experimental methodology, integrating microbial preparation, instrumental analysis, and data interpretation.

under non-Earth atmospheric conditions, specifically pure nitrogen (anoxic) and oxidized environments. To achieve this, a custom data processing pipeline was developed to isolate and accurately quantify trace biogenic signals.

Materials and Methods

The core approach builds directly upon the foundational framework proposed by Li (Li 2023) for evaluating trace volatile profiles. Figure 1 shows the schematic of experimental methodology adopted in this study. The workflow commenced with the selection and cultivation of the micro-organisms, followed by the configuration of the experimental set-up and the optimisation of instrumental parameters. The next stages were data acquisition from the experiments, followed by the rigorous processing. The final step was analysis and interpretation of the resulting measurements.

Model Organisms

Freeze-dried *Saccharomyces cerevisiae* (strain Sa-07140, commonly known as Brewer's yeast) was obtained from the Leibniz Institute DSMZ (German Collection of Microorganisms and Cell Cultures). Cells were initially hydrated in 5 mL of distilled water and cultured on agar plates. After one week, the colonies were used to inoculate 500 mL of Yeast Peptone Dextrose (YPD) medium. The liquid cultures were maintained under semi-aerobic conditions in an incubator at 27° C.

Cylindrotheca fusiformis was selected as the primary micro-algal model due to its high resilience and cultivation stability. The diatoms were cultured in 1 L Erlenmeyer flasks containing 500 mL of standard f/2 medium. Initial cultivation was performed in a silica-deficient f/2 medium before introducing silica during the scaling phase to accelerate the cellular replication rate. The vessels were maintained at a controlled temperature of 16° C under constant light irradiance.

These specific organisms were selected to establish a robust comparative framework between a well-characterised, non-chlorophyll based heterotroph and a resilient, chlorophyll-based photosynthetic micro-alga. While the metabolic gas emissions of yeast have been widely documented, the volatile biosignatures produced by diatoms remain largely understudied. Photosynthetic organisms are primary drivers of global atmospheric chemistry; therefore, addressing this gap presents an opportunity to expand the current catalogue of observable biogenic gases.

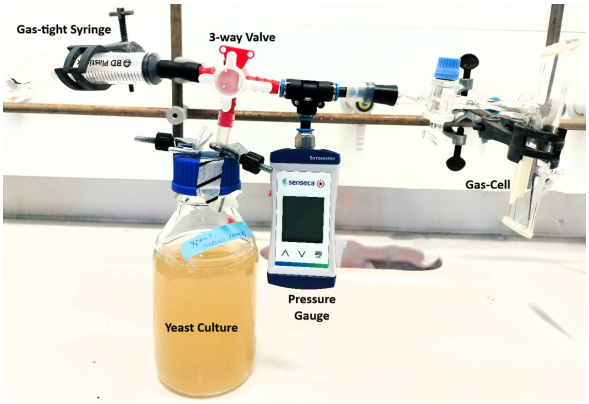

Figure 2: Schematic diagram of the modular gas collection and sampling loop. The closed-system set-up integrates a 500 mL culture flask with a 10 cm path-length gas cell with CaF_2 windows, monitored via a pressure gauge and regulated by a three-way valve for syringe-driven head-space extraction. The components are secured using non-reactive, flexible tubing to maintain a vacuum-tight, chemically inert path.

Experimental Set-up A modular, closed-loop gas collection system was engineered to couple non-invasive head-space measurement with direct culture assessments, as shown in Figure 2. The system comprised a 500 mL borosilicate glass culture flask, a 10 cm single-port gas cell equipped with CaF_2 windows (transmission range: 6670–1110 cm^{-1}), a pressure gauge, and a gas-tight syringe. These components were interconnected via non-reactive tubing and regulated by a three-way valve, as illustrated in Figure 2. Prior to each measurement, the gas cell was evacuated to a baseline pressure of $\sim$150 mbar before being integrated into the setup. To collect gas samples under laboratory conditions, the head-space gas was manually extracted from the culture flask using a gas-tight syringe. The three-way valve was then adjusted to inject the sampled gas into the evacuated cell until an operational pressure of 1007–1020 mbar was achieved, as verified by the integrated pressure gauge.To evaluate physiological adaptability, the target organisms were then subjected to two distinct environmental stress conditions. First, anoxic conditions were induced by sparging the cultures with pure N_2 gas for approximately 16 hours. The subsequent head-space responses were recorded after 4 to 5 days, spanning multiple sampling cycles. Second, oxidative stress was induced by adding 1000 μL of 30% H_2O_2 directly to the 500 mL cultures. The resulting gaseous metabolic responses were monitored over time, Using the same closed-loop gas extraction method as described above.

Spectral Data Acquisition Head-space gas measurements were conducted using a Bruker INVENIO X FT-IR spectrometer equipped with a liquid nitrogen-cooled Mercury Cadmium Telluride (LN-MCT) detector. Spectra were acquired over the 4000–1100 cm^{-1} wavenumber range at a resolution of 0.5 cm^{-1}. A small aperture (0.25 mm or 0.5 mm) was utilized to prevent detector saturation and cleanly separate individual spectral lines. Each acquisition consisted of 512 single-sided, backward-forward scans.

Data Processing and Analysis
A Python-based data processing pipeline was developed to interpret the resultant spectra. To establish theoretical detection boundaries and minimum detectable concentrations (MDC), a forward-modelling spectroscopy simulator was utilized which is described in Appendix A. The script calculates absolute absorption cross-sections using HITRAN (Gordon et al. 2026) transition parameters and NIST empirical shapes, applies thermodynamic broadening profiles, and convolves the result with the instrumental line shape (ILS) kernel to simulate hardware constraints. Background variations in the experimental spectra were isolated using the asymmetric reweighted penalized least squares (ARPLS) algorithm for global envelope smoothing, alongside localized Markov Chain Monte Carlo (MCMC) polynomial curve-fitting for targeted single-peak tracking. Baseline corrected features were integrated analytically using trapezoidal quadrature for continuous kinetics or threshold-gated Simpson's rule for automated multi-gas analysis to limit out-of-band noise. The absolute column density and chemical concentrations were derived by evaluating the Beer-Lambert law. To resolve cross-sensitivities in overlapping bands, simultaneous concentration fitting was executed using Classical Least Squares with a Non-Negative constraint (CLS-NNLS). Prior to quantification, specific gas presence was validated via windowed vector cosine similarity matching to prevent the fitting of unmodelled noise. A detailed explanation of the code is given in Appendix B. Signal-to-noise ratio (SNR_{peak}) metric was utilized to evaluate the spectral data and is defined as:

$$\mathrm{SNR}_{\mathrm{peak}} = \frac{\hat{A}}{\sigma_{\mathrm{noise}}}$$

where $\hat{A}$ is the maximum absorbance within the target band window, and σ_{noise} is the root-mean-square (RMS) baseline noise calculated in an absorption-free region. This metric indicates how distinctly a single spectral point stands above the noise floor, making it the primary criterion for verifying the presence of a specific chemical species.

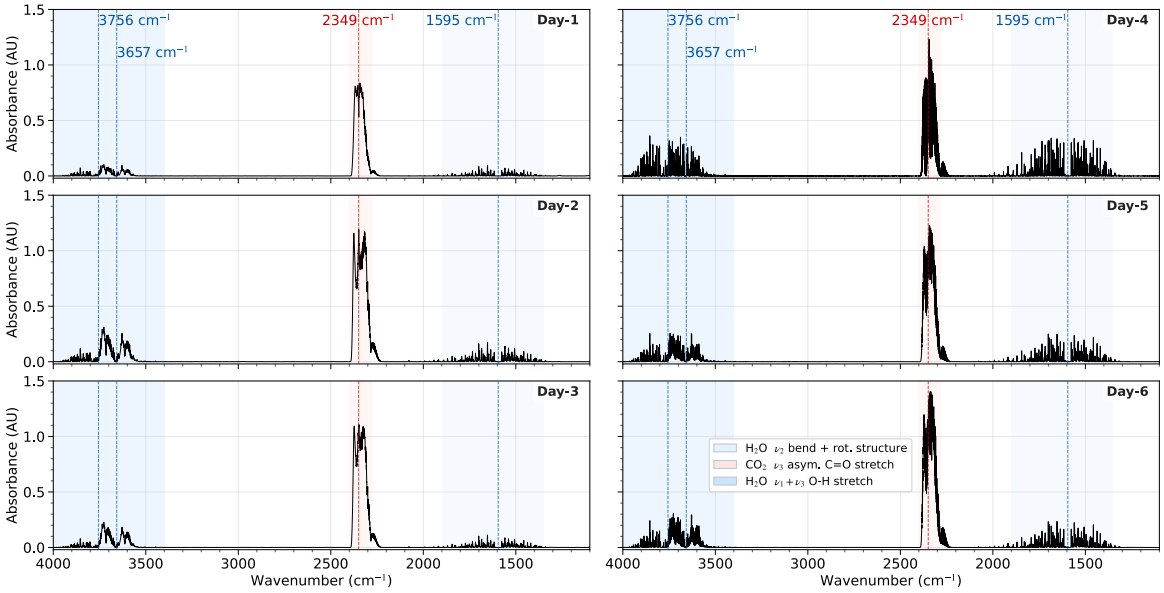

Figure 3: Gas-phase FT-IR head-space spectra of a *Saccharomyces cerevisiae* culture recorded over six days under Earth atmospheric conditions. Highlighted regions indicate characteristic CO_2 (red) and water vapour (blue) absorption bands.

Results

The spectral profiles obtained from the head-space monitoring experiments are presented below. Only distinct signals that could be visually interpreted were utilized to positively identify the presence of specific gas molecules. To quantify the reliability of the spectral detections and establish the instrument's limit of detection, the SNR was calculated for all identified absorption features. The background instrumental noise was determined by calculating the RMS absorbance within a signal-free baseline region. No signs of saturation were detected; therefore, the Beer-Lambert law is assumed to remain valid, maintaining a linear relationship between absorbance and concentration.

Yeast

Gas-phase measurements of the *Saccharomyces cerevisiae* head-space under standard laboratory conditions (Earth atmosphere) revealed absorbance peaks corresponding to H_2O and CO_2 shown in Figure 3. The integrated areas calculated shown in Table 1 and the SNR for CO_2 remained above 2300 across all readings. Within the spectral window for organic molecules between 2500 and $3500\,\mathrm{cm}^{-1}$, the peak SNR remained below 10, no spectral features were detected with confidence. The fundamental stretching (ν_1 and ν_3) and bending (ν_2) vibrations of H_2O is in region 4000–$3500\,\mathrm{cm}^{-1}$ and 2000–$1500\,\mathrm{cm}^{-1}$ regions, respectively.

Table 1: Integrated areas of CO_2 peaks over the six-day sampling period from Figure 3

Day	Integrated Area (A.U $\cdot$ cm^{-1})
1	54.120 ± 0.002
2	84.040 ± 0.002
3	79.400 ± 0.002
4	48.610 ± 0.001
5	67.740 ± 0.001
6	80.960 ± 0.001

Replacing the head-space atmosphere with pure nitrogen gas reduced CO_2 evolution compared to baseline laboratory conditions, with peak absorbance values dropping from 1.2–1.4 A.U. down to 0.2–0.5 A.U.. CO_2 production was suppressed during the initial two sampling intervals, and a localized increase was recorded by the third measurement. The presence of other organic compounds was not detected. The three distinct measurements were taken on different days. Each time, the container was purged with N_2 and sealed off for a couple of days before taking the measurement. For these three distinct measurements shown in Figure 4, the integrated CO_2 areas were calculated as 10.056 ± 0.001, 9.634 ± 0.001, and 23.518 ± 0.001 A.U. $\cdot$ cm^{-1}, respectively, maintaining a strong SNR of > 1300. Although the 2500–$3500\,\mathrm{cm}^{-1}$ range is the primary spectral window for identifying organic molecules, detection was limited by low SNR values: ~ 5 across the 2500–$3200\,\mathrm{cm}^{-1}$ sub-region and below 15 within the C – H stretching window (2900–$3050\,\mathrm{cm}^{-1}$).

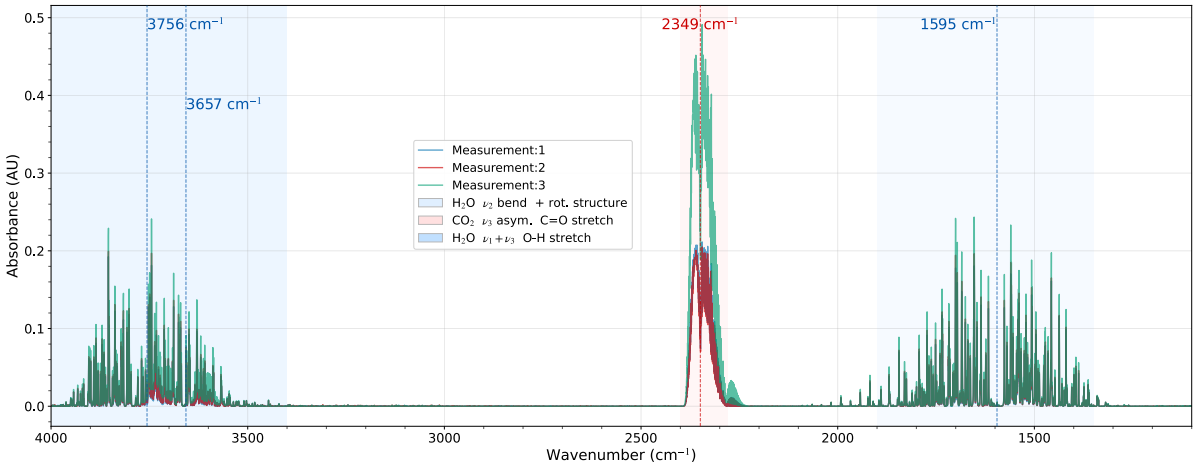

Figure 4: Gas-phase FT-IR absorbance spectra of the head-space gas collected from a yeast culture under anoxic (nitrogen-rich) conditions, highlighting the reduced levels of CO_2. Measurements were recorded on three distinct days; for each measurement, the head-space was freshly sparged with nitrogen and the culture was sealed for 3 to 4 days prior to sampling.

The administration of 30% H_2O_2 caused a drop in CO_2 evolution over time (Figure 5). This decline was interrupted by a temporary, localized increase in absorbance at t = 3 hours. The SNR remained above 2500, except on Day 12, when it fell to ~ 246. After the final measurement on Day 12, prolonged exposure led to the complete cessation of gas generation. This created a net negative pressure within the closed sample bottles, preventing any further manual extraction of head-space gas. Target volatile biomarkers such as acetic acid and acetaldehyde were not detected. Physical degradation of the cells was confirmed via optical microscopy (Figure 6).

Table 2: Integrated area of CO_2 for yeast under oxidative environment (A.U $\cdot$ cm^{-1}) over 12 days period

Time	Integrated Area
0 hours	18.1372 ± 0.0004
1 hour	19.6708 ± 0.0004
2 hours	19.6189 ± 0.0004
3 hours	42.7096 ± 0.0004
4 hours	27.5659 ± 0.0004
6 days	15.6306 ± 0.0006
12 days	1.2089 ± 0.0006

Cylindrotheca Fusiformis

The IR spectrum of the gaseous profile of the marine diatom *Cylindrotheca fusiformis* under Earth atmospheric conditions is shown in Figure 7. Head-space measurements on Days 1 and 2 established a stable baseline. On Day 3, an increase in CO_2 occurred, which returned to baseline levels by Day 4. The integrated CO_2 areas and corresponding SNR values over the four-day sampling period (Figure 7) were calculated as 2.864 ± 0.002 A.U $\cdot$ cm^{-1} (SNR = 147.8) on Day 1, 3.779 ± 0.002 A.U $\cdot$ cm^{-1} (SNR = 121.4) on Day 2, 15.330 ± 0.001 A.U $\cdot$ cm^{-1} (SNR = 2174.8) on Day 3, and 2.514 ± 0.001 A.U $\cdot$ cm^{-1} (SNR = 370.0) on Day 4.

Under nitrogen-induced anoxia, the head-space profile showed no variations between consecutive measurements (Figure 8), yielding stable integrated CO_2 areas of 2.5670 ± 0.0008 and 5.3100 ± 0.0009 A.U $\cdot$ cm^{-1}. The corresponding integration SNRs were 389.3 and 708.4. Nitrogen sparging caused no visible setbacks to population growth, and the cells maintained a normal morphology under microscopic inspection.

Table 3: Integrated CO_2 peak areas derived from the headspace response of *C. fusiformis* under oxidative stress over a 10-day period

Time	Integrated Area (A.U $\cdot$ cm^{-1})
0 hours	3.2845 ± 0.0004
1 hour	2.1316 ± 0.0004
2 hours	2.2547 ± 0.0004
3 hours	1.9079 ± 0.0005
4 days	3.5959 ± 0.0006
10 days	1.1498 ± 0.0006

The response to H_2O_2 by the micro-algae is shown Figure 9 and the integrated areas of CO_2 are tabulated in Table 3 . Head-space CO_2 levels dropped over time, interrupted by a transient increase at t = 4 days. The SNR remained above 500, but declined to 258 on Day 10. The system reached metabolic arrest, forming a net negative pressure within the sample bottles. Morphologically, the diatom culture underwent a colour transi-

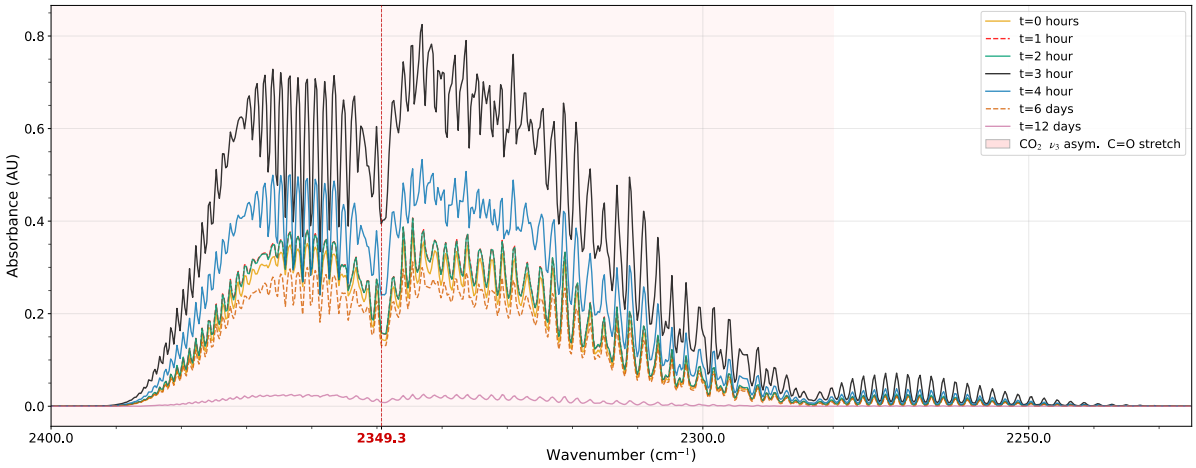

Figure 5: Gas-phase FT-IR absorbance spectra of the head-space gas collected from a *Saccharomyces cerevisiae* culture under oxidative stress conditions, focusing on the progressive decline in CO_2 levels over time.

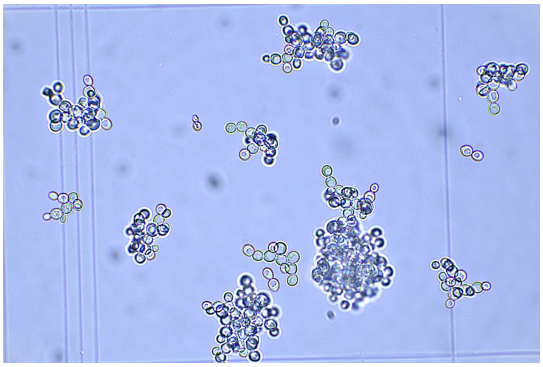

(a) Healthy *S. cerevisiae* cells under 40× magnification.

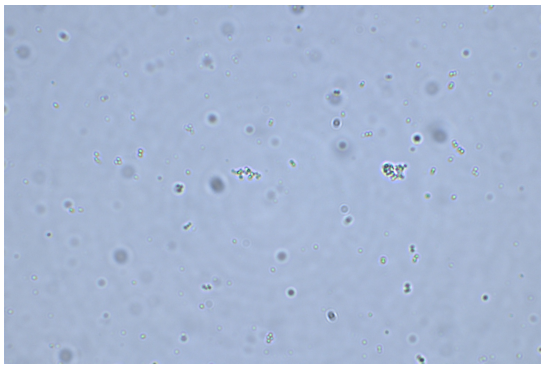

(b) Shrunken yeast cells following acute exposure to H_2O_2 under 40x magnification.

Figure 6: Morphological variations in *Saccharomyces cerevisiae* cell structural integrity before and after oxidative stress induction.

tion from dark brown-green to pale, light green. Microscopic analysis revealed structural degradation of the cells after long-term exposure (Figure 10).

Discussion

This study investigated the gas-phase spectral profiles of two distinct micro-organisms: the heterotrophic yeast *Saccharomyces cerevisiae* and the photosynthetic marine diatom *Cylindrotheca fusiformis*, to evaluate the detectability of biogenic CO_2 and volatile organic compounds (VOCs) under simulated anoxic and oxidative environments. The experimental outcomes observed across both the *S. cerevisiae* and *C. fusiformis* trials highlight the limits of detection regarding trace VOCs within closed-system FT-IR spectroscopy. Despite macroscopic modifications in culture morphology, such as the plasmolysis and structural shrinkage observed under oxidative stress, which indicated shifts in cellular metabolism, the corresponding spectral signatures from volatiles remained undetected. This decoupling of physical and spectral data can be attributed to several interrelated technical, biological, and temporal constraints.

First, the physical configuration of the current apparatus, specifically the short path-length of the gas cell, restricted the system's optical sensitivity. The noise level was of the order 10^{-4} in this experiment. Past experiments (Apolonski and Maiti 2021) conducted for volatile monitoring have shown that many biogenic VOCs manifest at trace levels on the order of 10^{-4} absorbance units or lower, even when utilizing specialized, long path-length cells measured in the order of meters . Within the short path-length cell used in this study, such low-amplitude signals fall below the baseline noise level of the instrument. Consequently, while the detection thresholds of modern standard FT-IR systems are nominally calibrated to parts-per-million (ppm) levels, the actual con-

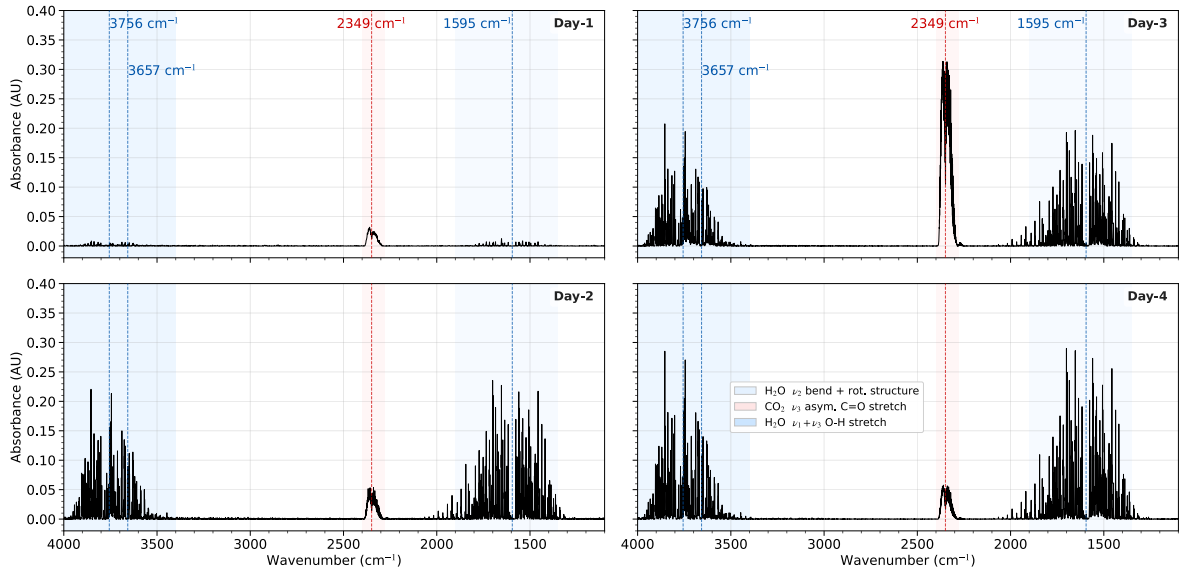

Figure 7: Gas-phase FT-IR absorbance spectra of the head-space gas collected from a *Cylindrotheca Fusiformis* culture under Earth atmospheric conditions on a six distinct days, highlighting characteristic CO_2 and water vapour (H_2O) bands.

centration of volatile chemical biomarkers generated by these stressed cultures likely hovered in the parts-per-billion (ppb) range. Furthermore, because the ν_3 asymmetric stretching band of CO_2 is a dominant absorption feature, trace biogenic volatiles containing N – H or alcohol O – H groups are likely masked by background water signatures. Because of this resolution limit, expected early-stress VOC profiles, such as the accumulation of acetaldehyde or stress-induced alkanes remained unresolved, leaving only the dominant H_2O and CO_2 signatures visible. Diagnostic aliphatic C – H stretching features remained undetectable even within the spectral windows clear of H_2O and CO_2 interference.

Second, a methodological constraint was the reliance on discrete, point-in-time measurements rather than continuous monitoring. Gathering data at fixed, isolated intervals creates a temporal blind spot, as it assumes that volatile accumulation is a linear process. In reality, biogenic volatile generation under stress is frequently transient, occurring in bursts as specific metabolic pathways are briefly activated before the culture succumbs or adapts. Since these experiments utilized snapshot sampling, variations in volatile production may have occurred within the unmonitored windows between measurements. Without continuous tracking, these time-resolved dynamics are lost to baseline averaging. For instance, the temporary CO_2 variations observed, such as the Day 3 spike in *C. fusiformis* baseline trials, point to transient metabolic bottlenecks. Long exposure to continuous light energy damages the D1 protein of Photosystem II, halting linear electron flow and temporarily arresting CO_2 fixation via the Calvin cycle before the population adapts (Pilcher 2003). Alternatively, this variation could be linked to ambient air leakage into the system.

Finally, this analytical limitation was compounded by biological and chemical dynamics within the head-space matrix itself. Biogenic volatiles may have undergone continuous consumption or metabolic recycling by the microorganisms as alternative substrates during prolonged stress exposure. Reactive chemical species may have experienced ambient degradation or oxidative breakdown before accumulating to a detectable steady-state concentration. Expected volatile biomarkers of oxidative stress, such as acetic acid and acetaldehyde, remained below detection (Liu and Yao 2025; Chen et al. 2022), and oxidative stress may trigger a behavioral shift in specific volatiles, such as 2-methylpentane, from net release to net consumption, rendering them undetectable via FT-IR. Ultimately, these findings underscore that a lack of volatile detection via standard infra-red spectroscopy cannot be interpreted as a lack of biological activity.

Beyond technical limitations, comparing the responses of *S. cerevisiae* and *C. fusiformis* reveals how distinct physiological pathways dictate atmospheric outputs. Under baseline conditions, the initial increase and stabilization of CO_2 levels indicated that the yeast culture reached a station-

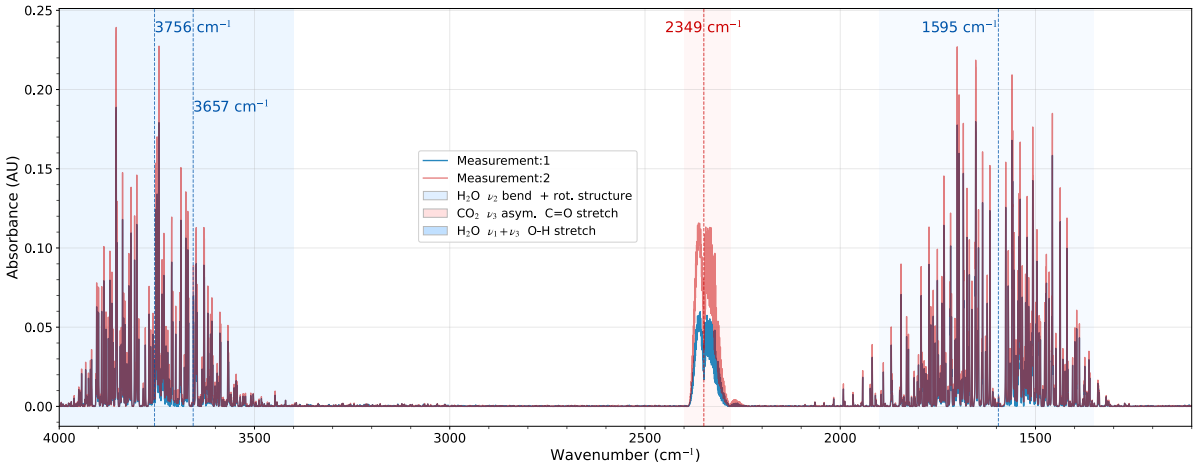

Figure 8: Gas-phase FT-IR absorbance spectra of the head-space gas collected from *C. fusiformis* culture under anoxic conditions (nitrogen-rich atmosphere), highlighting CO_2 levels comparable to those under Earth atmospheric conditions.

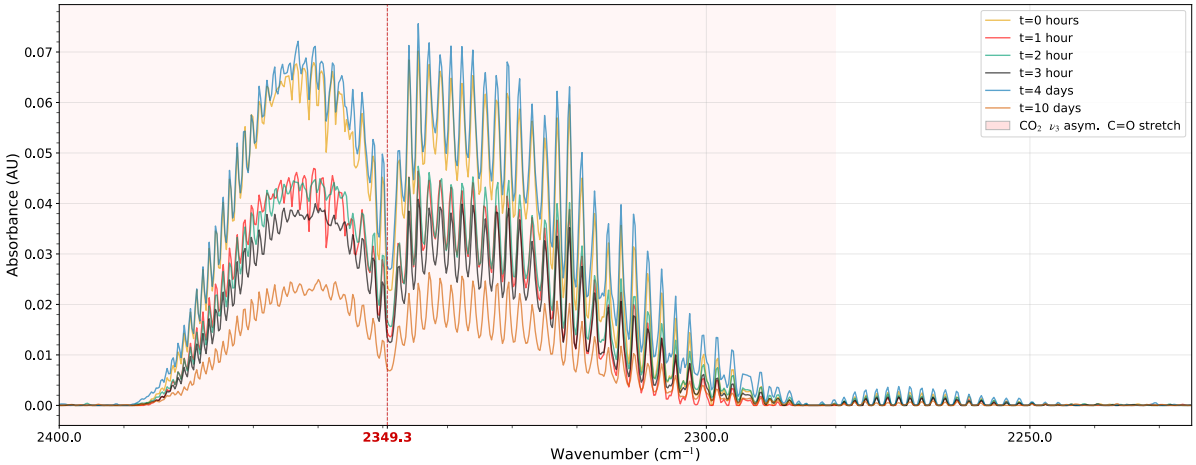

Figure 9: Gas-phase FT-IR absorbance spectra of the head-space gas collected from a *C.fusiformis* culture under oxidative stress conditions, focusing on the progressive decline in CO_2 levels over time.

ary growth phase characterised by metabolic equilibration. During anoxia, while gas exposure induces shifts in primary energy pathways (Pham et al. 2008), the decline in CO_2 marks a transition from aerobic respiration to lower-yield anaerobic pathways, exacerbated by glucose depletion. As a heterotroph, *S. cerevisiae* mobilizes internal storage carbohydrates like glycogen and trehalose to meet maintenance costs, and the endogenous fermentation of these reserves accounts for the transient secondary burst of CO_2 (Koutsokali and Valahas 2020). The sustained elevation of nitrogen may also inhibit fermentation (Mendes-Ferreira et al. 2011), and excess nitrogen sources can accelerate cell death (Tesnière et al. 2013).

The phototrophic *C. fusiformis* maintained a stable CO_2 baseline under nitrogen-induced anoxia. Because the cultures were maintained under constant illumination, photosynthetic activity remained linked to the cell cycle (Claquin et al. 2004), leaving mitochondrial respiration as the primary driver of continuous CO_2 generation. The stable net concentration under anoxia suggests that the conditions simultaneously disrupted the Calvin cycle, reducing active carbon fixation and balancing the decline in respiratory CO_2 release (Kaiser 1979). The physiological consequences of excess gaseous nitrogen on micro-algae remain poorly understood (Limongi and Rita 2022), and cellular stress sensitivity varies based on metabolic status (Lushchak 2010).

When subjected to oxidative stress via H_2O_2, both organisms exhibited a multi-phase decline punctuated by hyper-respiration, where cells expended energy reserves to drive defensive antioxidant enzymes. Diatoms utilize native detoxification pathways, including the glutathione and Mehler reaction cycles, to neutralize reactive oxygen species

(a) *C. fusiformis* cells 10× magnification.

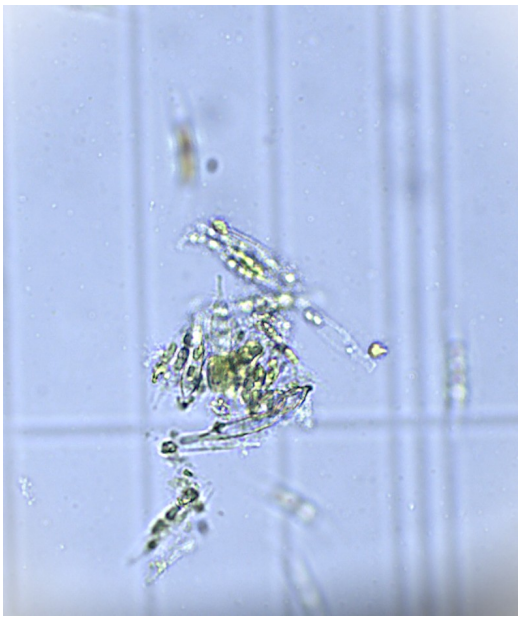

(b) Stressed *C. fusiformis* cells clustered under 40x magnification.

Figure 10: Microscopic characterization of *Cylindrotheca fusiformis* cellular distributions showing (a) baseline tracking morphologies and (b) dense aggregation features under stress.

(Waring et al. 2010; Foyer et al. 1994). However, the exogenous dose overwhelmed these mitigation systems, resulting in cellular collapse and a colour shift indicative of the direct chemical breakdown of fucoxanthin by hydrogen peroxide. Because microscopic analysis revealed structural degradation, the observed collapse cannot be decoupled from direct external oxidative lysis versus metabolic competition for reducing nutrients. In yeast, stationary-phase cells exhibit higher baseline resistance to oxidative damage (Madeo et al. 1999), leading to structural and metabolic breakdown over several days. This delayed kinetics may reflect a chemical cascade, where peroxide was consumed via oxidation of medium components before attacking the cells.

For astrobiological surveys, a biosphere's detectable atmosphere will depend on its primary metabolism. Photosynthetic ecosystems might recycle carbon and mask their stress signals, whereas heterotrophic ecosystems may produce temporary bursts of gas. Translating these localized dynamics to a planetary scale requires insights from Earth-based remote sensing. On Earth, continuous multi-platform monitoring is essential to distinguish biological fluxes, such as seasonal CO_2 draw-down or transient algal emissions, from background geological noise. This biologically driven atmospheric seasonality may be an inevitable, metabolism-independent feature of any surface biosphere exposed to fluctuating stellar radiation. Consequently, tracking these seasonal cycles offers a robust biosignature that mitigates false positives and negatives, enabling the characterization of exoplanetary ecosystems (Olson et al. 2018). Expanding this framework provides insights into the approach to exoplanetary biosignature detection, particularly when evaluating planets with N_2 dominated atmospheres or oxidative environments. As demonstrated by the *C. fusiformis* experiments, the temporal variation of CO_2 levels serves as a proxy for shifting metabolic states, transitioning from a respiratory or photoinhibitory burst to a stabilized equilibrium. On a planetary scale, tracking the time-dependent variation of atmospheric CO_2 across seasonal cycles or orbital variations could offer an indicator of surface life or large-scale photosynthetic and respiratory flux (Meadows et al. 2018).

However, these experimental models also mandate caution. In oxidative environments like Mars or irradiated icy moons, gas fluctuations are difficult to interpret. These shifts can be caused by geological or chemical processes rather than life, making it essential to rule out non-biological sources. Non-biological mechanisms, such as volcanic outgassing, mineral weathering, or photochemical destruction driven by stellar UV irradiance, can mimic the cyclical variations or spikes of biogenic gases, generating complex false positives (Schwieterman and Leung 2024).

Conversely, the metabolic adaptation observed in

these experiments exposes a risk of false negatives, which is also affected by observational gaps. Just as snapshot sampling in the lab can miss a burst of volatile production, sparse astronomical observations risk missing transient biogenic atmospheric shifts. In the phototrophic *C. fusiformis* trials, the stabilization of CO_2 output under stress likely reflects the activation of redox-controlled cellular circuit breakers (Dietz et al. 2016). When environmental stress restricts standard CO_2 fixation, photosynthetic organisms can prevent oxidative damage by actively shutting down linear electron flow and rerouting energy through alternative pathways, such as the photoreduction of O_2 via the Mehler reaction (Polle 1996). Consequently, the organism enters a protective, low-emission metabolic state that drops net gaseous output beneath the system's detection threshold, illustrating how survival mechanisms can effectively mask biological activity from spectroscopic detection. In an exoplanetary context, if an ambient biosignature gas declines or vanishes due to an ecosystem adapting to a transient planetary stressor, it could lead to the erroneous conclusion that the target world is lifeless.

Furthermore, just as trace biomarkers may have been re-consumed within the laboratory flasks, an active planetary biosphere may recycle its own volatile organic waste products, leaving the broader global atmosphere devoid of detectable, non-equilibrium trace gases (Catling et al. 2018). Ultimately, this study demonstrates that relying on discrete infra-red measurements of a single atmospheric component is unlikely to yield a definitive detection of life, nor can it confidently rule out its presence. Modifying the modes of environmental stress in laboratory simulations reveals that biological signatures are dynamic, nonlinear, and masked by technical limitations or cellular survival protocols. Developing a reliable astrobiological assessment of distant worlds therefore requires a multi-faceted approach that correlates transient gaseous outputs with comprehensive planetary models, stellar flux dynamics, and continuous, multi-wavelength observations capable of pulling trace, fast-moving signals out of the background noise.

Future Works

Based on the experimental outcomes and structural limitations encountered in this study, some key advancements are recommended. To ensure systematic progress, these recommendations are prioritized into immediate hardware upgrades, subsequent biological investigations, and long-term analytical developments.

The primary limitation in this study was the physical inability of the apparatus to detect trace signals through background noise and moisture. Therefore, the immediate priority for future research must be upgrading the physical hardware. To resolve the extensive spectral masking caused by water vapour, incorporating a dedicated cooling and heating system is critical to physically remove water vapour signatures and concentrate trace volatile organic compounds (VOCs) prior to FT-IR measurement. Concurrently, implementing a longer path-length gas cell is an essential first step to lower detection thresholds, enabling the detection of low-concentration volatiles that remained beneath the baseline in current trials. Structurally, transitioning to a fully hermetic bioreactor system equipped with a continuous gas flow mechanism must also be prioritized; this will eliminate ambient leaks, prevent culture contamination, and allow for continuous, time-resolved monitoring of gaseous variations.

Once the foundational detection hardware is optimized, subsequent investigations should prioritize resolving physiological responses by tracking micro-organism growth under controlled stress conditions from the inception of the culture. This includes flushing the head-space with N_2 from the initial growth stage to systematically evaluate the anoxic tolerance and adaptability of the growing population. Additionally, oxidative stress agents like H_2O_2 should be introduced at the beginning of the growth phase rather than waiting for the stationary phase. Following these baseline stress tests, a multi-parametric analysis should be conducted to determine how external variables impact the overall stress response. This approach will isolate the individual effects of specific culturing and environmental factors, such as temperature variations, irradiance, and pH levels.

Finally, as continuous and highly resolved datasets become available from the upgraded apparatus, the long-term focus can shift toward advanced computational and analytical frameworks. Work at this stage should prioritize detailed statistical analysis and the generation of synthetic gas mixture spectra to rigorously compare theoretical profiles with empirical experimental values. On the signal processing front, implementing the Matryoshka Method (Apolonski and Maiti 2021; Zenner et al. 2025) would then offer a robust mathematical pathway for uncovering heavily overlapping spectral signatures. This analytical layer can ultimately be enhanced by integrating

machine learning models trained for automated molecule identification and precise concentration estimation, turning complex spectra into highly quantifiable metabolic data.

Conclusions

This study evaluated the capability of gas-phase FT-IR spectroscopy to detect microbial volatiles from the heterotrophic *Saccharomyces cerevisiae* and the phototrophic *Cylindrotheca fusiformis*. Both microbial models were subjected to standard Earth atmospheric conditions, anoxic (N_2-rich) atmospheres, and oxidative environments induced by H_2O_2. Measurements were conducted using a modular experimental system consisting of a gas cell, a microbial culture flask, and a gas-tight syringe regulated by a three-way valve.

Under Earth conditions, the spectral profiles for both organisms were consistently dominated by water vapour (H_2O) and carbon dioxide (CO_2). However, subjecting the cultures to environmental stressors revealed distinct, metabolism-dependent gaseous responses. While anoxic, nitrogen-rich exposure altered the metabolic output of the yeast, the photosynthetic diatom maintained a stable CO_2 baseline, demonstrating resilience to oxygen deprivation. Conversely, severe oxidative stress induced a uniform reduction in CO_2 evolution across both species, reflecting an active transition into a protective metabolic state.

Crucially, despite observable macroscopic physical modifications in the cultures, such as cellular shrinkage and plasmolysis, no secondary trace volatile organic compounds (VOCs) were detected within the 3500–2500 cm^{-1} spectral window. The absence of these anticipated stress biomarkers underscores a limitation of closed-system, short-pathlength FT-IR measurements. The inability to detect these trace gases is likely due to instrumental limits and biological adaptation, not a complete halt in biological activity. As organisms trigger internal regulatory mechanisms to mitigate environmental stress, they shift into low-emission survival modes, effectively dropping biogenic outgassing below standard detection thresholds.

These laboratory findings carry direct implications for exoplanetary biosignature detection. They demonstrate that biological gaseous outputs are transient, non-linear, and highly sensitive to environmental perturbations. Relying on discrete, snapshot observations of a single atmospheric component risks yielding false negatives, particularly if a planetary biosphere is actively adapting to transient stressors. Therefore, the absence of trace non-equilibrium gases in a planetary atmosphere cannot be used to definitively rule out the presence of life. Future astrobiological surveys must integrate continuous, multi-wavelength observation strategies capable of tracking dynamic temporal or stress-induced atmospheric variations, shifting the analytical focus from static chemical profiles to complex metabolic fluxes.

Acknowledgments

During the initial stages of this research, Dr. Marta Cortesão and her team at the University of Porto provided critical insights into extremophiles and microbial characteristics. I am also grateful to Dr. Robbert Kleerebezem, Associate Professor of Environmental Biotechnology at TU Delft, for his ideas regarding the experimental setup and for patiently answering my queries. I extend my thanks to Dr. Santiago Garcia Espallargas from the Department of Aerospace Engineering at TU Delft for his valuable input on micro-algal characteristics and metabolism, and to Dr. Marrick Braam from the University of Bern for his insights into the atmospheres of planets and icy moons. Their willingness to share their knowledge of prebiotic chemistry was foundational in helping me understand these concepts and effectively shape the direction of the research.

I am extremely grateful to Christiaan Snaathorst for assisting me with microbial cultivation. Finally, I want to thank Ramon ter Horst and Mascha Slingerland, who patiently put up with my endless questions, and supported support to set-up the experiments safely.

References

Abis, Letizia et al. (Dec. 2020). “Reduced microbial diversity induces larger volatile organic compound emissions from soils”. In: *Scientific Reports* 10.1. ISSN: 20452322. DOI: 10.1038/s41598-020-63091-8.

Apolonski, Alexander and Kiran Sankar Maiti (May 2021). “Towards a standard operating procedure for revealing hidden volatile organic compounds in breath: the Fourier-transform IR spectroscopy case”. In: *Applied Optics* 60.14, p. 4217. ISSN: 1559-128X. DOI: 10.1364/ao.421994.

Bhartia, R. et al. (May 2012). “Noncontact, reagentless, nondestructive, detection of organics, biosignatures, and water”. In: *Sensors and Systems for Space Applications V*.

Vol. 8385. SPIE, 83850E-83850E–9. ISBN: 9780819490636. DOI: 10.1117/12.921420.

Catling, David C. et al. (June 2018). "Exoplanet Biosignatures: A Framework for Their Assessment". In: *Astrobiology* 18.6, pp. 709–738. ISSN: 15311074. DOI: 10.1089/ast.2017.1737.

Chen, Haoxuan et al. (July 2022). "Gene-Regulated Release of Distinctive Volatile Organic Compounds from Stressed Living Cells". In: *Environmental Science and Technology* 56.13, pp. 9546–9555. ISSN: 15205851. DOI: 10.1021/acs.est.2c01774.

Claquin, Pascal, Jacco C. Kromkamp, and Veronique Martin-Jezequel (Feb. 2004). "Relationship between photosynthetic metabolism and cell cycle in a synchronized culture of the marine alga Cylindrotheca fusiformis (Bacillariophyceae)". In: *European Journal of Phycology* 39.1, pp. 33–41. ISSN: 09670262. DOI: 10.1080/0967026032000157165.

Dietz, Karl Josef, Ismail Turkan, and Anja Krieger-Liszkay (July 2016). "Redox- and reactive oxygen species-dependent signaling into and out of the photosynthesizing chloroplast". In: *Plant Physiology* 171.3, pp. 1541–1550. ISSN: 15322548. DOI: 10.1104/pp.16.00375.

Ding, Junmei et al. (Nov. 2009). *Tolerance and stress response to ethanol in the yeast Saccharomyces cerevisiae*. DOI: 10.1007/s00253-009-2223-1.

Foyer, Christine H et al. (1994). "Photooxidative stress in plants". In: *Physiologia Plantarum* 92, pp. 696–717.

Gauthier, M. R., G. N.A. Senhorinho, and J. A. Scott (Dec. 2020). *Microalgae under environmental stress as a source of antioxidants*. DOI: 10.1016/j.algal.2020.102104.

Gillen, Catherine et al. (Nov. 2023). "The Call for a New Definition of Biosignature". In: *Astrobiology* 23.11, pp. 1228–1237. ISSN: 15311074. DOI: 10.1089/ast.2023.0010.

Gordon, I.E. et al. (Apr. 2026). "The HITRAN2024 molecular spectroscopic database". In: *Journal of Quantitative Spectroscopy and Radiative Transfer*, p. 109807. ISSN: 00224073. DOI: 10.1016/j.jqsrt.2026.109807.

Griffith, D. W. T. et al. (May 2012). *A Fourier transform infrared trace gas analyser for atmospheric applications*. DOI: 10.5194/amtd-5-3717-2012. URL: https://amt.copernicus.org/articles/5/2481/2012/amt-5-2481-2012-discussion.html.

Kai, Marco (Apr. 2020). *Diversity and Distribution of Volatile Secondary Metabolites Throughout Bacillus subtilis Isolates*. DOI: 10.3389/fmicb.2020.00559.

Kaiser, Werner M (1979). *Reversible Inhibition of the Calvin Cycle and Activation of Oxidative Pentose Phosphate Cycle in Isolated Intact Chloroplasts by Hydrogen Peroxide*. Tech. rep., pp. 377–382.

Kiang, Nancy Y. et al. (June 2018). *Exoplanet Biosignatures: At the Dawn of a New Era of Planetary Observations*. DOI: 10.1089/ast.2018.1862.

Koutsokali, Maria and Michael Valahas (Apr. 2020). "Anaerobic and Aerobic Respiration in Yeast: Small-Scale Variations on a Classic Laboratory Activity". In: *Journal of Chemical Education* 97.4, pp. 1041–1047. ISSN: 19381328. DOI: 10.1021/acs.jchemed.9b00994.

Krissansen-Totton, Joshua et al. (Sept. 2018). "Detectability of Biosignatures in Anoxic Atmospheres with the James Webb Space Telescope: A TRAPPIST-1e Case Study". In: *The Astronomical Journal* 156.3, p. 114. ISSN: 0004-6256. DOI: 10.3847/1538-3881/aad564.

Li, Yue (Apr. 2023). *Analytical methods for the analysis of volatile natural products*. DOI: 10.1039/d2np00079b.

Limongi and Antonina Rita (2022). "Green microalgae biohydrogen production". PhD thesis. Universita degli Studi della Basilicata.

Liu, Huaying and Maosheng Yao (Sept. 2025). "Time-resolved monitoring of yeast responses to lipopolysaccharide exposure by cell-released volatile organic compounds". In: *Applied and Environmental Microbiology* 91.9. ISSN: 10985336. DOI: 10.1128/aem.00785-25.

Lushchak, V. I. (Dec. 2010). "Oxidative Stress in Yeast". In: *Biochemistry (Moscow)* 75.3, pp. 281–296. ISSN: 16083040. DOI: 10.1134/S0006297910030041.

Madeo, Frank et al. (May 1999). "Oxygen Stress: A Regulator of Apoptosis in Yeast". In: *The Journal of Cell Biology* 145.4, pp. 757–767. URL: http://www.jcb.org.

Malaterre, Christophe et al. (Nov. 2023). "Is There Such a Thing as a Biosignature?" In: *Astrobiology* 23.11, pp. 1213–1227. ISSN: 15311074. DOI: 10.1089/ast.2023.0042.

Meadows, Victoria S. et al. (June 2018). "Exoplanet Biosignatures: Understanding Oxygen as a Biosignature in the Context of Its Environment". In: *Astrobiology* 18.6, pp. 630–662. ISSN: 15311074. DOI: 10.1089/ast.2017.1727.

Mendes-Ferreira, Ana et al. (2011). “The Impact of Nitrogen on Yeast Fermentation and Wine Quality”. In: *Ciencia Tec. Vitiv.* 26.1, pp. 17–32.

Morano, Kevin A., Chris M. Grant, and W. Scott Moye-Rowley (Apr. 2012). “The response to heat shock and oxidative stress in saccharomyces cerevisiae”. In: *Genetics* 190.4, pp. 1157–1195. ISSN: 00166731. DOI: 10.1534/genetics.111.128033.

Olson, Stephanie L. et al. (May 2018). “Atmospheric Seasonality as an Exoplanet Biosignature”. In: *The Astrophysical Journal Letters* 858.2, p. L14. ISSN: 2041-8205. DOI: 10.3847/2041-8213/aac171.

Olsson-Francis, Karen and Charles S. Cockell (Jan. 2010). *Experimental methods for studying microbial survival in extraterrestrial environments*. DOI: 10.1016/j.mimet.2009.10.004.

Parrilli, Ermenegilda et al. (Mar. 2021). *The art of adapting to extreme environments: The model system Pseudoalteromonas*. DOI: 10.1016/j.plrev.2019.04.003.

Pham, T. H. et al. (2008). “Gaseous environments modify physiology in the brewing yeast Saccharomyces cerevisiae during batch alcoholic fermentation”. In: *Journal of Applied Microbiology* 105.3, pp. 858–874. ISSN: 13652672. DOI: 10.1111/j.1365-2672.2008.03821.x.

Pilcher, Carl B. (2003). “Biosignatures of Early Earth”. In: *Astrobiology* 3.3, pp. 471–486.

Polle, Andrea (1996). “Mehler reaction: Friend or foe in photosynthesis?” In: *Botanica Acta* 109.2, pp. 84–89. ISSN: 09328629. DOI: 10.1111/j.1438-8677.1996.tb00546.x.

Rein, Hanno, Yuka Fujii, and David S. Spiegel (May 2014). “Some inconvenient truths about biosignatures involving two chemical species on Earth-like exoplanets”. In: *Proceedings of the National Academy of Sciences of the United States of America* 111.19, pp. 6871–6875. ISSN: 10916490. DOI: 10.1073/pnas.1401816111.

Schwieterman, Edward W and Michaela Leung (2024). “An Overview of Exoplanet Biosignatures”. In: *Reviews in Mineralogy and Geochemistry* 90.1, pp. 465–514.

Seager, S et al. (2020). *Laboratory studies on the viability of life in H2-dominated exoplanet atmospheres*. Tech. rep., pp. 802–806.

Seager, S., W. Bains, and J. J. Petkowski (June 2016). “Toward a List of Molecules as Potential Biosignature Gases for the Search for Life on Exoplanets and Applications to Terrestrial Biochemistry”. In: *Astrobiology* 16.6, pp. 465–485. ISSN: 15311074. DOI: 10.1089/ast.2015.1404.

Tesnière, Catherine et al. (Apr. 2013). “Impact of Nutrient Imbalance on Wine Alcoholic Fermentations: Nitrogen Excess Enhances Yeast Cell Death in Lipid-Limited Must”. In: *PLoS ONE* 8.4. ISSN: 19326203. DOI: 10.1371/journal.pone.0061645.

Thompson, Maggie A. (Mar. 2026). “On the importance of laboratory experiments for interpreting exoplanet observations”. In: *Astrophysics and Space Science* 371.3. ISSN: 1572946X. DOI: 10.1007/s10509-026-04564-6.

Thorn, Robin Michael Statham and John Greenman (June 2012). *Microbial volatile compounds in health and disease conditions*. DOI: 10.1088/1752-7155/6/2/024001.

Waring, Jen et al. (Dec. 2010). “Light-induced responses of oxygen photoreduction, reactive oxygen species production and scavenging in two diatom species”. In: *Journal of Phycology* 46.6, pp. 1206–1217. ISSN: 00223646. DOI: 10.1111/j.1529-8817.2010.00919.x.

Zenner, Christian et al. (Jan. 2025). “Measurement of Bacterial Headspaces by FT-IR Spectroscopy Reveals Distinct Volatile Organic Compound Signatures”. In: *Analytical Chemistry* 97.1, pp. 106–113. ISSN: 15206882. DOI: 10.1021/acs.analchem.4c02899.

Zuo, Zhaojiang et al. (Jan. 2015). “Reactive oxygen species contribute to the release of volatile organic compounds from Chlamydomonas reinhardtii during programmed cell death”. In: *Phycological Research* 63.1, pp. 37–42. ISSN: 14401835. DOI: 10.1111/pre.12071.

Appendix A

IR Spectrum Simulation

An AI-assisted Python script was developed to determine the theoretical detection limits of target gases within the 10 cm pathlength gas cell. This framework simulates molecular absorption spectra under realistic physical conditions. The resulting profiles provide a standardized baseline for direct comparison against empirical experimental data.

A.1. High-Fidelity FT-IR Spectrum Modelling

A.1.1. High-Fidelity FT-IR Spectrum Modelling and MDC Calculation

To establish the theoretical sensitivity boundaries and quantify the Minimum Detectable Concentrations (MDC) of the experimental platform, a high-fidelity forward-modeling spectroscopy engine was developed. The simulation framework evaluates gas-phase molecular absorption profiles from quantum first-principles over a continuous wavenumber grid spanning $500 \leq \nu \leq 4000$ cm^{-1} with a step size of $\Delta\nu_{\text{grid}} = 0.01$ cm^{-1}. For low-molecular-weight permanent gases and linear or symmetric top rotors (CO_2, H_2O, CH_4, CO, N_2O, NH_3, SO_2, HCl, NO), absolute absorption cross-sections (σ, cm^2/molecule) are calculated line-by-line using transition parameters extracted from the HITRAN database (Gordon et al. 2026) via the HITRAN Application Programming Interface (HAPI). The framework models the total continuous cross-section by positioning a standardized Voigt profile $V(\nu)$ at each discrete transition line i possessing line intensity S_i and center frequency $\nu_{0,i}$:

$$\sigma(\nu) = \sum_i S_i \cdot V(\nu; \nu_{0,i}, \sigma_{D,i}, \gamma_{L,i}) \tag{1}$$

The profile accounts for dual thermodynamic broadening regimes via complex error function evaluations. Thermal velocity distributions dictate the Gaussian Doppler half-width at half-maximum (HWHM$_D$), which is structurally parameterized by temperature (T) and molecular mass (M in g/mol):

$$\text{HWHM}_D = \nu_{0,i} \cdot 7.162 \times 10^{-7} \sqrt{\frac{T}{M}} \quad \Longrightarrow \quad \sigma_{D,i} = \frac{\text{HWHM}_D}{2\sqrt{2\ln(2)}} \tag{2}$$

Simultaneously, intermolecular collisions disrupt excited state lifetimes, generating a Lorentzian profile component governed by the atmospheric pressure (P_{atm}) and the air-broadening coefficient γ_{air} extracted from the database:

$$\gamma_{L,i} = \gamma_{\text{air},i} \cdot P_{\text{atm}} \tag{3}$$

For structurally heavy volatile organic compounds (VOCs) exhibiting dense, un-resolvable rotational manifolds (e.g., ethanol, dimethyl sulfide), line-by-line computations are bypassed in favor of empirical vapour-phase spectra acquired from the National Institute of Standards and Technology (NIST) WebBook database. These empirical shapes are converted to base-e absorbance and scaled by literature-established effective cross-sections (σ_{eff}). To correct for pressure differentials between low-pressure NIST recording conditions (P_{ref}) and the experimental cell environment (P_{meas}), additional collision broadening is manually induced via array convolution with a normalized discrete Lorentzian kernel matching the differential pressure width $\Delta\gamma_L = \gamma_{\text{air}} \cdot (P_{\text{meas}} - P_{\text{ref}})$:

$$L(x) = \frac{\Delta\gamma_L/\pi}{x^2 + \Delta\gamma_L^2} \tag{4}$$

Following the derivation of physically accurate cross-sections, the signals must be mathematically degraded to match the optical constraints of the physical apparatus. The raw cross-section grid is convolved with an Instrumental Line Shape (ILS) kernel to simulate the finite mirror travel truncation limits ($\text{FWHM}_{\text{ILS}} = 0.5$ cm^{-1}) of the physical Michelson interferometer (Griffith et al. 2012). The ILS is approximated as a localized Gaussian filter, where the pixel-space standard deviation (σ_{pixels}) is evaluated relative to the discrete grid interval:

$$\sigma_{\text{pixels}} = \frac{\text{FWHM}_{\text{ILS}}}{2\sqrt{2\ln(2)} \cdot \Delta\nu_{\text{grid}}} \tag{5}$$

To simulate macroscopic Absorbance (A) in analytical units (AU), the state-variable density of the gas must be parametrized. Assuming ideal gas behaviour ($PV = nRT$) holds true for trace components inside the cell, the target gas concentration expressed in parts-per-million (ppm) is translated to an absolute molecular number density (n, molecules/cm^3) by evaluating partial pressures in Pascals relative to Boltzmann's constant (k_B) and the experimental temperature ($T_{\text{meas}} = 296.0$ K):

$$P_{\text{pa}} = (\text{ppm} \times 10^{-6}) \times P_{\text{total\_atm}} \times 101,325 \tag{6}$$

$$n = \left(\frac{P_{\text{pa}}}{k_B \cdot T_{\text{meas}}} \right) \times 10^{-6} \tag{7}$$

Applying the Beer-Lambert law over the fixed physical length of the transmission gas cell ($L_{\text{path}} = 10.0$ cm), the modelled frequency-dependent absorbance is expressed as:

$$A(\nu) = \sigma_{\text{ILS}}(\nu) \cdot n \cdot L_{\text{path}} \tag{8}$$

The forward-modelling engine concludes by conducting an analytical assessment of detection limits across all library species. The absolute peak attenuation factor (f_{ILS}) resulting from slit blurring is resolved by tracking the ratio of maximum intensities, $f_{\text{ILS}} = \max(\sigma_{\text{ILS}}) / \max(\sigma_{\text{raw}})$, exposing the mathematical "crushing" of narrow lines under low-resolution conditions. Finally, the absolute Minimum Detectable Concentration (MDC_{ppm}) is derived by anchoring the peak instrument cross-section directly to the physical noise floor of the infrared detector ($\text{Noise}_{\text{AU}} = 0.001$ AU):

$$\text{MDC}_{\text{ppm}} = \frac{\text{Noise}_{\text{AU}} \cdot k_B \cdot T_{\text{meas}} \cdot 10^6}{\max(\sigma_{\text{ILS}}) \cdot P_{\text{total\_pa}} \cdot L_{\text{path}} \cdot 10^{-6}} \tag{9}$$

By resolving the specific concentration required to generate a baseline-corrected signal that perfectly breaks through this electronic white noise wall, the simulation architecture maps quantum transition probabilities and macro-environmental hardware constraints directly to objective, research-grade detection limits.

Table 4: Calculated Peak Cross-Sections, Instrumental Attenuation Factors, and Minimum Detectable Concentrations (MDC) Across Target Gas Species

Gas Species	Data Source	Peak σ_{raw} (cm^2/molecule)	Peak σ_{ILS} (cm^2/molecule)	ILS Factor (f_{ILS})	MDC (ppm)
CO_2	HITRAN	1.5246×10^{-17}	5.3512×10^{-18}	0.3510	0.7537
H_2O	HITRAN	1.2025×10^{-18}	4.5665×10^{-19}	0.3798	8.8324
Methane	HITRAN	2.2539×10^{-18}	9.8549×10^{-19}	0.4372	4.0927
Ethanol	NIST	1.9998×10^{-19}	1.9961×10^{-19}	0.9981	20.2054
DMS	NIST	1.4997×10^{-19}	1.4963×10^{-19}	0.9977	26.9554
CO	HITRAN	2.3037×10^{-18}	6.9178×10^{-19}	0.3003	5.8303
H_2S	HITRAN	1.0812×10^{-20}	5.3436×10^{-21}	0.4942	754.7925
N_2O	HITRAN	4.2685×10^{-18}	1.6789×10^{-18}	0.3933	2.4024
NO	HITRAN	7.0371×10^{-19}	2.2069×10^{-19}	0.3136	18.2758
SO_2	HITRAN	1.0520×10^{-18}	9.4567×10^{-19}	0.8989	4.2650
Ethyl acetate	NIST	2.9996×10^{-19}	2.9948×10^{-19}	0.9984	13.4677
Acetaldehyde	NIST	2.0000×10^{-19}	2.0000×10^{-19}	1.0000	20.1664
Ethyl propanoate	NIST	3.4998×10^{-19}	3.4936×10^{-19}	0.9982	11.5446
Propanal	NIST	2.5000×10^{-19}	2.5000×10^{-19}	1.0000	16.1331
Ethane	HITRAN	1.5866×10^{-18}	6.8437×10^{-19}	0.4313	5.8934
Ethylene	HITRAN	1.6986×10^{-18}	1.1623×10^{-18}	0.6843	3.4700

A.1.2. Simulated Spectrum

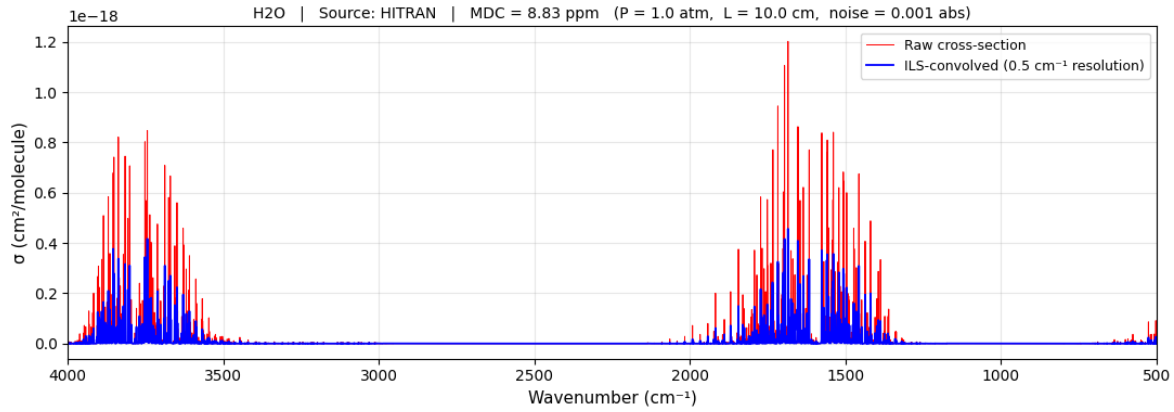

Figure 11: Simulated water vapour spectrum

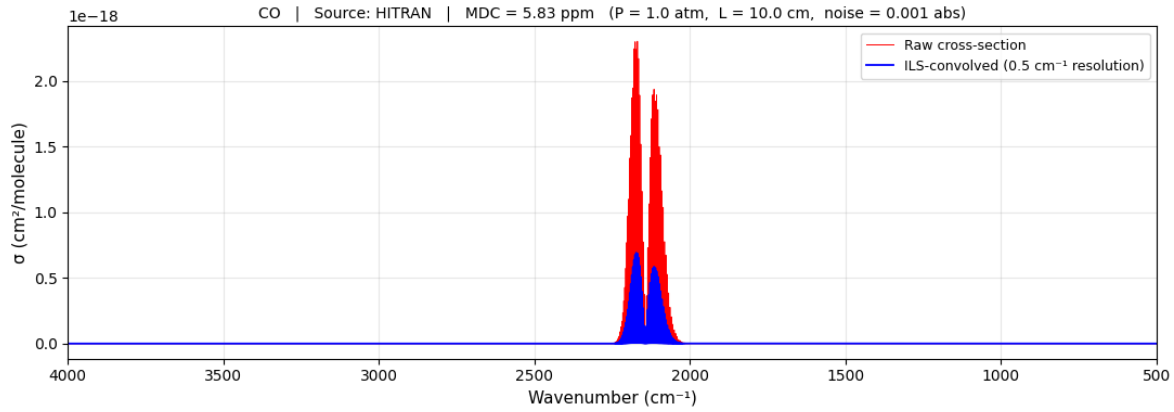

Figure 12: Simulate carbon-monoxide spectrum

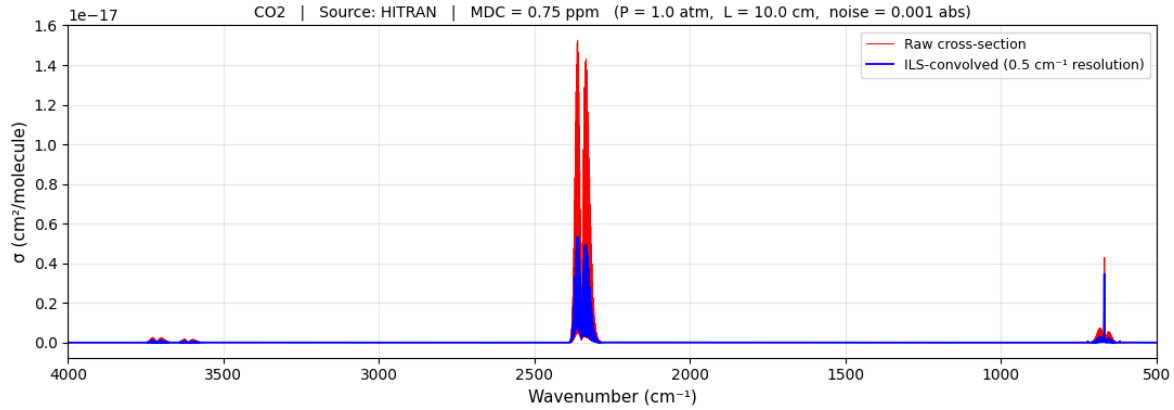

Figure 13: Simulated carbon-dioxide spectrum

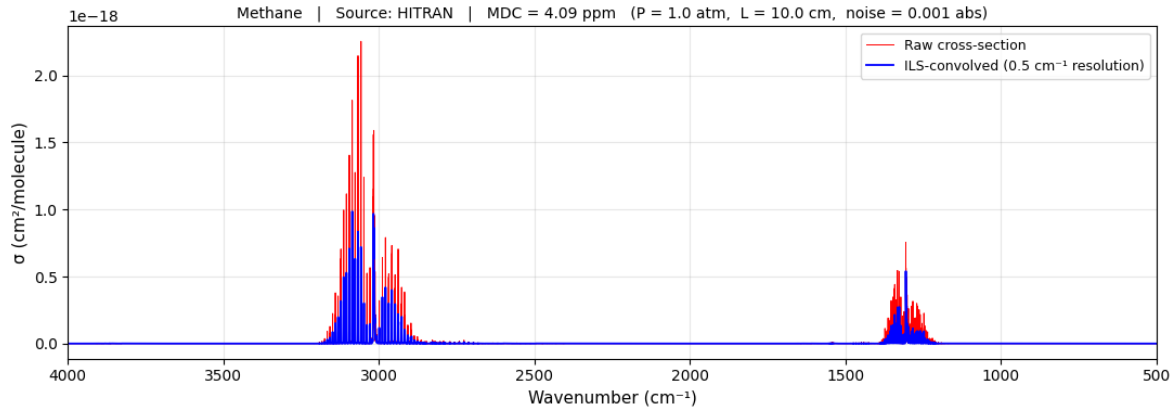

Figure 14: Simulated methane spectrum

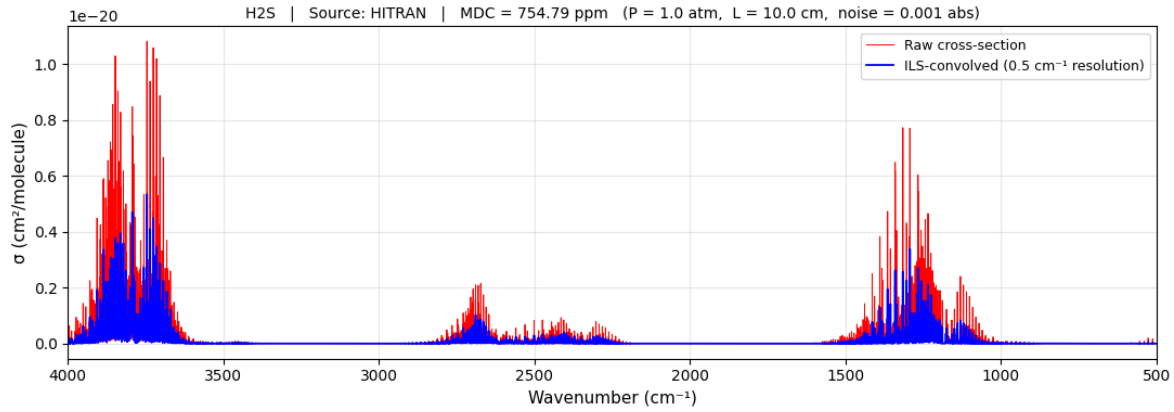

Figure 15: Simulated hydrogen-sulfide

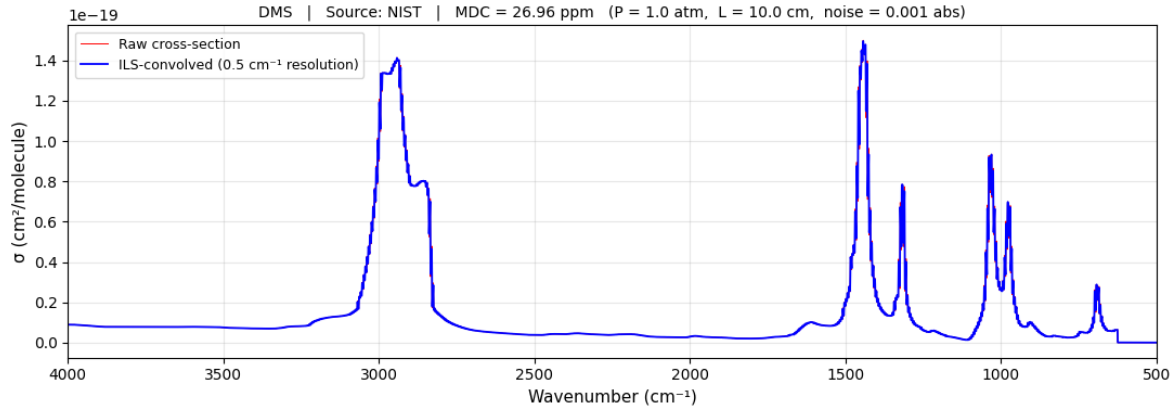

Figure 16: Simulated dimethyl-sulphide

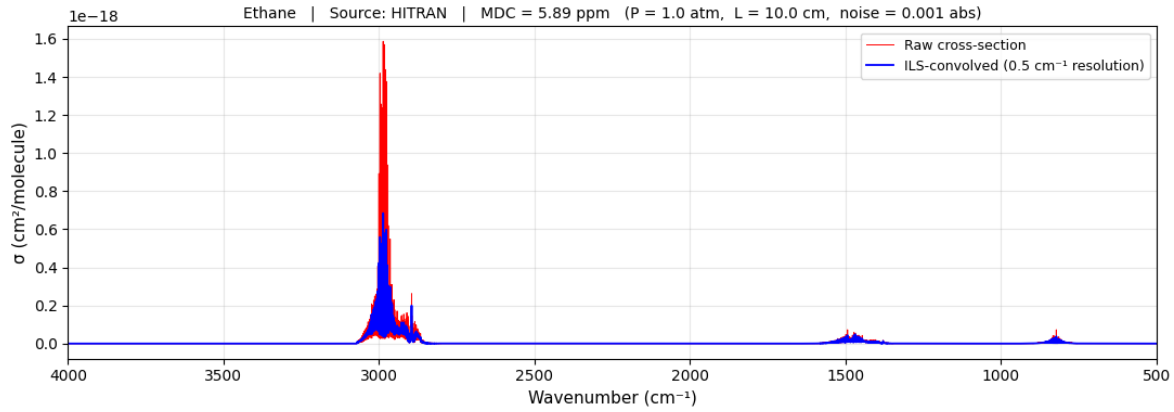

Figure 17: Simulated ethane spectrum

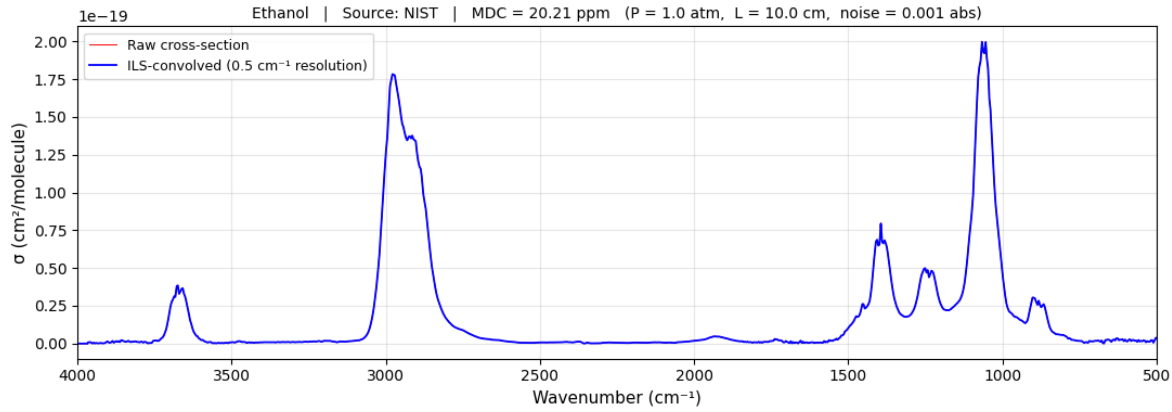

Figure 18: Simulated ethanol spectrum

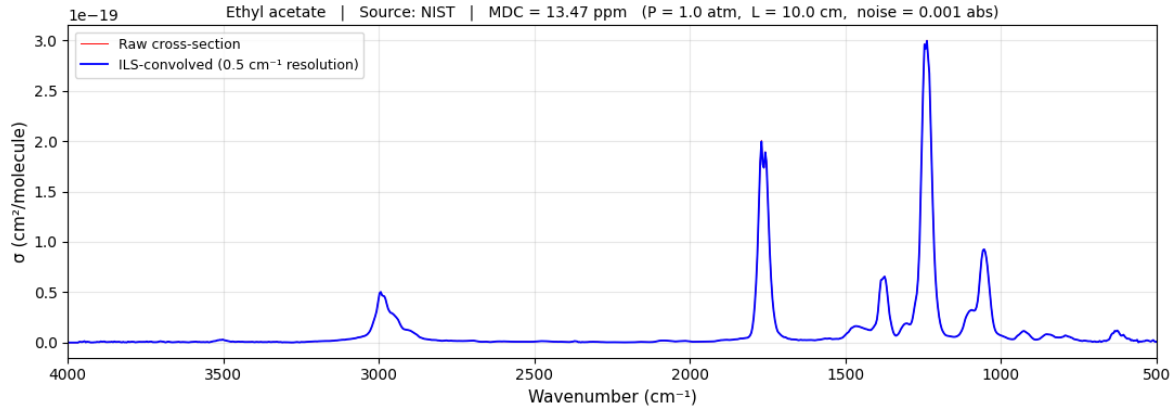

Figure 19: Simulated ethyl-acetate spectrum

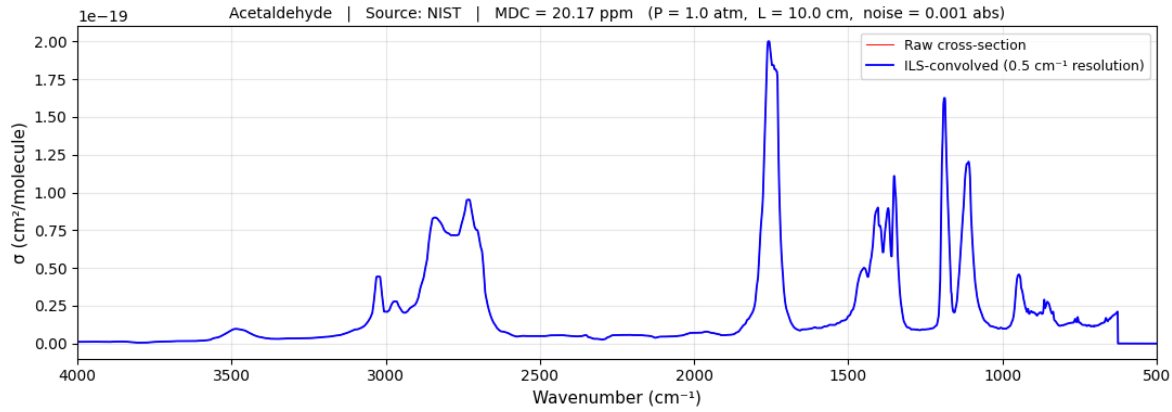

Figure 20: Simulated acetaldehyde spectrum

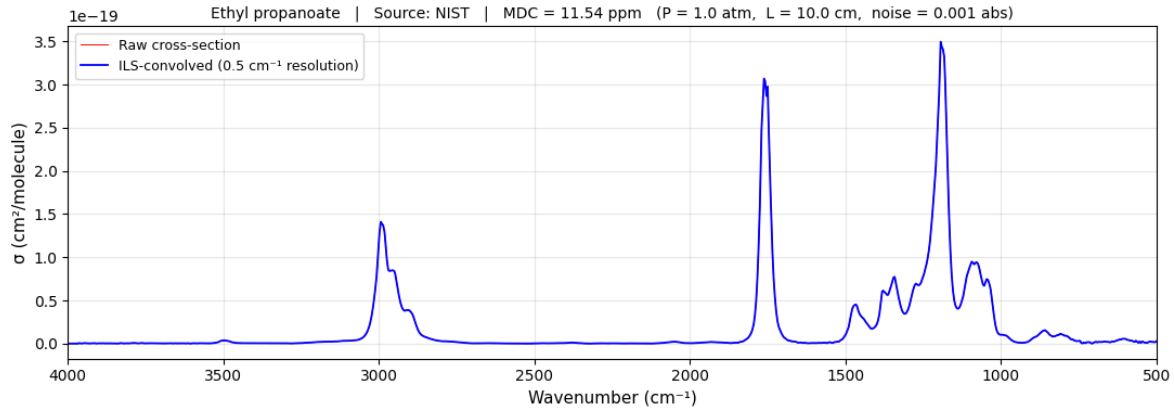

Figure 21: Simulated ethyl-propanoate spectrum

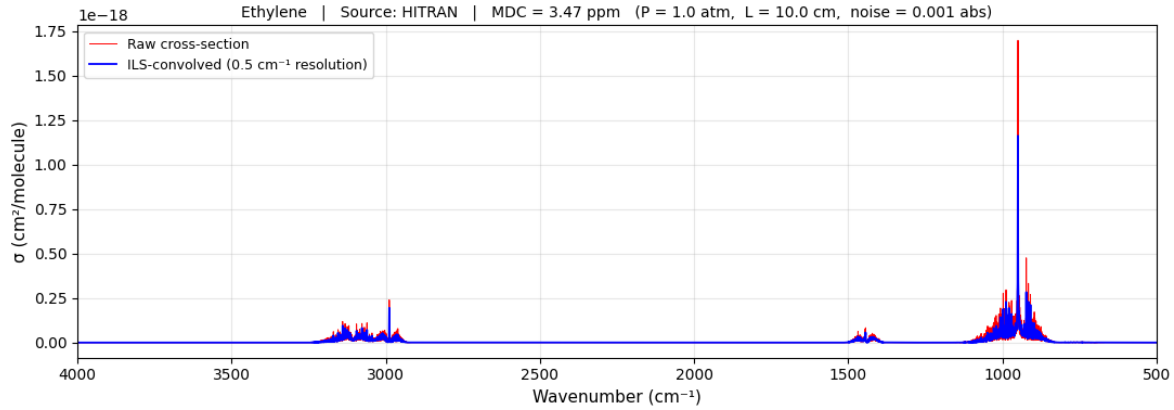

Figure 22: Simulated ethylene spectrum

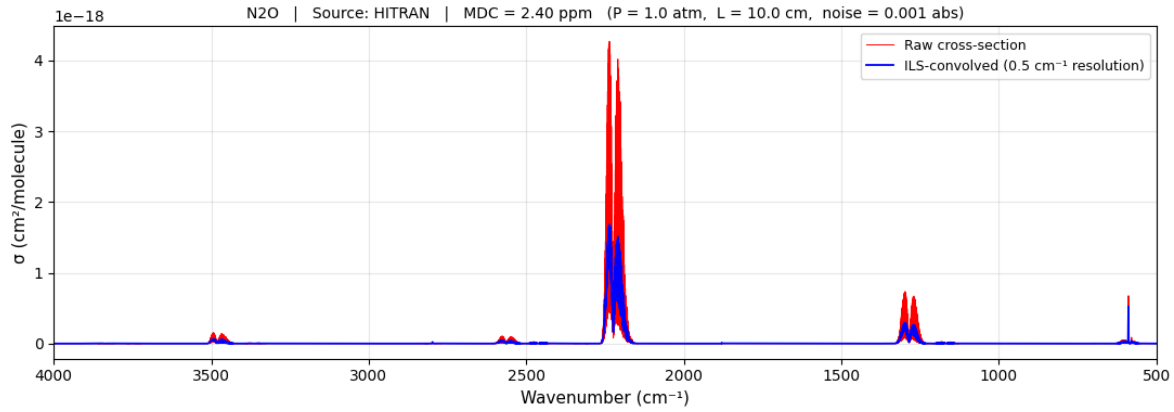

Figure 23: Simulated nitrous-oxide spectrum

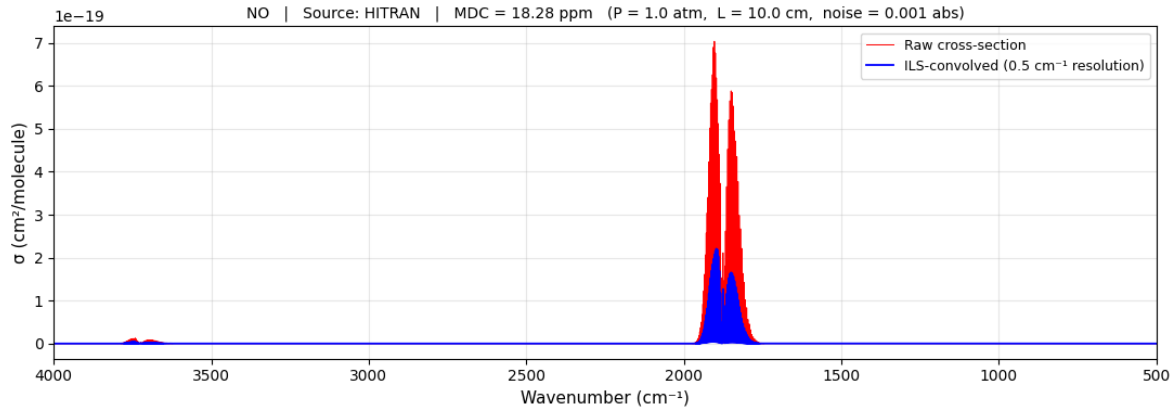

Figure 24: Simulated nitric-oxide spectrum

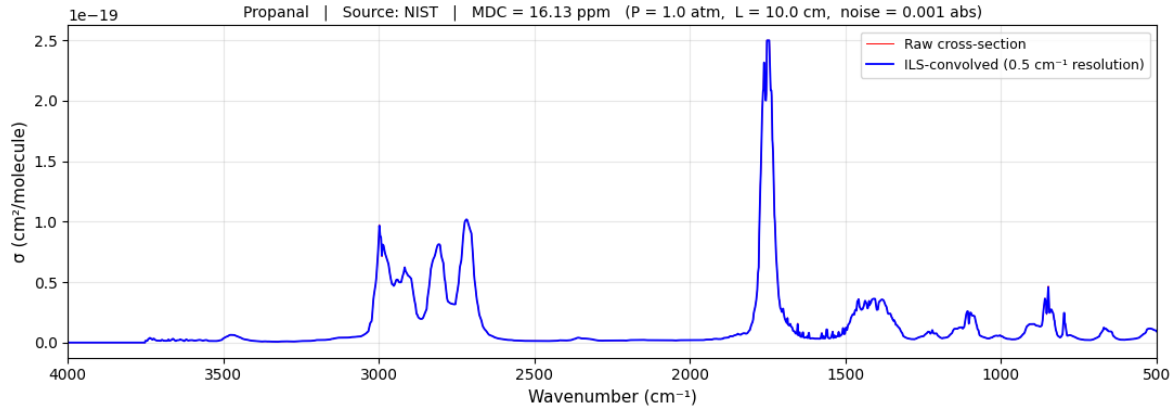

Figure 25: Simulated propanal spectrum

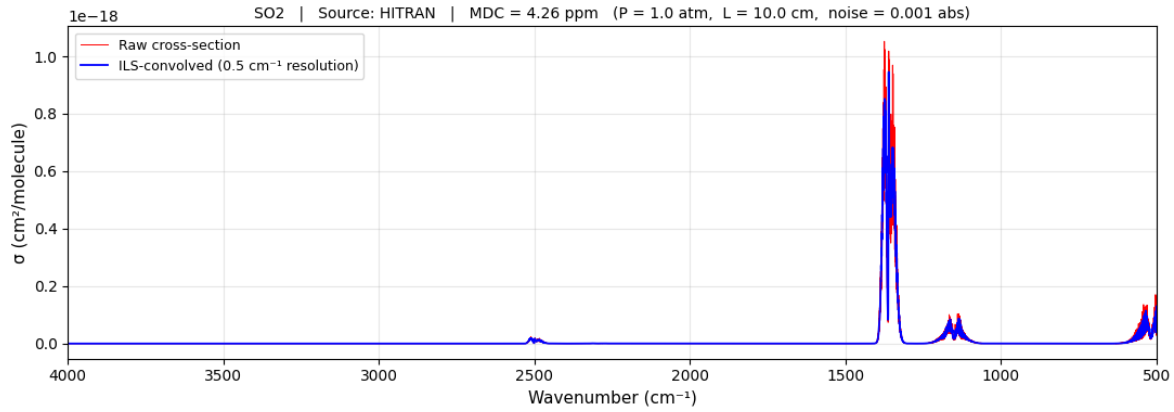

Figure 26: Simulated sulphur-dioxide spectrum

Appendix B

Framework for Data Analysis

This appendix provides a comprehensive technical overview of the data analysis pipeline developed to process, validate, and quantify the multi-phase spectral datasets acquired across this study. To reliably isolate and quantify trace biogenic volatile organic compounds (VOCs) and permanent gases within highly complex spectral matrices, a structured, automated data processing architecture was developed using a custom Python framework and AI assistance. The algorithmic workflows is adapted from the Bruker OPUS software environment.

B.0.1. Baseline Correction Framework

Gas-phase infrared spectra frequently suffer from shifting baselines caused by light scattering, window etaloning, or ambient temperature drift. To isolate the true molecular absorption signatures from these background variations, our pipeline employs a two-tier correction strategy: a global automated lower-envelope smoothing technique supplemented by a localized polynomial fit when tracking specific features over time .

Global Baseline Estimation via Asymmetric Least Squares

For automated multi-gas analysis, the global baseline envelope ($\mathbf{z}$) is isolated from the raw absorbance spectrum ($\mathbf{y}$) using the Asymmetric Reweighted Penalized Least Squares (ARPLS) algorithm. The algorithm balances two competing goals: staying close to the experimental data points while maintaining a smooth baseline curve. Mathematically, it minimizes a penalized cost function:

$$S = \sum_{i=1}^{N} w_i (y_i - z_i)^2 + \lambda \sum_{i=1}^{N-2} (\Delta^2 z_i)^2 \tag{10}$$

where Δ^2 represents the discrete second-difference operator ($\Delta^2 z_i = z_i - 2z_{i-1} + z_{i-2}$) used to measure baseline roughness, and $\lambda = 10^6$ is a user-defined stiffness parameter that controls how flexible the baseline is allowed to be . To prevent the baseline from being pulled upward into actual absorption peaks, the weights (w_i) are updated iteratively based on whether a data point lies above or below the current baseline guess:

$$w_i = \begin{cases} 1 & \text{if } y_i < z_i \\ \exp\left(-\frac{(y_i - z_i)}{\sigma_{\text{noise}}}\right) & \text{if } y_i \geq z_i \end{cases} \tag{11}$$

By using this exponential decay scheduler, noise valleys and flat background regions retain full weight ($w_i = 1$), whereas data points within absorption peaks are heavily discounted, forcing the baseline to pass cleanly underneath the molecular signatures .

Bayesian MCMC and Curve-Fitting Alternatives

For targeted studies of single absorption features, the codebase provides alternate baseline techniques using classical curve-fitting or Markov Chain Monte Carlo (MCMC) sampling. The algorithm isolates flat regions of the baseline flanking the peak—referred to as anchor regions—and fits a first-order polynomial baseline ($f(x) = ax + b$) across these points. Under the MCMC framework, rather than computing a single deterministic line, the system samples thousands of plausible baselines by evaluating a Gaussian log-likelihood function ($\ln L$) across the anchors:

$$\ln L(a, b) = -0.5 \sum_{i \in \text{anchors}} \left[\frac{(y_i - (ax_i + b))^2}{\sigma^2_{\text{noise}}} + \ln(\sigma^2_{\text{noise}}) \right] \tag{12}$$

This generates a statistical distribution of possible baselines, allowing the code to construct a visual uncertainty gradient and directly propagate baseline selection errors into the final integrated peak areas
.

B.0.2. Spectral Area Integration and Error Propagation

Once the baseline is subtracted, the total area under an absorption feature must be integrated. Because detector noise and grid precision introduce uncertainty, the code implements rigorous analytical error propagation alongside its integration routines.

Trapezoidal Integration with Quadrature Uncertainty Tracking

For continuous kinetics tracking, the baseline-corrected absorbance spectrum (y) is integrated across its discrete wavenumber axis (ν) using the trapezoidal rule. To guarantee that noise levels are correctly accounted for, the variance of the integration step is analytically propagated through each individual slice. For a single trapezoidal segment between index i and $i+1$, the area element (A_i) and its associated variance ($\sigma^2_{A_i}$) are defined as:

$$A_i = \left(\frac{y_i + y_{i+1}}{2}\right) \cdot (\nu_{i+1} - \nu_i) = \bar{y}_i \cdot \Delta\nu_i \tag{13}$$

$$\sigma^2_{A_i} = \left(\frac{\partial A_i}{\partial \bar{y}_i}\right)^2 \sigma^2_{\bar{y}_i} + \left(\frac{\partial A_i}{\partial \Delta\nu_i}\right)^2 \sigma^2_{\Delta\nu_i} \tag{14}$$

Taking the partial derivatives with respect to the mean absorbance ($\bar{y}_i$) and the wavenumber step size ($\Delta\nu_i$), and assuming independent errors (σ_y and σ_ν), yields the exact standard deviation formula used by the script:

$$\sigma_{A_i} = A_i \sqrt{\left(\frac{\sigma_y\sqrt{2}}{y_i + y_{i+1}}\right)^2 + \left(\frac{\sigma_\nu\sqrt{2}}{\Delta\nu_i}\right)^2} \tag{15}$$

The cumulative band area (A_{total}) and its total propagated standard error ($\sigma_{A_{\text{total}}}$) are then computed by summing the individual intervals in quadrature :

$$A_{\text{total}} = \sum_{i=1}^{N-1} A_i \quad \text{and} \quad \sigma_{A_{\text{total}}} = \sqrt{\sum_{i=1}^{N-1} \sigma^2_{A_i}} \tag{16}$$

Threshold-Gated Simpson's Rule

In the automated multi-gas comparison script, the pipeline defaults to Simpson's rule for parabolic alignment accuracy . To protect the calculation from accumulating baseline noise from uninformative flat regions, an intensity gate is applied. The code builds a binary mask that only activates when the corresponding reference database gas spectrum exceeds a designated fraction of its maximum intensity (typically set to 10%):

$$\text{Mask}(\nu) = \text{True} \quad \Longleftrightarrow \quad A_{\text{ref}}(\nu) \geq 0.10 \cdot \max[A_{\text{ref}}(\nu)] \tag{17}$$

This threshold gating restricts numerical integration to the exact physical envelope of the molecular vibration, shielding the integrated area metric from out-of-band noise.

B.0.3. Physical Derivation of Column Density and Concentration

To convert an abstract, integrated optical absorbance area ($AU \cdot \text{cm}^{-1}$) into a meaningful chemical concentration, the pipeline solves the fundamental equations governing the Beer-Lambert law. Absorbance is physically modeled as a linear function of the intrinsic quantum cross-section ($\sigma(\nu)$ in $\text{cm}^2/\text{molecule}$), the optical path length of the gas cell ($L_{\text{meas}} = 10.0$ cm), and the molecular number density (n in molecules/cm^3):

$$A(\nu) = \sigma(\nu) \cdot n \cdot L_{\text{meas}} \tag{18}$$

Integrating this physical relationship over a given absorption band provides the absolute column density (N_{col} in molecules/cm^2), representing the total population of target gas molecules intersecting a unit cross-sectional area along the beam path:

$$N_{\text{col}} = n \cdot L_{\text{meas}} = \frac{\int_{\text{band}} A_{\text{meas}}(\nu) d\nu}{\int_{\text{band}} \sigma(\nu) d\nu} \tag{19}$$

Because reference gas databases are recorded at specific standard temperatures (T_{ref}), the code applies the Ideal Gas Law ($PV = NRT$) to execute a state-variable density expansion, correcting for differences in molecular gas volume between database conditions and active laboratory temperatures (T_{meas}):

$$N_{\text{col}} = \left(\frac{A_{\text{meas, int}}}{A_{\text{ref, int}}} \right) \cdot L_{\text{ref}} \cdot \left(\frac{T_{\text{meas}}}{T_{\text{ref}}} \right) \cdot n_{\text{total\_STP}} \tag{20}$$

where $n_{\text{total\_STP}}$ is the total number density of ideal gas particles available under current pressure conditions, computed via Boltzmann's constant (k_B) :

$$n_{\text{total\_STP}} \left[\frac{\text{molecules}}{\text{cm}^3} \right] = \left(\frac{P_{\text{meas\_pa}}}{k_B \cdot T_{\text{meas\_K}}} \right) \times 10^{-6} \tag{21}$$

When analyzing complex matrices where multiple gases share overlapping absorption bands, calculating concentrations using independent window integrals causes severe double-counting errors . The pipeline resolves this cross-sensitivity by compiling all validated reference cross-sections into a single design matrix ($\mathbf{R}$) and solving for all species simultaneously using Classical Least Squares with a Non-Negative constraint (CLS-NNLS) :

$$\min_{\mathbf{x} \geq \mathbf{0}} \|\mathbf{W}^{1/2}(\mathbf{R}\mathbf{x} - \mathbf{m})\|_2^2 \tag{22}$$

The inclusion of a diagonal weight matrix ($W_{ii} = 10^{-2m_i}$) accounts for the heteroscedastic nature of photodetector noise in absorbance space . This forces the linear algebra solver to trust clear, highly sensitive transmission windows while discounting heavily absorbing, saturated peak tips ($A > 1.0$ AU), producing stable, physically bounded mole fractions ($\mathbf{x}$) .

B.0.4. Gas Identification

Before calculating concentrations, the pipeline confirms whether a specific gas is actually present in the gas cell . If a gas is absent, its reference column must be excluded from the simultaneous matrix solver; otherwise, the linear algebra routine will fit unmodeled background noise to false chemical parameters .

To evaluate peak identity without allowing background shifts to bias the outcome, the code performs windowed vector cosine similarity matching . The spectrum is partitioned into narrow, isolated target windows (Ω) that capture only the characteristic quantum transitions of the analyte . To prevent any residual, uncorrected baseline offsets from artificially inflating the vector alignment score, an independent local minimum subtraction is executed within each active sub-window for both the measured spectrum ($\mathbf{s}$) and the reference library array ($\mathbf{r}$) :

$$s'_\omega = s_\omega - \min_{\omega \in \Omega}(s_\omega) \quad \text{and} \quad r'_\omega = r_\omega - \min_{\omega \in \Omega}(r_\omega) \tag{23}$$

These baseline-isolated intervals are concatenated into unified morphological descriptors ($\mathbf{s}'$ and $\mathbf{r}'$) . The final confidence index is determined by calculating the normalized inner product between the vectors :

$$\text{Similarity Score} = \cos(\theta) = \frac{\mathbf{s}' \cdot \mathbf{r}'}{\|\mathbf{s}'\|_2 \|\mathbf{r}'\|_2} = \frac{\sum_{\omega \in \Omega} s'_\omega r'_\omega}{\sqrt{\sum_{\omega \in \Omega} (s'_\omega)^2} \sqrt{\sum_{\omega \in \Omega} (r'_\omega)^2}} \tag{24}$$

Because local centering ensures that a flat, elevated background evaluates to a null vector direction, a high similarity score can only be achieved if the sharp slope changes of the experimental peaks mirror the underlying quantum morphology of the reference standard . Species scoring below a definitive validation threshold (Score < 0.10) are automatically blocked from the optimization system .

Part 3: The Closing

9

Supplementary Results

Attenuated Total Reflection (ATR) FT-IR is used for liquid and solid samples unsuitable for transmission FT-IR, enabling analysis without extensive sample preparation by measuring the sample's infra-red spectrum in contact with an ATR crystal (Tiquia-Arashiro et al. 2023). The sample culture was autoclaved and subsequently measured in a PerkinElmer Spectrum 100 FT-IR Spectrometer, utilising a diamond crystal. The measurement was taken at a 4 cm^{-1} resolution, and eight scans were performed per sample. The sterile growth medium was taken as the optical background to isolate the small changes and variations caused by the biomass; because the medium is largely water, which strongly absorbs infra-red radiation, failing to subtract it makes it difficult to identify other trace components present.

9.1. Data Processing Methodology

A Savitzky-Golay filter (window length = 15, polynomial order = 2) was applied to the raw data before plotting. These specific parameters were chosen with inspiration from the works of Zimmermann and Kohler (Zimmermann and Kohler 2013) and as a trade-off determined after performing a residual analysis. While this approach indicated some minor signal attenuation near 2350 cm^{-1}, this effect was deemed acceptable as this region corresponds exclusively to atmospheric CO_2 fluctuations.

When absorbance is measured with the growth medium as the background, a negative absorbance essentially means that light passes through at wavelengths that were previously blocked by components in the medium, indicating that those specific compounds are being consumed by the microorganisms. Conversely, regions of positive absorbance mean that new compounds are present which were not previously found in the background medium. Finally, a rubber-band baseline correction was applied to resolve minor instrumental drift.

9.2. Experimental Results and Discussion: FT-IR-ATR

9.2.1. Yeast in N_2 Environment

While the sterile growth medium served as the optical background, the pre-stressed, healthy yeast culture under standard laboratory conditions was utilised as the reference. This approach allows for the direct identification of compounds consumed or generated by the microorganisms relative to their normal physiological state.

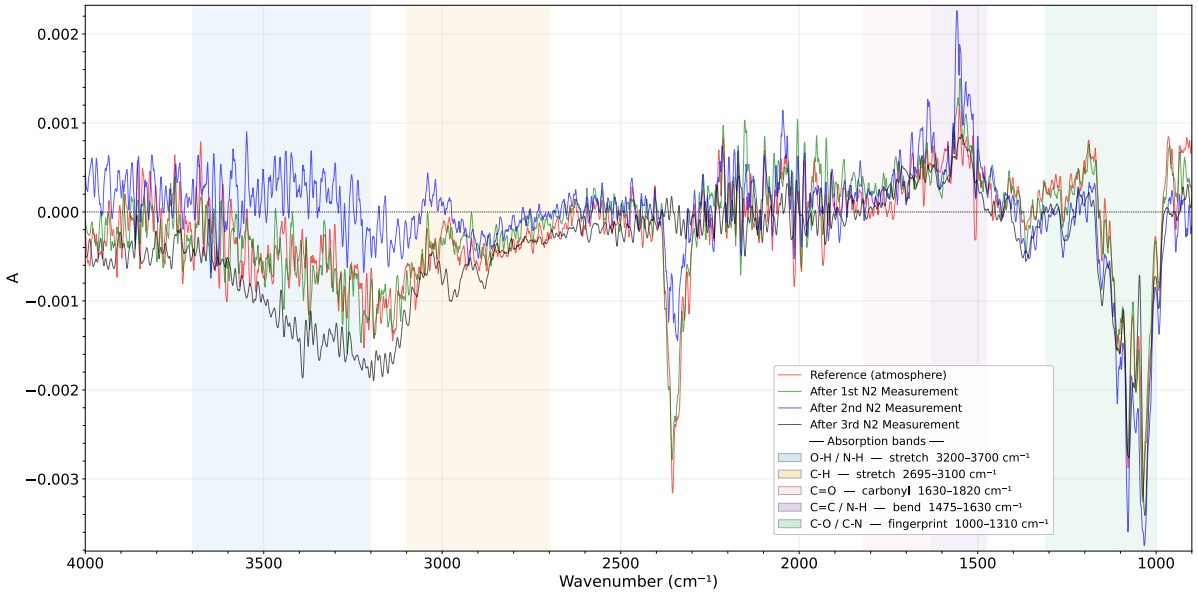

Figure 9.1: Comparison of yeast culture after exposure to N_2 environment using FT-IR-ATR

As seen in Figure 9.1, the most prominent feature is a sharp negative absorption band that steadily deepens between 1100 cm^{-1} and 1000 cm^{-1}, reaching its lowest point by the final measurement. Concurrently, an immediate negative dip was observed exactly at 2350 cm^{-1}. In contrast to these negative markers, distinct positive peaks were observed pushing upward over time at 1650 cm^{-1} and 1540 cm^{-1}. Notably, a corresponding gas-phase ethanol signal near 2957 cm^{-1} was not detected in the spectrum.

The negative region between 1100 cm^{-1} and 1000 cm^{-1} corresponds to the stretching of C – O and C – C bonds within carbohydrate ring structures. Its downward direction provides clear, direct evidence of internal sugar depletion, demonstrating that the yeast were rapidly burning through their own storage reserves to survive. Furthermore, because the ATR crystal selectively probes the liquid boundary layer, the negative shift at 2350 cm^{-1} tracks the loss of dissolved carbon dioxide in the medium. This indicates that the initial nitrogen flush mechanically swept away the existing carbon equilibrium in the fluid, creating a massive pressure imbalance compared to the initial control.

The positive peaks pushing upward at 1650 cm^{-1} and 1540 cm^{-1} align with the Amide I (C = O stretching) and Amide II (N – H bending) protein bands. Their steady upward growth points to a physical settling of the biomass, capturing the dense yeast cells slowly gathering directly on the crystal surface as cell motility and active metabolic mixing slowed down under severe anoxic stress.

When these liquid-phase adjustments are compared directly to the gas-phase headspace data, they reveal a tightly connected mass transfer across the phase boundary. The clearest correlation occurs within the carbon dioxide stretching window at 2350 cm^{-1}. The deepening negative valley in the liquid broth perfectly mirrors the sudden vertical growth of the gaseous CO_2 double-peak in the headspace, which climbs to around 0.50 AU (as detailed in previous gas-phase results) by the third measurement. From a physical chemistry standpoint, this behaviour follows Henry's Law: stripping the existing atmosphere with nitrogen created a vacuum that forced the saturated fluid to rapidly desorb its dissolved inorganic carbon to restore thermodynamic balance. The drop in internal sugars seen in the liquid phase acts as the metabolic engine driving this outgassing, confirming that the yeast actively relied on emergency fermentation to handle the high maintenance costs of surviving total anoxia. Interestingly, the lack of a gas-phase ethanol signal near 2957 cm^{-1} suggests that the trace volatile organic outputs remained dissolved or were re-consumed within the liquid slurry, keeping them completely below the gas-phase detection limits of the system.

9.2.2. Yeast in Oxidative Environment

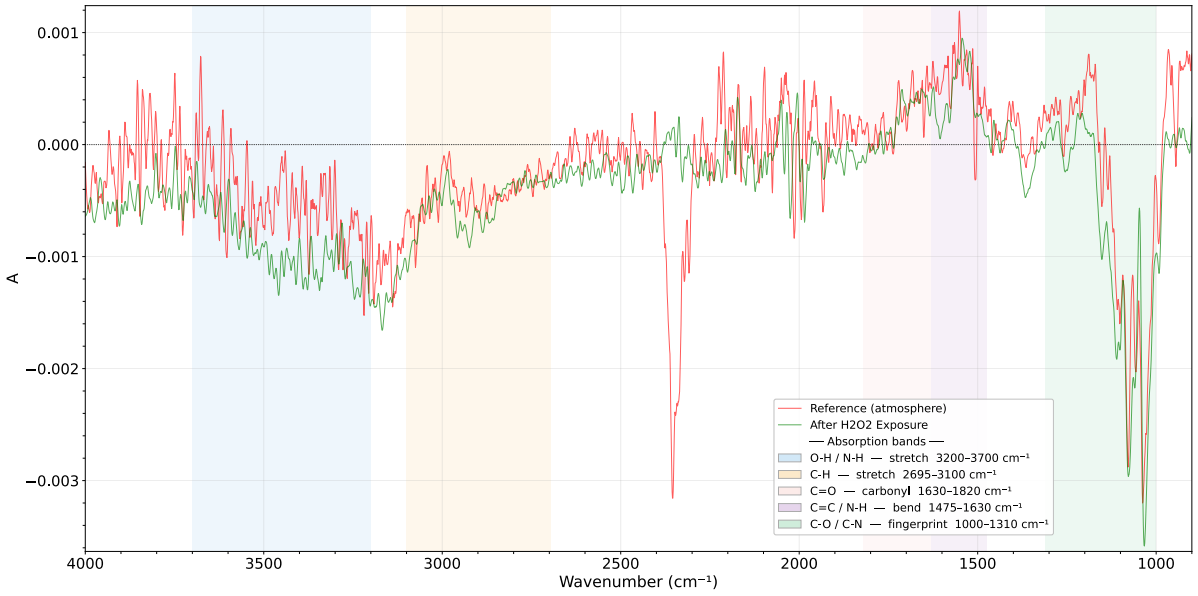

Figure 9.2: Comparison of yeast culture after long exposure to H_2O_2 environment using FT-IR-ATR

The tracking of the liquid yeast matrix before and after exposure to a lethal dose of hydrogen peroxide reveals distinct spectral alterations. In Figure 9.2, when evaluating the "After H_2O_2 exposure" spectrum (green line) against the pre-stressed reference control (red line), the distinct negative absorption peak in the carbohydrate fingerprint region (1100–1000 cm^{-1}) loses its clean, defined structures. Simultaneously, a highly significant shift occurs at 2350 cm^{-1}, where the prominent negative dissolved CO_2 peak present in the control spectrum completely flattens out and disappears following peroxide exposure. Furthermore, there is a distinct flattening of the Amide protein regions around 1650 cm^{-1} and 1540 cm^{-1}.

These observations indicate acute oxidative degradation and substantial metabolic collapse. The loss of structure in the pyranose ring (a six-membered cyclic chemical structure primarily found in carbohydrates) vibration band (1100–1000 cm^{-1}) reflects the chemical oxidation and broad disintegration of the yeast cell walls and storage carbohydrate pools under severe peroxide attack. The disappearance of the negative absorbance at 2350 cm^{-1} indicates that the liquid matrix is no longer showing a deficit of carbon dioxide relative to the starting baseline, suggesting a substantial release of molecular carbon directly into the solution. Additionally, the flattening of the Amide protein regions confirms widespread cellular lysis and protein denaturation, demonstrating that the exogenous peroxide dose caused catastrophic damage to the structural integrity of the cell suspension.

When these liquid-phase alterations are correlated with the time-resolved headspace gas profiles, they reveal a profound narrative of metabolic shock, hyper-acceleration, and eventual biological flatlining. The disappearance of the negative dissolved CO_2 peak corresponds directly to massive gas-phase kinetic shifts. During the initial hours, frontline localised enzymes (like catalase) work to buffer the incoming chemical attack. However, around the third hour, a dramatic metabolic "last stand" typically occurs, driving a massive headspace gas spike. This hyper-respiration event represents the cell population rapidly accelerating its internal mitochondrial respiration to generate the emergency ATP and NADPH required to fuel desperate antioxidant defence mechanisms.

This hyper-respiration phase perfectly explains the liquid-phase data: the rapid intracellular burning of energy reserves drives the severe degradation of the carbohydrate ring structures, while the resulting burst of metabolic waste gas fills the liquid boundary layer, flattening out the initial dissolved carbon deficit. Having entirely exhausted their internal energy reserves, the cells subsequently undergo widespread plasmolysis, lose membrane osmoregulatory control, and experience complete cellular lysis. The eventual flatlining of the headspace CO_2 signal to baseline levels is the direct atmospheric

signature of a completely dead, metabolically arrested culture, showing how a severe chemical shock effectively terminates the biological footprint of the ecosystem.

9.2.3. C. fusiformis in N_2 Environment

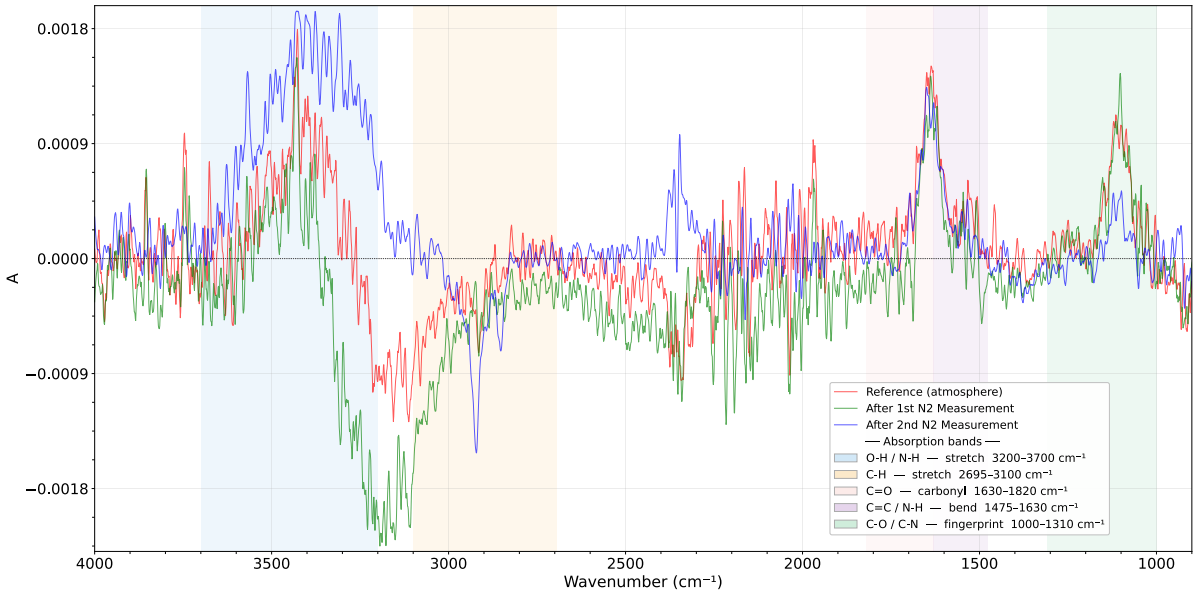

Figure 9.3: Comparison of *C. fusiformis* culture after exposure to N_2 environment using FT-IR-ATR

In Figure 9.3, the FT-IR-ATR liquid-phase profile of the *Cylindrotheca fusiformis* reveals a remarkably consistent structure. Evaluating the post-sparging intervals (blue and green lines) against the baseline control (red line), the absorption profiles in the fingerprint region between 1100 cm^{-1} and 1000 cm^{-1} remain highly stable and tightly clustered near the zero baseline. Similarly, the protein-associated Amide I and Amide II regions show no significant vertical accumulation or negative drops. The only notable dynamic feature is a minor fluctuation in the broad hydroxyl (O – H) region near 3000 cm^{-1} and a small baseline shift at 2900 cm^{-1}.

The spectral stability highlights a highly resilient biochemical matrix with minimal structural or metabolic disruption. The 1100–1000 cm^{-1} region typically monitors accessory pigments like fucoxanthin and structural cell-wall carbohydrates in diatoms; its stability indicates that the cells held up well against the nitrogen stress without undergoing structural decay, chlorosis, or major lysis. The lack of changes in the Amide regions confirms the absence of rapid cell sedimentation or catastrophic protein denaturation. The minor shifts near 3000 cm^{-1} and 2900 cm^{-1} point to minor, non-lethal adjustments in extracellular water binding properties or surface mucous layers as the fluid phase equilibrates with the dry nitrogen atmosphere.

Comparing the liquid-phase data directly with the headspace gas measurements helps explain how the micro-algae adjusted to the sudden nitrogen environment. Even with intensive nitrogen sparging, gas-phase analyses showed that CO_2 levels remained remarkably flat and stable. If the nitrogen environment had pushed the diatoms into severe stress or starvation, the cells would have been forced to quickly burn through internal energy stores, leading to widespread cellular degradation. However, the liquid ATR data shows that the structural biomass remained entirely intact. Because the growth medium contained filtered seawater, phosphate, nitrate, trace potassium, and vitamins, the small negative peak in the carbohydrate region cannot imply the cells were consuming external sugars. Instead, it indicates that the physical sparging slightly displaced the sugary extracellular polymeric substances (EPS) coating the outer cell walls, gently moving them away from the immediate surface of the ATR crystal.

This structural stability, combined with a steady headspace gas profile, indicates that *C. fusiformis* entered a well-regulated metabolic holding pattern. The anoxic conditions stripped away ambient oxygen,

which naturally slowed down the pathways that release CO_2 (mitochondrial respiration and photorespiration). Simultaneously, because the cells were not under destructive stress, carbon consumption within the Calvin cycle must have slowed down at a matching rate. Because these two opposing pathways slowed down in unison, the net concentration of carbon dioxide in the headspace stayed completely constant. Ultimately, linking the stable liquid matrix to the steady gas-phase profile shows that *C. fusiformis* can maintain its internal balance during sudden nitrogen stress without needing to desperately drain its internal energy reserves, although further experiments over an extended growth period will help definitively confirm this.

9.2.4. C. fusiformis in Oxidative Environment

Figure 9.4: Comparison of *C. fusiformis* culture after exposure to H_2O_2 environment using FT-IR-ATR

The FT-IR-ATR liquid-phase profile of the *C. fusiformis* culture, recorded after prolonged exposure to oxidative stress induced by a lethal dose of hydrogen peroxide (Figure 9.4), provides a stark chemical snapshot of cellular degradation. Comparing this end-point spectrum (green line) to the pre-stressed reference control (red line) reveals a deep negative absorption band dominating the spectrum from 3600 cm^{-1} down to 3000 cm^{-1}. Furthermore, the structural Amide I and Amide II protein bands (1650 cm^{-1} and 1540 cm^{-1}) show significant deformation and flattening compared to the sharp peaks in the reference spectrum. Finally, a notable positive peak emerges near 2900 cm^{-1}.

These massive spectral alterations point to ultimate structural destruction. The broad negative region from 3600–3000 cm^{-1} is characteristic of intense hydroxyl (O – H) and amine (N – H) stretching vibrations. Its extreme downward trajectory indicates the catastrophic loss of structural hydration and the complete breakdown of the hydrogen-bonded water networks surrounding the cells. This serves as the direct physical signature of severe cellular dehydration, prolonged plasmolysis, and the broad destruction of the cell's outer mucilage and membrane integrity caused by chemical burning. The deformation of the Amide bands directly indicates widespread protein denaturation and enzymatic collapse. The positive peak near 2900 cm^{-1}, an area associated with asymmetric C – H stretching in lipids, points to the physical rupture of the cellular lipid bilayers (the cell membranes). This rupture allowed internal lipid components to spill out and accumulate directly against the ATR sensing crystal as the biomass degraded.

When the structural destruction observed in the liquid phase is paired with the time-resolved headspace gas measurements, the resulting correlation illustrates a rapid and complete biological collapse. The gas-phase analysis captures a sharp, uninterrupted decline in CO_2 concentration from the exact moment the hydrogen peroxide was introduced, reflecting the immediate failure of both mitochondrial respiration and active photorespiration pathways.

Unlike the yeast culture, which exhibited a massive hyper-respiratory CO_2 spike in an active attempt to combat the peroxide attack, *C. fusiformis* demonstrates no such metabolic "last stand". Instead, the micro-algae succumbed immediately to the chemical shock. This initial atmospheric free-fall aligns perfectly with the extreme physical destruction confirmed by the liquid-phase analysis. The peroxide rapidly destroyed the cell membranes, causing the lipids to spill out at 2900 cm^{-1}. This damage, along with severe dehydration, completely shut down the cell's internal processes and respiration cycle instantaneously.

Interestingly, while a transient spike in headspace CO_2 may occasionally be recorded in such experiments before the signal flatlines, this late-stage gas spike cannot be attributed to active algal metabolism. Instead, it represents the passive chemical degradation of the necrotic biomass, where dissolved cellular carbon components slowly outgas into the closed atmosphere as the physical remnants of the cells decompose. Ultimately, synthesising the real-time atmospheric decline with the liquid-phase graveyard spectrum confirms that *C. fusiformis* possesses negligible resistance to severe oxidative stress, suffering immediate metabolic arrest followed by complete structural lysis.

10

Conclusion

This thesis sought to evaluate the detectability of microbial biosignatures by coupling biological stress responses with gas-phase Fourier-transform infrared (FT-IR) spectroscopy. By simulating exoplanetary-analogue environments, specifically nitrogen-rich anoxia and severe oxidative stress,this research mapped the volatile metabolic outputs of the heterotrophic yeast *Saccharomyces cerevisiae* and the phototrophic marine diatom *Cylindrotheca fusiformis*. The integration of a closed-loop bioreactor with a time-resolved, discrete sampling framework provided critical insights into how biological trace gases behave, accumulate, and degrade under extreme conditions.

The experimental outcomes demonstrated that microbial gaseous emissions are highly dynamic and intrinsically tied to primary metabolic pathways. Under baseline Earth conditions, both organisms produced stable, identifiable CO_2 and H_2O spectral fingerprints. However, the introduction of environmental stressors induced stark metabolic shifts. Under a pure nitrogen atmosphere, *S. cerevisiae* transitioned to anaerobic fermentation, resulting in an overall reduction of CO_2 output marked by transient metabolic bursts. Conversely, *C. fusiformis* maintained a remarkably stable CO_2 equilibrium under the same anoxic conditions, suggesting a resilience driven by the synchronized down-regulation of both mitochondrial respiration and active photorespiration.

When exposed to an acute oxidative environment (H_2O_2), both cultures ultimately succumbed to metabolic arrest. *S. cerevisiae* exhibited a pronounced, temporary hyper-respiratory spike, a metabolic fuelled by the rapid consumption of internal energy reserves to power antioxidant defences—before complete structural lysis. In contrast, the diatoms suffered a rapid atmospheric free-fall aligned with immediate chemical degradation and plasmolysis.

Crucially, despite clear macroscopic and microscopic evidence of profound cellular stress, targeted trace volatile organic compounds (VOCs) remained entirely undetected within the mid-infrared spectra. This absence highlights several systemic vulnerabilities in current analytical and remote sensing frameworks. Instrumentally, the detection of trace biogenic VOCs (likely present in the parts-per-billion range) was severely restricted by the short optical path-length of the gas cell and the overwhelming spectral masking caused by ambient water vapour. Biologically, the results underscore that survival protocols often drive organisms into low-emission, protective states. Furthermore, active microbial communities may continuously recycle their own volatile waste, preventing these secondary metabolites from accumulating to spectroscopically detectable steady states.

The implications of these findings for exoplanetary astrobiology are significant. The inability to detect trace VOCs during acute biological degradation proves that a lack of observed chemical disequilibrium does not equate to an absence of life. Biological outgassing is transient, non-linear, and heavily influenced by temporal adaptation. In the context of space observation, relying on discrete, snapshot spectral measurements risks missing critical, time-dependent metabolic bursts, thereby increasing the probability of false negatives.

To advance the empirical search for extraterrestrial life, future laboratory analogue studies must pri-

oritise continuous, in situ monitoring frameworks paired with advanced water-suppression hardware and multi-pass, long-pathlength optical cells. On a macroscopic scale, astrobiological surveys evaluating terrestrial exoplanets must account for atmospheric seasonality and transient stress responses. Ultimately, identifying robust biosignatures requires shifting the scientific paradigm from searching for static, isolated chemical imbalances to tracking dynamic, planetary-scale metabolic fluxes over time.

References

Adadi, Parise et al. (Dec. 2021). “The effect of sound frequency and intensity on yeast growth, fermentation performance and volatile composition of beer”. In: *Molecules* 26.23. ISSN: 14203049. DOI: 10.3390/molecules26237239.

Ali, Nawab, Muhammad Nughman, and Syed Majid Shah (May 2023). “Extremophiles and Limits of Life in a Cosmic Perspective”. In: *Life in Extreme Environments - Diversity, Adaptability and Valuable Resources of Bioactive Molecules*. IntechOpen. DOI: 10.5772/intechopen.110471.

Andreichikov, B. M. et al. (Sept. 1997). “Chemical composition and structure of Venus clouds from results of X-ray radiometric experiments made with the Vega 1 and Vega 2 automatic interplanetary stations.” In: *Kosmicheskie Issledovaniia* 25, pp. 737–743.

Anglade, Jean-Yves et al. (Jan. 2006). “Response of electrically stimulated cells of Pseudomonas oleovorans strain ATCC 29347 suspended in silicone oil”. In: *FEMS Microbiology Letters* 199.1, pp. 119–123. DOI: 10.1111/j.1574-6968.2001.tb10661.x.

Apolonski, Alexander and Kiran Sankar Maiti (May 2021). “Towards a standard operating procedure for revealing hidden volatile organic compounds in breath: the Fourier-transform IR spectroscopy case”. In: *Applied Optics* 60.14, p. 4217. ISSN: 1559-128X. DOI: 10.1364/ao.421994.

Arao, Toshiaki et al. (2005). “Effect of high-pressure gas on yeast growth”. In: *Bioscience, Biotechnology and Biochemistry* 69.7, pp. 1365–1371. ISSN: 09168451. DOI: 10.1271/bbb.69.1365.

Arnaud, J P et al. (1993). *Shear stress effects on growth and activity of Lactobacillus delbrueckii subsp, bulgaricus*. Tech. rep., pp. 157–175.

Arney, Giada, Shawn D. Domagal-Goldman, and Victoria S. Meadows (Mar. 2018). “Organic Haze as a Biosignature in Anoxic Earth-like Atmospheres”. In: *Astrobiology* 18.3, pp. 311–329. ISSN: 15311074. DOI: 10.1089/ast.2017.1666.

Avice, G. et al. (July 2018). “Evolution of atmospheric xenon and other noble gases inferred from Archean to Paleoproterozoic rocks”. In: *Geochimica et Cosmochimica Acta* 232, pp. 82–100. ISSN: 00167037. DOI: 10.1016/j.gca.2018.04.018.

Ayala, Antonio, Mario F. Muñoz, and Sandro Argüelles (May 2014). “Lipid peroxidation: Production, metabolism, and signaling mechanisms of malondialdehyde and 4-hydroxy-2-nonenal”. In: *Oxidative Medicine and Cellular Longevity* 2014. ISSN: 19420994. DOI: 10.1155/2014/360438.

Bains, William et al. (2021a). “Phosphine on Venus Cannot be Explained by Conventional Processes”. In: *Astrobiology* 21.10, pp. 1277–1304.

Bains, William et al. (2021b). “Production of ammonia makes Venusian clouds habitable and explains observed cloud-level chemical anomalies”. In: *Proceedings of the National Academy of Sciences* 118.52. DOI: 10.1073/pnas.2110889118/-/DCSupplemental. URL: http://www.pnas.org/lookup/.

Ball, David.W. (May 2006). “Field Guide to Spectroscopy”. In: *SPIE Press, Bellingham.* DOI: 10.1117/3.682726.

Ball, Philip (Mar. 2008). “Water-an enduring mystery”. In: *Nature* 452, pp. 291–292.

Barge, Laura M. et al. (Apr. 2022). “Determining the ”biosignature Threshold” for Life Detection on Biotic, Abiotic, or Prebiotic Worlds”. In: *Astrobiology* 22.4, pp. 481–493. ISSN: 15311074. DOI: 10.1089/ast.2021.0079.

Barker, Edwin S (1979). *DETECTION OF SO 2 IN THE UV SPECTRUM OF VENUS*. Tech. rep. 2.

Barone, Maria Elena et al. (Dec. 2021). “Comparative Response of Marine Microalgae to H2O2-Induced Oxidative Stress”. In: *Applied Biochemistry and Biotechnology* 193.12, pp. 4052–4067. ISSN: 15590291. DOI: 10.1007/s12010-021-03690-x.

Basak, Suryoday et al. (May 2021). “Habitability classification of exoplanets: a machine learning insight”. In: *European Physical Journal: Special Topics* 230.10, pp. 2221–2251. ISSN: 19516401. DOI: 10.1140/epjs/s11734-021-00203-z.

Batty, Claire A. et al. (Oct. 2024). *Volatile organic compounds (VOCs) in terrestrial extreme environments: implications for life detection beyond Earth*. DOI: 10.1039/d4np00037d.

Benoit, Stéphanie et al. (2001). *Induction of vap genes encoded by the virulence plasmid of Rhodococcus equi during acid tolerance response*. Tech. rep., pp. 439–449.

Bernard, J. M. et al. (Dec. 2003). "Experimental simulation of Titan's atmosphere: Detection of ammonia and ethylene oxide". In: *Planetary and Space Science*. Vol. 51. 14-15, pp. 1003–1011. DOI: 10.1016/j.pss.2003.05.009.

Bhartia, R. et al. (May 2012). "Noncontact, reagentless, nondestructive, detection of organics, biosignatures, and water". In: *Sensors and Systems for Space Applications V*. Vol. 8385. SPIE, 83850E-83850E–9. ISBN: 9780819490636. DOI: 10.1117/12.921420.

Bhattacharjee, Pijush Kanti (Feb. 2023). *Fundamental to Electromagnetic Waves*. Tech. rep., pp. 454–526. URL: www.ijtsrd.com.

Billi, Daniela et al. (Feb. 2021). "Exploiting a perchlorate-tolerant desert cyanobacterium to support bacterial growth for in situ resource utilization on Mars". In: *International Journal of Astrobiology* 20.1, pp. 29–35. ISSN: 14753006. DOI: 10.1017/S1473550420000300.

Blachowicz, Adriana et al. (2019). "Proteomic and metabolomic characteristics of extremophilic fungi under simulated Mars conditions". In: *Frontiers in Microbiology* 10.MAY. ISSN: 1664302X. DOI: 10.3389/fmicb.2019.01013.

Blitz, Jonathan P and Douglas G Klarup (2002). *Signal-to-Noise Ratio, Signal Processing, and Spectral W Information in the Instrumental Analysis Laboratory*. Tech. rep. 11.

Borysow, Aleksandra (1994). "Pressure-Induced Molecular Absorption in Stellar Atmospheres". In: *International Astronomical Union Colloquium* 146, pp. 209–222. ISSN: 0252-9211. DOI: 10.1017/s0252921100021345.

Bower, C K and M A Daeschel (1999). *Resistance responses of microorganisms in food environments*. Tech. rep., pp. 33–44.

Boza, Y., D. Barbin, and A. R.P. Scamparini (June 2004). "Effect of spray-drying on the quality of encapsulated cells of Beijerinckia sp". In: *Process Biochemistry* 39.10, pp. 1275–1284. ISSN: 00329592. DOI: 10.1016/j.procbio.2003.06.002.

Brack, André (Apr. 2012). *Reflections on astrobiology, exobiology, bioastronomy, and cosmobiology*. DOI: 10.1089/ast.2012.3050.

Bradley, Michael S (Jan. 2015). "Lineshapes in IR and Raman Spectroscopy: A Primer". In: *Spectroscopy* 30.11. URL: https://www.spectroscopyonline.com/view/lineshapes-ir-and-raman-spectroscopy-primer.

Breeding, Christopher M. and Nicole J. Ahline (Dec. 2024). "Infrared Spectroscopy and its use in Gemology". In: *Gems and Gemology* 60.4, pp. 474–492. ISSN: 0016626X. DOI: 10.5741/GEMS.60.4.474.

Casey, William H and William M White (2018). *Encyclopedia of geochemistry: a comprehensive reference source on the chemistry of the earth*. URL: http://www.springerlink.com/reference-works/.

Catling, David C and Kevin J Zahnle (2020). *The Archean atmosphere*. Tech. rep. URL: https://www.science.org.

Cavalazzi, Barbara and Frances Westall (2019). *Biosignatures for Astrobiology*. Ed. by Andre Brack and Greda Horneck. Springer. URL: http://www.springer.com/series/5118.

Chen, Haoxuan et al. (July 2022). "Gene-Regulated Release of Distinctive Volatile Organic Compounds from Stressed Living Cells". In: *Environmental Science and Technology* 56.13, pp. 9546–9555. ISSN: 15205851. DOI: 10.1021/acs.est.2c01774.

Chyba, C P and C Sagan (1997). *Comets as a Source of Prebiotic Organic Molecules for the Early Earth*. Tech. rep.

Civiš, Svatopluk, Martin Ferus, and Antonín Knížek (2019). *The Chemistry of CO2 and TiO2 From Breathing Minerals to Life on Mars*. Springer. ISBN: 978-3-030-24032-5. DOI: https://doi.org/10.1007/978-3-030-24032-5. URL: http://www.springer.com/series/8898.

Colomb, Aurélie et al. (2008). "Screening volatile organic compounds (VOCs) emissions from five marine phytoplankton species by head space gas chromatography/mass spectrometry (HS-GC/MS)". In: *Journal of Environmental Monitoring* 10.3, pp. 325–330. ISSN: 14640325. DOI: 10.1039/b715312k.

Colthup, Norman B (2001). *Infrared Spectroscopy*. Tech. rep.

Condon, James J and Scott M Ransom (Oct. 2018). *Essential Radio Astronomy*. URL: https://www.cv.nrao.edu/~sransom/web/Ch7.html.

Cortesão, Marta et al. (2019). “Bacillus subtilis spore resistance to simulated mars surface conditions”. In: *Frontiers in Microbiology* 10.FEB. ISSN: 1664302X. DOI: 10.3389/fmicb.2019.00333.

Cosciotti, Barbara et al. (Dec. 2019). “Survivability of anhydrobiotic cyanobacteria in salty ice: implications for the habitability of icy worlds”. In: *Life* 9.4. ISSN: 20751729. DOI: 10.3390/life9040086.

Cottin, Hervé et al. (July 2017). *Astrobiology and the Possibility of Life on Earth and Elsewhere…* DOI: 10.1007/s11214-015-0196-1.

Dakal, Tikam Chand, Lisa Solieri, and Paolo Giudici (Aug. 2014). *Adaptive response and tolerance to sugar and salt stress in the food yeast Zygosaccharomyces rouxii*. DOI: 10.1016/j.ijfoodmicro.2014.05.015.

De Mol, Maarten L. (Mar. 2023). “Astrobiology in Space: A Comprehensive Look at the Solar System”. In: *Life* 675.13. ISSN: 20751729. DOI: 10.3390/life13030675.

Ding, Junmei et al. (Nov. 2009). *Tolerance and stress response to ethanol in the yeast Saccharomyces cerevisiae*. DOI: 10.1007/s00253-009-2223-1.

Domagal-Goldman, Shawn D. et al. (June 2011). “Using biogenic sulfur gases as remotely detectable biosignatures on anoxic planets”. In: *Astrobiology* 11.5, pp. 419–441. ISSN: 15311074. DOI: 10.1089/ast.2010.0509.

Domagal-Goldman, Shawn D. et al. (Sept. 2014). “Abiotic ozone and oxygen in atmospheres similar to prebiotic earth”. In: *Astrophysical Journal* 792.2. ISSN: 15384357. DOI: 10.1088/0004-637X/792/2/90.

Donahue, T M and R R Hodges (1992). *Past and Present Water Budget of Venus*. Tech. rep., pp. 6083–6091.

Dong, Yongsheng et al. (Nov. 2007). “Effects of high pressure on the accumulation of trehalose and glutathione in the Saccharomyces cerevisiae cells”. In: *Biochemical Engineering Journal* 37.2, pp. 226–230. ISSN: 1369703X. DOI: 10.1016/j.bej.2007.04.004.

Driese, Steven G. et al. (Aug. 2011). “Neoarchean paleoweathering of tonalite and metabasalt: Implications for reconstructions of 2.69Ga early terrestrial ecosystems and paleoatmospheric chemistry”. In: *Precambrian Research* 189.1-2, pp. 1–17. ISSN: 03019268. DOI: 10.1016/j.precamres.2011.04.003.

Duarte, Rubens T.D. et al. (Oct. 2012). “Brazilian research on extremophiles in the context of astrobiology”. In: *International Journal of Astrobiology* 11.4, pp. 325–333. ISSN: 14735504. DOI: 10.1017/S1473550412000249.

Eager-Nash, Jake K. et al. (Apr. 2024). “Biosignatures from pre-oxygen photosynthesising life on TRAPPIST-1e”. In: URL: http://arxiv.org/abs/2404.11611.

Ellert, Michael et al. (1998). *Calibration of a Field Spectroradiometer Calibration and Characterization of a Non-Imaging Field Spectroradiometer Supporting Imaging Spectrometer Validation and Hyperspectral Sensor Modelling*. Tech. rep.

Encrenaz, T. et al. (Mar. 2011). “Hydrogen peroxide on Mars: Observations, interpretation and future plans”. In: *Planetary and Space Science*. Vol. 68. 1, pp. 3–17. DOI: 10.1016/j.pss.2011.03.019.

Erdmann, N et al. (1997). *Effect of Gravity Changes on the Cyanobacterium Synechocystis sp. PCC 6803*. Tech. rep., pp. 348–355.

Etiope, Giuseppe and Barbara Sherwood Lollar (June 2013). “Abiotic methane on earth”. In: *Reviews of Geophysics* 51.2, pp. 276–299. ISSN: 19449208. DOI: 10.1002/rog.20011.

Eyles, M J and A D Warth (1989). *The response of Gluconobacter oxydans to sorbic and benzoic acids*. Tech. rep., pp. 335–342.

Fang, A et al. (1997). *Secondary metabolism in simulated microgravity:-lactam production by Streptomyces clavuligerus*. Tech. rep., pp. 22–25.

Farquhar, James et al. (Dec. 2001). “Observation of wavelength-sensitive mass-independent sulfur isotope effects during SO2 photolysis: Implications for the early atmosphere”. In: *Journal of Geophysical Research: Planets* 106.E12, pp. 32829–32839. ISSN: 01480227. DOI: 10.1029/2000JE001437.

Favier, Gabriela I et al. (2000). *Survival of Yersinia enterocolitica and Mesophilic Aerobic Bacteria on Eggshell after Washing with Hypochlorite and Organic Acid Solutions*. Tech. rep. 8, pp. 1053–1057.

Felton, Ryan C. et al. (Mar. 2022). “The Role of Atmospheric Exchange in False-Positive Biosignature Detection”. In: *Journal of Geophysical Research: Planets* 127.3. ISSN: 21699100. DOI: 10.1029/2021JE006853.

Flahaut, Sigrid et al. (1997). *Alkaline Stress Response in Enterococcus faecalis: Adaptation, Cross-Protection, and Changes in Protein Synthesis*. Tech. rep. 2, pp. 812–814. URL: https://journals.asm.org/journal/aem.

Forterre, Patrick (2015). "The universal tree of life: An update". In: *Frontiers in Microbiology* 6.JUN. ISSN: 1664302X. DOI: 10.3389/fmicb.2015.00717.

Fu, Huihui, Jie Yuan, and Haichun Gao (Oct. 2015). *Microbial oxidative stress response: Novel insights from environmental facultative anaerobic bacteria*. DOI: 10.1016/j.abb.2015.08.012.

Gao, Peter et al. (June 2015). "STABILITY OF CO2 ATMOSPHERES ON DESICCATED M DWARF EXOPLANETS". In: *Astrophysical Journal* 806.2. ISSN: 15384357. DOI: 10.1088/0004-637X/806/2/249.

Gauthier, M. R., G. N.A. Senhorinho, and J. A. Scott (Dec. 2020). *Microalgae under environmental stress as a source of antioxidants*. DOI: 10.1016/j.algal.2020.102104.

Gillen, Catherine et al. (Nov. 2023). "The Call for a New Definition of Biosignature". In: *Astrobiology* 23.11, pp. 1228–1237. ISSN: 15311074. DOI: 10.1089/ast.2023.0010.

Goldstein, E Bruce and Ralph Hale (2015). *Cognitive psychology: Connecting mind, research, and everyday experience*. Cengage Learning Stamford, CT.

Gordon, I.E. et al. (Apr. 2026). "The HITRAN2024 molecular spectroscopic database". In: *Journal of Quantitative Spectroscopy and Radiative Transfer*, p. 109807. ISSN: 00224073. DOI: 10.1016/j.jqsrt.2026.109807.

Goyal, Arun (Oct. 1989). "Intracellular glycerol in Dunaliella is depleted by intracellular metabolism in response to hypoosmotic stress by dilution". In: *FEMS Microbiology Letters* 61.1-2, pp. 145–148. ISSN: 15746968. DOI: 10.1111/j.1574-6968.1989.tb03568.x.

Greaves, Jane S. et al. (July 2021). "Phosphine gas in the cloud decks of Venus". In: *Nature Astronomy* 5.7, pp. 655–664. ISSN: 23973366. DOI: 10.1038/s41550-020-1174-4.

Griffith, D. W. T. et al. (May 2012). *A Fourier transform infrared trace gas analyser for atmospheric applications*. DOI: 10.5194/amtd-5-3717-2012. URL: https://amt.copernicus.org/articles/5/2481/2012/amt-5-2481-2012-discussion.html.

Griffiths, Peter R. and James A. de Haseth (Apr. 2007). *Fourier Transform Infrared Spectrometry*. John Wiley & Sons, Inc., pp. 19–74. ISBN: 9780471194040. DOI: 10.1002/047010631X.

Guyon, Olivier (Nov. 2017). "Habitable exoplanets detection: overview of challenges and current state-of-the-art [Invited]". In: *Optics Express* 25.23, p. 28825. ISSN: 10944087. DOI: 10.1364/oe.25.028825.

Hamblin, Michael R. (Jan. 2022). "Molecular and Cellular Mechanisms of Water-Filtered IR". In: *Water-filtered Infrared A (wIRA) Irradiation: From Research to Clinical Settings*. Springer International Publishing, pp. 273–284. ISBN: 9783030928803. DOI: 10.1007/978-3-030-92880-3{_}23.

Hanikenne, Marc, RenÃ© Fernand Matagne, and Roland Loppes (Mar. 2001). " Pleiotropic mutants hypersensitive to heavy metals and to oxidative stress in Chlamydomonas reinhardtii ". In: *FEMS Microbiology Letters* 196.2, pp. 107–111. ISSN: 03781097. DOI: 10.1111/j.1574-6968.2001.tb10549.x.

Haqq-Misra, Jacob, James F. Kasting, and Sukyoung Lee (May 2011). "Availability of O2 and H2O2 on pre-photosynthetic earth". In: *Astrobiology* 11.4, pp. 293–302. ISSN: 15311074. DOI: 10.1089/ast.2010.0572.

Harman, C. E. et al. (Oct. 2015). "Abiotic O2 levels on planets around F, G, K, and M stars: Possible false positives for life?" In: *Astrophysical Journal* 812.2. ISSN: 15384357. DOI: 10.1088/0004-637X/812/2/137.

Harrison, T. Mark, Elizabeth A. Bell, and Patrick Boehnke (2017). "Hadean Zircon Petrochronology". In: *Reviews in Mineralogy and Geochemistry* 83.1, pp. 329–363. ISSN: 15296466. DOI: 10.2138/rmg.2017.83.11.

Helmreich, Stefan (2006). *The Signature of Life: Designing the Astrobiological Imagination*. Tech. rep., pp. 66–95.

Hessler, Angela M. et al. (Apr. 2004). "A lower limit for atmospheric carbon dioxide levels 3.2 billion years ago". In: *Nature* 428.6984, pp. 736–738. ISSN: 00280836. DOI: 10.1038/nature02471.

Hinkel, Natalie R., Allison Youngblood, and Melinda Soares-Furtado (July 2024). "Host Stars and How Their Compositions Influence Exoplanets". In: *Reviews in Mineralogy and Geochemistry* 90.1, pp. 1–26. ISSN: 1529-6466. DOI: 10.2138/rmg.2024.90.01.

Hitchcock, Dian R and James E Lovelock (1967). *Life Detection by Atmospheric Analysis*. Tech. rep., pp. 149–159.

Hu, Renyu, Luke Peterson, and Eric T. Wolf (Jan. 2020). “O2 and CO-rich Atmospheres for Potentially Habitable Environments on TRAPPIST-1 Planets”. In: *The Astrophysical Journal* 888.2, p. 122. ISSN: 0004-637X. DOI: 10.3847/1538-4357/ab5f07.

Huang, Jingcheng (Sept. 2022). “Planetary Science Meets Chemistry: Studying Potential Biosignature Gases in Terrestrial Exoplanet Atmospheres”. PhD thesis. Massachusetts Institute of Technology.

Huang, Jingcheng et al. (2022a). “Assessment of Ammonia as a Biosignature Gas in Exoplanet Atmospheres”. In: *Astrobiology* 22.2, pp. 171–191.

Huang, Jingcheng et al. (July 2022b). “Methanol—A Poor Biosignature Gas in Exoplanet Atmospheres”. In: *The Astrophysical Journal* 933.1, p. 6. ISSN: 0004-637X. DOI: 10.3847/1538-4357/ac6f60.

Huang, Shuo and Chris W. Ormel (Jan. 2022). “The dynamics of the TRAPPIST-1 system in the context of its formation”. In: DOI: 10.1093/mnras/stac288. URL: http://arxiv.org/abs/2109.10984%20http://dx.doi.org/10.1093/mnras/stac288.

Impey, Chris (Aug. 2022). “Life beyond Earth: How will it first be detected?” In: *Acta Astronautica* 197, pp. 387–398. ISSN: 00945765. DOI: 10.1016/j.actaastro.2022.03.019.

Ito, Yuichi et al. (Apr. 2020). “H2O2-induced Greenhouse Warming on Oxidized Early Mars”. In: *The Astrophysical Journal* 893.2, p. 168. ISSN: 0004-637X. DOI: 10.3847/1538-4357/ab7db4.

Jana, T K et al. (2000). “Agglutination potential of Pseudomonas ¯uorescens in relation to energy stress and colonization of Macrophomina phaseolina”. In: *Soil Biology and Biochemistry* 32, pp. 511–519. URL: www.elsevier.com/locate/soilbio.

Johnson, D. Barrie and Raquel Quatrini (2020). “Acidophile microbiology in space and time”. In: *Current Issues in Molecular Biology* 39, pp. 63–76. ISSN: 14673045. DOI: 10.21775/cimb.039.063.

Johnson, Francis S (Apr. 1968). “The Atmosphere of Venus: A Conference Review”. In: *Journal of the Atmospheric Sciences* 25, pp. 658–662.

Johnson, Jena E. et al. (May 2014). “O2 constraints from Paleoproterozoic detrital pyrite and uraninite”. In: *Bulletin of the Geological Society of America* 126.5-6, pp. 813–830. ISSN: 19432674. DOI: 10.1130/B30949.1.

Kadoya, Shintaro and David C. Catling (Oct. 2019). “Constraints on hydrogen levels in the Archean atmosphere based on detrital magnetite”. In: *Geochimica et Cosmochimica Acta* 262, pp. 207–219. ISSN: 00167037. DOI: 10.1016/j.gca.2019.07.041.

Kale, Shubha P. and S. Michal Jazwinski (1996). “Differential response to UV stress and DNA damage during the yeast replicative life span”. In: *Developmental Genetics* 18.2, pp. 154–160. ISSN: 0192253X. DOI: 10.1002/(SICI)1520-6408(1996)18:2<154::AID-DVG8>3.0.CO;2-8.

Kaltenegger, Lisa (July 2017). “How to Characterize Habitable Worlds and Signs of Life”. In: *The Annual Review of Astronomy and Astrophysics*, pp. 433–485. DOI: 10.1146/annurev-astro-082214. URL: https://doi.org/10.1146/annurev-astro-082214-.

Kanzaki, Yoshiki and Takashi Murakami (June 2015). “Estimates of atmospheric CO<inf>2</inf> in the Neoarchean-Paleoproterozoic from paleosols”. In: *Geochimica et Cosmochimica Acta* 159, pp. 190–219. ISSN: 00167037. DOI: 10.1016/j.gca.2015.03.011.

Kasting, J. F., H. D. Holland, and J. P. Pinto (1985). “Oxidant abundances in rainwater and the evolution of atmospheric oxygen.” In: *Journal of Geophysical Research* 90.D6, pp. 10497–10510. ISSN: 01480227. DOI: 10.1029/JD090iD06p10497.

Kasting, James F, Alexander A Pavlov, and Janet L Siefert (2001). *A COUPLED ECOSYSTEM-CLIMATE MODEL FOR PREDICTING THE METHANE CONCENTRATION IN THE ARCHEAN ATMOSPHERE*. Tech. rep.

Kasting, James F, Daniel Whitmire, and Ray T Reynolds (1993). “Habitable zones around main sequence stars”. In: *ICARUS* 101.1, pp. 108–128. URL: https://www.researchgate.net/publication/11809380.

Kaur, Jasvinder, Jaspreet Kaur, and Aeshna Nigam (June 2024). *Extremophiles in Space Exploration*. DOI: 10.1007/s12088-024-01297-4.

Kharecha, P, J Kasting, and J Siefert (2005). *A coupled atmosphere-ecosystem model of the early Archean Earth*. Tech. rep., pp. 53–76. URL: http://www.gsfc.nasa.gov/goddardnews/.

Kim, Woojin S. et al. (Oct. 2001). “Survival Response and Rearrangement of Plasmid DNA of Lactococcus lactis during Long-Term Starvation”. In: *Applied and Environmental Microbiology* 67.10, pp. 4594–4602. ISSN: 00992240. DOI: 10.1128/AEM.67.10.4594-4602.2001.

Kotsyurbenko, O. R. (June 2023). “Searching for Life on Venus: History of the Problem and Basic Concepts”. In: *Solar System Research* 57.3, pp. 221–235. ISSN: 16083423. DOI: 10.1134/S0038094623030052.

Kowalski, Piotr M. (2014). “Infrared absorption of dense helium and its importance in the atmospheres of cool white dwarfs”. In: *Astronomy and Astrophysics* 566. ISSN: 14320746. DOI: 10.1051/0004-6361/201424242.

Kozakis, Thea, João M. Mendonça, and Lars A. Buchhave (Sept. 2022). “Is ozone a reliable proxy for molecular oxygen?: I. The O2-O3relationship for Earth-like atmospheres”. In: *Astronomy and Astrophysics* 665. ISSN: 14320746. DOI: 10.1051/0004-6361/202244164.

Kral, Timothy A et al. (n.d.). *HYDROGEN CONSUMPTION BY METHANOGENS ON THE EARLY EARTH*. Tech. rep.

Krasnopolsky, Vladimir A. (Nov. 2006). “Chemical composition of Venus atmosphere and clouds: Some unsolved problems”. In: *Planetary and Space Science* 54.13-14, pp. 1352–1359. ISSN: 00320633. DOI: 10.1016/j.pss.2006.04.019.

Krissansen-Totton, Joshua, David S. Bergsman, and David C. Catling (Jan. 2016). “On Detecting Biospheres from Chemical Thermodynamic Disequilibrium in Planetary Atmospheres”. In: *Astrobiology* 16.1, pp. 39–67. ISSN: 15311074. DOI: 10.1089/ast.2015.1327.

Krissansen-Totton, Joshua, Stephanie Olson, and David C Catling (Jan. 2018a). “Disequilibrium biosignatures over Earth history and implications for detecting exoplanet life”. In: *Science Advances* 4.1. URL: https://www.science.org.

Krissansen-Totton, Joshua et al. (Sept. 2018b). “Detectability of Biosignatures in Anoxic Atmospheres with the James Webb Space Telescope: A TRAPPIST-1e Case Study”. In: *The Astronomical Journal* 156.3, p. 114. ISSN: 0004-6256. DOI: 10.3847/1538-3881/aad564.

Krissansen□Totton, Joshua et al. (June 2021). “Oxygen False Positives on Habitable Zone Planets Around Sun□Like Stars”. In: *AGU Advances* 2.2. ISSN: 2576-604X. DOI: 10.1029/2020av000294.

Kuzucan, Asena et al. (Jan. 2025). “The Role of Atmospheric Composition in Defining the Habitable Zone Limits and Supporting E. coli Growth”. In: *Life* 15.1. ISSN: 20751729. DOI: 10.3390/life15010079.

Lammer, Helmut et al. (Nov. 2018). *Origin and evolution of the atmospheres of early Venus, Earth and Mars*. DOI: 10.1007/s00159-018-0108-y.

Leconte, Jérémy et al. (2013). “Increased insolation threshold for runaway greenhouse processes on Earth-like planets”. In: *Nature* 504.7479, pp. 268–271. ISSN: 00280836. DOI: 10.1038/nature12827.

Leung, Michaela et al. (Oct. 2022). “Alternative Methylated Biosignatures. I. Methyl Bromide, a Capstone Biosignature”. In: *The Astrophysical Journal* 938.1, p. 6. ISSN: 0004-637X. DOI: 10.3847/1538-4357/ac8799.

Li, Zhengke et al. (Aug. 2020). “Dynamic Photophysiological Stress Response of a Model Diatom to Ten Environmental Stresses”. In: *Phycological Society of America* 57, pp. 484–495.

Ligterink, Niels F.W. et al. (June 2022). “The ORIGIN Space Instrument for Detecting Biosignatures and Habitability Indicators on a Venus Life Finder Mission”. In: *Aerospace* 9.6. ISSN: 22264310. DOI: 10.3390/aerospace9060312.

Limaye, Sanjay S. et al. (Sept. 2018). “Venus’ spectral signatures and the potential for life in the clouds”. In: *Astrobiology* 18.9, pp. 1181–1198. ISSN: 15311074. DOI: 10.1089/ast.2017.1783.

Lin, Wei et al. (2022). *Detection of biosignatures in Terrestrial analogs of Martian regions: Strategical and technical assessments*. DOI: 10.26464/epp2022042.

Liu, Huaying and Maosheng Yao (Sept. 2025). “Time-resolved monitoring of yeast responses to lipopolysaccharide exposure by cell-released volatile organic compounds”. In: *Applied and Environmental Microbiology* 91.9. ISSN: 10985336. DOI: 10.1128/aem.00785-25.

Lloyd, D. et al. (2003). “Nitrosative stress induced cytotoxicity in Giardia intestinalis”. In: *Journal of Applied Microbiology* 95.3, pp. 576–583. ISSN: 13645072. DOI: 10.1046/j.1365-2672.2003.02008.x.

López-García, Purificación and Patrick Forterre (1999). “Control of DNA topology during thermal stress in hyperthermophilic archaea: DNA topoisomerase levels, activities and induced thermotolerance during heat and cold shock in Sulfolobus”. In: *Molecular Microbiology* 33.4, pp. 766–777. ISSN: 0950382X. DOI: 10.1046/j.1365-2958.1999.01524.x.

Lovelock, J.E (Aug. 1965). “A Physical Basis for Life Detection Experiments”. In: *Nature* 207, pp. 568–570. DOI: 10.1038/207568a0. URL: https://doi.org/10.1038/207568a0.

Luger, R. and R. Barnes (Feb. 2015). “Extreme water loss and abiotic O2 buildup on planets throughout the habitable zones of m dwarfs”. In: *Astrobiology* 15.2, pp. 119–143. ISSN: 15311074. DOI: 10.1089/ast.2014.1231.

Luger, Rodrigo et al. (May 2017). “A seven-planet resonant chain in TRAPPIST-1”. In: DOI: 10.1038/s41550-017-0129. URL: http://arxiv.org/abs/1703.04166%20http://dx.doi.org/10.1038/s41550-017-0129.

Madeo, Frank et al. (May 1999). “Oxygen Stress: A Regulator of Apoptosis in Yeast”. In: *The Journal of Cell Biology* 145.4, pp. 757–767. URL: http://www.jcb.org.

Malaterre, Christophe et al. (Nov. 2023). “Is There Such a Thing as a Biosignature?” In: *Astrobiology* 23.11, pp. 1213–1227. ISSN: 15311074. DOI: 10.1089/ast.2023.0042.

Mangum, Jeffrey G and Yancy L Shirley (2014). *HOW TO CALCULATE MOLECULAR COLUMN DENSITY*. Tech. rep.

Marty, Bernard et al. (2013). “Nitrogen isotopic composition and density of the Archean atmosphere”. In: *Science* 342.6154, pp. 101–104. ISSN: 10959203. DOI: 10.1126/science.1240971.

Mathias, Jennifer (July 2018). *A Beginner’s Guide to FTIR Analysis: Interpreting & Analyzing Results*. URL: https://www.innovatechlabs.com/newsroom/1882/interpreting-analyzing-ftir-results/.

Meadows, Victoria S. (Oct. 2017). *Reflections on O2 as a Biosignature in Exoplanetary Atmospheres*. DOI: 10.1089/ast.2016.1578.

Meadows, Victoria S., Andrew P. Lincowski, and Jacob Lustig-Yaeger (Oct. 2023). “The Feasibility of Detecting Biosignatures in the TRAPPIST-1 Planetary System with JWST”. In: *Planetary Science Journal* 4.10. ISSN: 26323338. DOI: 10.3847/PSJ/acf488.

Meadows, Victoria S. et al. (June 2018). “Exoplanet Biosignatures: Understanding Oxygen as a Biosignature in the Context of Its Environment”. In: *Astrobiology* 18.6, pp. 630–662. ISSN: 15311074. DOI: 10.1089/ast.2017.1727.

Méndez, Abel et al. (Aug. 2021). *Habitability Models for Astrobiology*. DOI: 10.1089/ast.2020.2342.

Merrell, D. Scott et al. (Nov. 2003). “Growth Phase-Dependent Response of Helicobacter pylori to Iron Starvation”. In: *Infection and Immunity* 71.11, pp. 6510–6525. ISSN: 00199567. DOI: 10.1128/IAI.71.11.6510-6525.2003.

Millerl, Stanley L (Feb. 1953). *A Production of Amino Acids Under Possible Primitive Earth Conditions*. Tech. rep. G. H. Jones Chemical Laboratory, University of Chicago, Chicago, Illinois.

Mogul, Rakesh et al. (Apr. 2021). “Venus’ Mass Spectra Show Signs of Disequilibria in the Middle Clouds”. In: *Geophysical Research Letters* 48.7. ISSN: 19448007. DOI: 10.1029/2020GL091327.

Morano, Kevin A., Chris M. Grant, and W. Scott Moye-Rowley (Apr. 2012). “The response to heat shock and oxidative stress in saccharomyces cerevisiae”. In: *Genetics* 190.4, pp. 1157–1195. ISSN: 00166731. DOI: 10.1534/genetics.111.128033.

Mukhin, L.M. et al. (May 1982). “Venera 13 and Venera 14 gas-chromatography analysis of the Venus atmosphere composition”. In: *Pis’ma Astron* 8, pp. 399–403.

Nakasono, Saiki Satoshi, and Hiroshi (2000). “Effect of ELF Magnetic Fields on Protein Synthesis in Escherichia coli K12”. In: *Radiation Research* 154.2, pp. 208–216. DOI: 10.1667/0033. URL: https://doi.org/10.1667/0033-.

Napoli, Alessandro et al. (Dec. 2022). “Absence of increased genomic variants in the cyanobacterium Chroococcidiopsis exposed to Mars-like conditions outside the space station”. In: *Scientific Reports* 12.1. ISSN: 20452322. DOI: 10.1038/s41598-022-12631-5.

Nascimento-Dias, Bruno Leonardo Do and Jesús Martinez-Frias (Feb. 2023). *Brief review about history of astrobiology*. DOI: 10.1017/S1473550422000386.

National Academies of Sciences and Medicine and Division on Engineering and Physical Sciences and Space Studies Board and Committee on Astrobiology Science Strategy for the Search for Life in the Universe (2019). *An Astrobiology Strategy for the Search for Life in the Universe*. National Academies Press, p. 175. ISBN: 9780309484169.

Nebra, Yolanda, Joan Jofre, and Anicet R Blanch (2002). “The effect of reducing agents on the recovery of injured Bifidobacterium cells”. In: *Journal of Microbiological Methods* 49, pp. 247–254. URL: www.elsevier.com/locate/jmicmeth.

Newman, S F et al. (2007). *HYDROGEN PEROXIDE ON ENCELADUS*. Tech. rep., pp. 143–146.

Nixon, Conor A. (Mar. 2024). *The Composition and Chemistry of Titan's Atmosphere*. DOI: 10.1021/acsearthspacechem.2c00041.

Oise Berger, Franç, Philippe Normand, and Patrick Potier (1997). *capA, a cspA-Like Gene That Encodes a Cold Acclimation Protein in the Psychrotrophic Bacterium Arthrobacter globiformis SI55*. Tech. rep. 18, pp. 5670–5676. URL: https://journals.asm.org/journal/jb.

Olsson-Francis, Karen and Charles S. Cockell (Jan. 2010). *Experimental methods for studying microbial survival in extraterrestrial environments*. DOI: 10.1016/j.mimet.2009.10.004.

Oyama, V. I. et al. (Dec. 1980). "Pioneer Venus gas chromatography of the lower atmosphere of Venus". In: *Journal of Geophysical Research: Space Physics* 85.A13, pp. 7891–7902. ISSN: 0148-0227. DOI: 10.1029/ja085ia13p07891.

Oyama, Vance I. and Bonnie J. Berdahl (Sept. 1977). "The Viking Gas Exchange Experiment results from Chryse and Utopia surface samples". In: *Journal of Geophysical Research* 82.28, pp. 4669–4676. DOI: 10.1029/js082i028p04669.

Palmfeldt, Johan and Barbel Hahn-Hagerdal (2000). *Influence of culture pH on survival of Lactobacillus reuteri subjected to freeze-drying*. Tech. rep. URL: www.elsevier.nl.

Panoff, Jean Michel, Bouachanh Thammavongs, and Micheline Guéguen (2000). "Cryoprotectants lead to phenotypic adaptation to freeze-thaw stress in Lactobacillus delbrueckii ssp. bulgaricus CIP 101027T". In: *Cryobiology* 40.3, pp. 264–269. ISSN: 00112240. DOI: 10.1006/cryo.2000.2240.

Parker, Eric T. et al. (Jan. 2014). "Conducting miller-urey experiments". In: *Journal of Visualized Experiments* 83. ISSN: 1940087X. DOI: 10.3791/51039.

Pasek, Matthew A. (Apr. 2020). "Plume Sample Modification at Icy Moons: Implications for Biosignatures". In: *Frontiers in Astronomy and Space Sciences* 7. ISSN: 2296987X. DOI: 10.3389/fspas.2020.00014.

Paynter, David (Apr. 2008). "Measurements and Interpretations of the Water Vapour Continuum at Near Infrared Wavelengths". PhD thesis. The University of Reading.

Pedbost, Marven F. et al. (Mar. 2020). "Defining the Really Habitable Zone". In: URL: http://arxiv.org/abs/2003.13722.

Periago, Paula M. et al. (2002). "Identification of proteins involved in the heat stress response of Bacillus cereus ATCC 14579". In: *Applied and Environmental Microbiology* 68.7, pp. 3486–3495. ISSN: 00992240. DOI: 10.1128/AEM.68.7.3486-3495.2002.

Pham, T. H. et al. (2008). "Gaseous environments modify physiology in the brewing yeast Saccharomyces cerevisiae during batch alcoholic fermentation". In: *Journal of Applied Microbiology* 105.3, pp. 858–874. ISSN: 13652672. DOI: 10.1111/j.1365-2672.2008.03821.x.

Pilcher, Carl B. (2003). "Biosignatures of Early Earth". In: *Astrobiology* 3.3, pp. 471–486.

Piper, Peter et al. (2001). *Weak acid adaptation : the stress response that confers yeasts with resistance to organic acid food preservatives*. Tech. rep., pp. 2635–2642.

Pitcher, Carl B (2003). "Biosignatures of Early Earths". In: *Astrobiology* 3.3.

Poirier, I et al. (1998). "Escherichia coli and Lactobacillus plantarum responses to osmotic stress". In: *Appl Microbiol Biotechnol* 50, pp. 704–709.

Porshnev, N. V. et al. (Sept. 1987). "Gas-chromatographic analysis of products of thermal reactions of aerosol in the Venus cloud layer on board Vega 1 and Vega 2". In: *Kosmicheskie Issledovaniia* 25, pp. 715–720.

Qian, Zhen, Richard D. Sagers, and William G. Pitt (1999). "Investigation of the mechanism of the bioacoustic effect". In: *Journal of Biomedical Materials Research* 44.2, pp. 198–205. ISSN: 00219304. DOI: 10.1002/(SICI)1097-4636(199902)44:2<198::AID-JBM10>3.0.CO;2-P.

Qin, Yusheng et al. (Apr. 2023). "The Effect of Spectral Resolution on the Quantification of OP-FTIR Spectroscopy". In: *Photonics* 10.4. ISSN: 23046732. DOI: 10.3390/photonics10040475.

Ramirez, Ramses M. (Aug. 2018). *A more comprehensive habitable zone for finding life on other planets*. DOI: 10.3390/geosciences8080280.

Rampelotto, Pabulo Henrique (Aug. 2013). *Extremophiles and extreme environments*. DOI: 10.3390/life3030482.

Reilly, John T et al. (1992). *Analysis of FT-IR spectroscopic data: the Voigt profile*. Tech. rep. 10, pp. 1459–1479.

Rein, Hanno, Yuka Fujii, and David S. Spiegel (May 2014). "Some inconvenient truths about biosignatures involving two chemical species on Earth-like exoplanets". In: *Proceedings of the National*

Academy of Sciences of the United States of America 111.19, pp. 6871–6875. ISSN: 10916490. DOI: 10.1073/pnas.1401816111.

Rincé, Alain et al. (Dec. 2003). "Physiological and molecular aspects of bile salt response in Enterococcus faecalis". In: *International Journal of Food Microbiology*. Vol. 88. 2-3. Elsevier, pp. 207–213. DOI: 10.1016/S0168-1605(03)00182-X.

Rivera, Nicholas and Ido Kaminer (2020). "Light-matter interactions with photonic quasiparticles". In: *Nature Reviews Physics* 2.10, pp. 538–561.

Rozen, Yael and Shimshon Belkin (Dec. 2001). "Survival of enteric bacteria in seawater: Table 1". In: *FEMS Microbiology Reviews* 25.5, pp. 513–529. DOI: 10.1111/j.1574-6976.2001.tb00589.x.

Rozycki, Torsten von and Dietrich H. Nies (2009). *Cupriavidus metallidurans: Evolution of a metal-resistant bacterium*. DOI: 10.1007/s10482-008-9284-5.

Rugheimer, S. et al. (Aug. 2015). "EFFECT of UV RADIATION on the SPECTRAL FINGERPRINTS of EARTH-LIKE PLANETS ORBITING M STARS". In: *Astrophysical Journal* 809.1. ISSN: 15384357. DOI: 10.1088/0004-637X/809/1/57.

S N, Auirapetian et al. (Mar. 2001). "Effect of mechanical stress on Ion mutant strain of Escherichia coli K-12". In: *Mikrobiologiia* 70.2, pp. 248–252.

Sagan, Carl et al. (Oct. 1993). "A search for life on Earth from the Galileo spacecraft". In: *Nature* 365, pp. 715–721. DOI: 10.1038/365715a0. URL: https://doi.org/10.1038/365715a0.

Scanlan, David J et al. (1997). *An Immunological Approach To Detect Phosphate Stress in Populations and Single Cells of Photosynthetic Picoplankton †*. Tech. rep. 6, pp. 2411–2420. URL: https://journals.asm.org/journal/aem.

Schnider-Keel, Ursula et al. (Dec. 2001). "The Sigma Factor AlgU (AlgT) Controls Exopolysaccharide Production and Tolerance towards Desiccation and Osmotic Stress in the Biocontrol Agent Pseudomonas fluorescens CHA0". In: *Applied and Environmental Microbiology* 67.12, pp. 5683–5693. ISSN: 00992240. DOI: 10.1128/AEM.67.12.5683-5693.2001.

Schultz, Júnia et al. (2023). *Shedding light on the composition of extreme microbial dark matter: alternative approaches for culturing extremophiles*. DOI: 10.3389/fmicb.2023.1167718.

Schwieterman, Edward W and Michaela Leung (2024). "An Overview of Exoplanet Biosignatures". In: *Reviews in Mineralogy and Geochemistry* 90.1, pp. 465–514.

Schwieterman, Edward W. et al. (June 2018). *Exoplanet Biosignatures: A Review of Remotely Detectable Signs of Life*. DOI: 10.1089/ast.2017.1729.

Schwieterman, Edward W. et al. (Oct. 2022). "Evaluating the Plausible Range of N2O Biosignatures on Exo-Earths: An Integrated Biogeochemical, Photochemical, and Spectral Modeling Approach". In: *The Astrophysical Journal* 937.2, p. 109. ISSN: 0004-637X. DOI: 10.3847/1538-4357/ac8cfb.

"Terrestrial Planet Atmospheres and Biosignatures" (Dec. 2010). In: *Exoplanets*. Ed. by S Seager and V Meadows. Tucson, AZ: University of Arizona Press, pp. 441–470. ISBN: ISBN978-0-8165-2945-2. URL: https://ui.adsabs.harvard.edu/abs/2010exop.book..441M.

Seager, S et al. (2020). *Laboratory studies on the viability of life in H2-dominated exoplanet atmospheres*. Tech. rep., pp. 802–806.

Seager, S., W. Bains, and R. Hu (Nov. 2013). "Biosignature gases in H2-Dominated atmospheres on rocky exoplanets". In: *Astrophysical Journal* 777.2. ISSN: 15384357. DOI: 10.1088/0004-637X/777/2/95.

Seager, S., W. Bains, and J. J. Petkowski (June 2016). "Toward a List of Molecules as Potential Biosignature Gases for the Search for Life on Exoplanets and Applications to Terrestrial Biochemistry". In: *Astrobiology* 16.6, pp. 465–485. ISSN: 15311074. DOI: 10.1089/ast.2015.1404.

Seager, Sara, Janusz J Petkowski, and William Bains (2025). "The diversity of exoplanetary environments and the search for signs of life beyond Earth". In: *Philosophical Transactions B* 380.1931. URL: https://exoplanetarchive.ipac.caltech.edu/.

Segura, Ana et al. (Apr. 2004). "Fatty acid biosynthesis is involved in solvent tolerance in Pseudomonas putida DOT-T1E". In: *Environmental Microbiology* 6.4, pp. 416–423. ISSN: 14622912. DOI: 10.1111/j.1462-2920.2004.00578.x.

Segura, Antígona et al. (2005). "Biosignatures from Earth-like planets around M dwarfs". In: *Astrobiology* 5.6, pp. 706–725.

Sessions, Alex L. et al. (July 2009). *The Continuing Puzzle of the Great Oxidation Event*. DOI: 10.1016/j.cub.2009.05.054.

Sinha, Sweta et al. (Jan. 2023). “Spectroscopy—Principle, types, and applications”. In: *Basic Biotechniques for Bioprocess and Bioentrepreneurship*. Elsevier, pp. 145–164. ISBN: 9780128161098. DOI: 10.1016/B978-0-12-816109-8.00008-8.

Smith, Brian C. (Apr. 2024). “Infrared Spectral Interpretation, In The Beginning I: The Meaning of Peak Positions, Heights, and Widths”. In: *Spectroscopy (Santa Monica)* 39.4, pp. 18–24. ISSN: 08876703. DOI: 10.56530/SPECTROSCOPY.FI6379N1. URL: https://www.spectroscopyonline.com/view/infrared-spectral-interpretation-in-the-beginning-i-the-meaning-of-peak-positions-heights-and-widths.

Smith, Harrison B. and Cole Mathis (Dec. 2023). “Life detection in a universe of false positives: Can the Fatal Flaws of Exoplanet Biosignatures be Overcome Absent a Theory of Life?” In: *BioEssays* 45.12. ISSN: 15211878. DOI: 10.1002/bies.202300050.

Som, Sanjoy M. et al. (Apr. 2012). “Air density 2.7 billion years ago limited to less than twice modern levels by fossil raindrop imprints”. In: *Nature* 484.7394, pp. 359–362. ISSN: 00280836. DOI: 10.1038/nature10890.

Som, Sanjoy M. et al. (June 2016). “Earth’s air pressure 2.7 billion years ago constrained to less than half of modern levels”. In: *Nature Geoscience* 9.6, pp. 448–451. ISSN: 17520908. DOI: 10.1038/ngeo2713.

Sousa-Silva, Clara et al. (Feb. 2020). “Phosphine as a Biosignature Gas in Exoplanet Atmospheres”. In: *Astrobiology* 20.2, pp. 235–268. ISSN: 15311074. DOI: 10.1089/ast.2018.1954.

Steele, Derek (2006). “Infrared Spectroscopy: Theory”. In: *Handbook of vibrational spectroscopy* 1, pp. 44–70. DOI: 10.1002/9780470027325.s0103.

Stefanov, Bozhidar (2015). “Photocatalytic TiO2 thin films for air cleaning: Effect of facet orientation, chemical functionalization, and reaction conditions”. PhD thesis. Acta Universitatis Upsaliensis. ISBN: 978-91-554-9387-5. URL: http://urn.kb.se/resolve?urn=urn:nbn:se:uu:diva-265056.

Stuart, Barbara. (2004). *Infrared spectroscopy : Fundamentals and Applications*. J. Wiley, p. 224. ISBN: 0470854278.

Surkov, Iu. A. et al. (Dec. 1982). “Aerosols in the clouds on Venus - Preliminary Venera 14 data”. Russian. In: *Pisma v Astronomicheskii Zhurnal* 8, pp. 700–704.

Tesei, Donatella et al. (Mar. 2021). “Effects of Simulated Microgravity on the Proteome and Secretome of the Polyextremotolerant Black Fungus Knufia chersonesos”. In: *Frontiers in Genetics* 12. ISSN: 16648021. DOI: 10.3389/fgene.2021.638708.

Thammavongs, Bouachanh et al. (Dec. 2008). *Response to environmental stress as a global phenomenon in biology: The Example of microorganisms*. DOI: 10.1264/jsme2.23.20.

Thibessard, Annabelle et al. (Apr. 2004). “Identification of Streptococcus thermophilus CNRZ368 Genes Involved in Defense against Superoxide Stress”. In: *Applied and Environmental Microbiology* 70.4, pp. 2220–2229. ISSN: 00992240. DOI: 10.1128/AEM.70.4.2220-2229.2004.

Thombre, Rebecca S., Parag A. Vaishampayan, and Felipe Gomez (Jan. 2020). “Applications of extremophiles in astrobiology”. In: *Physiological and Biotechnological Aspects of Extremophiles*. Elsevier, pp. 89–104. ISBN: 9780128183229. DOI: 10.1016/B978-0-12-818322-9.00007-1.

Thompson, Maggie A et al. (2022). “The case and context for atmospheric methane as an exoplanet biosignature”. In: DOI: 10.1073/pnas. URL: https://doi.org/10.1073/pnas.2117933119.

Tian, Feng (Dec. 2015). “History of water loss and atmospheric O2 buildup on rocky exoplanets near M dwarfs”. In: *Earth and Planetary Science Letters* 432, pp. 126–132. ISSN: 0012821X. DOI: 10.1016/j.epsl.2015.09.051.

Tian, Feng, J. F. Kasting, and K. Zahnle (Aug. 2011). “Revisiting HCN formation in Earth’s early atmosphere”. In: *Earth and Planetary Science Letters* 308.3-4, pp. 417–423. ISSN: 0012821X. DOI: 10.1016/j.epsl.2011.06.011.

Tiquia-Arashiro, Sonia et al. (2023). *Applications of Fourier Transform-Infrared spectroscopy in microbial cell biology and environmental microbiology: advances, challenges, and future perspectives*. DOI: 10.3389/fmicb.2023.1304081.

Tourdot-Marechal, R et al. (2000). *Membrane fluidity of stressed cells of Oenococcus oeni*. Tech. rep., pp. 269–273. URL: www.elsevier.nl.

Trainer, Melissa G et al. (2006). *Organic haze on Titan and the early Earth*. Tech. rep. URL: www.pnas.orgcgidoi10.1073pnas.0608561103.

Trent, Jonathan D (2000). *Extremophiles in Astrobiology: Per Ardua ad Astra*. Tech. rep. 2.

Trotter, Eleanor W. and Chris M. Grant (2002). “Thioredoxins are required for protection against a reductive stress in the yeast Saccharomyces cerevisiae”. In: *Molecular Microbiology* 46.3, pp. 869–878. ISSN: 0950382X. DOI: 10.1046/j.1365-2958.2002.03216.x.

Trumbo, Samantha K. et al. (July 2023). “Hydrogen peroxide at the poles of Ganymede”. In: *Science Advances* 9.29. ISSN: 23752548. DOI: 10.1126/sciadv.adg3724.

Turbet, Martin et al. (Aug. 2020). *A Review of Possible Planetary Atmospheres in the TRAPPIST-1 System*. DOI: 10.1007/s11214-020-00719-1.

Van Kranendonk, J and R B Bird (Apr. 1951). *Pressure-Induced Absorption in Hydrogen*. Tech. rep. Amsterdam: Institute for Theoretical Physics, University of Amsterdam, pp. 964–965.

Vandaele, Ann C. et al. (Oct. 2024). “Composition and Chemistry of the Martian Atmosphere as Observed by Mars Express and ExoMars Trace Gas Orbiter”. In: *Space Science Reviews* 220.7. ISSN: 15729672. DOI: 10.1007/s11214-024-01109-7.

Von Zahn’, U and V I Moroz (1985). *CHAPTER V COMPOSITION OF THE VENUS ATMOSPHERE BELOW 100 km ALTITUDE*. Tech. rep. 11, pp. 173–195.

Vvedensky, Dimitri Dimitrievich (Jan. 2016). “Symmetry and spectroscopy”. In: *Encyclopedia of Spectroscopy and Spectrometry*. Elsevier, pp. 396–400. ISBN: 9780128032244. DOI: 10.1016/B978-0-12-409547-2.12172-9.

Webster, Chris R. et al. (July 2013). “Abundance and Isotopic Composition of Gases in the Martian Atmosphere from the Curiosity Rover”. In: *Science* 341.6143, pp. 260–263. ISSN: 10959203. DOI: 10.1126/science.1237961.

Wenzel, Thomas (n.d.). *MOLECULAR AND ATOMIC SPECTROSCOPY*. Tech. rep. URL: https://LibreTexts.org.

Wolf, Eric T. (Apr. 2017). “Assessing the Habitability of the TRAPPIST-1 System Using a 3D Climate Model”. In: *The Astrophysical Journal Letters* 839.1, p. L1. ISSN: 2041-8205. DOI: 10.3847/2041-8213/aa693a.

Wordsworth, Robin and Raymond Pierrehumbert (Apr. 2014). “Abiotic oxygen-dominated atmospheres on terrestrial habitable zone planets”. In: *Astrophysical Journal Letters* 785.2. ISSN: 20418213. DOI: 10.1088/2041-8205/785/2/L20.

Wunderlich, Fabian et al. (Mar. 2021). “Detectability of biosignatures on LHS 1140 b”. In: *Astronomy and Astrophysics* 647. ISSN: 14320746. DOI: 10.1051/0004-6361/202039663.

Yu, Chun Chieh et al. (Dec. 2020). “Vibrational couplings and energy transfer pathways of water’s bending mode”. In: *Nature Communications* 11.1. ISSN: 20411723. DOI: 10.1038/s41467-020-19759-w.

Yu, Yi jun et al. (Apr. 2019). “Volatile compounds released by microalgae-water phase from Taihu Lake in China”. In: *Harmful Algae* 84, pp. 56–63. ISSN: 18781470. DOI: 10.1016/j.hal.2019.01.009.

Yun, Jong-Ho, Man-Young Park, and Shi-Woo Rhee (1998). *Fourier transform infrared diagnostics of gas phase reactions in the metalorganic chemical vapor deposition of aluminum from dimethylethylamine alane*. Tech. rep.

Zahnle, K., M. Claire, and D. Catling (Dec. 2006). “The loss of mass-independent fractionation in sulfur due to a Palaeoproterozoic collapse of atmospheric methane”. In: *Geobiology*. Vol. 4. 4, pp. 271–283. DOI: 10.1111/j.1472-4669.2006.00085.x.

Zahnle, Kevin J (2819). *Photochemistry of Methane and the Formation of Hydrocyanic Acid (HCN) in the Earth’s Early Atmosphere*. Tech. rep. D2.

Zahnle, Kevin J., Marko Gacesa, and David C. Catling (Jan. 2019). “Strange messenger: A new history of hydrogen on Earth, as told by Xenon”. In: *Geochimica et Cosmochimica Acta* 244, pp. 56–85. ISSN: 00167037. DOI: 10.1016/j.gca.2018.09.017.

Zasova, L V, V A Krasnopolsky, and V I Moroz (1981). “Vertical distribution of SO2 in upper cloud layer of Venus and origin of UV-absorption”. In: *Advances in Space Research* 1.9, pp. 13–16.

Zenner, Christian et al. (Jan. 2025). “Measurement of Bacterial Headspaces by FT-IR Spectroscopy Reveals Distinct Volatile Organic Compound Signatures”. In: *Analytical Chemistry* 97.1, pp. 106–113. ISSN: 15206882. DOI: 10.1021/acs.analchem.4c02899.

Zhan, Z et al. (2021). “Assessment of Isoprene as a Possible Biosignature Gas in Exoplanets with Anoxic Atmospheres”. In: *Astrobiology* 21.7, pp. 765–792.

Zhan, Zhuchang et al. (May 2022). “Organic Carbonyls Are Poor Biosignature Gases in Exoplanet Atmospheres but May Generate Significant CO”. In: *The Astrophysical Journal* 930.2, p. 133. ISSN: 0004-637X. DOI: 10.3847/1538-4357/ac64a8.

Zimmermann, Boris and Achim Kohler (Aug. 2013). “Optimizing Savitzky-Golay Parameters for Improving Spectral Resolution and Quantification in Infrared Spectroscopy”. In: *Applied Spectroscopy*. Vol. 67. 8, pp. 892–902. DOI: 10.1366/12-06723.

Zueck, Robert F (June 2018). “Insights of the Vortex-Induced Vibration Phenomenon: Ideal Models Versus Reality”. In: DOI: 0.1115/OMAE2018-77708.

Zuo, Zhaojiang et al. (Jan. 2015). “Reactive oxygen species contribute to the release of volatile organic compounds from Chlamydomonas reinhardtii during programmed cell death”. In: *Phycological Research* 63.1, pp. 37–42. ISSN: 14401835. DOI: 10.1111/pre.12071.